Faculty of Sciences
Department of Analytical Chemistry
X-Ray Microspectroscopy and -Imaging Group

SPATIALLY RESOLVED X-RAY MICRO/NANO-SPECTROSCOPY AND IMAGING ON THE MODEL ORGANISM DAPHNIA MAGNA USING LABORATORY AND SYNCHROTRON SOURCES

Thesis submitted in fulfillment of the requirements for the degree of
Doctor (Ph.D.) in Sciences: Chemistry

by

Björn De Samber

Promotor: Prof. Dr. L. Vincze
Co-Promotor: Prof. Dr. F. Vanhaecke

May 2010

Acknowledgements

Already as a child I was doing chemistry experiments, probably encouraged by my uncle holding a PhD in chemistry. This enthousiasm never really faded out at high school, causing me to study a Master's degree in Chemistry at Ghent University. After coming back from my Erasmus period at Bordeaux University, I went to several group leaders of research groups in order to find an interesting topic for my Master thesis. Prof. Frank Vanhaecke immediately provided me with a clear and useful project in the field of mass spectrometry concerning the detection of metabolites in biological samples. It turned out that the project was so well of quality and guidance that I finished it with a lot of scientific enthousiasm and sincere gratitude.

However, when the time arrived to apply for a PhD grant, my research was at a slow pace and somewhere during this period I followed a course from Prof. Laszlo Vincze concerning X-ray analysis using synchrotron radiation facilities. When I saw the potential of biological imaging using X-rays, I was very quickly convinced this could be a great PhD topic. Because I didn't want to let down Frank, I suggested him if I could apply this technique on Daphnia magna, a biological organism of ecotoxicological relevance that his group was investigating in an interdisciplinary approach using stable isotopic tracers. Even though this more or less meant I chose for a different research field, Frank stayed generous and together with Laszlo a strong PhD project was written for the Fund for Scientific Research in Flanders for which I am very thankful to both of them.

Thanks to the support of the FWO, I could engage on the scientific matter, but suddenly the mass spectrometry research started to provide the envisaged results. Suddenly I was getting a bit afraid whether it wouldn't be a shame to leave this very nice topic behind and start with something completely new. In the department, a poster drew my attention offering the possibility to attend a summerschool of 8 weeks at the Hamburg Synchrotron Radiation Laboratory. I thought this could be the ideal opportunity to have a nice start for my PhD research topic. During this stay I received many great lectures and got hands-on experience. Within this context, I would like to thank Dr. Gerald Falkenberg, responsible at that time for the Hard X-ray Microprobe Beamline L at the DORIS III storage ring in Hamburg, Germany. Gerald, many thanks for your patience during my first steps in the

X-ray field and for providing so much help and support! I am also very grateful to Dr. Karen Rickers for offering her crucial help and support during the beamtimes which followed after that. Also Dr. Gerd Wellenreuther was a great help in providing us a cryogenic gas stream allowing to perform X-ray analysis on fully hydrated biological samples.

I would like to use this opportunity to express my thanks to my supervisor Prof. Laszlo Vince. Thanks to him, I can look back to a memorable PhD research period. His assistance and provided skills during most of the beamtimes were admirable. During my entire PhD period he was always willing to provide information and support. His continuous encouragement and enthousiasm were of crucial importance to continue the research. Thanks to his generosity and high level scientific research I was also able to present my scientific research at several international conferences. Laszlo, you were a great supervisor and have become a good friend, thanks for everything!

Even though highly sophisticated analyses can be performed at synchrotrons, they often mean nothing if samples with little scientific relevance are measured. Throughout the PhD work, Prof. Colin Janssen supported our X-ray experiments on Daphnia magna. I also wish to thank Dr. Karel De Schamphelaere for further practical advice and scientific input. I am also extremely grateful to Roel Evens, Leen Pieters and Shanna Vanblaere for preparing the samples and their assistance during the beamtime experiments.

For this work I would also like to express my gratitude to the X-ray tomography research group under the supervision of Prof. Luc Van Hoorebeke. I remember how impressed I was by their home built X-ray scanning instrument and software tools. They were always willing to receive me and performed many CT scans on Daphnia magna. Thanks to Bert's and Manu's excellent work and skills, we were able to couple our elemental information with an accurate 3D absorption tomography dataset, delivering us images of unseen quality.

I would also like to sincerely thank my collegues from the X-Ray Microspectroscopy and Imaging (XMI) group. Without their help, it would never have been possible to obtain the experimental results in this PhD. Tom Schoonjans was great in establishing a good computer infrastructure. Also, every computer problem I encountered which would make me loose days, he managed to solve in a quick and efficient way. Also Dr. Geert Silversmit, the postdoc of the group was a great collegue. I very much enjoyed our scientific discussions in general and his ability to convert any dataprocessing problem towards an efficiently working program which could solve the problem was admirable. He was also a great help for gaining more expertise in the field of X-ray absorption spectroscopy experiments. I would also like to express my gratitude to Dr. Bart Vekemans. Several software tools such as AXIL, MICROXRF2, K-means clustering and Principal Component analysis were of crucial importance for the datatreatment performed in this thesis. Moreover Bart also ensured that we obtained a first laboratory based X-ray microprobe, which allowed me to perform inhouse X-ray experiments

on Daphnia magna. Within this context, I would also like to thank Deepti Gholap and Dr. Andrei Izmer for their mass spectrometry imaging on Daphnia magna which enabled a comparison of the elemental imaging results by both techniques.

I would also like to express my gratitude to a number of people from the European Synchrotron Radiation Facility (ESRF). I was especially very much inspired by the opportunity to attend the sample preparation and nanochemical analysis of individual neurons at the ID22NI Hard X-ray Nanoprobe together with Dr. Sylvain Bohic. I would also like to thank the ID22NI staff for help and support during our measurements on Daphnia magna: Gemma Martinez-Criado, Remi Tucoulou, Peter Cloetens and Jean Susini. Their assistance and support allowed us to perform X-ray experiments using submicrometer X-ray beams at a truly unique beamline!

During my PhD, I had to work together with several students. I enjoyed very much introducing them into the X-ray research field and it was a nice experience to gradually see them taking initiatives. Obtaining the three-dimensional confocal elemental isosurfaces and fourier filtering of element sinograms was the result of several interesting Bachelor projects. I would also like to thank my thesis student Inge Lindemann for her assistance during beamtimes and datatreatment during the last year of my PhD.

Motivated and good research can only be performed on a solid basis of friendship and love. Therefore I would also like to thank my collegues, friends and family for their support and help. I am especially very thankful to my parents, who always encouraged me to study hard and gave me all the financial means to obtain my degree. Finally, I also would like to thank my fiancé Nele, who had to put up with my distracted behaviour. Nele, you were a continuous support for me all the way through, thank you so much!

Björn De Samber
Gent 2010

Contents

Chapter 1

Introduction and Scope of the Research

This work demonstrates and further develops spatially resolved laboratory and synchrotron X-ray spectroscopic and imaging experiments to answer specific ecotoxicological questions on the model organism *Daphnia magna*. The first phase of this work consisted of developing appropriate sample preparation procedures for this organism in order to be able to perform X-ray analyses on *Daphnia magna* subjected to ecotoxicological experiments. In the second phase, X-ray set-ups at different laboratories and synchrotron facilities were optimized and characterized in order to be able to perform the X-ray spectral imaging experiments of interest on *Daphnia magna*. Finally, various data reduction strategies were employed to process the vast amount of spectral data for evaluation and interpretation.

1.1 X-ray analysis

X-rays were originally defined by their energy: electromagnetic radiation which has a wavelength in the range of 10 to 0.01 nm, which are corresponding to energies in the range of 120 eV to 120 keV (Van Grieken & Markowicz, 2002). However, X-rays produced by linear accelerators and astrophysical processes can have a higher energy than gamma rays. Because of this overlap in energy ranges, X-rays are now defined by their origin; they are emitted by electrons outside the nucleus, while gamma rays are emitted by the nucleus or from other particle decays or annihilation events.

X-rays were discovered in 1895 by Wilhelm Conrad Röntgen, for which he received the first Nobel prize in physics in 1901. He found that their density dependent attenuation in matter allows the visualization of the internal structure of the irradiated material, which was the base of modern radiography. In 1914, another Nobel prize in physics was awarded for discovering that X-rays diffract when sent through crystals. This work provided the spark for using X-

rays and crystals to uncover the secrets of chemical compounds at the atomic level, for which a Nobel prize was awarded to William Bragg in 1915. Besides the absorption and diffraction of X-rays, the discovery of the emission of characteristic secondary X-rays from a material that has been excited by bombarding with high-energy X-rays led to another Nobel prize for Charles Glover Barkla in 1917 (Nobel Prize Website, 2009).

Based on the emission of characteristic X-rays, X-ray fluorescence analysis (XRF) developed into a well-established and mature multi-element technique, capable of yielding accurate quantitative information on the elemental composition of a variety of samples in a non-destructive manner. With the discovery and further ongoing development of focusing optics and electronic detection systems for X-rays, XRF evolved from a non-visual phase towards a visual phase. Micro-XRF (μ-XRF) became available as an important variant of the bulk technique yielding spatially resolved quantitative elemental information on the microscale (Janssens *et al.*, 1996). Due to the polychromatic nature of X-ray tube emission, detection limits which can be obtained using laboratory remained on the *ppm* level. However, at synchrotron facilities, X-rays are produced with unique properties compared to X-ray tubes in the form of synchrotron radiation. Although synchrotron radiation was originally considered as a nuisance, its unique properties were quickly recognized, resulting in the construction of dedicated second generation synchrotron radiation facilities (Von Bohlen & Tolan, 2008). Synchrotron micro-XRF became one of the few analytical techniques allowing spatially resolved elemental information on the microscale at the *ppb* level. Moreover, with the recent development of micro-XRF CT (Vincze, 2004) and confocal micro-XRF (Vincze *et al.*, 2004), the elemental distributions can be visualised in 3D. Since at a synchrotron source the energy of the X-ray beam can also be continuously varied, the absorption edge of a target element can be investigated. This ability makes additional techniques possible, such as micro-XANES (X-ray absorption Near-Edge Structure) and micro-EXAFS (Extended X-ray Absorption Fine Structure) which provide non-destructive local information on the valence and coordination environment of a target element which may be present in traces (Newville, 2009). Since 1995, third generation synchrotron sources became available with a tremendous increase in brilliance (Weckert, 2004). Recently, submicrometer sized X-ray beams reaching the diffraction limit allow the chemical investigation of samples at this unprecedented resolution (Mimura *et al.*, 2007). Since the human being is a highly visual-centric species, many fields of science are embracing this visual phase in elemental analysis (Kemp, 2008). With the interdisciplinary integration and ongoing improvements of state-of-the art detectors, optical components and innovative experimental set-ups (Fig. 1.1), synchrotron and laboratory based X-ray spectroscopy is thus currently a quickly developing field of research, which has even been argumented to evolve faster than Moore's law (Adams, 2008).

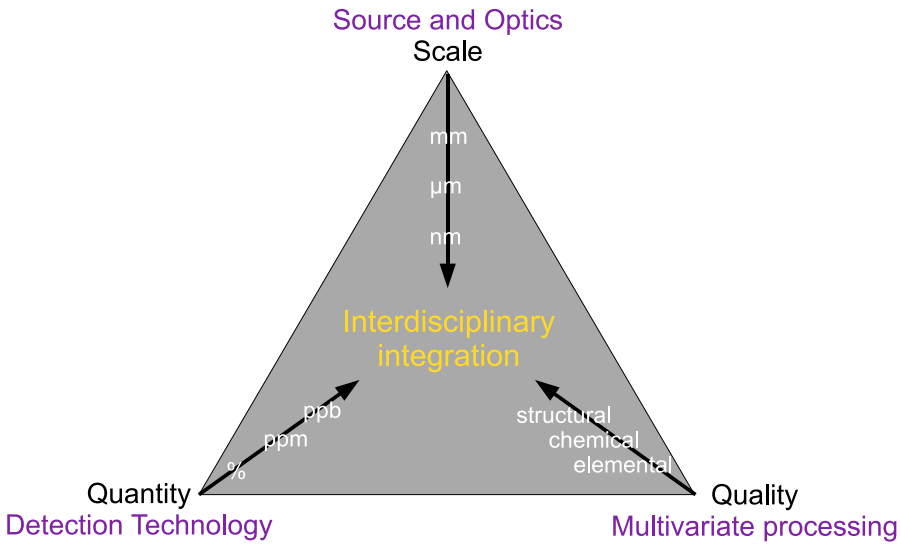

Figure 1.1: Synchrotron radiation-based microanalytical techniques provide multi-scale information. Reproduced from Bouvet *et al.* (2007).

1.2 Aquatic toxicology

In the field of environmental toxicology, the study on the effects of the presence of transition metals such as Cu, Ni and Zn on the health of pelagic and benthic invertebrates is an important research topic. The benthic zone is the ecological region at the lowest level of a body of water such as an ocean or a lake (including the sediment surface and some sub-surface layers), while the pelagic zone is the ecological zone not close to the bottom or near to the shore. Efforts are being made to develop increasingly accurate biotic ligand models (BLMs) which can then be used to predict the metal toxicity as a function of the metal concentration and the physicochemical characteristics of the surface water. On the basis of reliable BLMs, scientifically more relevant environmental regulations can be defined (Paquin *et al.*, 2002). Within the laboratory of Environmental Toxicology and Aquatic Ecology at Ghent University, the ecotoxicological model organism *Daphnia magna*, a freshwater crustacean, is frequently used to investigate the mechanisms of toxicity metals (Heijerick *et al.*, 2005).

Historically, it has often been difficult to link bioaccumulation of metals to toxic effects in *Daphnia* because few analytical techniques are able to determine and visualise the three-dimensional trace level metal distributions at the micro- and nanoscale within these delicate millimeter sized organisms while providing local structural information of the elements envisaged at the same time (Petitbois & Guidi, 2008). However, for a further refinement and a more direct underpinning of these models, relating toxicological effects at the (sub)tissue level is a necessity since organisms must regulate transcription, translation, proper assimila-

tion, incorporation and detoxification of metals to function (Szpunar, 2004). *Metallomics* has recently even been defined as a new field of science referring to investigation of the entirety of individual metal species in a cell and encompass the inorganic (free and complexed) element content and the ensemble of its complexes with endogenous or bio-induced biomolecules (Haraguchi, 2004). Therefore, in this dissertation, the previously mentioned dramatic progress in X-ray spectroscopy and imaging is highlighted by illustrating its potential within the ecotoxicological research on *Daphnia magna*.

1.3 Structure of the dissertation

In Chapter 2 of this work, an overview is given of the various components that are necessary for performing laboratory and synchrotron X-ray spectroscopy experiments. This involves the production and focusing of X-ray beams, the interaction of X-rays with matter, followed by the detection of X-ray photons and processing of the spectral data.

A general description on ecotoxicology, aquatic toxicology and metal toxicity on *Daphnia magna* will be further elaborated in the first three sections of Chapter 3. A first bottleneck is the appropriate fixation of the biological system for X-ray analysis, which will be discussed in the final section of Chapter 3.

In Chapter 4, we characterize a laboratory micro-XRF probe and verify its possibilities for the detection, imaging and quantification of metals within *Daphnia magna*. The obtained results are compared with those attainable by laser ablation inductively coupled plasma mass spectrometry (LA-ICPMS), which is very often highlighted as a more sensitive technique. The difference in sensitivity between both techniques is investigated and the imaging capabilities of LA-ICPMS on *Daphnia magna* are shown.

Synchrotron radiation based scanning XRF however offers the possibility of 2D/3D non-destructive elemental imaging with (sub)microscopic resolution coupled with the necessary trace level detection limits. In Chapter 5 and Chapter 6, we illustrate various scanning modes (2D micro-XRF, micro-XRF CT and confocal micro-XRF) on *Daphnia magna* under conventional and cryogenic conditions. Moreover, we investigate the combination of the previously mentioned micro-XRF techniques with X-ray absorption microtomography, providing an accurate frame of reference of the sample investigated.

In Chapter 7, the potential of X-ray absorption fine structure (XAFS) is investigated. XAFS is a technique which can deliver informaton about the chemical environment selected within metal-enriched microscopic structures, which could provide insight in possible detoxification of target elements.

With the above mentioned improvements of SR-sources in brilliance and in available spa-

tial resolution at various facilities, the microscopic research is now rapidly shifting towards nanoscopic research. In chapter 8, we investigate metal distributions within *Daphnia magna* at the nanoscopic level.

Chapter 2

Laboratory and Synchrotron Radiation X-ray Spectroscopy

2.1 Introduction

In this chapter, we first discuss the generation of X-rays by means of laboratory and synchrotron radiation sources. X-rays are produced when electrical charges are strongly accelerated, for instance by striking a metal surface, as in an ordinary X-ray tube, or by being deflected in a magnetic field, as in a synchrotron or in a free electron laser (FEL). The generated X-rays can then interact with matter by various processes like photoelectric absorption, elastic (Rayleigh) and inelastic (Compton) scattering, which will be discussed in a next section. By making use of their interaction properties with matter, X-rays can subsequently be collimated, monochromatised and focussed by advanced X-ray optics. Therefore, we introduce the working principle of several X-ray optics such as polycapillaries, compound refractive lenses, zone plates and Kirkpatrick-Baez mirror systems. After the interaction of the X-ray beam with the sample, the response needs to be measured with sophisticated detection systems. We therefore introduce different detection systems of interest for X-ray analysis. Finally, the raw data needs to be processed efficiently and quantification algorithms can be applied, which will be discussed in a final section.

2.2 Production of X-rays

2.2.1 X-ray tube based X-ray production

Historical aspects

X-rays were discovered by Röntgen in 1895 by accident while studying the conduction of electric current through gases at low pressure using an experimental discharge tube called a *Crookes' tube*. Röntgen observed that a barium platino-cyanide fluorescent screen a few

meters from his experiment suddenly started to glow. Röntgen concluded that the glow was caused by certain unknown rays that were given off in his experiment. Because of its unknown character, Röntgen called this radiation X-rays. As the medical and other uses of X-rays became apparent, workshops began to manufacture specialized Crookes tubes to produce X-rays. The Crookes tube was improved by William Coolidge in 1913, also called a *Coolidge tube* and led to the development of the *rotating anode tube* (Beckhoff *et al.*, 2005).

General design of an X-ray tube

In an X-ray tube, the method by which X-rays were produced in Röntgen's first experiments is basically the one still used today. In these devices, an electric field causes electrons emitted by a negatively charged metal surface (the cathode) to accelerate and bombard a positively charged metal plate (the anode).

In a Coolidge tube (Fig. 2.1), the electrons are produced by thermionic effect from a tungsten filament heated by an electric current. The filament is the cathode of the tube. The applied high voltage between the cathode and the anode accelerates the electrons towards the anode surface, where the electron beam interactions generate X-rays. The generated X-ray spectrum consists of discrete components corresponding to the characteristic lines of the anode material, and a continuous component due to braking radiation (Bremsstrahlung) emitted by the deccelerating electrons. Because X-ray production is very inefficient (99% of incident energy is converted to heat) the dissipation of heat at the focal spot is one of the main limitations on the power which can be applied.

The rotating anode tube (Fig. 2.2) is an improvement of the Coolidge tube. By sweeping the anode past the focal spot the heat load can be spread over a larger area, greatly increasing the power rating. The anode consists of a disc with an annular target close to the edge. The anode disc is supported on a long stem which is supported by bearings within the tube. The anode can then be rotated by electromagnetic induction from a series of stator windings outside the evacuated tube. Because the entire anode assembly has to be contained within the evacuated tube, adequate heat removal must be assured since direct cooling by conduction or convection, as in the Coolidge tube, is difficult (Als-Nielsen & McMorrow, 2001).

Theoretical aspects

Classical electrodynamics tells us that when charged particles are accelerated, they emit radiation (Jackson, 1975). The total radiation power of a charge e moving with velocity $v < c$ in an external field is given by the Larmor formula:

$$P = \frac{1}{4\pi\epsilon_0}\frac{2e^2}{3c^3}a^2 \tag{2.1}$$

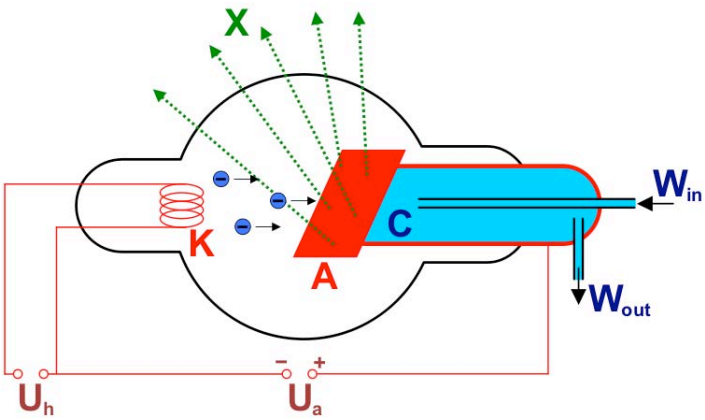

Figure 2.1: Coolidge side-window tube schematic: filament K, anode A, cooling device C with water inlet W_{in} and outlet W_{out}. Reproduced from Wikipedia (2009c).

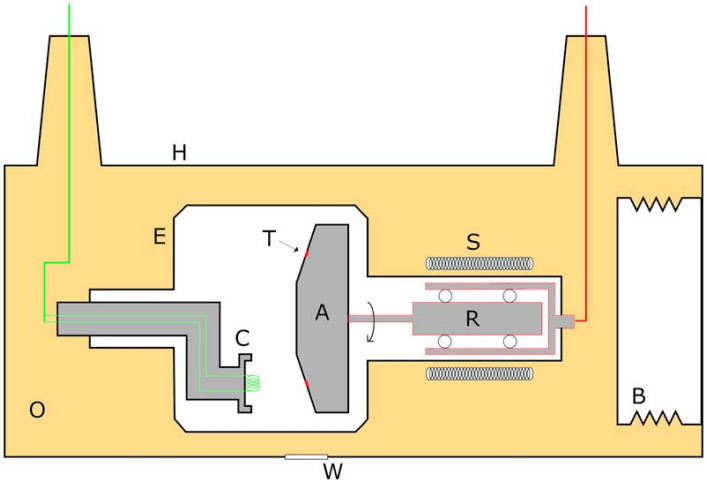

Figure 2.2: Simplified rotating anode tube schematic: Anode A, cathode C, anode target T, X-ray window W. Reproduced from Wikipedia (2009c).

where a is the acceleration of the charge and ϵ_0 denotes the permittivity of vacuum. When highly energetic electrons impinge on a metal surface, they can be deflected by other charged particles such as electrons and nuclei. As the electrons decelerate, they lose their kinetic energy. The higher the applied voltage, the greater the kinetic energy of the electrons striking the anode. A large part of the kinetic energy of the decelerating electrons is converted into heat. Due to the decelaration the electron also emits part of this energy in the form of X-ray radiation called *Bremsstrahlung*, which is German for braking radiation (Haug & Nakel, 2004). The electrons can also expel bound electrons out of the shells of the atoms in the target metal. This process creates vacancies in the atomic shells. Electrons from shells with higher energy levels can fill these vacancies, giving off surplus energy in the form of discrete X-ray lines. The energy of these lines depends on the energy levels of the anode material in question and differs from one metal to another. It is therefore called *characteristic radiation*. Both *Bremsstrahlung* and *characteristic radiation* form the X-ray excitation spectrum of an X-ray tube. Typically, voltages between 10 and 40 kV are typically used to produce X-rays. (Als-Nielsen & McMorrow, 2001).

2.2.2 Synchrotron based X-ray production

Historical overview

Man-made synchrotron radiation (SR) was observed for the first time in April 1947 at General Electric in an advanced type of accelerator, an *electron synchrotron* (Elder *et al.*, 1947). Fig. 2.3 shows a photograph of the emitted (visible) synchrotron light observed at the General Electrics synchrotron accelerator. Since synchrotron radiation represents a source of energy loss for the accelerated particles, it was initially considered as a nuisance by accelerator designers and particle physicists. However, scientists investigating the nature of this energy loss quickly recognised the unique characteristics of synchrotron radiation, emitted from the bending magnets of synchrotrons built for particle physics experiments. These unique properties of synchrotron radiation can be summarized as follows:

- energy/wavelength tunability over a large range of the electromagnetic spectrum.
- natural collimation.
- very high intensity.
- polarization properties.
- a pulsed time structure.

The benefits of SR due to its remarkable features in many respects revolutionized X-ray based scientific research. Very quickly, a broader research community applied the highly brilliant

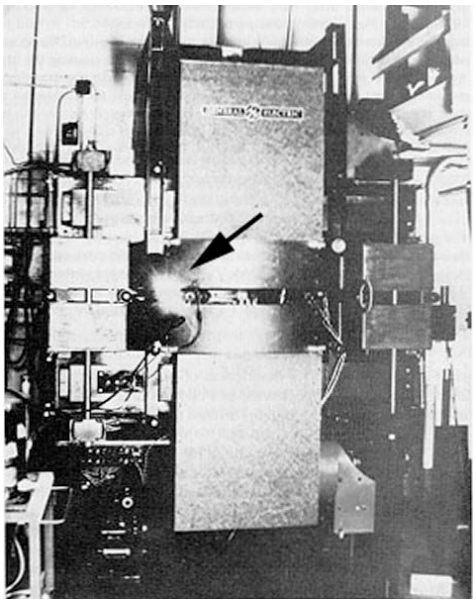

Figure 2.3: General Electric synchrotron accelerator. Reproduced from Wikipedia (2009b).

radiation emerging from synchrotrons in pioneering experiments and they recognised the potential offered to a variety of scientific disciplines (Von Bohlen & Tolan, 2008). Because of the huge surge of interest, the so-called first generation synchrotrons were soon followed by the second generation sources, providing radiation from synchrotron storage rings dedicated exclusively to the generation of SR. In addition to SR emitted by bending magnets, linear, periodic magnetic arrays of small dipoles, so-called wigglers have also been installed in these second generation sources for producing even more intense SR. Such wigglers provide a 30-100 fold flux compared to a bending magnet. All these machines have in common relatively large particle beam (electron or positron) cross sections of the order of one millimeter. They therefore provide rather broad photon beams, which are very well suited for studies of samples of millimeter to centimeter sizes. However, for the third generation sources, a further, rather dramatic improvement of the photon beam quality has been achieved by exploiting the constructive interference of the radiation emitted from the individual poles of periodic magnetic structures called *undulators*. For these devices to function efficiently rather small and parallel particle beams are needed, which lead to the construction of the so-called low-emittance third-generation storage rings. The demanding requirements and the fast growth of the user community led to the construction of dedicated synchrotron radiation sources specialized for serving undulators with particle energies matching the photon energy range needed for the main applications. The highly brilliant undulator beams can be focussed in order to investigate small samples or sample regions in the sub-millimeter to sub-micrometer range. The most suitable parameter to characterize sources of the 3^{rd} generation is brilliance,

which represents the number of photons per second in a given energy range normalized to the size of the source and to the solid angle under which the radiaton is emitted. Fig. 2.4 shows the brilliance of the first operational 3^{rd} generation synchrotron source (ESRF) compared to the brilliance of sources of other generations. The dramatic increase in brilliance from 2^{nd} to 3^{rd} generation facilities has triggered a large number of new techniques and experiments unthinkable before. Due to these dramatic improvements, many synchrotron radiation techniques have reached a considerable state of maturity and a high degree of automation, thus making these techniques available for a wide user community (Weckert, 2004).

Currently, an increasing number of dedicated synchrotron sources are available, specifically constructed to provide optimum conditions for a variety of experiments in a broad field of applications. The development of experimental techniques answering a wide variety of scientific questions is progressing at an unprecedented pace. In more than fifty facilities spread over the whole world, about 40000 scientists are using synchrotron radiation very often in an interdisciplinary approach. During the past 30 years, research carried out at synchrotron radiation facilities has made significant contributions to basic as well as applied sciences. In Fig. 2.5, the evolution of published articles containing the word *synchrotron* through time is given. The distribution is represented by the vertical blue bars, the orange bars represent a combined search for *synchrotron* and *spectroscopy*. Both graphs show a dramatic increase of publishing activities in 1991, which is connected to the construction of three large third generation synchrotron facilities: the European Synchrotron Radiation Facility (ESRF), Grenoble, France; Advanced Photon Source (APS), Argonne, USA; and Super Photon ring-8 GeV (SPring-8), Hyogo, Japan. The construction was finished in 1994, 1996, and 1997, respectively (horizontal green line), while ESRF started operating in 1994 (horizontal blue line) (Von Bohlen & Tolan, 2008).

General design of a synchrotron storage ring

SR facilities typically consist of an injection system, a storage ring and beamlines. In the injection system, electrons are generated, pre-accelerated and sometimes a second accelerator further accelerates these electrons to more than 1 GeV before injection into the storage ring. In the ring, bunches of electrons periodically circulate at relativistic speeds for periods of up to many hours. The storage ring consists of bending magnets, insertion devices (the actual sources of SR), radio-frequency (RF) cavities, and other control systems as shown in Fig. 2.6 (Ide-Ektessabi, 2007).

Bending magnets (Fig. 2.7) bend the trajectory of charged elementary particles (electrons or positrons) and force them to circulate in a closed orbit. Synchrotron radiation is emitted when the electrons/positrons are passing through the magnetic field of the bending magnet, and are accelerated by the arising Lorentz force. The magnitude of the relativistic (vertical)

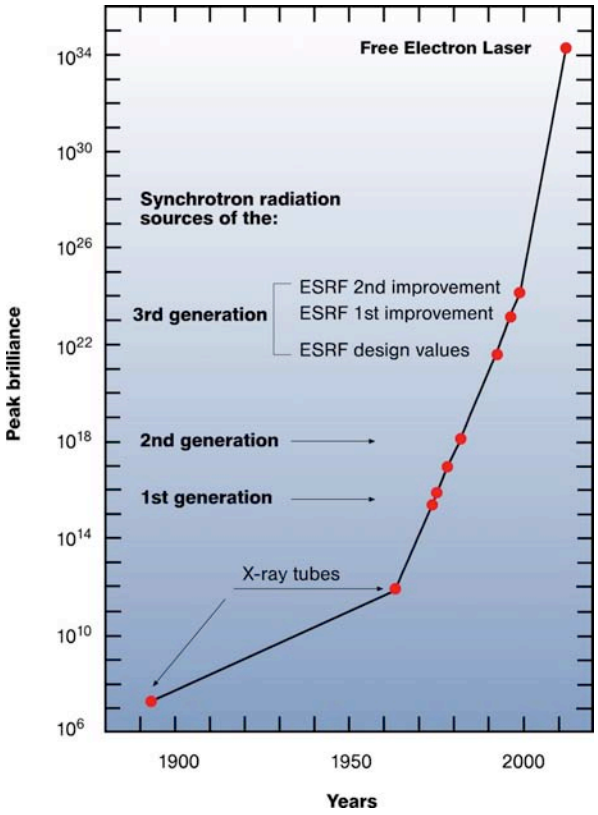

Figure 2.4: Increase of brilliance through time. Reproduced from European XFEL (2009).

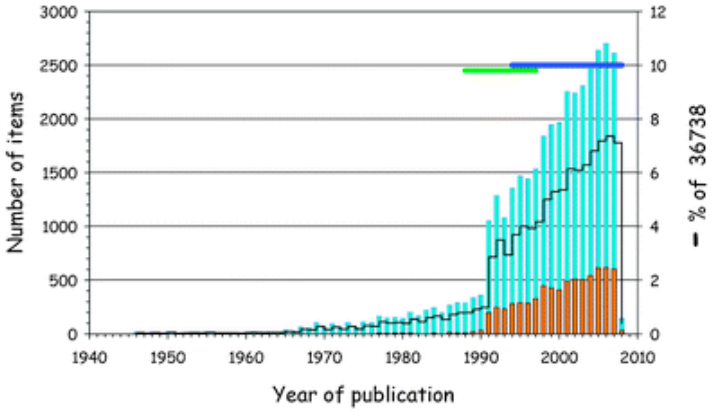

Figure 2.5: Publications containing synchrotron listed in the ISI Web of Science. Reproduced from Von Bohlen & Tolan (2008).

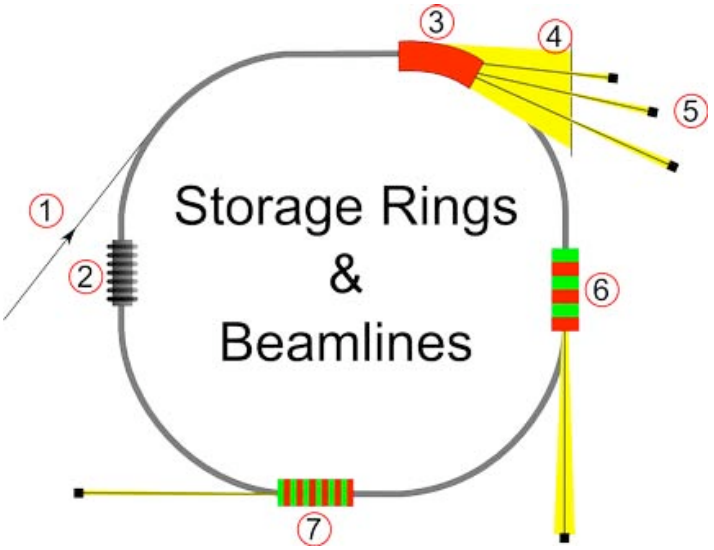

Figure 2.6: Schematic overview of the different components of a synchrotron. (1) injection system, (2) RF system, (3) storage ring/bending magnets, (4) beamlines, (5) experiments, (6) wigglers, (7) undulators. Reproduced from Hasylab (2009c).

angular width of the bending magnet radiation$\Delta\ \psi$ is given by:

$$\Delta\psi = \frac{1}{\gamma} \tag{2.2}$$

where $\gamma = \frac{E}{m_0 c^2}$ is the Lorentz contraction factor.

The critical wavelength is given by:

$$\lambda_c[nm] = \frac{18.64}{BE^2} \tag{2.3}$$

where B is the magnetic field of the bending magnet in Tesla and E is the electron/positron beam energy (machine energy) in the accelerator expressed in GeV. One half of the power is radiated above and one-half below the critical wavelength (Fig. 2.8). As can be seen in Fig. 2.8 bending magnets provide a limited brilliance as compared to **wigglers** and **undulators**, which will be discussed in a next section (Raven, 1998).

Insertion devices are comprised of periodic arrays of dipole magnets with alternating polarity. The efficiency of photon production is increased by forcing the electrons/positrons to oscillate perpendicularly to their direction of motion. This oscillation is given by the movement in a periodic alternating magnetic field. As electrons pass through the insertion device, the trajectories of electrons wiggle several times and the electrons emit synchrotron radiation. According to the magnitude of the oscillation of the electron trajectory, there are two types insertion devices: **wigglers** and **undulators** (Fig. 2.7). The difference between a wiggler

and an undulator is the amplitude of the transverse oscillation K/γ, where K is the so-called deflection parameter ($K \gg 1$ for wigglers and $K \preceq 1$ for undulators), which determines the degree of electron beam deflection in the magnetic structures:

$$K = \frac{e}{2\pi mc}\lambda_u B_0 \tag{2.4}$$

where λ_u is the period and B_0 is the amplitude of the magnetic field (Raven, 1998).

In a **wiggler** (Fig. 2.7), $K \gg 1$ is valid, i.e. the angular deviation (or deflection angle) of the electron beam is large compared to the natural opening of synchrotron radiation $1/\gamma$ due to a sequence of bending magnets with a strong magnetic field. An observer on the electron axis sees only the radiation emitted over a small part of the trajectory, each bunch of a duration being smaller than the time between two bunches. The different bunches therefore cannot interfere with each other and the resulting radiation is the incoherent addition from each pole. This produces radiation which has a continuous spectrum with higher fluxes and with shorter wavelengths compared with bending magnet radiation (Fig. 2.8). The wiggler is often used as a source in order to increase the flux at shorter wavelenghts. A sequence of bending magnets with n poles of alternating polarities can enhance the flux by $2n$ times. The critical wavelength for a wiggler is lower that that of a bending magnet (Raven, 1998).

The angular deviation (or deflection angle) of an **undulator** (Fig. 2.7) is smaller than the natural opening of synchrotron radiation ($K \preceq 1$) due to a periodic array of relatively weak magnetic fields, i.e., all radiation is constantly emitted within a cone of $1/\gamma$ and the contributions from every pole add up coherently, giving rise to quasi-monochromatic undulator radiation which can be orders of magnitude larger than the natural synchrotron radiation (Fig. 2.8). The coherent interference effects produce highly collimated radiation, which has one or a few spectrally narrow peaks (a fundamental one and harmonics). For an n-pole undulator, the beam's opening angle is decreased by $n^{1/2}$ and thus the intensity per solid angle increases as n^2 (Raven, 1998).

The **RF cavity** system restores energy, which the electrons loose because of the emission of SR. The frequency of acceleration voltage is fixed to an integral multiple of the orbital frequency. That is, in the phase of RF, the voltage is synchronized when electrons come to the RF cavity on the reference orbit. Electrons that are slightly fast, get less acceleration and slow down because the phase of the acceleration voltage is ahead and the RF voltage is smaller. On the other hand, electrons that are slightly slow get more acceleration and speed up. Thus, the electrons exhibit longitudinal oscillations around the reference center of the bunch and the bunch of electrons that are accelerated together is stabilized (Ide-Ektessabi, 2007).

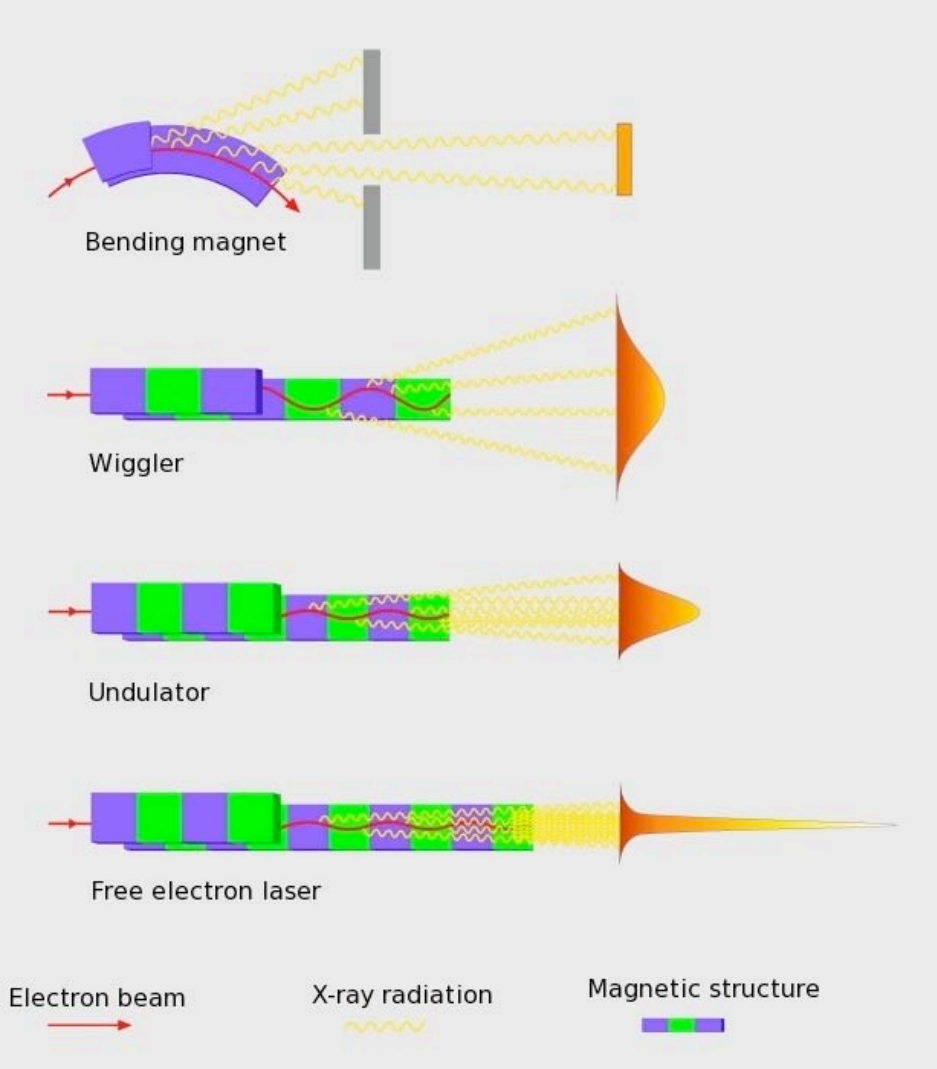

Figure 2.7: Schematic depiction of a bending magnet, wiggler, undulator and free electron laser. Reproduced from Hasylab (2009c).

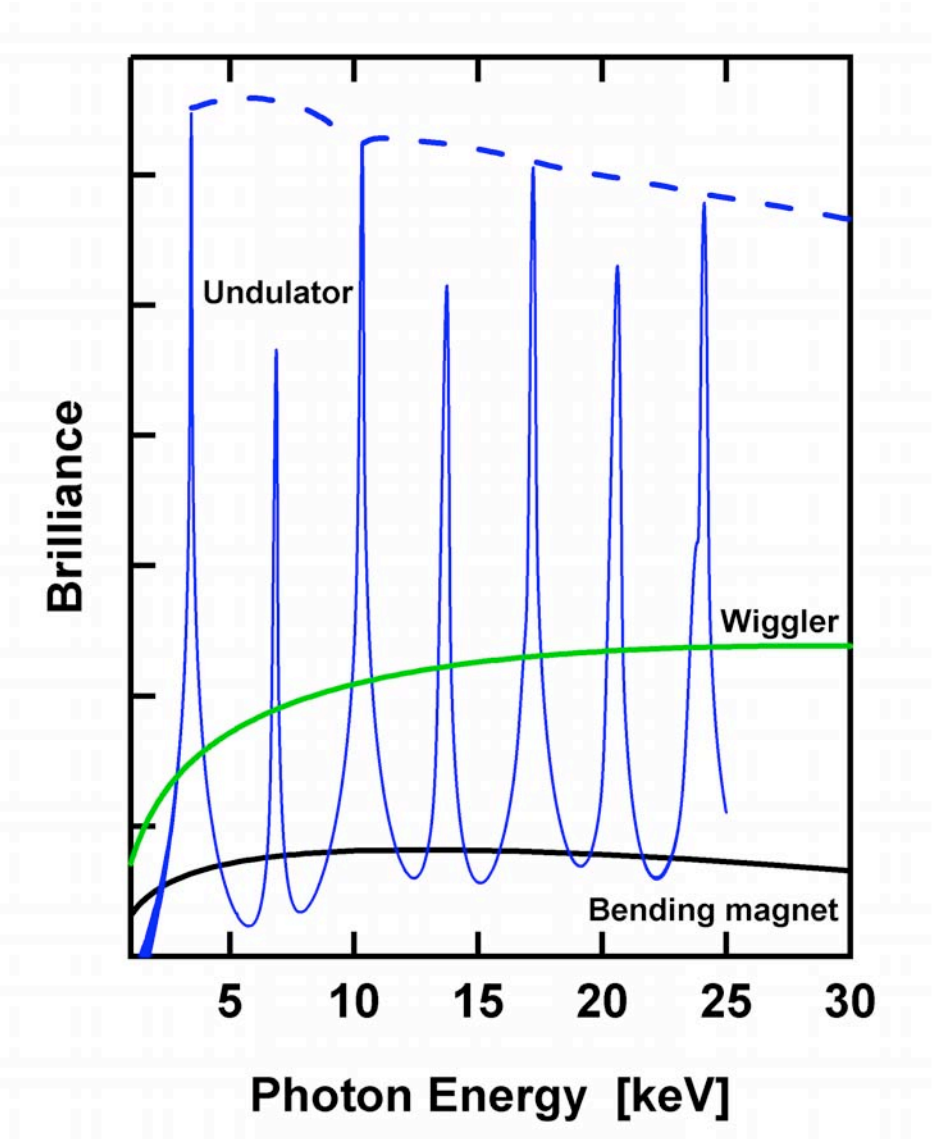

Figure 2.8: Comparison of the spectra of bending magnets, wigglers and undulators. Reproduced from Hasylab (2009c).

Theoretical aspects

The Lorentz Invariant Representation of the Larmor Formula gives the total power radiated by a relativistic point charge as it accelerates:

$$P = \frac{e^2 c}{6\pi\epsilon_0}\frac{1}{(m_0c^2)^2}\left[\left(\frac{\mathrm{d}\vec{p}}{\mathrm{d}\tau}\right)^2 - \frac{1}{c^2}\left(\frac{\mathrm{d}E}{\mathrm{d}\tau}\right)^2\right] \tag{2.5}$$

where e is the charge of electrons, c the speed of light, m_0 the rest mass of an electron, $\frac{\mathrm{d}\vec{p}}{\mathrm{d}\tau}$ and $\frac{\mathrm{d}E}{\mathrm{d}\tau}$ the derivative of momentum and energy with respect to time $\mathrm{d}\tau = 1/\gamma \mathrm{d}t$ respectively, using the Lorentz contraction factor $\gamma = \frac{E}{m_0c^2}$.

If electrons that are moving with nearly the velocity of light ($v \sim c$) are constrained to move in a curved path (e.g. a circle, spiral or undulating) they will be accelerating towards the inside of the curve and will also radiate what we call synchrotron light or synchrotron radiation. Although the total power radiated by linear acceleration can often be neglected, this is not the case for radiation by a circular acceleration, which is given by (Hasylab, 2009a):

$$P = \frac{e^2 c}{6\pi\epsilon_0}\frac{1}{(m_0c^2)^4}\frac{E^4}{R^2} \tag{2.6}$$

where R is the bending radius and E the energy of the particle, indicating that the power emitted increases for high energy particles and decreases for larger accelerator facilities. Since $(\frac{m_{proton}}{m_e})^4 = 1836^4$, synchrotron radiation is only playing a role for electrons/positrons.

The emitted radiation power within the solid angle $\mathrm{d}\Omega$ is given by (Hasylab, 2009a):

$$\frac{\mathrm{d}P(t)}{\mathrm{d}\Omega} = \frac{e^2}{4\pi c}\frac{\dot{\beta}^2}{(1-\cos\theta)^3}\left(1 - \frac{\sin^2\theta\cos^2\phi}{\gamma^2(1-\beta\cos\theta)^2}\right) \tag{2.7}$$

where $\beta = v/c$, $\gamma = (1-\beta^2)^{-1/2}$, while θ and ϕ represent the angular coordinates within a classic spherical coordinate system. Due to relativistic effects, the dipole pattern expected from non-relativistic theory is therefore not isotropic, but transformed into an extremely forward-pointing cone of radiation as shown in Fig. 2.9.

Other interesting properties of synchrotron radiation are its linear polarisation and its pulsed time structure. Fig. 2.10 illustrates that the planar acceleration geometry makes the radiation linearly polarized when observed in the orbital plane. Outside from the orbital plane, the radiation has an elliptical polarisation with strongly declining intensity (Hasylab, 2009a). The importance of the linear polarisation of synchrotron radiation for X-ray fluorescence applications will be shown in the section dealing with interaction of X-rays with matter. The characteristics of the pulsed time structure of synchrotron radiation can be derived theoretically. Subsequently, the spectral photon density of the excitation spectrum can be calculated by means of a Fourier-transformation of the time spectrum (Jackson, 1975). However, since

the pulsed time structure of synchrotron radiation was not used within this study, further discussion is not within the scope of this work.

Characterization of synchrotron radiation

Several quantities together with their practical units are frequently used to measure the intensity of synchrotron radiation, such as flux, angular flux and brilliance.
The **Flux** F is the number of photons per time and energy interval:

$$[F] = \frac{[\text{Number of photons}]}{[0.1\%\text{BW}][s]} \tag{2.8}$$

The **Angular Flux** or **Brightness** B_{ang} is the number of photons per time, energy and also per solid angle:

$$[B^{ang}] = \frac{[\text{Number of photons}]}{[mrad^2][0.1\%\text{BW}][s]} \tag{2.9}$$

The **Brilliance** B is often used to characterize synchrotron radiation sources, since in most cases the number of photons arriving at the sample is more important as the number of photons emitted by the source. Therefore, it indicates the number of photons per time, energy, solid angle and also source size:

$$B = \frac{F}{4\pi^2 \epsilon_x \epsilon_y} = \frac{F}{4\pi^2 \sigma_{Tx} \sigma_{Ty} \sigma_{Tx'} \sigma_{Ty'}} \tag{2.10}$$

$$[B] = \frac{[\text{Number of photons}]}{[mm^2][mrad^2][0.1\%\text{BW}][s]} \tag{2.11}$$

where F is the spectral photon flux; σ_{Tx} and σ_{Ty} are the total photon source sizes in horizontal and vertical direction, respectively; $\sigma_{Tx'}$ and $\sigma_{Ty'}$ are the total beam divergence in horizontal and vertical direction. The total photon source size and divergence are given by the convolution of the size ($\sigma_{x,y}$) and divergences ($\sigma_{x',y'}$) of the electron beam with the intrinsic radiation characteristics ($\sigma_r, \sigma_{r'}$) of a single electron. For that reason the horizontal emittance

$$\epsilon_x = \sigma_x \cdot \sigma_{x'} \tag{2.12}$$

of a storage ring is of crucial importance for the photon beam parameters. The vertical emittance is given by $\epsilon_y = \kappa \cdot \epsilon_x$ with the so-called coupling factor κ that depends mainly on the precision of the alignment of the storage ring. Typical values for κ at present synchrotron radiation storage rings are in the range of 1%. The brilliance is usually given in units of $(photons/(smm^2 0.1\% BW)$ and characterizes the number of photons per unit phase space volume. Undulator sources at modern 3^{rd} generation storage rings are very well suited to

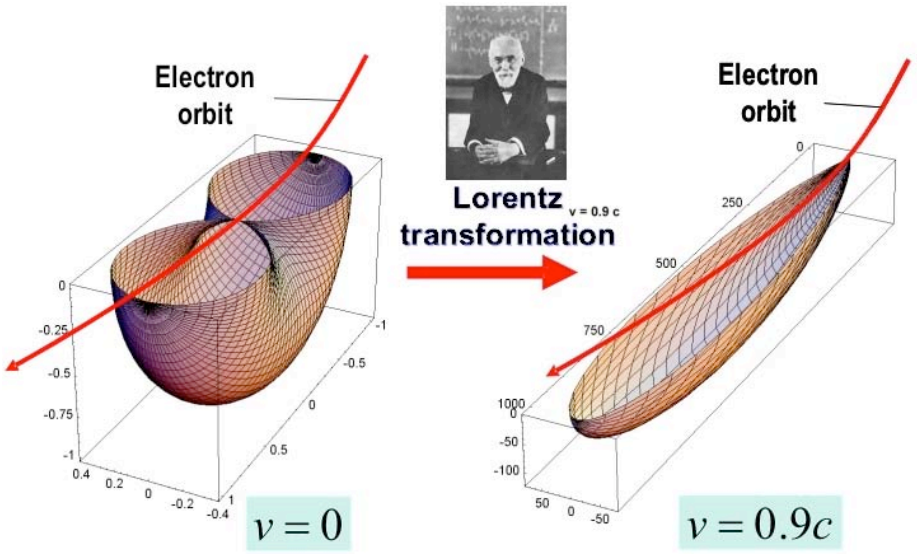

Figure 2.9: Emission of radiation in the electron's frame and after transformation into the lab frame. Reproduced from Komitee Forshung mit Synchrotronstrahlung (2009).

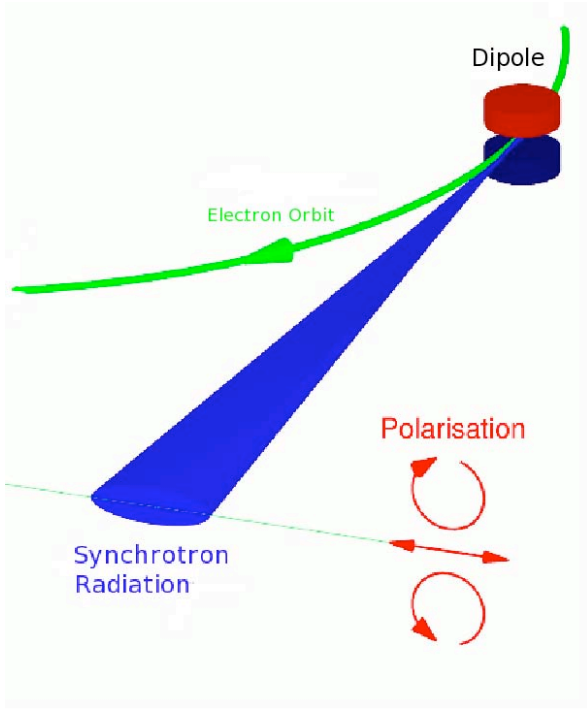

Figure 2.10: Linearly and elliptically polarised synchrotron radiation. Reproduced from Hasylab (2009a).

produce high brilliance due to the small source size and the low divergence of the emitted radiation (Weckert, 2004).

To a certain extent it is also possible to focus the relatively large beam of a wiggler of a 2^{nd} generation source onto a small sample area at the expense of an increased divergence in the focus. However, due to limitations in the achievable demagnification ratio and the small aperture of X-ray optical elements, the large source size of 2^{nd} generation storage rings imposes a lower limit for the smallest achievable focal spot size. If an experiment requires both, high flux on a very small sample area and a beam as parallel as possible, then only 3^{rd} generation sources are able to fulfill these demands (Weckert, 2004).

2.2.3 Large scale synchrotron facilities

In this section two large scale synchrotron facilities are introduced, which were used in this work: the Hamburger Synchrotronstrahlungslabor (HASYLAB) in Hamburg, Germany and the European Synchrotron Radiation Facility (ESRF), Grenoble, France.

HASYLAB at DESY

The Hamburger Synchrotronstrahlungslabor (HASYLAB) is part of the Deutsches Elektronen-Synchrotron (DESY), one of the worlds leading centres for the investigation of the structure of matter. DESY runs and uses various accelerators for photon science and particle physics. In Fig. 2.11, a schematic overview is given of the different accelerator devices present at DESY: several LINACs preaccelerate particles which are then injected in circular storage rings such as the orginal DESY (Deutches Elektronen Synchrotron) ring and the DORIS (Double Ring Storage) ring. DESY also features larger accelerators, such as PETRA and HERA, where major scientific breakthroughs were achieved until summer 2007. Originally the DORIS storage ring was used for particle physics experiments. After rebuilt it was called DORIS III and was operated by the Hamburger Synchrotronstrahlungslabor. It provides a considerable flux also at photon energies in the hard X-ray regime beneficial to a number of applications that require penetration into or through larger bulk specimen. The large positron beam at DORIS III provides relatively large photon beams which are ideally suited for the investigation of milli- to centimeter samples. The different beamlines available at DORIS III can be seen in Fig. 2.12.

However, small samples, extremely small foci, experiments at extremely high resolution in reciprocal space or in energy or coherence experiments, are beyond the capability of the radiation provided by the DORIS III storage ring. For that reason the 2304 m long storage ring PETRA II was rebuilt into a 3^{rd} generation synchrotron radiation source called PETRA III, which can be seen on Fig. 2.13. The particle energy of this new source is 6 GeV at an initial current of 100 mA. The emittance of PETRA III will be 1 $nmrad$ which is a so

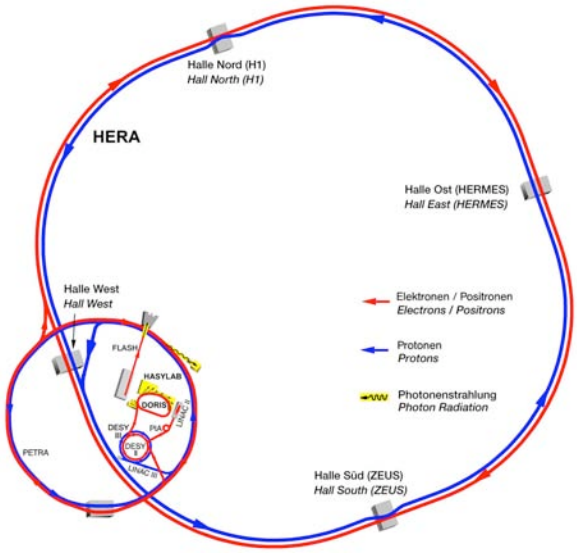

Figure 2.11: Schematic view of the facilities availabe at DESY. Reproduced from Hasylab (2009b).

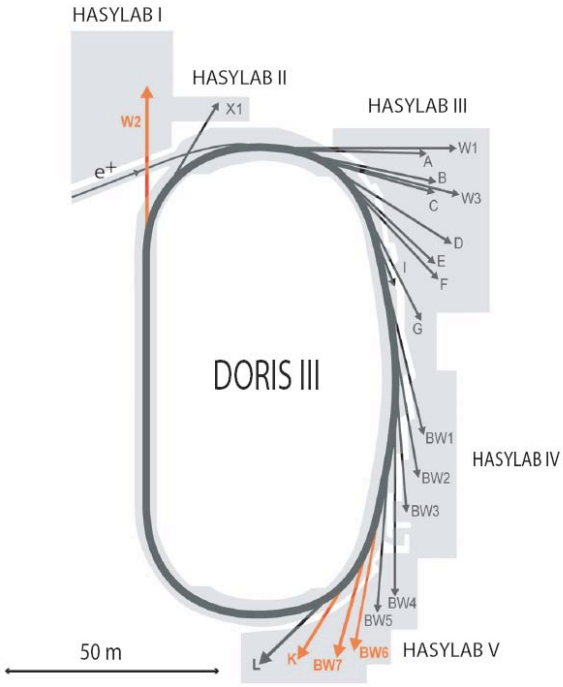

Figure 2.12: DORIS III and its beamlines. Reproduced from Hasylab (2009b).

far unrivaled value for storage rings operated at a comparable high particle energy for the production of hard X-rays. PETRA III will provide a maximum brilliance of the order of 10^{21} $ph/s/mm^2/0.1\%BW$ with a considerable fraction of coherent photons also in the hard X-ray range. With a coupling ratio of 1% PETRA III will be diffraction limited in the vertical direction up to a photon energy of about 10 keV. The choice of a particle energy of 6 GeV was motivated by an optimization for a small beam emittance, which scales with the square of the energy, and a sufficiently high particle energy which is needed to provide tunable high-energy photon beams with sufficient flux and brilliance.

Recently, DESY has also been investing in other research areas. Therefore the FLASH facility has also been built, which generates extremely intense short-wavelength laser pulses which are used to produce images of nanoparticles, viruses and cells. Since recently, the final plans for the XFEL (X-ray Free Electron Laser) have been approved. XFEL will complement the unique range of light sources in the Hamburg region. The high-intensity X-ray laser flashes from the XFEL will, for example, enable movies to be made with atomic resolution. An areal overview of the unique facilities within the DESY campus can be seen in Fig. 2.13 (Hasylab, 2009b).

The European Synchrotron Radiation Facility

The European Synchrotron Radiation Facility (ESRF) was the first third generation synchrotron radiation source, starting its user operation in 1995. Located in Grenoble, France, it is one of the three high energy 3^{rd} generation SR sources operational worldwide (Fig. 2.14). The source is optimised to produce hard X-rays in the 1 to 100 keV range. The comissioning of the source started in 1992 and it has been open to the user community since 1994. The majority of the beamlines use an insertion device (ID) as a source point which generates high fluxes and brilliance in the 2 to 40 keV range of photon energy (Fig. 2.15). Recently, an ambitious Upgrade Programme, spread over ten years (2009-2018) was approved. The upgrade programme will involve 1) a radical upgrade of the performance of the ESRF's beamlines and open up the possibility for new beamlines 2) improvement of the X-ray source to become even brighter and more intense 3) widen and improve the range of experimental instruments 4) develop more research partnerships with academic groups and also industry.

2.2.4 Laboratory synchrotron facilities

Recently, prototypes of laboratory synchrotrons are being developed. The laboratory MIRRORCLE synchrotron has two basic components, a classical microtron, and a storage ring. The microtron emits and accelerates electrons and then injects them into the storage ring. Depending on the configuration of the MIRRORCLE synchrotron, a target in the circulating electrons produces X-rays. The covered X-ray energy range of MIRRORCLE is from a few keV to 6 MeV and the 85 $mrad$ radiation angle are both wider than that of a conventional

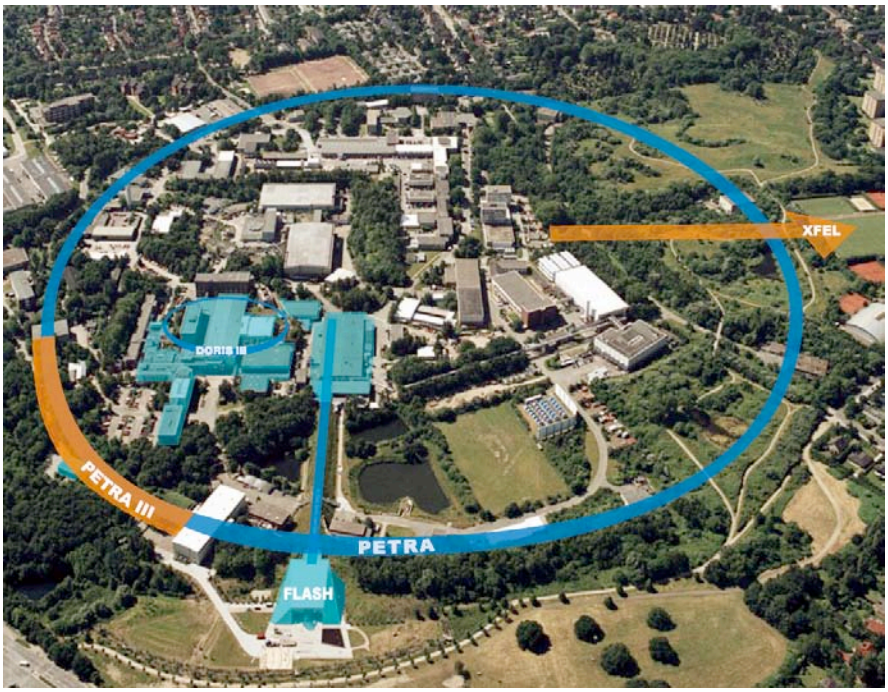

Figure 2.13: Areal view of the facilities where research activities are performed: DORIS III, PETRA III, FLASH and the future XFEL. Reproduced from Hasylab (2009b).

Figure 2.14: The European Synchrotron Radiation Facility (ESRF). Reproduced from ESRF (2009).

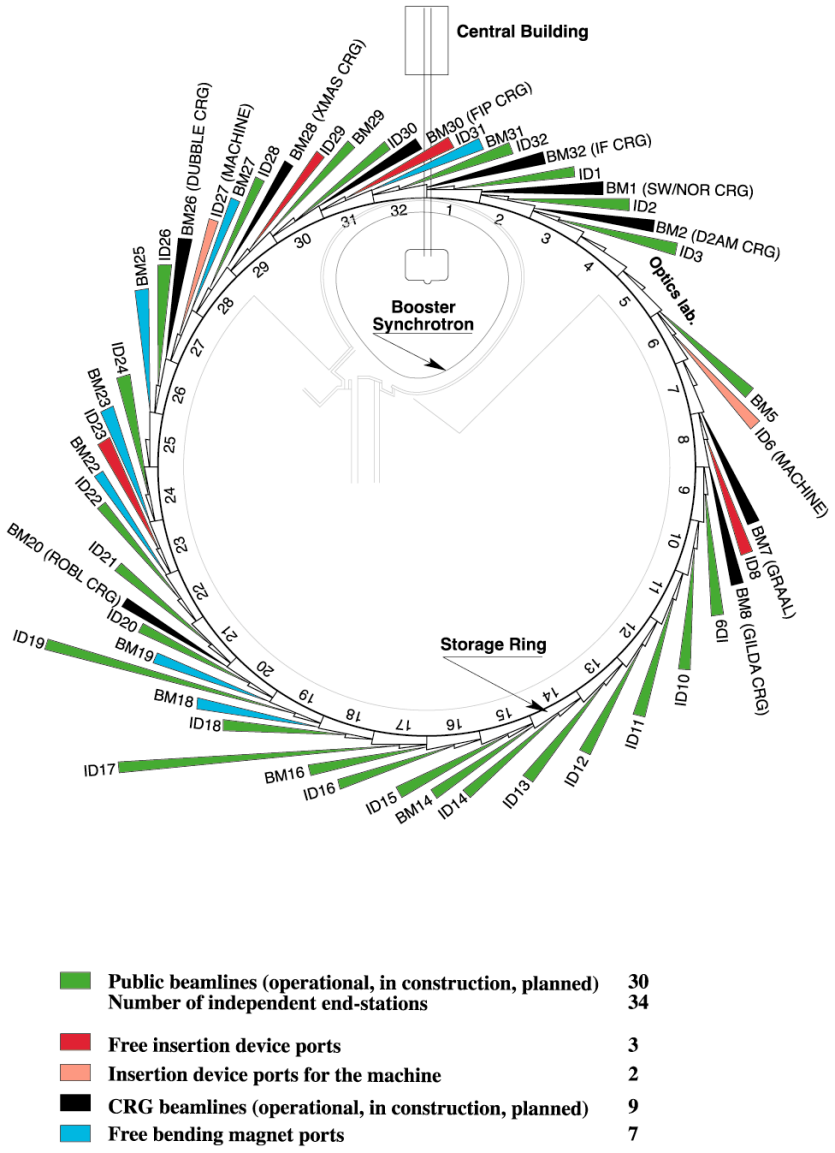

Figure 2.15: Schematic of the experimental hall with different beamlines. Reproduced from ESRF (2009).

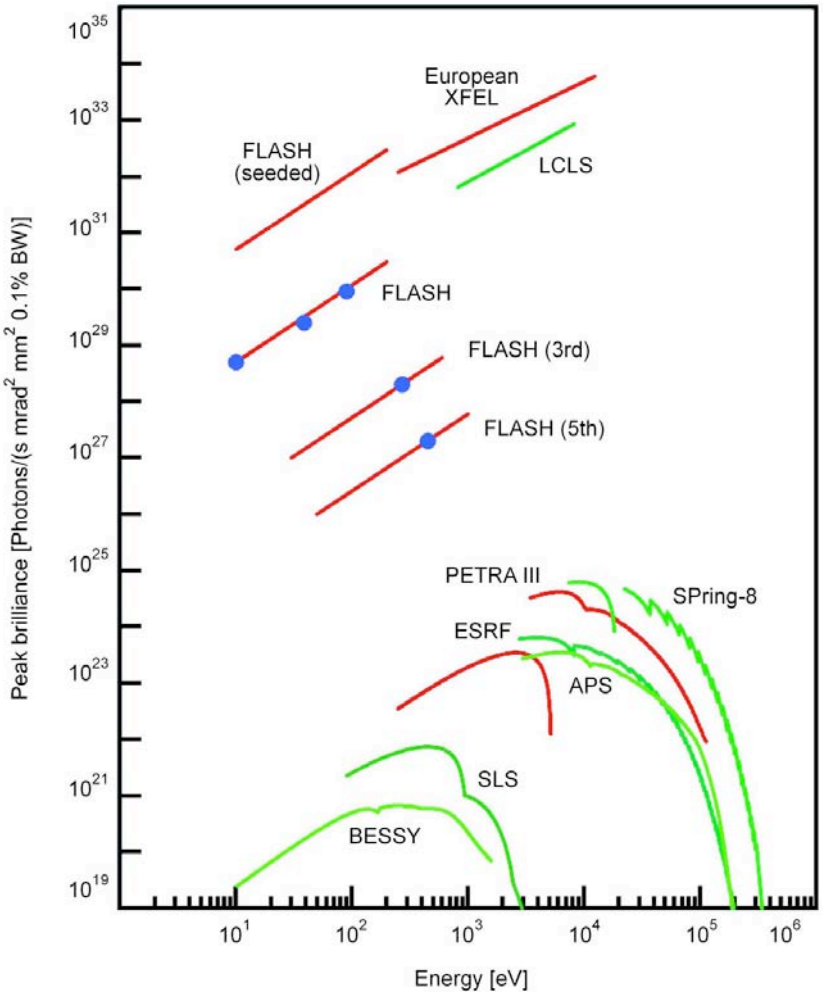

Figure 2.16: Comparison of brilliance of different accelerator facilities. Reproduced from European XFEL (2009).

synchrotron. Therefore, the total X-ray flux of 10^{14} $photons/s$, $0.1\%bandwidth$ is brighter, but the brightness of 10^9 $photons/s\ mrad^2\ mm^2$ $0.1\%bandwidth$ is comparable. Due to the large beam spread, the instrument provides a wide imaging field and edge enhancement without additional optical elements. Besides X-ray imaging, it has been illustrated that the technique also provides potential for X-ray diffraction, scattering, fluorescence and XAFS (Photon Production Laboratory, 2009).

LYNCEAN technologies introduces a laboratory synchrotron using an electron beam and a laser beam undulator (Ruth, 2009). A laser beam colliding with an opposing electron beam has the same effect as an electron beam passing through an undulator magnet. The electric and magnetic fields of the laser beam cause the electron to wiggle and induces a radiation spectrum similar to that from a long undulator magnet. The much smaller period length of the laser based undulator source, governed by the employed laser wavelength, reduces the scale and energy of the device by a factor of about 200 and results in a storage ring with a footprint comparable to that of a large office desk.

2.3 Interaction of X-Rays with matter

2.3.1 Introduction

When an X-ray beam passes through matter, a certain fraction of the photons will be *absorbed* inside the material or *scattered* away from the original path. The intensity I_0 of an X-ray beam passing through a layer of thickness x and density ρ is reduced to an intensity I according to the well-known law of Lambert-Beer:

$$I(x) = I_0 e^{-\mu_L x} = I_0 e^{-\frac{x}{\lambda}} \tag{2.13}$$

where $\mu_L[cm^{-1}]$ is called the linear attenuation coefficient, $\lambda = 1/\mu_L[cm]$ is the attenuation length and $\mu = \mu_L/\rho[cm^2/g]$ is the mass attenuation coeffient. In the energy range of 1-100 keV the mass attenuation coefficient can be described as:

$$\mu = \tau + \sigma_R + \sigma_C \tag{2.14}$$

where $\tau(E, Z)$ is the photo-electric effect, $\sigma_R(E, Z)$ is the Rayleigh (elastic/coherent) scattering and $\sigma_C(E, Z)$ is the Compton (inelastic/incoherent) scattering (Van Grieken & Markowicz, 2002). At most X-ray energies, the mass attenuation coefficient μ is a smooth function of energy, with a value that depends on the sample density ρ, the atomic number Z, atomic mass A, and the X-ray energy E roughly as (Newville, 2009):

$$\mu \approx \frac{\rho Z^4}{AE^3} \tag{2.15}$$

When the sample consists of a mixture of several chemical elements (e.g. a biological sample), the mass attenuation coefficient μ can be calculated from the mass attenuation coefficients of the n constituting elements:

$$\mu(compound) = \sum_{i=1}^{n} w_i \mu_i \tag{2.16}$$

where w_i is the weight fraction of element i.

Fig. 2.17 shows the contributions of the photo-electric, Rayleigh and Compton cross-sections to the total cross-section of Zn within the energy range of 1-100 keV. The smooth dependance of the mass attenuation coefficient with $1/E^3$ can be seen, although a sharp absorption K-edge can be observed at 9.659 keV, whereas the $L_1/L_2/L_3$ edges are present at 1.196/1.044/1.021 keV.

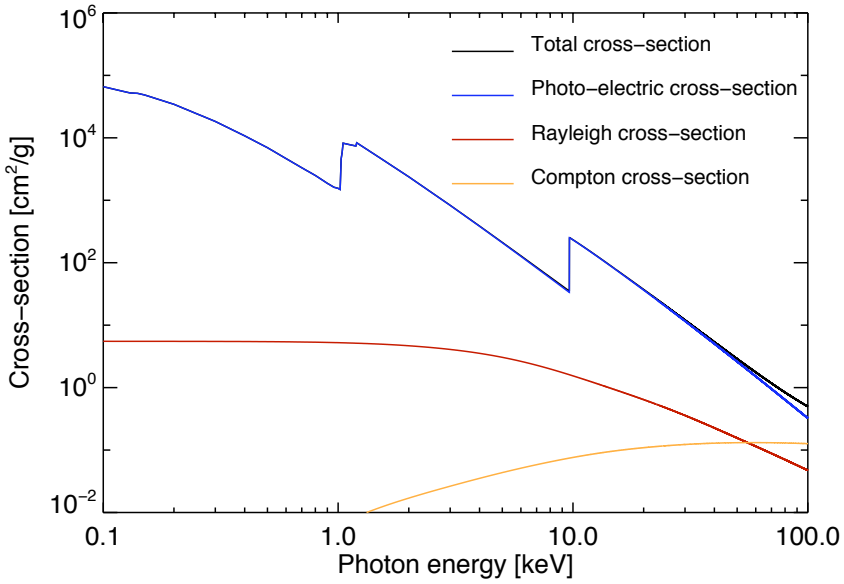

Figure 2.17: Cross-section for photon scattering from Zn showing the contributions of photo-electric, Rayleigh and Compton cross-sections to the total cross-section. Calculated from Brunetti *et al.* (2004).

2.3.2 Photoelectric effect

In the photoelectric effect, the incoming X-ray photon with energy E_x interacts with a bound atomic electron and is completely absorbed as shown in Fig. 2.18. The excited atom emits a photoelectron with energy $E = E_x - E_{shell}$, where E_{shell} is the binding energy of the electron. As a secondary effect, the hole in the atomic shell is immediately filled by less bound electrons

from outer shells, resulting in a cascade process involving the emission of fluorescence X-rays characteristic for the absorbing atom as illustrated in Fig. 2.19. A fraction of the absorbed energy is also emitted by ejection of Auger electrons. The intensity of this characteristic radiation is directly related to the amount of each element in the material (Beckhoff *et al.*, 2005).

2.3.3 Scattering

While photoelectric interactions result in an isotropic emission of characteristic radiation, scattering interactions produce photons having highly anisotropic angular distributions. Therefore the ratio of fluorescence/scatter intensities can be strongly influenced by the choice of excitation/detection geometry. Quantitatively, the intensity of Rayleigh/Compton scattered radiation can be characterized by the so-called differential scattering cross-sections $d\sigma/d\Omega$, which characterize the angular distribution for the scattered photons. For the description of a linearly polarized photon beam, the local coordinate system is chosen in such a way that the photon beam (having an initial propagation vector $\vec{k_0}$) travels along the Z-axis prior to the interaction and its (net) electric field vector $\vec{\epsilon_0}$ is parallel with the X-axis (Fig. 2.20). After the scattering event, the new direction of photon propagation is characterized by the (unit) progation vector $\vec{k_1}$ and the net electric vector $\vec{\epsilon_1}$ (Vincze, 2004).

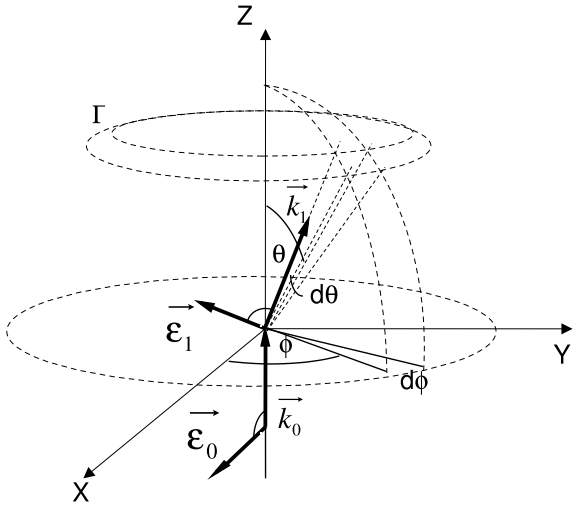

Figure 2.20: The cöordinate system attached to the photon used to describe the scattering phenomenon. Reproduced from Vincze *et al.* (1999).

In case of linearly polarized radiation having a degree of polarization p with respect to the reference plane XZ, the expression for the Rayleigh ($d\sigma_R/d\Omega$) and Compton ($d\sigma_C/d\Omega$)) differential scattering cross-sections are, respectively, given by:

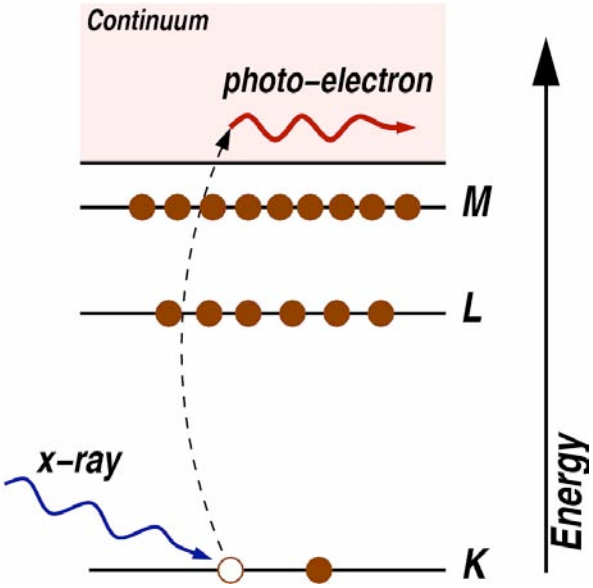

Figure 2.18: The photo-electric effect, in which an X-ray is absorbed and a core-level electron is promoted out of the atom. Reproduced from Newville (2009).

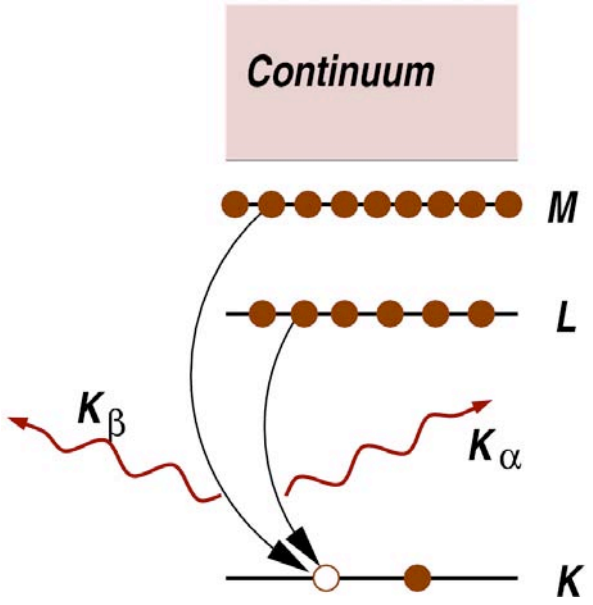

Figure 2.19: A less bound electron from the L or M shell falls back to a hole created in the K-shell by the photo-electric effect, causing X-ray fluorescence as a secondary effect. Reproduced from Newville (2009).

$$\frac{d\sigma_R}{d\Omega}(\theta,\phi,E) = \frac{d\sigma_T}{d\Omega}(\theta,\phi)F^2(x,z) \quad (2.17)$$

$$= \frac{r_e^2}{2}\left[2 - sin^2\theta(1-p+2cos^2\phi)\right]F^2(x,Z) \quad (2.18)$$

$$\frac{d\sigma_C}{d\Omega}(\theta,\phi,E) = \frac{d\sigma_{KN}}{d\Omega}(\theta,\phi)S(x,z) \quad (2.19)$$

$$= \frac{r_e^2}{2}\left(\frac{E}{E_0}\right)^2\left[\frac{E}{E_0}+\frac{E_0}{E} - sin^2\theta(1-p+2cos^2\phi)\right]S(x,Z) \quad (2.20)$$

where $d\sigma_T/d\Omega$ denotes the Thomson and $d\sigma_{KN}/d\Omega$ the Klein-Nishina differential cross-section. $F(x,Z)$ and $S(x,Z)$ are the atomic form factor and the incoherent scattering function respectively, for an element with atomic number Z. $x = sin(\theta/2)E(keV)/12.39$ is the momentum transfer of the photon and r_e is the classical electron radius (Vincze, 2004) .

The previous equations show that $d\sigma_R/d\Omega = 0$ and that $d\sigma_C/d\Omega$ reaches a minimum for $p = 1$, $\theta = 90°$ and $\phi = 0°$. Since the degree of linear polarization can approach 99.8 % at 3^{rd} generation SR sources and also the angle between the incoming beam and the scattering angle is not exactly 90 ° for the complete detector surface, implying that there will still be an influence of the Rayleigh and Compton scatter. However, for X-ray fluorescence applications, the angle between the incoming beam and the detector in the plane of the synchrotron (assuming $p \sim 1$) is set to 90 °, so that the Compton scatter will reach its minimum (Vincze, 2004).

2.4 focusing optics for X-rays

Focusing of hard X-rays has long been considered unfeasible. This was mainly the consequence of the weak refraction of this type of electromagnetic radiation with matter, resulting in a refractive index n very close to unity. While lenses for visible light are made of a transparent material with an index of refraction substantially different from 1, there is no equivalent material for X-rays. First solutions for X-ray focusing were proposed by M.A. Kumakhov, and were originally thought out as the total reflection of X-rays from smooth surfaces (Gibson & Kumakhov, 1992). Today, several focusing solutions exist for hard X-rays also including refractive and diffractive optics as illustrated by Fig. 2.21. There has been tremendous progress over the last ten years in X-ray optics. An extrapolation of the current trend is shown in Fig. 2.22 (Bouvet *et al.*, 2007).

2.4.1 Polycapillary optics

A polycapillary X-ray optic consists of an array of a large number of small hollow glass tubes formed into a certain shape. The optic collects X-rays that emerge from an X-ray source

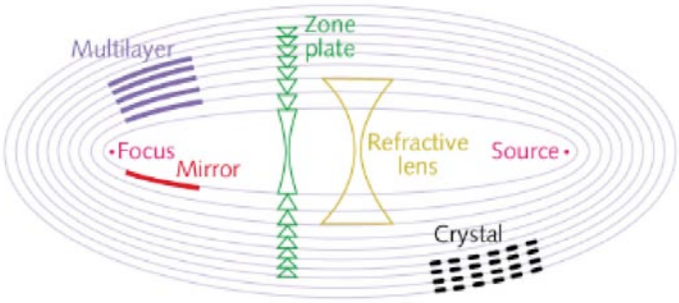

Figure 2.21: Schematic illustration of various X-ray optical elements. Reproduced from Bouvet *et al.* (2007).

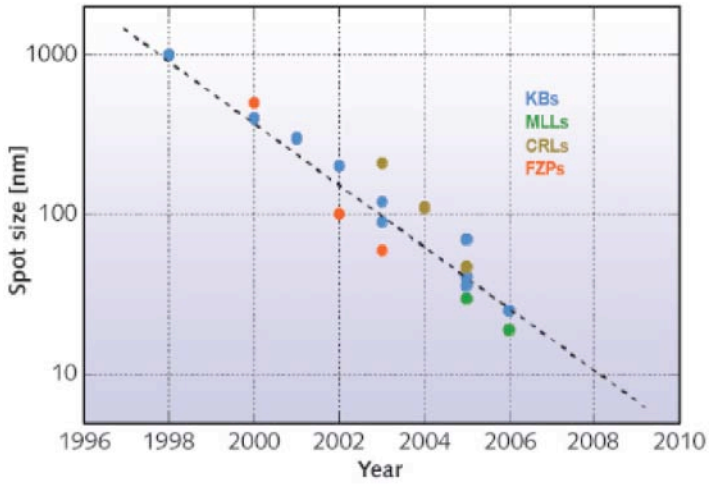

Figure 2.22: Historical evolution of the measured spot size (in nanometres) for different hard X-ray focusing elements (KB: Kirkpatrick-Baez mirror pair; MLL: multilayer Laue lenses; CRL: compound refractive lenses; FZP: Fresnel zone plate). Reproduced from Bouvet *et al.* (2007).

within a large solid angle and redirects them, by multiple external total reflections, to form either a focused beam or a parallel beam, as illustrated by Fig. 2.23. As shown in Fig. 2.24, the direction of X-ray radiation can be changed when X-rays undergo multiple total reflections within a bent capillary, as long as the incident angle at each reflection is less than a critical angle θ_c. As this critical angle is very small (of the order of a few $mrad$ for X-rays in the 5-30 keV for reflection on glass surfaces), the bending curvature of the capillary has to be gentle and the capillary diameter has to be small to maintain the total reflection condition. The typical radius of curvature of the individual hollow glass tubes within a polycapillary optics is about a few hundreds of mm and the channel diameter is anywhere from a few μm to a few tens of μm (Gao & Janssens, 2004).

Monolithic polycapillary devices are a new generation of polycapillary devices that, instead of using supporting metal screens, the polycapillary fibers are closely packed and then fused together and formed into the desired shape through a heating process. One of the most distinguishing properties of a monolithic optic is that the cross-section of an individual channel changes along the length of the optic so that each individual channel points to the focus of the optic. As a result, the transmission efficiency of the optic is significantly increased and other beam properties, such as the focal spot size and beam divergence are improved (Gao & Janssens, 2004).

Several Monte Carlo ray tracing simulation programs are available that are able to calculate the trajectory of individual X-ray photons within a particular hollow glass tube that form part of a polycapillary lens. Each of them has unique features that greatly help researchers to better understand the properties of the polycapillary optics and their potential application capabilities. State-of-the-art simulation programs can handle various optic profiles, including circular, parabolic, elliptical, and polynomial shapes. The photon position and angular distributions can be obtained at any image plane, so the dimensions and divergence of the output beam can be calculated. The simulation has become an essential tool to provide information for the optic design, performance analysis and evaluation of potential applications (Gao & Janssens, 2004).

Important performance specifications for a polycapillary focusing optic include: the focal spot size, the output focal distance and the intensity gain. The *focal spot size* is usually determined by a number of factors such as (1) the focal distance, (2) the channel diameter, (3) the optic profile, (4) the X-ray source. The most commonly used method to measure the beam size is the knife-edge scan, where a sharp knife edge is moved across the beam and the derivative of the knife-edge scan profile (obtained in fluorescence mode) is used to determine the beam size. In another often-used method, a thin wire is moved across the beam and the intensity of the fluorescent X-rays is recorded as a function of the wire position. The obtained scan curve is the convolution of the wire thickness and the beam size S_b. If S is the $FWHM$ of

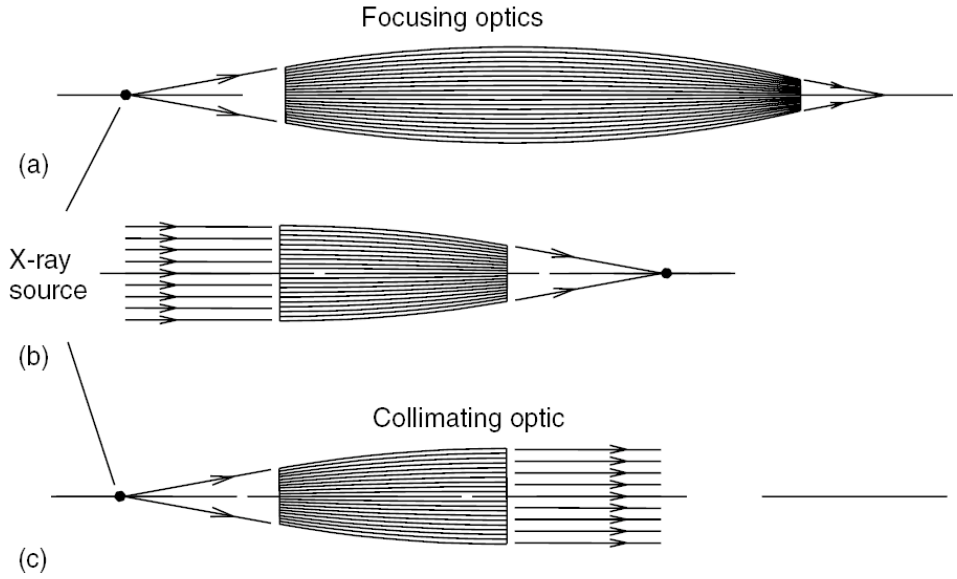

Figure 2.23: Polycapillary X-ray optics that produce a focused (a,b) or parallel beam (c), starting rom a X-ray point source (micro-focus X-ray tube (a,c) or a quasi-parallel X-ray source (e.g. synchrotron (b)). Reproduced from Gao & Janssens (2004).

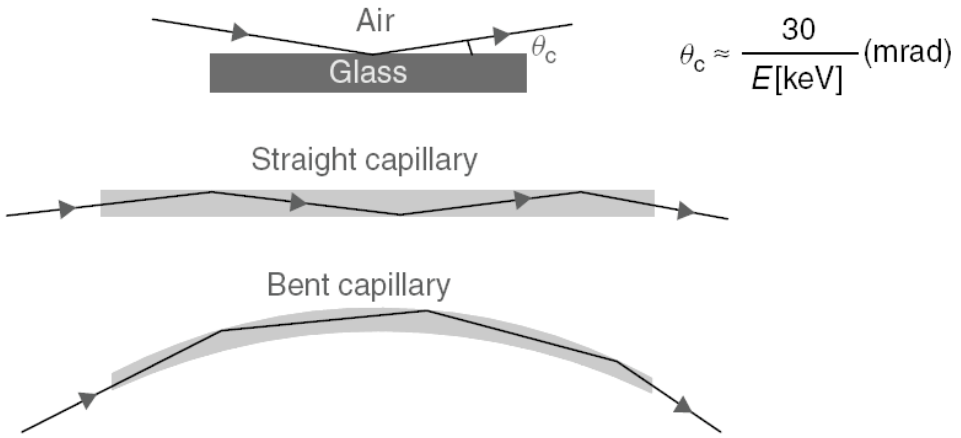

Figure 2.24: Schematic representation of the principles of capillary optics. θ_c is the critical angle for total reflection. Reproduced from Gao & Janssens (2004).

the measured scan curve and T_{wire} the thickness of the wire, the beam size can be estimated by means of the following formula:

$$S_b \approx \sqrt{S^2 - T_{wire}^2} \tag{2.21}$$

The *flux density gain* of an optic is defined at the focus of the optic to that obtained with a pinhole aperture placed at a certain distance to the source. The combination of the large collecting angle and small focal spot size of a focusing optic results in a high flux density, defined as the number of photons passing through a unit area per unit time. The gain clearly depends upon how far the pinhole is placed from the X-ray source. It is therefore important to specify the source-to-sample distance. The flux density gain is also a function of the source size because of the dependency of the optic performance on the source size (Gao & Janssens, 2004).

Although polycapillary optics obtain a maximal resolution in the μm range and their alignment requires considerable effort, they are ideal optics for X-ray focusing due to their high flux density gain when aiming at medium resolution applications. The application of polycapillary optics will be illustrated in Chapter 4, involving laboratory micro-XRF and in Chapter 5 and 6 respectively for 2D/CT and confocal micro-XRF and finally in Chapter 7 for conventional and confocal micro-XAFS experiments.

2.4.2 Fresnel zone plates

Unlike polycapillaries, zone plates use diffraction instead of total reflection. Created by Augustin-Jean Fresnel, they are called Fresnel zone plates in his honor. A zone plate consists of a set of radially symmetric rings, known as Fresnel zones, which alternate between opaque and transparent. X-rays hitting the zone plate will diffract around the opaque zones. The zones can be spaced so that the diffracted X-rays constructively interfere at the desired focus, creating an image of the source there. Zone plates produce equivalent diffraction patterns no matter whether the central disk is opaque or transparent, as long as the zones alternate in opacity. It should be noted that unlike a standard lens for visible light, a zone plate produces subsidiary intensity maxima along the axis of the plate through higher order diffraction, although these are less intense than the principal focus (Di Fabrizio *et al.*, 1999).

In order to get complete constructive interference at the focus, the amplitude of the diffracted light waves from each zone in the zone plate must be the same. This means that for an evenly illuminated zone plate, the area of each zone is equal. To get constructive interference at the focus, the zones should switch from opaque to transparent at radii where:

$$r_n = \sqrt{n\lambda f + \frac{n^2\lambda^2}{4}} \tag{2.22}$$

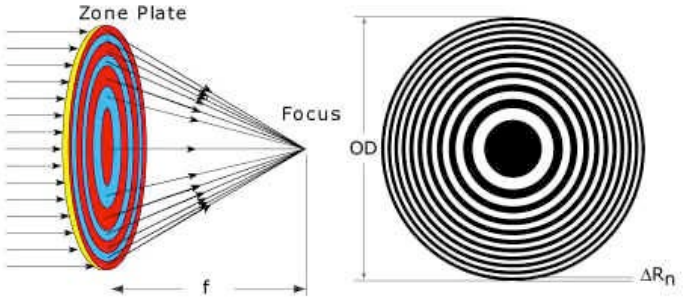

Figure 2.25: Working principle of a Fresnel zone plate. Reproduced from XRadia (2009a).

where n is an integer, λ is the wavelength of the light the zone plate is meant to focus and f is the distance from the center of the zone plate to the focus.

The width of the zones must decrease further from the center since the area of each zone must be equal. Therefore, the maximum possible resolution of a zone plate depends on the smallest zone width. Because of this, the smallest size object which can be imaged is limited by the accuracy of zone plate fabrication. Zone plates are mostly manufactured using lithography. As lithography technology improves and the size of features that can be manufactured decreases, the possible resolution of zone plates manufactured with this technique can improve (Di Fabrizio *et al.*, 1999). Zone plates currently provide the best spatial resolution for two-dimensional X-ray focusing, but due to their low efficiency they are mainly used for soft X-ray applications and were not used in the scope of this work.

2.4.3 Compound refractive lenses

The techniques previously discussed for focusing were based on total *reflection* (polycapillary) or *diffraction* (Fresnel zone plate). Until not too long ago, it was thought that using traditional lenses based on refraction to focus X-rays would be highly impractical, since the refractive index of all materials for the high-energy X-rays is almost $n = 1$. Recently, another technique has been added: focusing by *refractive* multiple lenses (Snigirev, 1996). Since the real part of the index of refraction $(1 - \delta)$ for X-rays is less than one, the focusing lens must have a concave form. The thin lens law states that the focal length of a lens is determined by the index of refraction, the radius of curvature of the front surface of the lens, and the radius of curvature of the back surface of the lens (Jacobsen, 2009):

$$\frac{1}{f} = \frac{2(n-1)}{R} \tag{2.23}$$

One would think a refractive lens may not be appropriate for focusing X-rays since refraction effects are extremely small coupled with considerable absorption through the lens. A small

radius of curvature is needed in order to achieve appreciable refraction. A typical value would be $R = 180\mu m$. Due to the very weak refraction of hard X-rays in matter, many lenses have to be stacked behind each other in an aligned manner. A simple way to realize this form is by drilling many fine holes in a line and to use the material between the holes as refracting medium, which should be made in a material with minimal mass absorption coefficient (e.g. Be, Al) in order to optimize the transmission. It can be derived then that the focal length of a compound refractive lens with N individual lenses in the thin lens approximation is given by (RWTH Aachen, 2009):

$$f = \frac{R}{2\delta N} \tag{2.24}$$

CRLs are very convenient and robust optical systems, requiring little or no (re)alignment and having long focal distances (20 cm - 2 m). They can also be removed quickly and effortlessly from the beam, allowing to alternate between focused and unfocussed beam operations. Disadvantages are their small solid angle not allowing to capture many photons prior to focusing and their chromatic nature. Since their recent introduction, these optics are not yet widely used and were therefore not used within this work.

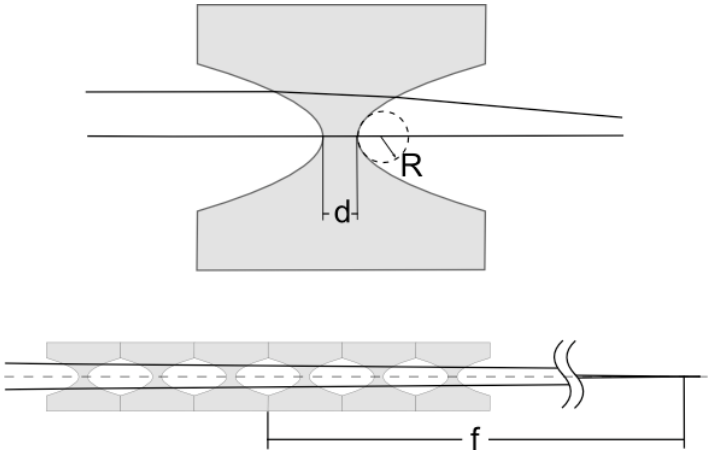

Figure 2.26: Working principle of Compound Refractive Lenses (CRLs). Reproduced from Hasylab (2009c).

2.4.4 Mirrors

A classic way of focusing an X-ray beam is using mirrors. To achieve total external reflection of the high-energy X-rays, the incident angle has to be extremely small, typically around 0.5 degrees, a value which reduces for higher energies. The mirror thus acts as a low-pass, i.e. it filters out high energy X-rays, an effect which can be useful for e.g. the elimination of higher harmonics from the monochromatized beam. The focusing effect of a mirror always originates from the way it is curved. Two designs are commonly used. A toroidal mirror is curved in

two directions, called tangential and sagittal. The respective curving radii are r (around 10 cm) and R (several kilometres) as depicted. Since the focal length for sagittal and tangential focusing needs to be the same, the angle α and the two radii r and R are mutually dependent. The sagittal focal length is given by:

$$\frac{2cos\alpha}{r} = \frac{1}{f_{sag}} \tag{2.25}$$

whereas the tangential focal length is given by:

$$\frac{2}{Rcos\alpha} = \frac{1}{f_{tan}} \tag{2.26}$$

Therefore, the angle α is given by:

$$cos\alpha = \sqrt{r/R} \tag{2.27}$$

One disadvantage of this design is that it produces aberration. To avoid this, the mirror surface has to be ellipsoidal, which is exceedingly difficult to manufacture due to the extreme accuracy needed to reproduce the doubly curved ellipsoidal shape. The Kirkpatrick-Baez (KB) design circumvents this problem by using two separate elliptical mirrors, each of which focuses the beam in one direction.

KB systems require a much more elaborate alignment procedure compared to CRLs or FZP lenses, tend to gradually loose their alignment over time through temperature drift and are not that easily removed from the optical axis of the beamline. The most prominent advantage of KB mirrors is the ability to capture the primary beam in a large collection angle and focus it with high transmission efficiency in an achromatic manner down to μm or sub-μm diameters. Another advantage is that they can be combined with bent graded multilayers, where alternating layers of a high and low electron density material are deposited by a lateral thickness gradient on the surface of the substrate to account for the variation of the Bragg angle, which allows monochromatisation and focusing at the same time (Hignette *et al.*, 2005). Such a KB system will be illustrated in Chapter 8 for conventional and confocal nano-XRF imaging experiments on *Daphnia magna*.

2.5 Detection of X-Ray (Fluorescence) Radiation

2.5.1 Historical overview

The discovery of X-rays by Röntgen was based on the observation of fluorescence in materials well away from his tube. With this discovery, the basis for X-ray detection was laid 100 years ago. Soon it was recognized that *photographic plates* were also sensitive to X-rays and very quickly gas-filled *ionization chambers* were developed, enabling the instantaneous detection of

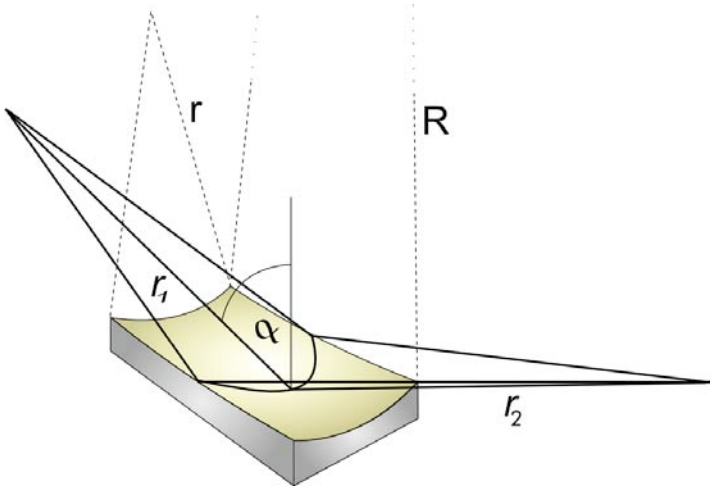

Figure 2.27: Toroidal mirror, curved in two directions. Reproduced from Hasylab (2009c).

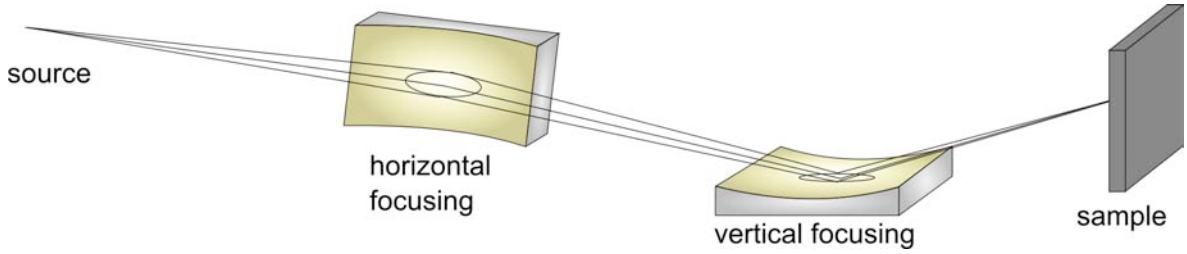

Figure 2.28: Kirkpatrick-Baez (KB) design, using two separate elliptically bent plane mirrors, each of which focuses the beam in one direction. Reproduced from Hasylab (2009c).

radiation. Some general properties apply to X-ray detectors enabling instantaneous detection: in order for the detector to respond at all, the radiation must undergo interaction. The interaction time is almost instantaneous (typically a few ns in gases or a few ps in solids). The net result of the radiation interaction is the appearance of a given amount of electric charge within the detector active volume. The collection of this charge is accomplished through the imposition of an electric field within the detector which causes the positive and negative charges created by the radiation to flow in opposite directions. The time required to fully collect the charge varies greatly from one detector to another. For example, in ionisation chambers, the collection time can be as long as a few ms, whereas in semiconductors diode detectors the time is a few ns. These times reflect both the mobility of the charge carriers within the detector active volume and the average distance that must be traveled before arrival at the collection electrodes (Beckhoff *et al.*, 2005).

Proportional counters have been in use for 100 years and were the first able to measure the photon energy of X-rays. These detectors are cheap and easy to operate because the internal gas-amplification yields a high charge output, which can be quickly and easily processed. They are also specifically insensitive to electronic interference and thus suited for harsh environments. Gas detectors are also a good choice if large areas are needed for detection. The main disadvantage of gas detector is its low density that results in a low efficiency for X-ray detection. An alternative with much higher detection efficiency for high energy photons was the *scintillation detector*. While early observation of ionizing radiation was made by looking at fluorescence screens in darkened laboraties, state-of-the-art scintillation detectors use a scintillating material coupled to photomultipliers, photodiodes or CCDs for the detection of fluorescence light. The benefit of these detectors is that they can be made very small and effective for hard X-rays by using scintillating crystals of heavy metals. Depending on the scintillator, the speed of these detectors can also be increased. When large areas of scintillating material are coupled to a large number of light detectors, a high-efficiency imaging detector is obtained which can be used for, e.g. medical applications. The disadvantage of scintillation detectors is their poor energy resolution (Beckhoff *et al.*, 2005).

Therefore, there has constantly been a search for a way to realise the principle of the ionization chamber with a high density material. Consequently, shortly after high-purity germanium and silicon became available, the first $HPGe$ and $Si(Li)$ detectors were produced in the 1970s. In these detectors, radiation is measured by means of the number of charge carriers set free in the detector material, which is arranged between two electrodes as shown in Fig. 2.29. Ionizing radiation produces free electrons and holes. The number of electron-hole pairs is proportional to the energy transmitted by the radiation to the semiconductor. As a result, a number of electrons are transferred from the valence band to the conduction band, and an equal number of holes are created in the valence band. Under the influence of an electric field, electrons and holes travel to the electrodes, where they result in a pulse that can be measured in an

outer circuit. As the amount of energy required to create an electron-hole pair is known, and is independent of the energy of the incident radiation, detecting the number of electron-hole pairs allows the energy of the incident radiation to be measured. These detectors offer a much better energy resolution than the previously mentioned gas detectors and scintillators. The reason is that the mean energy needed to create one primary elementary charge is about 20 to 30 eV for gases while for semiconductors it is only a few eVs. Thus, a ten times higher number of primary charge carriers is produced reducing the statistical fluctuations of the pulse height by about a factor of 3. Furthermore, the higher charge generated allows for the direct measurement by low-noise electronics, increasing the energy resolution. Compared with gaseous ionization detectors, the density of a semiconductor detector is very high, resulting in a high detector efficiency. For the proportional counters, the gas amplification process adds additional noise. The planar $HPGe$ and $Si(Li)$ detectors are thus semiconductor analogue to the ionization chamber. In principle a solid state proportional counter, the avalanche diode also exists. Due to the high noise of the avalanche process, however, it can not be used for high-resolution applications (Knol, 1979).

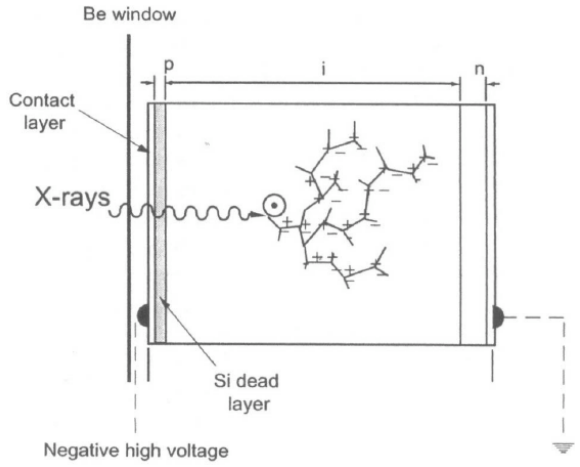

Figure 2.29: Working Principle of an energy dispersive detector. Reproduced from Van Grieken & Markowicz (2002).

The search for a solid-state analogue to the multiwire chambers, resulted in a versatile device-*the silicon drift detector (SDD)*. Originally introduced for spatially resolving detectors for high energy particle detection, the device became one of the most promising new X-ray detectors. One of the main disadvantages of the planar $HPGe$ and $Si(Li)$ detectors is the need for liquid nitrogen cooling to produce spectroscopic data. The cryostats make these detection system rather large and difficult to handle as the detector requires hours to cool down to operating temperature before it can be used. The reason for the cooling is that at higher temperatures,

the electrons can easily cross the band gap in the crystal and reach the conduction band, where they are free to respond to the electric field, resulting in too much electrical noise. This results in a high leakage current at room temperature combined with a rather high read-out capacitance. The high read-out capacitance is due to the fact that the detector area is proportional to the capacitance. The high capacitance results in a high contribution of the serial noise component that requires longer shaping time. For long shaping time, however, the shot-noise contribution from the leakage current increases. In the SDD, the charge is drifted from a large area into a small read-out node with low capacitance. Thus, the serial noise decreases and shorter shaping time can be used. This offers two advantages: faster counting is enabled and at the same time, higher leakage current can be accepted, drastically reducing the need for cooling. Presently, SDD at room temperature achieves an energy resolution of the order of 180 eV, comparable to the early liquid nitrogen cooled systems, with shaping times of 350 ns (Knol, 1979).

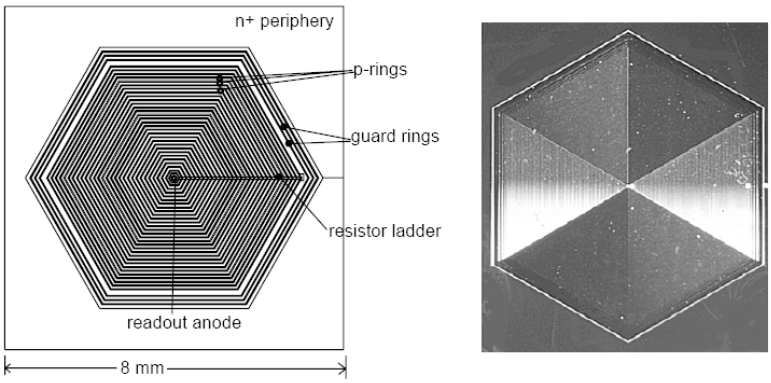

Figure 2.30: Basic structure of the $Vortex^{TM}$ silicon multi-cathode detector (left). A photo of the real detector diode is shown on the right, where the anode in the center and the multiple p^+ rings (the multi-cathode) are clearly seen. Reproduced from Iwanczyk (1999).

Single SDDs of large area shown in Fig. 2.30, ranging from a few tens of mm^2 up to few cm^2 have also been produced. When cooled, these detectors offer an energy resolution similar to the one achievable with SDD of smaller area, thanks to the reduction of the leakage current by cooling and to the independance of the detector capacitance with respect to the active area. However, when a large active area is required in measurements near room temperature, the contribution of the leakage current to the electronics noise can still be relevant. In this case, the energy resolution of the detector can still be maintained by means of a segmentation of the detector area in single smaller units, each one with its own amplifying chain. This solution offers also two additional advantages. If a single unit (i.e. 5 mm^2) can operate without significant degradation of the energy resolution up to 100000 cps, a detection system based on arrays of several units could operate with a very high counting rate capability. As a

second advantage, several single units can be suitably arranged in almost any kind of shape in one array in order to match the special geometrical configurations required by specific applications (Barkan, 2003; Feng, 2004).

An important characteristic of a solid state detector is its detection efficiency, which is defined as the fraction of the total number of photons emitted by the source, which actually interacts in the detector volume and is completely absorbed. A first limitation of the detection efficiency arises from the limited active area of the detector and from the distance with respect to the source: the *geometrical efficiency*). The geometrical efficiency is the fraction of the photons emitted by the source which enter the detector volume and is calculated as:

$$\eta_G = \Omega/4\pi \tag{2.28}$$

where Ω is the solid angle under which the detector is seen from the source. In the case of a thin cylindrical detector, with the axis passing through the point source, $\Omega = S/h^2$ where S is the detector cross-section and h the source-detector distance. The *intrinsic* efficiency is the fraction of the number of photons entering the detector which interact in the detector material. In the low X-ray energy range (100 eV-1 keV), the detection efficiency is also limited by the absorption in the window material and the absorption in a dead layer of the detector material itself. If μ represents the mass attenuation coefficient of the Be window or detector material, ρ the density and T the thickness of the layer, then the intrinsic efficiency of a detector can therefore be calculated according to the formula:

$$\phi(E) = e^{\mu_{Be}\rho_{Be}T} \times (1 - e^{-\mu_{(Si,Ge)}\rho_{Si,Ge}T}) \tag{2.29}$$

Although the detector efficiency of a Ge detector is better at higher energies than a Si detector, a Si detector is often preferred due to the better position of escape peaks. Typical values for escape peaks are 1.74 keV for Si and 9.9 keV for Ge. The occurence of escape peaks can be explained as follows: when an external electron fills the vacancy left in an atom as a consequence of the absorption of an X-ray photon, another X-ray photon of an energy equal to the energy difference between the two levels involved can be emitted. This photon has a high probability to be re-absorbed in the material itself leading to a full-energy absorption of the primary photon. However, when the incoming X-ray photon is absorbed close to the detector surface (as in the case of low-energy X-rays), there is a not negligible probability that the re-emitted photon escapes from the detector without being absorbed. The consequence of this effect is the presence of an escape peak in the spectrum whose energy is equal to the difference between the energy of the primary photon E and the energy of the escaping photon E_f.

Fig. 2.31 shows the detector efficiency of a Si and Ge detector of 5 mm thickness, covered with a 10 or 20 μm thin Be window. The *photopeak efficiency* is the fraction of the photons

interacting in the detector, which deposit their full energy in the material. It can be observed that for X-ray energies up to 100 keV, photo-electric interaction is dominant with respect to Compton scattering and the probability of re-absorption of the Compton scattered photon in the detector itself is also rather high.

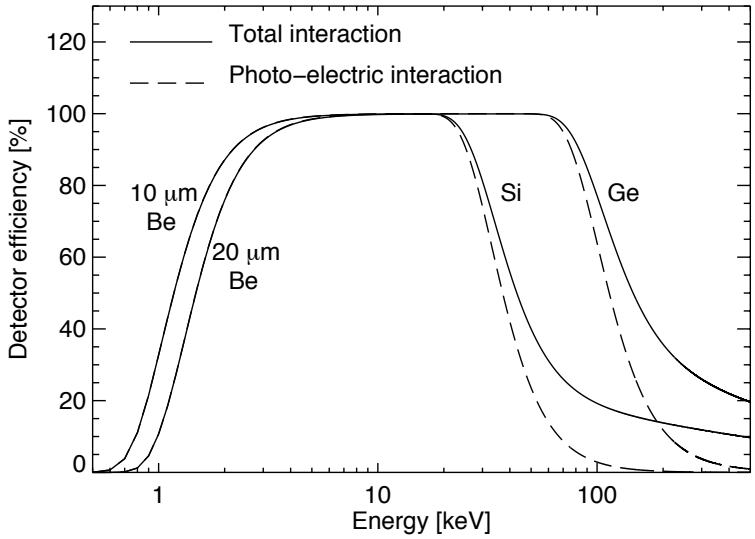

Figure 2.31: Detector efficiency of a Si and Ge detector (thickness 5 mm). Both detectors are covered with a beryllium window (thickness 10/20 μm). Both the total interaction and photo-electric interaction are shown. Calculated from (Brunetti *et al.*, 2004).

2.5.2 New detector developments

Full field X-ray cameras are currently under development by SKYSCAN based on the new type of pinhole optics with square aperture and pyramidal opening on both sides. This specific shape allows sensitivity increasing by 25% in the central part of the image and up to 70% in the corners (Sasov *et al.*, 2008). Unlike methods based on collimated beam and detector, this type of detector includes a full-field acquisition system based on an energy-sensitive detector with 512 $\times$ 512 pixels operating in photon counting mode. It allows detection of two-dimensional photon energy distribution in the range of 3-20 keV. Up to 8 sets of energy windows can be selected for independent and simultaneous collection of micro-XRF images. Due to the pinhole optics, a large portion of the fluorescence photons are however not captured. Current X-ray element maps generated with this type of detector are therefore obtained on pure metallic samples delivering high fluorescent yield, combined with a SR white beam when short measuring times are required.

Recently, XRADIA developed the nanoXFI fluorescence imager which collects fluorescence

images and maps them onto a CCD (Fig. 2.32). The instrument consists of a tube approximately 70 *cm* long and 10 *cm* across with a zone plate focusing element that is positioned within a few *mm* to the sample under probe and collects the fluorescence emanating from surface and subsurface structures. Since a zone-plate is a chromatic optical element, it focuses different wavelengths at different points. The lens focuses one wavelength at a time, meaning one element at a time on a scintillator and then a CCD camera. A motor drive mechanism incorporated into the cylinder sets the lens position at different focal points, enabling the mapping of elements with different fluorescent energies. The fluorescence imager has already been attached to an electron microscope, capturing the X-ray fluorescence resolving < 80 *nm* features. Unfortunately, this detection system is only applicable to low X-ray energies at high intensities (XRadia, 2009b).

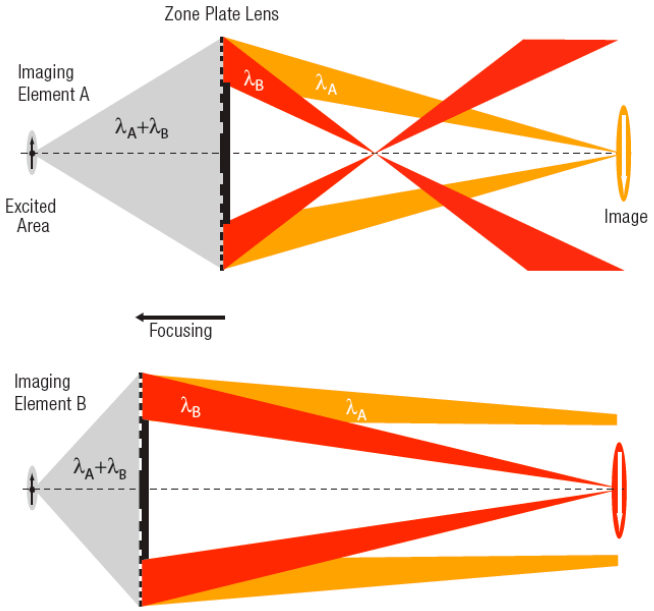

Figure 2.32: Working principle for the imaging of two different element with the Xradia nanoXFI. Reproduced from XRadia (2009b).

A new spectroscopy detector Maia has been developed in cooperation of CSIRO and Brookhaven National Laboratory, which uses a multiparameter approach in which each photon event is tagged by sample XY position and detector identity. These events are then streamed for further processing or storage. This strategy exhibits zero read-out overhead and enables faster raster scanning. The spectroscopy detector system is composed of a low-leakage peltier cooled *Si* pad array and dedicated application specific integrated circuits (ASICs) for signal processing. The plane monolithic silicon detector offers the potential for large solid angle collection (1.5 *sr*), with the resulting high count rates spread over a large number of detectors. The

speed of field-programmable gate array (FPGA) computation permits real-time processing of each event from such an array. Tests using a 96 element prototype detector demonstrated (1) count rates up to 6 M/s, (2) image sizes up to 4.3 megapixels, (3) dwell times as short as 0.8 ms. Given these capabilities, the choice of pixel size and dwell time are now dictated by the needs of the application, and not by data acquisition limitations (Ryan *et al.*, 2009).

2.6 Processing of X-ray fluorescence data

2.6.1 Introduction

When X-ray fluorescence analysis is performed with solid state detectors (e.g. $Si(Li)$, SDD), the equipment required is mechanically of simple design and relatively inexpensive, making energy-dispersive XRF (ED-XRF) the method of choice. Due to the relatively low resolving power of solid state detectors, however, the process of evaluating ED-XRF spectra (i.e., accurately determining the net X-ray intensities associated with each chemical element) is prone to many errors and requires dedicated software. The need for a spectrum evaluation procedure which can be applied in an increasingly unsupervised manner, without having to compromise on the accuracy of the net peak area determination is critical for micro-XRF where vast amounts of spectra (e.g. several tens of thousands) need to be processed. Therefore, a software package was developed: AXIL (Analysis of X-ray Spectra by Iterative Least Squares) which is based on the non-linear fitting of a mathematical function (describing the photopeaks and the spectral background) to experimental data was used in this work (Vekemans *et al.*, 1994). Recently, also PyMca has been developed by the Beamline Instrumentation Software Support (BLISS) group of the ESRF (Solé *et al.*, 2007), but was not used within this work.

2.6.2 Mathematical background

Non-linear least-squares fitting

The AXIL program employs a non-linear least squares strategy using a modified Marquardt algorithm to minimize the weighted sum of differences χ^2 between the experimental data y and a mathematical fitting function y_{fit}:

$$\chi^2 = \frac{1}{n-m} \sum_i \frac{[y_i - y_{fit}(i)]^2}{Y_i} \tag{2.30}$$

where $y(i)$ is the observed content of channel i in the spectrum and $y_{fit}(i)$ the calculated value of the fitting function in this channel; n is the total number of channels in the fitting window while m represents the number of parameters of the fitting function that are estimated during the fitting process. The fitting function itself consists of two parts describing the spectral background and the fluorescence peaks, respectively:

$$y_{fit}(i) = y_{back}(i) + y_{peak}(i) = y_{back}(i) + \sum_j y_j i \tag{2.31}$$

where the index j runs over all characteristic line groups which appear in the spectrum. For each line group j, (e.g. $Fe-K$, $Pb-L_3$), the contribution $y_j(i)$ to the i^{th} channel content is calculated as:

$$y_j(i) = A_j(\sum_{k=1}^{N_j} R_{jk} G(E_{jk}, i) t(E_{jk})) \tag{2.32}$$

where A_j represents the total area of all photopeaks (e.g. $Fe-K\alpha$ and $Fe-K\beta$) belonging to this group. The A_js are optimizable parameters during the least squares fitting process. The index k runs over all lines in group j, each line having a relative abundance R_{jk} and $\sum_k R_{jk} = 1$. G_{jk} represents a Gaussian function centred around energy E_{jk} which optionally also accounts for escape peaks. $t(E_{jk})$ denotes the total attenuation factor for X-rays with energy E_{jk} as defined by absorption of radiation in the detector, in absorbers placed between sample and detector and in the sample itself. To describe the non-gaussian components of (intense) photopeaks, a numerical peak shape correction (PSC) can be added to the Gaussian function of Eq. 2.32. This correction takes the form of an array of number, which, prior to being added tot the Gaussian $y_j(i)$ are scaled in such a way that the total intensity of the correction represents a fixed fraction of the intensity $A-j$ of the Gaussian part of the photopeak. The relation between peak energy E and channel number i, and between peak full-width-at-half maximum W and energy is provided by the following relations:

$$E(i) = E_0 + i \times \Delta E \tag{2.33}$$

$$W^2(E) = W_0^2 + (2ln2)F\epsilon E \tag{2.34}$$

where E_0 andΔ E are the energy calibration parameters and W_0 and F the resolution calibration parameters of the fitting model; ϵ denotes the band-gap of Si. Similar to the net peak areas, best fitting values for these parameters are calculated as part of the least squares procedure. The value of the calibration parameters can be constrained to vary within certain limits only in order to stabilize the behaviour of the fit procedure. The last series of parameters which are optimized during the fitting process are those of the background model function (Vekemans *et al.*, 1995).

Background modelling and estimation

The term *background modelling* refers to the description of the background shape by some mathematical function. This function forms part of the fitting model that describes the complete spectrum (i.e. background spectrum + fluorescence peaks). During the spectrum

evaluation, the parameters of the background function are optimized together with the other parameters in the fitting model in order to obtain the best match between model and spectral data. In contrast, *background estimation* involves the a priori calculation of an approximate background shape $b(i)$ by applying a suitable stripping or filtering or filtering algorithm on the original spectral data $y(i)$, which are then fitted with an appropriate fitting model containing the estimated background shape as fixed part of the model. This is equivalent to using the net spectrum $n(i) = y(i) - b(i)$ for the peak area determination of the characteristic lines. The essential difference between background *modelling* and *estimation* procedures is that the latter class of algorithms produces a background shape that is not fine-tuned during subsequent stages of the (iterative) spectrum evaluation procedure. The background modelling procedures do show this behaviour, which, provided the fitting model is complete, allows the background shape to be optimally adapted to all non-characteristic information in the spectrum (Vekemans, 2000).

2.7 Quantification methods

2.7.1 Minimum detection limits (MDL)

The mathematical definition of minimum detection limit (MDL) is based on the standard counting deviation. It is defined as the amount of analyte that gives a net intensity equal to three times the standard counting error of the background intensity. Since the emission of N photons is described by a Poisson distribution, the standard deviation or standard counting error is given by $\sigma = \sqrt{N}$. If an element i with a concentration C_i provides N_N net counts and N_B background counts, then the minimum detection limit is given by:

$$C_{MDL,i} = \frac{3\sqrt{N_B}}{N_N} \times C_i \tag{2.35}$$

Since micro-XRF is a non-destructive technique, a variety of samples can be measured. Therefore, it is often valuable to express the MDLs in different units depending on the sample analysed and the variant of micro-XRF used (2D/CT/confocal). When performing 2D/CT micro-XRF, concentration (%,*ppm*,*ppb*) for infinitely thick samples, areal density (mg/cm^2, $\mu g/cm^2$) for samples less than infinitely thick, or mass (μg) for small particulate or filamentary samples are used. Therefore, in Eq. 2.35 C_i can be expressed as the areal concentration $C_{i,areal}$ (providing the minimum areal detection limit in $\mu g/cm^2$ for example), as the mass concentration $C_{i,mass}$ (providing the minimum relative detection limit in $\mu g/g$) or as the absolute illuminated mass in the sample (providing the absolute detection limit). Although the concentration is immediately given with the reference material, the areal concentration and absolute mass sampled by an X-ray beam need to be calculated. The areal concentration can be easily calculated by dividing the total mass of the reference material by its area. In order to calculate the sampled mass of the microbeam, a simplified approach can be used, which

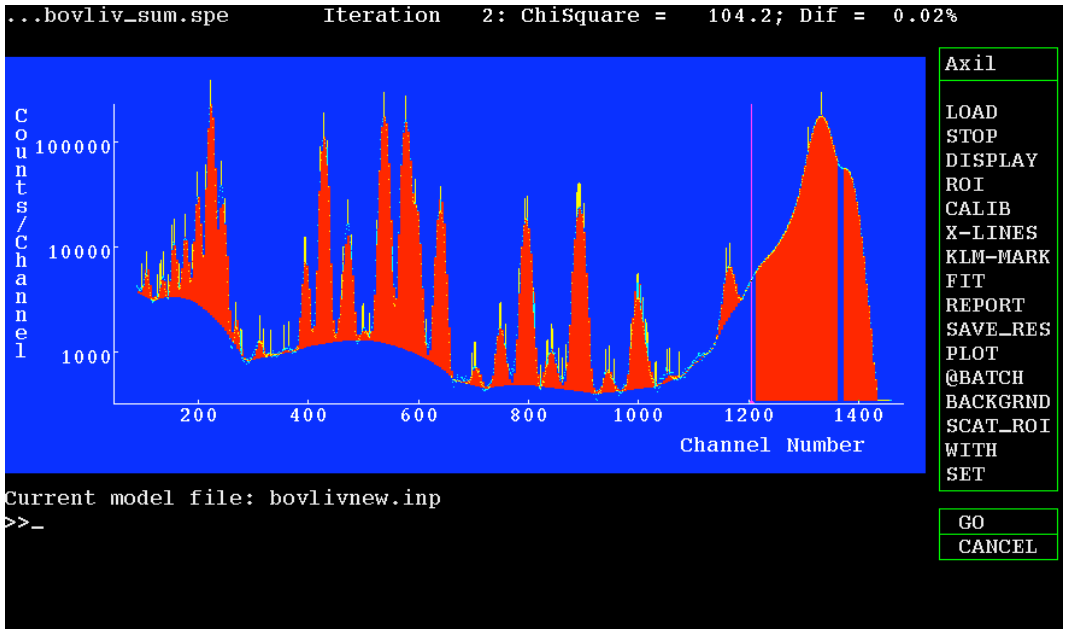

Figure 2.33: Spectrum Evaluation of NIST SRM 1577B using AXIL.

is shown in Fig. 2.34. Suppose the X-ray beam has a rectangular shape with horizontal and vertical size S_x and S_z respectively, hitting a thin pellet with thickness t under an angle of 45°. The calculation of the volume material illuminated by the beam is then given by Eq. 2.37. Subsequently, V can be substituted delivering a formula only containing known values, such as the weight fraction of the material in the standard w_i, density of the material ρ, beam dimensions S_x and S_z and thickness of the pellet. When confocal micro-XRF is applied in which a specific microvolume is created from wich the XRF signal is detected in the coinciding focii of the detection-side polycapillary and the incoming microbeam, calculating detection limits involves careful estimation of the geometry of this analytical volume, which will be discussed in Chapter 6. Although the expression of the MDLs in concentration (%, ppm, ppb) and absolute mass (μg, fg) are still useful, a volume density (mg/cm^3,$\mu g/cm^3$) should be used instead of an areal density (mg/cm^2, $\mu g/cm^2$).

$$V = S_z A \tag{2.36}$$
$$= S_z S_x t\sqrt{2} \tag{2.37}$$

$$m_i = \omega_i m \tag{2.38}$$
$$= \omega_i \rho V \tag{2.39}$$
$$= \omega_i \rho S_x S_z t\sqrt{2} \tag{2.40}$$

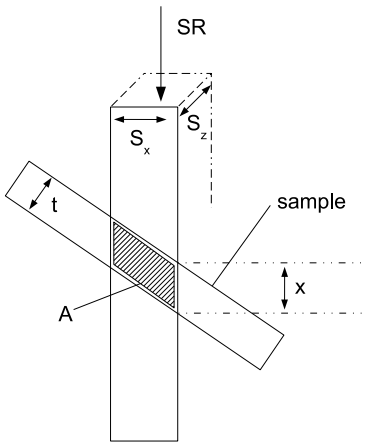

Figure 2.34: Analysed volume of a single pellet.

2.7.2 Semi-quantitative elemental analysis

Analytical determinations with an accuracy of 30-50 % are known as semi-quantitative. A semi-quantitative analysis requires the measurement of a single multi-element standard reference material. Afterwards, an element yield can be calculated for each element and element yield curves can be rendered, providing valuable information on how many fluorescence counts for a specific element are generated per second in the targeted area by the microbeam. If standard reference material which contains an element i in a concentration C_i generates I_i counts while measuring during a life time T_{real}, then the elemental yield Y_i is for example given by:

$$Y_i = \frac{I_i}{T_{real}}/C_i \tag{2.41}$$

The elemental yields for elements that are not present in the calibration standard can be graphically derived by fitting a curve through the data points obtained for the calibration standard in a diagram where the intensity is plotted versus the analyte mass. These relative sensitivity factors will vary for each element depending on the photoelectric cross-section and the operating conditions selected for the determination. Concentrations of analytes in unknown samples can be estimated by dividing the measured netto line intensities by the elemental yields for the specific element under investigation. Because elemental yields are

dependent on the specific operating conditions, they should be re-established whenever adjustments or modifications are made to instrumental parameters. In analogy with the detection limits, the quantification results can be expressed in different units according to the sample investigated and variant of micro-XRF used. When performing 2D/CT micro-XRF, elemental yields can be expressed in $counts/s/fg$ or $counts/s/(\mu g/cm^2)$ to generate the absolute mass (fg) and areal concentration ($\mu g/cm^2$) respectively. When confocal micro-XRF is used, elemental yield in $counts/s/(\mu g/cm^3)$ is preferably calculated, delivering the volume concentration ($\mu g/cm^3$).

2.7.3 Quantitative elemental analysis

Analytical determinations with an accuracy better than 10 % are known as quantitative analyses. Below, three calibration approaches for quantitative analysis are discussed: (1) external standardisation (2) fundamental parameter approach and (3) Monte Carlo simulation.

External standardisation

In quantitative analysis via external standardization, several multiple concentration standards containing the analyte(s) of interest are involved. Scans of these standards are performed before, during, and after samples are scanned under the same operating conditions. The fluorescence intensities are obtained and then a calibration curve of intensity vs. concentration generated. Matrix-matched standards are required for improved accuracy which feature same thickness, density and bulk composition. While this is the most accurate approach, matrix matched standards that are spatially homogeneous at the μm scale (both at the surface and/or at depth) are scarce.

Fundamental parameter methods

The fundamental parameter (FP) approach is very effective when coupled with standards analysis. Here, the relationship between concentration and intensity is determined with the standards, while FP algorithms are used to correct for absorption differences between the sample and standards. This computation takes into account various parameters of the analysis conditions (absorption of the X-rays by the beryllium windows, the air path between the sample and the detector, fluorescence yields, photoionization efficiencies, self-absorption, secondary fluorescence) and the matrix composition (thickness, density, major elemental composition). The results of this approach are within 5-10 % of actual values. A further advantage is that it is not necessary for the standard to contain all the elements of interest in the sample (Rousseau, 2006) (Elam *et al.*, 2004) (Beckhoff *et al.*, 2005).

Fig. 2.35 shows a schematic representation of a single layer of an unknown sample with thickness T being hit by an incoming beam I_0. The length of the incoming and outgoing path

of X-ray photons x and y is given by:

$$\begin{cases} x = \frac{z}{\sin\alpha} \\ y = \frac{z}{\sin\beta} \\ dx = dz/\sin\alpha \end{cases} \tag{2.42}$$

Whereas the mass attenuation coefficient of the incoming exciting ($E = E_0$) and outgoing fluorescent ($E = E_1$) photons within the sample can be calculated by taking into account the mass attenuation coefficient of the different constituents :

$$\begin{cases} \mu_0 = \mu(E_0) = \sum_{i=1}^{n} \omega_i \mu_{i,0} \\ \mu_1 = \mu(E_1) = \sum_{i=1}^{n} \omega_i \mu_{i,1} \end{cases} \tag{2.43}$$

By differentiating the absorption law of Lambert-Beer for the incoming exciting photons, the K_α fluorescence from a certain element i *generated* within a depth $(x, x + \mathrm{d}x)$ is then given by:

$$\begin{aligned} \mathrm{d}I^*_{i,K\alpha} &= I_0 e^{-\mu_0 \rho x} \mu_0 \rho \mathrm{d}x \frac{\omega_i \tau_{i,K}}{\mu_0} p_{K\alpha} \omega_K & (2.44) \\ &= I_0 e^{-\mu_0 \rho x} \omega_i \tau_{i,K} p_{K\alpha} \omega_K \rho \mathrm{d}x & (2.45) \\ &= I_0 e^{-\mu_0 \rho x} \omega_i Q_{i,K\alpha} \rho \mathrm{d}x & (2.46) \end{aligned}$$

where $\tau_{i,K}$ denotes the photo-electic cross section, $p_{K\alpha}$ the transition probability and ω_K the fluorescence yield.

The *detected* K_α fluorescence from this depth $(x, x + \mathrm{d}x)$ is obtained by implementing the absorption law of Lambert-Beer for the outgoing fluorescent photons:

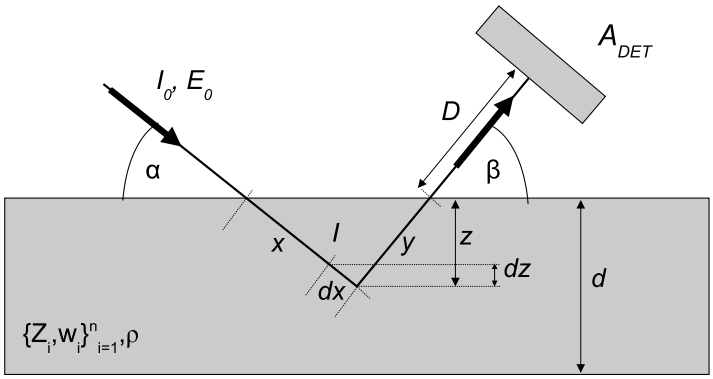

Figure 2.35: The Fundamental Parameter Method.

$$
\begin{aligned}
dI_{i,K\alpha} &= dI^{*}_{i,K\alpha}\frac{\Omega_{\mathrm{DET}}}{4\pi}e^{-\mu_1\rho y} && (2.47)\\
&= I_0\frac{\Omega_{\mathrm{DET}}}{4\pi}e^{-\mu_0\rho x}e^{-\mu_1\rho y}\omega_i Q_{i,K\alpha}\rho dx && (2.48)\\
&= I_0\frac{\Omega_{\mathrm{DET}}}{4\pi}e^{-(\mu_0/\sin\alpha+\mu_1\sin\beta)\rho z}\omega_i Q_{i,K\alpha}\rho dx && (2.49)\\
&= I_0\frac{\Omega_{\mathrm{DET}}}{4\pi}\omega_i Q_{i,K\alpha}e^{-\chi\rho z}\rho dz/\sin\alpha && (2.50)\\
&= I_0 G\omega_i Q_{i,K\alpha}e^{-\chi\rho z}\rho \mathrm{d}z && (2.51)
\end{aligned}
$$

whereΩ_{DET} denotes the solid angle of the detector.

Integration over the sample thickness T gives the *total detected intensity*:

$$
\begin{aligned}
I_{i,K\alpha} &= \int_0^T dI_{i,K\alpha} && (2.52)\\
&= I_0 G\omega_i Q_{i,K\alpha}\rho\int_0^T e^{-\chi\rho z}\rho \mathrm{d}z && (2.53)\\
&= I_0 G\omega_i Q_{i,K\alpha}\frac{1-e^{-\chi\rho T}}{\chi} && (2.54)\\
&= I_0 G\omega_i Q_{i,K\alpha}\rho T\frac{1-e^{-\chi\rho T}}{\chi\rho T} && (2.55)\\
&= I_0 G\omega_i Q_{i,K\alpha}\rho T A_{corr} && (2.56)
\end{aligned}
$$

The term A_{corr} is called the absorption correction term for which $0 < A_{corr} < 1$. In some specific cases, this term can be simplified:

- If the sample is very thin then $T << 1/\chi\rho$ and thus $I_{i,K\alpha} = I_0 G\omega_i Q_{i,K\alpha}\rho T$
- If the sample is infinitely thick then $T >> 1/\chi\rho$ and thus $I_{i,K\alpha} = I_0 G\omega_i Q_{i,K\alpha}\chi^{-1}$

Using the fundamental parameter, absorption effects of X-ray fluorescence within a biological matrix can be studied. Fig. 2.36 shows the fluorescence intensity of $P-K_\alpha$, $Ca-K_\alpha$, $Fe-K_\alpha$, $Zn-K_\alpha$ and $Sr-K_\alpha$ produced from a H_2O matrix in function of its thickness (containing 100 *ppm* P, Ca, Fe, Zn and Sr). The angle of the incoming X-ray beam/detector with respect to the surface was set to 45° and the incoming X-ray flux was chosen to be 10^{12} $photons/s$. The detector solid angle was chosen to be 1 sr and the excitation energy of the monochromatic incident X-ray beam set to 20 keV.

Monte carlo methods

Quantification is based on a Monte Carlo technique describing the relevant photon-matter interactions as a photon beam in the energy range of 1-100 keV illuminates an arbitrary heterogeneous specimen. The exciting radiation can have any given energy distribution in the

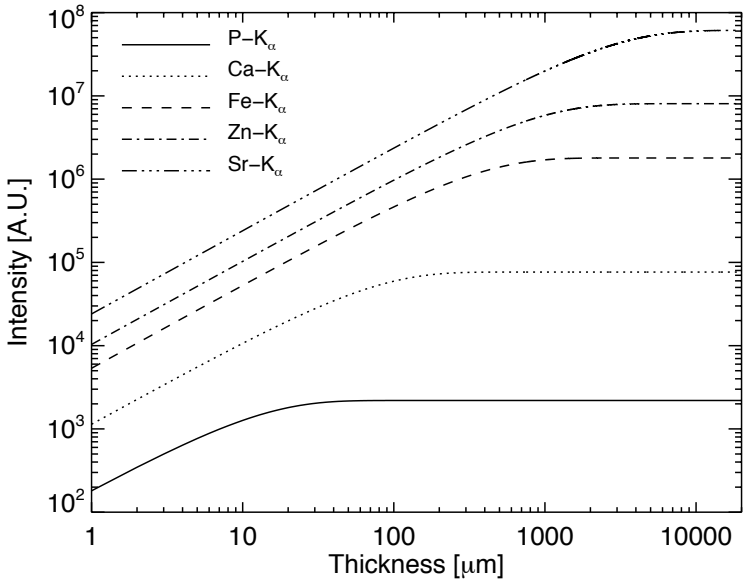

Figure 2.36: Investigation of the self-absorption effects of different biological trace elements in a phantom sample. Calculated from Brunetti *et al.* (2004).

above energy range and can be either unpolarized or linearly polarized. The modeled multi-element sample can contain a maximum 92 elements from H to U. The simulated interaction types include (1) photoelectric effect (2) Rayleigh (elastic) scattering (3) Compton (inelastic) scattering. By simulating a statistically significant number of these interactions within the sample and its environment and calculating the probability of subsequent fluorescence or scatterd X-ray emission within the solid angle of the modeled detector, the complete spectral response of a given sample can be calculated. The simulated spectrum can be compared directly to the experimental data in its entirety, including the scattered background of the XRF spectra, as well as the fluorescence line intensities (Vincze, 2004).

The model can be applied in an iterative manner for the quantitative XRF analysis of homogeneous bulk samples, consisting of three steps (Vincze, 1995). First, the mean atomic number $\langle Z \rangle$ is estimated, based on the experimental Compton to Rayleigh scatter peak intensity ratio, which decreases with increasing average atomic number, since one of the problems associated with a general quantitative analysis approach for XRF data is the estimation of the composition of the non-fluorescent matrix. Next, the mass of the sample ρd is calculated using thickness calibration curves. The correct estimation of $\langle Z \rangle$ and ρd is important for samples of intermediate thickness, since they have a significant influence on the self absoption characteristics of the examined material. Finally, once ρd and $\langle Z \rangle$ are known, the concentrations of the trace elements are established by means of the following simple iterative scheme. On the

basis of the experimental fluorescent intensities I_j^{exp} for each constituent j and its elemental yield Y_j, an initial estimate of the concentration of the j-th element $c_j^{(0)}$ is calculated via:

$$c_j^{(0)} = \frac{I_j^{exp}}{Y_j} \tag{2.57}$$

These initial concentrations are used as input parameters of the simulation program, resulting in a simulated spectrum from which simulated X-ray intensities $I_j^{(0)}$ can be derived. In their turn, these intensities are used to adjust the current estimate of the elemental concentrations c_j^n according to:

$$c_j^{(n)} = c_j^{(n-1)} \times \frac{I_j^{exp}}{I_j^{(n-1)}} \tag{2.58}$$

where c_j^n is the nth estimate of the concentration of element j. The method typically requires 4 to 5 iteration steps to converge to constant values (i.e., $c_j^n \approx c_j^{n-1}$ within 5 %). Once these concentrations are obtained, the initial estimates of $\langle Z \rangle$ and ρd can be refined by recalculating the previously mentioned calibration curves for the particular sample composition. If significant differences in $\langle Z \rangle$ or ρd are found, the iteration process is repeated with the refined values until a self-consistent solution is obtained. Relative deviations in the range of 2-15 % have been achieved by the Monte Carlo quantification scheme, depending on the analyzed element and sample type. Errors are mostly due to the uncertainties in the physical constants (cross section, fluorescence yields, transition probabilities) applied in the simulations. As a result of the large penetration depth, the conversion of the measured X-ray fluorescent intensity into elemental concentration is not straightforward when dealing with non-homogeneous materials with a varying sample topology. However, in making some a priori assumptions, the procedure can been adapted for simple heterogeneous systems such as (1) layered structures (2) spherical inclusions/particles in a given host material (Vincze *et al.*, 2002).

Chapter 3

Aquatic toxicology experiments on *Daphnia magna* using X-rays

3.1 Aquatic toxicology

The term ecotoxicology was coined by Truhaut in 1969 who defined it as the branch of toxicology concerned with the study of toxic effects, caused by natural or synthetic pollutants, to the constituents of ecosystems, animals (including human), plants and microbial, in an integral context (Truhaut, 1977). It aims to quantify the effects of stressors upon natural populations, communities, or ecosystems. Ecotoxicology differs from environmental toxicology in that it integrates the effects of stressors across all levels of biological organisation from the molecular to whole communities and ecosystems, whereas environmental toxicology focuses upon effects at the level of the individual and below (Maltby & Naylor, 1990). Ecotoxicology thus incorporates aspects of ecology, toxicology, physiology, molecular biology and analytical chemistry. The ultimate goal of this approach is to be able to predict the effects of pollution so that the most efficient and effective action to prevent or remediate any detrimental effect can be identified. Aquatic toxicology, the part of ecotoxicology dealing with aquatic ecosystems has received increasing attention over the last few decades as the problems of water pollution are faced in both industrialized and developing countries. In those aquatic systems that are already impacted by pollution, aquatic toxicology studies can inform as to the best course of action to restore ecosystem services and functions efficiently and effectively (Peter, 1987). A frequently used approach is the study of indicator species, which are defined as any biological species that define a trait or characteristic of the environment. For example, a species may delineate an ecoregion or indicate an environmental condition such as a disease outbreak, pollution, species competition or climate change. Indicator species can be among the most sensitive species in a region, and sometimes act as an early warning to monitoring biologists. (Fields & Johnston, 2005)

3.2 *Daphnia magna*

Daphnia magna is one the most frequently used invertebrates in standard acute and chronic tests in aquatic toxicology. The reasons for the selection of daphnids for routine use in toxicity testing are both scientific and practical (Peter, 1987):

- they are broadly distributed in freshwater bodies and are present throughout a wide range of habitats.
- they are an important link in many aquatic food chains (they graze on primary producers and are food for many fish species).
- they have a relatively short life cycle (important for reproduction tests) and are relatively easy to culture in the laboratory.
- they reproduce parthenogenetically, which allows testing of clones with little genetic variability and with reproducible testing results.
- they are sensitive to a broad range of aquatic contaminants.
- their small size means that only small volumes of test water and little bench space are required.
- because they are nearly transparent, their internal organs are easy to study in live specimens.

Daphnia magna (Fig. 3.1) is a small planktonic crustacean (2 to 5 mm in length) and are often termed as water fleas because of their saltatory swimming style. *Daphnia magna* belongs to the order of the cladocerans. Cladocerans carry a chitinous carapax which encloses the trunk but not the head and often terminates in an apical spine as shown in Fig. 3.1. The head projects ventrally and possesses one reduced nauplius eye and a sessile compound median eye which can be rotated. Furthermore the head carries five pairs of appendages. The first pair of antennas is used as a sensory organ, the second pair is used for swimming. Movement is largely vertical. The other three pairs of appendages form the mouth parts. Like most branchiopods, cladocerans are mainly non-selective suspension feeders which collect food particles with fine setae arranged on the trunk appendages to form a distinct comb. The water current passes from anterior to posterior and collected particles are transferred via the food groove towards the gut, where the food is digested and assimilated. The food of cladocerans consists of microalgae (1 to 25 μm), bacteria, protozoans and detritus. The thin, vasicular epipodite on each of the trunk appendages is a called a gill and may perform similar functions as fish gills. The tip of the trunk, commonly called the post-abdomen, is turned ventrally and forward and bears special claws and spines for cleaning the thoracic appendages and the carapax and

for preventing the eggs falling out of the brood chamber. Oviducts open into a dorsal brood chamber inside the carapax. Development in most cladocerans is direct, and the young are released from the brood chamber by the ventral flexion of the post-abdomen of the female. When the young leave the brood chamber, the skeleton is moulted and a new batch of eggs is released into the new brood chamber. Most branchipods are pale and transparent, but rose or red colours are sometimes observed (cause by the presence of haemoglobin within the body). The presence of hemoglobin frequently depends on the amount of oxygen in the water, so the animals are colourless in well-aerated water and pink in stagnant waters (De Schamphelaere, 2002).

3.3 Zinc related aquatic toxicology experiments on *Daphnia magna*

Life has evolved in the presence of metals and essential metals have become incorporated into metabolic processes crucial for the survival, growth and reproduction of organisms (Linder, 1991) (Finney & O'Halloran, 2003). An element is considered essential when: (1) it is determined to be present in all healthy tissues (2) deficiency symptoms are noted with depletion or removal, which disappear when the elements are returned to the tissue and (3) the deficiency symptons are linked to a distinct biochemical defect at the molecular level. Some metals such as Fe, Mn, Zn, Cu, Co and Mo are essential for all living organisms. Although Zn is toxic at high concentrations, it is also an essential element required for many biological processes. The functioning of over 200 enzymes is dependent on this metal (Linder, 1991) and the essentiality of zinc has been established for most phyla (Vallee, 1991). Aquatic biota regulate their internal concentrations of essential metals through active regulation, storage/detoxification, or a combination of both (ICME, 1995).

According to Liebig's law of the minimum, each species has for each essential element an optimal concentration range in which it can satisfy its metabolic requirements and develop and perform in an optimal way (Hopkin, 1989). This range is termed the optimal concentration range of essential elements (OCEE) (Van Assche, 1996). The OCEE is linked with the natural concentration of the essential element in the species natural habitat. It is further determined by the species' homeostatic capacity that allows it to regulate actively its metabolically required tissue concentrations and maintain optimal levels under varying external concentration of the essential element. However, when the external concentration of the element becomes too low or too high, homeostatic regulation will not be sufficient and deficiency or toxicity can occur (Fig. 3.2). Recently, studies have demonstrated the existence of an OCEE for *Daphnia magna* for Zn (Muyssen & Janssen, 2002; Muyssen *et al.*, 2006). These studies have also indicated that the OCEE may shift to lower or higher concentrations upon acclimation to lower or higher concentrations (Fig. 3.2). However, based on acute and

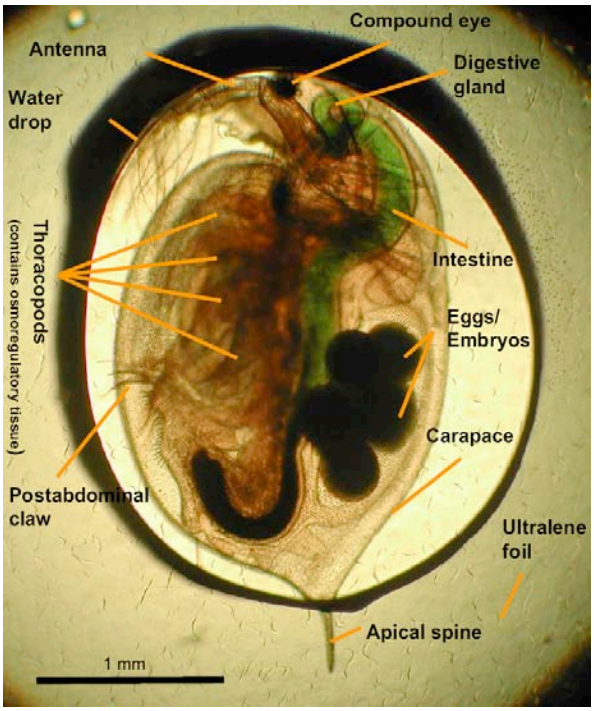

Figure 3.1: Optical image of *Daphnia magna* swimming in a small drop of water.

chronic toxicity test data these authors only report a maximum of a factor of two to three decrease in sensitivity of *Daphnia magna* for Zn, whereas bioavailability has been demonstrated to account for differences well over 2 orders of magnitude within the same species (Paquin *et al.*, 2002; Erickson, 1996). The latter clearly illustrates the high importance of bioavailability as compared to acclimation for correctly assessing the environmental risks of (essential) metals such as Zn.

During the last decades, numerous definitions have been put forward for the term bioavailability, but it seems that no single sentence is capable of fully covering its entire meaning. The main idea however is that the toxic effect of a metal does not only depend on the total concentration of that metal in the surrounding environment, but rather that it depends on a complex interaction between physico-chemical and biological factors, i.e. the same total metal concentration does not result in the same degree of toxic effect under all conditions (Newman & Jagoe, 1994; Campbell *et al.*, 1988; Wagner, 1979). The first key step in evaluating metal bioavailability is to recognize the importance of metal speciation, both physically (dissolved versus particulate material) and chemically (free metal ions versus complexed metal forms), as some metal species intrinsically have different potencies to adversely affect organisms (De Schamphelaere, 2002). In the context of bioavailability modelling, computer models allow the computation of chemical activities and concentrations of the free metal ion and metal

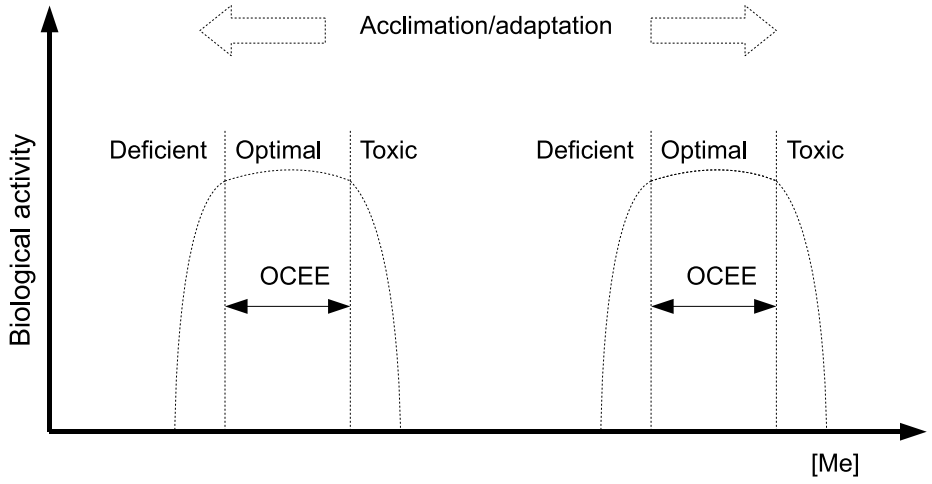

Figure 3.2: The OCEE concept. Biological activity is maximal within the OCEE and decreases at lower (deficiency) or higher concentrations (toxicity). Acclimation and adaptation to lower or higher concentrations can shift the OCEE to lower or higher concentrations, respectively. Reproduced from De Schamphelaere (2002).

complexes. Since these computations are relatively straightforward, these computer models have become an integral part of the most advanced model, i.e. the biotic ligand model (BLM), which is an integrative framework to evaluate and predict bioavailability and toxicity of metals for freshwater model organisms (Paquin *et al.*, 2002). It considers both metal speciation in the solution surrounding the organism and the interactions between metal ions and competing ions at binding sites on the organism-water interface (e.g. epithelial cell or gill tissue) as illustrated in Fig. 3.3.

The relationships between metal bioaccumulation and toxicity in *Daphnia magna* is still poorly understood. As shown in Fig. 3.4, a possible uptake of metals can occur for example via the gill tissue (uptake route A) and or via the gut (uptake route B). Since *Daphnia magna* feed on live green algae which can accumulate Zn, they provide a potential source of Zn via ingestion. When considering waterborne and dietary exposure to metals, the gill and gut tissue of *Daphnia magna*, respectively, are commonly considered to be the primary target for metal uptake and/or toxicity (Paquin *et al.*, 2002). The mechanisms of dietary toxicity are generally less investigated than those of waterborne toxicity. The issue of dietary metal toxicity (especially for essential metals) is currently a matter of intensive debate and research (Heijerick *et al.*, 2005; Muyssen *et al.*, 2006). Total body metal contents are most often not predictive of the onset of toxic effects, most likely because high metal concentrations in possible target organs and tissues are diluted by lower metal concentrations in the rest of the body. The determination of tissue specific metal concentration in small zooplankton is

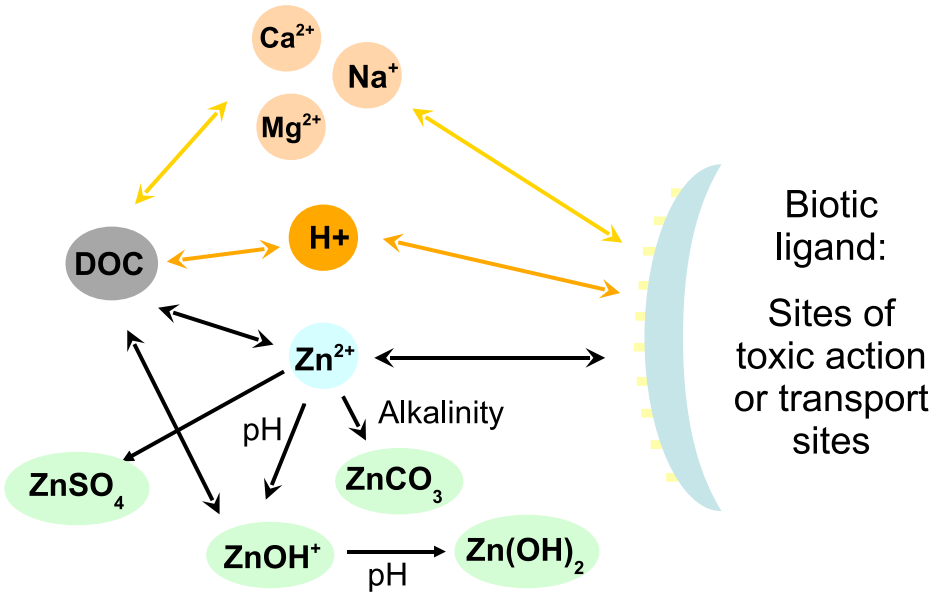

Figure 3.3: Schematic of *Zn* biotic ligand model for *Daphnia magna*. The toxic effect of *Zn* does not only depend on the total concentration of that metal in the surrounding environment, but rather it depends on a complex interaction between physico-chemical and biological factors. Reproduced from Paquin *et al.* (2002).

not plausible by a combination of tissue dissection, tissue digestion and conventional ICP or AAS analysis.

Another interesting topic is the toxicity mechanism at the subtissue level. Metal ions can enter a cell in different ways: lipid permeation, complex permeation, carrier mediated, ion channels, ion pumps and endocytosis (Soto *et al.*, 2009). Toxicity is then caused by non-specific binding of metal ions causing: 1) blocking of the essential biological functional groups of biomolecules, 2) displacing essential metal ions in biomolecules, and 3) modifying the active conformation of biomolecules (Mason & Jenkins, 1995). For *Daphnia magna*, three different toxicity mechanisms have been proposed: 1) the metal reacts with biomolecules on the apical membrane of epithelial tissue, causing tissue damage and/or inhibition of transport channels, 2) the metal enters the epithelial tissue and reacts with transport channels on the basolateral membrane, and 3) the metal enters the extracellular fluids (blood or haemolymfe) from where it is distributed into other tissues (De Schamphelaere, 2002). Although sub-cellular metal distribution in aquatic invertebrates has often been studied by means of sub-cellular fractionation by differential centrifugation (Wallace *et al.*, 2003; Wallace & Luoma, 2003), this technique has two major shortcomings: (i) it is often conducted on whole organism homogenates, which may cause a dilution effect, and (ii) several organelles are fractionated into the same fraction (e.g. mitochondria, microsomes and nucleus). Hence, with this technique it is not possible

to relate metal accumulation to different types of organelles within specific cell types within specific tissues.

Subsequently, detoxification can occur according to the following mechanisms: 1) specific soluble ligands which form complexes with metal ions of which the most important are metallothionins 2) compartimentalisation of metals in membrane limited vesicles or lysosomal organelles 3) formation of insoluble precipitates such as Ca/Mg or Ca/S granules in which the metal ions are bound. The two types of granules can be subdivided according to their location, composition and structure (Stanley, 2003).

3.4 Sample preparation of *Daphnia magna* for X-ray analysis

If we consider *Daphnia magna* in its natural environment, we quickly realize its biological complexity. The organism is three-dimensional and composed primarily of light elements, most of which are organized into a mixture of periodic and aperiodic structures. These structures range from simple molecules and macromolecules to complex heteropolymers, all bathed in an aqueous solution of ions and electrolytes. *Daphnia magna* lives at ambient temperature and pressure in an aqeous environment, is sensitive to ionizing radiation and is thermodynamically unstable. The X-ray microanalysis techniques used in this work (micro-XRF, micro-XAS, micro-CT) require however that the biological sample remains unchanged during a time frame of several hours. The guiding principle of specimen preparation for chemical analysis is that the sample should be as close as possible to its natural state, which resulted in only two different approaches:

1. *Low temperature fixation*, in which only the phase of the liquid environment is changed. Although they require more specialised equipment and damage to the morphology of the sample is frequent, the low temperature methods are generally acknowledged to be the most reliable for X-ray analysis (Goldstein *et al.*, 2004) .

2. *Chemical fixation*, in which the natural chemical and liquid environment is changed to varying degrees. Although easier to perform and requiring little instrumentation, techniques designed to retain the chemical content of samples usually do not adequately preserve the morphology (Goldstein *et al.*, 2007).

Scanning electron microscopy (SEM) equipped with energy dispersive X-ray detectors (EDX) is a well established technique which also requires an unchanging sample. It is important to note however that many of the sample preparation techniques for SEM are not straightforward to extrapolate towards synchrotron X-ray microanalysis since there are some crucial differences between both analytical techniques: (1) there is a difference in sample environment: X-ray analyses at SR beamlines are mostly performed under ambient temperature and pressure instead of vacuum conditions (2) the resolution of a scanning X-ray microprobe currently

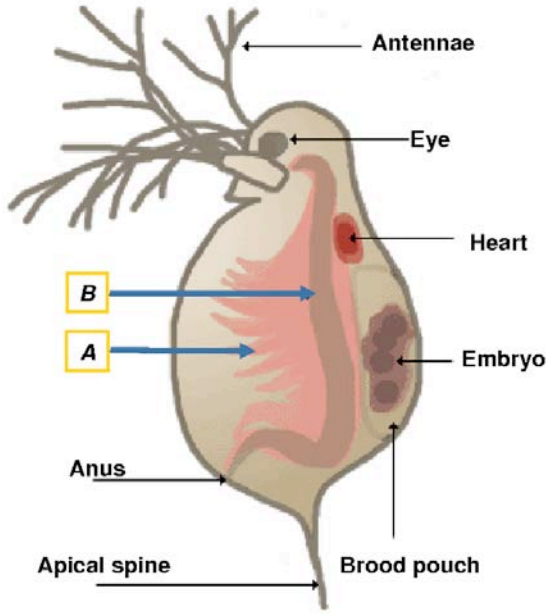

Figure 3.4: Schematic representation of *Daphnia magna* visualising different uptake routes.

varies in a range from 20 μm to 100 nm, whereas SEM can reveal surface details from 1-5 nm. (3) X-ray probes can study a variety of properties e.g. chemical distribution (XRF), chemical state and coordination (XAS) whereas SEM provides information regarding the surface morphology due to the shallow penetration of electrons as opposed to X-rays (Kanngieser *et al.*, 2007). In what follows, we discuss both approaches for fixation of biological samples with their specific application to *Daphnia magna*

3.4.1 Low temperature fixation

Freezing of biological specimens

Freezing a sample is a chemically non-invasive preparative procedure and it is known that sufficiently low temperatures effectively immobilize dynamic and physiological processes. Converting a biological organism to its frozen solid state while preserving its internal microstructure is not a trivial task. The triphasic state that exists within the biological organism should be maintained and dissolved elements, compounds and molecules have to remain in situ within the solidified matrix. The disadvantage of the low-temperature approach to specimen preparation is the possible formation of crystalline materials during the liquid-to-solid phase transition, which should be avoided. When hydrated samples are cooled, they generally form highly ordered eutectic mixtures of pure ice crystals and partitioned solids which bear little structural relationship to their original random organization, which should be avoided when performing X-ray analysis at the submicron level. However, if the samples are cooled

fast enough, this structural reorganization can either be significantly diminished or entirely avoided (Goldstein *et al.*, 2004).

Depending on temperature and pressure, water can exist in several different stable crystalline forms and one metastable amorphous form. *Hexagonal ice* is the most favorable crystalline arrangement below 273 K, when water is transformed from a highly disorganized liquid to a highly organized solid phase. This phase change is accompanied by massive dimensional changes. *Amorphous ice*, on the other hand, is a non-crystalline or glassy form of ice. It can be formed by rapidly cooling ($\sim 10^6$ K/s) minute quantities of aqueous solutions (≤ 100 μm^3). It should also be noted that the binding state of water has an important bearing on its ability to solidify. In *surface-modified water*, molecules are in transient contact with a solid surface, as distinct from perturbed or *bound water*, which is in intimate contact with hydrated ions, molecules, and macromolecules. The more closely liquid water is hydrogen-bonded to solutes or hydrophilic solids, the less readily it will form ice (Goldstein *et al.*, 2004).

In general, the conversion of liquid water to ice involves three distinct, but closely related processes that occur in the following order: (1) heat removal: the low-temperature in the immediate environment of the specimen acts as a heat sink and removes thermal energy from the specimen until it is in equilibrium with the environment. (2) nucleation: as liquid water is cooled, the random movements of the water molecules produce clusters of the correct size and shape for the condensation of further water molecules, which form the nucleus of an ice crystal. The process whereby water provides its own nucleation sites is called *homogeneous nucleation*. Water invariably contains dissolved materials and particulates, which may act as catalysts for heterogeneous nucleation. The probability of heterogeneous nucleation occurring increases with the volume of water and decreases with temperature. (3) ice crystal growth: following nucleation, the ice crystals grow (Goldstein *et al.*, 2004).

The rate of growth is determined by the speed at which water molecules move to the point of crystal growth, the accommodation of water molecules at the crystal interface, and the transport of heat away from the growing interface. The rate of ice crystal growth is critically dependent on the rate at which heat can be removed from the system. Heat removal is categorised by the rate of cooling: (1) very slow cooling (~ 0.01 K/s): numerous nucleation events occur and few, but very large crystals develop (2) fast cooling ($\sim$ 1-100 K/s): more nucleation events occur and more smaller ice crystals are produced (3) very fast cooling ($\sim$ 1000 K/s): many more nucleation events occur, but much smaller ice crystals develop (4) ultrarapid cooling ($\sim 10^6$ K/s): so many nucleation events occur that there is virtually no time for crystallization. At this cooling rate amorphous or vitreous ice may be produced (Goldstein *et al.*, 2004).

The following procedures can be adopted prior to rapidly cooling the sample: (1) minimizing sample size and specimen holders: wherever possible, the surface area-to-volume ratio of the

sample should be maximized and the sample made as small as possible (2) maximizing undercooling: the sample should be undercooled as much as possible without altering its natural state and before nucleation occurs (3) altering the nucleation process: pressure can be applied to the sample momentarily before it is rapidly cooled to improve nucleation (4) depressing the sample freezing point: achieved by using cryoprotectants, a group of polyhydroxy chemicals that suppress ice crystal formation. Once amorphous ice is formed, it must be maintained below the glass transition temperature T_g in order to maintain the random arrangements of the water molecules and prevent devitrification and subsequent recrystallization (for water T_g is 135 K) (Goldstein *et al.*, 2004).

Recent advances in instrumentation for cryofixation

Recent advances in cryofixation have focussed on improving the methods of heat removal from specimens, thereby increasing the size of specimens that can be succesfully frozen. A first method, plunge freezing is inexpensive and simple and provides specimens without ice crystals, but only in the outer 10-20 μm layer of a specimen will freezing be rapid enough to ensure good preservation (Ryan, 1992). The other, high pressure (hyperbaric) freezing, requires a specially designed apparatus, but is capable of preserving specimens that are 500-600 μm thick (Studer *et al.*, 2001).

In case of plunge freezing, liquid nitrogen at its boiling point (77 K) is used to cool a secondary cryogenic liquid. The specimens are frozen by plunging them rapidly and deeply into the secondary cryogen: the flow of cryogen over specimen surfaces ensures rapid dissipation of heat. Cryogens should have the following properties: (1) a low melting point and a high boiling point to minimize surface film boiling (2) a high thermal conductivity an thermal capacity (3) a high density and low viscosity at the melting point (4) safe, environmentally friendly, inexpensive and readily available. The low boiling point of liquid nitrogen prevents it from being used directly on specimens in plunge freezing, since it boils on contact with the warm specimen. The resultant insulating layer of gas slows freezing sufficiently to allow large and disruptive ice crystals to form in cells. Even adiabatically frozen nitrogen slush (about 64 K) is unsuitable for any but the smallest specimens due to the limited heat capacity of the medium (Ryan, 1992).

Pressurization of liquid nitrogen inhibits boiling, allowing it to be used directly on specimens for high-pressure freezing. The concept and method of freezing biological specimens under high pressure were developed from the late 1960s to the 1980s and resulted in the design and manufacture of high pressure freezing machines. The technique and apparatus of high-pressure freezing continue to be refined, in response to new applications and results. In brief, specimens are sandwiched between two small metal cups or plates, locked into a special holder, which is inserted into the pressure chamber and then frozen in a 0.5 s burst of liquid

nitrogen pressurized to 2-3 *kbar*. Rapid transfer of the frozen specimens to liquid nitrogen at normal pressure prevents rewarming after freezing. To prevent specimens from freezing before they are fully pressurized, warm isopropyl alcohol is injected into the chamber just ahead of the nitrogen burst. A temperature controlled closed circuit water supply keeps the pressure chamber and alcohol supply from cooling during operation. In Fig.3.5, a high pressure freezing device from Leica is shown, which represents the latest developments in this field. The equipment is complex and expensive, although it is easy to use and gives a high throughput of well-preserved samples. It provides high quality freezing up to 200 μm into the specimen. After freezing, pressure and temperature curves can be visualised (Studer *et al.*, 2001).

Further treatment of frozen samples

If wanted, further manipulation of the sample is possible involving (1) cryosectioning: a flow process involving extensive plastic deformation of the ice as the material is thinly sliced at the knife and sample interface. (2) cryofracturing: separation of the frozen specimen along a line of least resistance parallel to the applied force (3) cryopolishing: produces very flat surfaces of frozen material suitable for X-ray microanalysis. The quench frozen sample is cryosectioned at as low a temperature as possible and the sections discarded or the frozen sample is cryofractured close to the region of interest and the undulating fracture face polished (Goldstein *et al.*, 2004).

After cryofixation and/or further sectioning, X-ray analysis upon the manipulated frozen-hydrated samples at temperatures below T_g is in principle possible. Moreover, when X-ray analyses are performed at very low temperatures, there is a reduction of high-energy beam-induced radiation damage. However, the frozen sample has to be transferred to the experimental table while remaining below the glass transition temperature when (sub-)microscopic analysis is envisaged. This involves a cumbersome transferstep and the use of cooling equipment at the experimental table which can cause (1) vibration of the sample stage (2) temperature drifts possibly influencing the position of the sample stage, and in some cases the X-ray focusing optics. Currently, only a very few X-ray micro/nanoprobes are equipped with cryogenic sample stages and transfer systems. Therefore, an option is to *sublime* the frozen water at low temperature and high vacuum and study the so-called frozen-dried sample. The rate of sublimation is a function of temperature and vacuum, with typical drying times being several hours or longer. Ideally freeze drying should be carried out at temperatures below the recrystallisation point of ice, but this would require inordinately long drying times. In practice temperatures of 220 K have been found to give reasonable results under vacuum levels achievable with two-stage rotary pumps. After freeze drying, the sample chamber needs to be brought back to atmospheric pressure with a dry inert gas (Quorumtech, 2009). There are only few commercial devices available for sufficiently delicate freeze drying, an example

Figure 3.5: Leica EM PACT 2. Reproduced from Leica microsystems (2009).

of which is shown in Fig. 3.6. The system is composed of a Peltier cooler with temperature controllers. The samples are left overnight at 220 K and are then brought to ambient temperature over a 2 hours ramp. They are then left for 30 min before purging with dry N_2. Another approach is to perform a sublimation under atmospheric conditions. A requirement is to bring the sample very slowly to ambient temperature under a slow temperature gradient, which can be done by e.g. a Leica EM AFS2 instrument, shown in Fig. 3.7. After freezing the sample it is normally used for freeze substitution with an adeaquate solvent using progressive lowering of temperature (PLT) and low temperature resin embedding (Leica microsystems, 2009).

X-ray analysis on *Daphnia magna* by means of cryogenic methods

When X-ray analysis at the microscale is foreseen, ice crystal formation does not interfere with the analysis and the sample can be cooled with a wide range of freezing procedures. X-ray analysis on *Daphnia magna* using a laboratory X-ray spectrometer discussed in Chapter 4 was performed under non-cryogenic conditions since the design of the small spectrometer vacuum does not allow cooling. Moreover, since cryogenic sample preparation techniques such as cryosectioning followed by the necessary freezedrying did not retain the morphology on the microscale in these highly hydrated samples, chemical fixation methods were used upon *Daphnia magna* (paraffin embedding and hexamethyldisilazane fixation), which will be introduced in section 3.4.2.

Figure 3.6: K750X Peltier Cooled Freeze Dryer. Reproduced from Quorumtech (2009).

Figure 3.7: Leica EM AFS2. Reproduced from Leica microsystems (2009).

Although SR microprobes provide the additional space for cryogenic material, they are typically not equipped with such cooling devices. However, in a pilot experiment, a cryostream equipment was installed at the HASYLAB Beamline L microprobe in order to compare the 2D/CT elemental distributions obtained for low-temperature and a chemical fixation procedure (hexamethyldisilazane fixation). A dual detector XRF-tomography and mapping under cryogenic conditions is also demonstrated in Chapter 5.

Due to problems associated with cryo-analysis at SR microprobes, e.g. availability of cryostream equipment and possible damage to the X-ray optics, confocal micro-XRF and 2D/confocal micro-XANES on *Daphnia magna* discussed in Chapter 6 and 7 respectively, were performed under non-cryogenic conditions using a chemical fixation method (hexamethyldisilazane fixation).

In Chapter 8, submicrosopic X-ray analysis on *Daphnia magna* was envisaged at the ESRF ID22NI nanoprobe. Due to problems associated with cryo-analysis at SR nanoprobes, e.g. sample vibrations and misalignment of the optics due to temperature drift, submicroscopic analysis was performed under ambient temperature. Cryogenic sample preparation techniques such as shock freezing or high pressure freezing only allow a perfect vitrification up until a depth of 200 μm. The sample carrier for high pressure freezing does not allow a sample greater in size then 1 mm, making possible the investigation of isolated sub-structures of interest. When dealing with delicate aquatic organisms, an efficient and reproducible isolation of structures of interest is more cumbersome, also given the fact that during isolation the organism is not in its native environment anymore which can induce changes within the sample. The nanochemical imaging experiments were therefore performed on chemically fixed samples (karnovsky fixation).

3.4.2 Chemical fixation

Fixation

In the previous chapter, low temperature methods on biological samples were discussed for X-ray analysis. However, sometimes this approach can not be applied due to a lack of instrumentation available or due to the size of the sample. Therefore, chemical fixation methods need to be used which are generally invasive and are less concerned with preserving the precise chemical constitution of the specimen. Adequate sample preparation by wet chemical procedures is often difficult to achieve in practice because techniques designed to preserve the ultrastructure tend to retain macromolecules at the expense of soluble constituents. Several guidelines should be followed: (1) the structural detail should be preserved at a spatial resolution better than the expected analytical resolution (2) preparative chemicals which don't mask or contribute to the X-ray spectrum should be used (3) information available from complementary studies can help to evaluate the preparative procedure. Fixation is the most

critical part of sample preparation and it is important to give this process careful attention. Fixation is a chemically invasive process of stabilisation, which involves crosslinking an preserving macromolecules, usually at the expense of small molecules and electrolytes. Most of the methods evolved from EM and light microscopy and every fixation protocol must be tailored for a given sample because of differences in e.g. sample size, water content, diffusion rates, penetrability, physiological state, osmolarity and pH. All chemical fixatives cause changes in cell permeability and the main concern is how to staunch the flow of elements from and within the sample. Heavy metal fixatives are much worse than organic fixatives and in addition may mask the elements being analyzed. Wherever possible, organic fixatives should be used. Chemical fixation is too slow for analysis of diffusible elements, therefore one should either try to precipitate the element concerned as an insoluble salt or use cryopreservation methods as previously discussed (Goldstein *et al.*, 2007).

Dehydration

After fixation, the liquid phase needs to be removed from the sample which must be achieved with minimal extraction of ions and minimal distortion. There are several ways to remove water from specimens: (a) physicochemical dehydration is the standard procedure used in all forms of microscopy and involves passing the fixed and washed specimen through increasing concentrations of a large volume of ethanol, methanol, or acetone (b) chemical dehydratation takes advantage of the reaction between 2-2 dimethoxypropane and water to form a mixture of acetone and methanol (c) critical point drying. It should be noted that all organic solvents will cause loss of elements, although this effect is ameliorated if there is a progressive lowering of temperature as the dehydrating agent becomes more concentrated. Freeze substitution, in which the ice is dissolved in organic solvents at low temperatures, can also be used. Embedding is necessary if sections are to be cut to reveal the inside of the specimen. Embedding in epoxy or acrylate resins may result in loss of elemental material from the sample and the resins may contribute elements to the sample, e.g. S and Cl. Hydrophilic Lowicryl and LR White acrylate resins are more promising because they can be polymerized at subzero temperatures. Subsequently, the sample needs to be deposited on a good sample support with the following characteristics: (1) low absorption of X-rays, (2) no trace elements should be present, (3) possibility of growing cell monolayers upon the surface, (4) good transparancy for observations under the microscope, (5) easy to handle during plunge freezing and lyofilisation, (6) constant specifications (e.g. thickness/flat surface) among different supports (Goldstein *et al.*, 2007).

X-ray analysis on *Daphnia magna* by means of chemical fixation

For micro-XRF/XAS analyses discussed in Chapter 5, 6 and 7, entire fixed organisms were required. *Daphnia* species dehydrated in graded acetone solutions (70 %, 80 %, 90 %, 2x98 % and 2x100 %) and immersed in 1-1.5 mL 1,1,1,3,3,3-hexamethyldisilazane (HMDS), followed

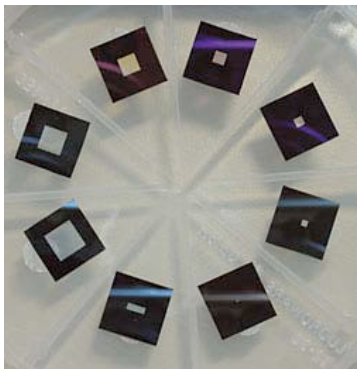

Figure 3.8: Examples of the silicon nitride supports. Reproduced from Silson (2009).

by removal of the excess of HMDS by a desiccator overnight revealed an excellent internal/external preservation for SEM investigations (Laforsch & Tollrian, 2000), even without gold coating as shown in Fig. 3.10. A comparison between critical point drying and HMDS fixation is shown in Fig. 3.9. The good results, low costs, easy operation without the requirement of special equipment and full three-dimensional preservation of the organism favoured this method above other chemical fixation methods.

For laboratory micro-XRF/LA-ICPMS measurements in Chapter 4 and SR nano-XRF in Chapter 8 respectively, chemically fixed thin sections were necessary for obtaining high quality elemental distributions. In Chapter 4, dehydration through water/aceton series and substitution with paraffin followed by sectioning using a microtome was used. In Chapter 8, a chemical fixation procedure was used (Karnovsky, 1965), followed by an alcohol dehydration. After dehydration, embedding in Spurr resin (Spurr, 1969) and subsequent cutting in thin sections was performed. Afterwards, the thin sections were immediately analyzed or first deposited on square silicon nitride ultra-thin membranes in square silicon supporting frames, as shown in Fig. 3.8. For this study, a Si_3N_4 membrane window with a $3.0 \times 3.0\ mm$ membrane size was used. The membrane thickness was 500 nm and the size of the frame was 7.5×7.5 mm. The thickness of the frame itself is 200 μm.

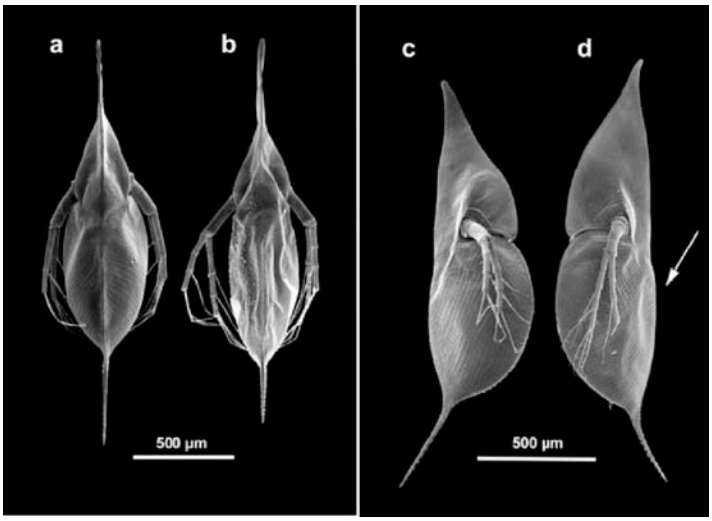

Figure 3.9: Dorsal view of *Daphnia cucullata* dried with HMDS **(a)** and CPD **(b)**. Lateral view of *Daphnia cucullata* dried with HMDS **c** and CPD **d**. Deformations are visible after CPD, while HMDS provides a better surface structure. In particular, the carapace of the daphnids is susceptible for shrinkages in the region of the neck and the brood chamber (arrow). Reproduced from Laforsch & Tollrian (2000).

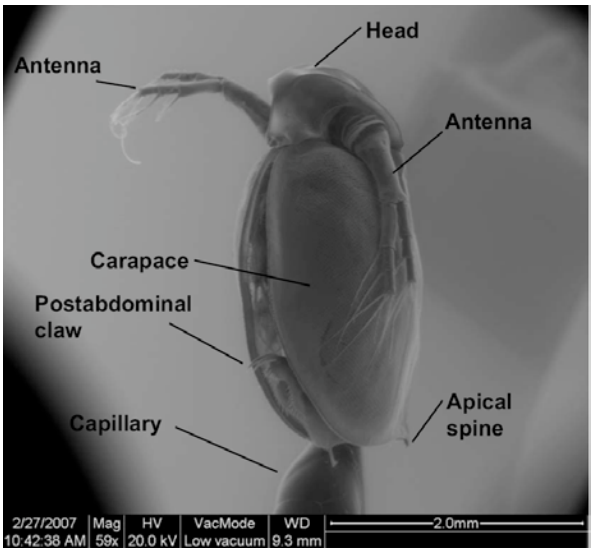

Figure 3.10: SEM analysis of the non-exposed HMDS-dried *Daphnia magna* sample.

Chapter 4

Laboratory micro-XRF on *Daphnia magna*

4.1 Introduction

In this chapter we discuss the microchemical imaging on *Daphnia magna* by means of laboratory micro-XRF. Although synchrotron radiation based micro-XRF has a much higher sensitivity, it is not always readily available. Therefore, laboratory micro-XRF is a wise choice to explore the analytical problem before making use of highly competitive synchrotron radiation sources. The technique is also useful to optimise sample preparation methods and detect and tackle problems before heading to a state-of-the-art synchrotron facility. Since beamtime for a given project is typically limited to a period of 1-2 weeks per year, a highly optimised measuring procedure on the samples of interest is desired. Also, the worse detection limits of laboratory micro-XRF can be partially compensated by means of longer measuring times, which are affordable on an instrument with permanent access.

First, the historical developments in laboratory micro-XRF are discussed. Then, the instrumental parameters of the employed EDAX Eagle III micro-XRF instrument are characterised. This is followed by the investigation on which elements the laboratory 2D micro-XRF can provide spatially resolved information and whether differences in Zn distribution between differently exposed *Daphnia magna* samples can be detected and/or visualised. Since laboratory -XRF on *Daphnia magna* has not yet been performed in the past, an organism wide view on the tissue specific element distributions seemed to be the most informative approach to the problem. In order to obtain an organism wide view on the tissue specific element distributions, the preferred strategy was to scan the entire organism, of which the relevant areas are often as large as several square millimeters. Since also analysis of specific areas of metal accumulation was envisaged, thin sections of *Daphnia magna* were analysed, which could provide insight in this matter. In a final part of this chapter, the detection limits and imaging capabilities of

LA-ICPMS on *Daphnia magna* were compared with those of laboratory micro-XRF.

4.2 Historical development of laboratory micro-XRF

Laboratory based micro-XRF underwent a quick evolution. In the 1960s, X-ray microbeams were produced by collimating a broad cone of radiation originating from an X-ray tube by means of suitable apertures or crossed-slit systems. This concept did not receive a lot of attention, the major reason being the low count rates observed for small area samples. Also, although the use of photons as an excitation source intrinsically features a number of advantages over charged particle excitation, the rapid development of electron microscopy with its much higher lateral resolution, overshadowed further developments. In the early 1980s, micro-XRF was rediscovered with the first use of energy dispersive (ED) detectors for X-ray imaging applications. As the solid angle of the Si(Li) detectors can be much larger than that of crystal spectrometers, fluorescent signals of much lower intensity could be used to advantage. A step further in the development in the late 1980s was the manufacturing and use of straight, conical and ellipsoidal capillaries as X-ray concentrators (Rindby, 1986; Rindby *et al.*, 1989). A recent and interesting development is the maturation of the production technology for monolithic polycapillary X-ray lenses having the marked advantage that a large solid angle of the X-ray source is captured. These recent developments resulted in a boost of commercially available instruments. In 1997, a desktop scanning X-ray analytical microscope using paraboloidal glass capillaries was introduced by Horiba, Kyoto, Japan to produce a 10 and 100 μm sized beam (Hosokawa *et al.*, 1997). In 2003, a third generation Eagle μ-Probe micro-focus XRF was introduced by Edax, USA using an XOS (X-ray Optical sytems Inc., N.Y., USA) polycapillary (Edax, 2009). With the advent of miniaturized X-ray tubes and detectors, several handheld portable XRF analyzers for bulk analysis became commercially available (Bruker AXS, 2009; Oxford Instruments, 2009; Innov-X Systems, 2009; Thermo Scientific, 2009; Skyray, 2009; Spectro, 2009).

4.3 EDAX Eagle III, a laboratory XRF microprobe

In this chapter we will discuss in greater detail an EDAX Eagle III XRF microprobe, shown in Fig. 4.1. On the left, the exterior of the sample chamber with two handles can be seen which houses a precision controlled XYZ stage. At the upper part of the housing, a window is present which enables the direct observation of the sample in the chamber during analysis. Using the main control panel on the right, the instrument can be activated with a key and the status of the sample chamber vacuum, tube voltage and shutter can be monitored. A shielding cap for the liquid nitrogen dewar is also present. In Fig. 4.2, a top view of the sample chamber is shown. The liquid nitrogen cooled $Si(Li)$ detector with an active area of 80 mm^2 is entering the sample chamber from the right side. A detailed image of the liquid

nitrogen vessel with attached detector can be seen in Fig 4.3. Two low and high magnification CCD cameras are also present with 10 and 100 times magnification for sample positioning and set-up of scanning micro-XRF experiments. Behind, an air cooled *Rh* X-ray tube can be seen. A detailed image of the X-ray tube with attached polycapillary is shown in Fig. 4.4. Between the X-ray tube and the capillary, a rotating wheel is present with different types of absorbers and a beamstop. Fig. 4.5 shows the upper part of the EDAX Eagle III sample chamber interior. The detector and detector collimator can be seen on the left. Sample illumination is provided by LEDs placed around the microscope aperture. The mean angle of incidence for the X-ray microbeam is 55° with respect to the sample surface, defined by the optical axis of the polycapillary. Around these parts, a printboard can be seen with infrared (IR) LEDs on the right side, and IR sensors on the left. During alignment, when the sample surface is crossing the plane defined by the LEDs, an automatic crash protection system is activated in order to prevent that the sample runs into the polycapillary optic.

4.4 Characterisation of the 2D micro-XRF setup

4.4.1 Beamsize characterisation

The module consisting of the X-ray tube and polycapillary optic is motorised and can move further away from the sample surface. Using this so-called varispot system, a variable incident X-ray microbeam size can be obtained. The principle is shown in Fig. 4.7: by moving the polycapillary away from the sample compared to the ideal working (focal) distance, the divergent beam covers a larger area on the sample. By increasing the polycapillary-sample distance, beam spots of approximately 20, 100, 200 and 300 μm can be obtained so that samples with a wide variety in size can be scanned with a practical number of steps. In Fig. 4.7, a line scan result is shown, corresponding to a scan over a 10 μm thin copper wire

Figure 4.1: Front view of the EDAX Eagle III microprobe.

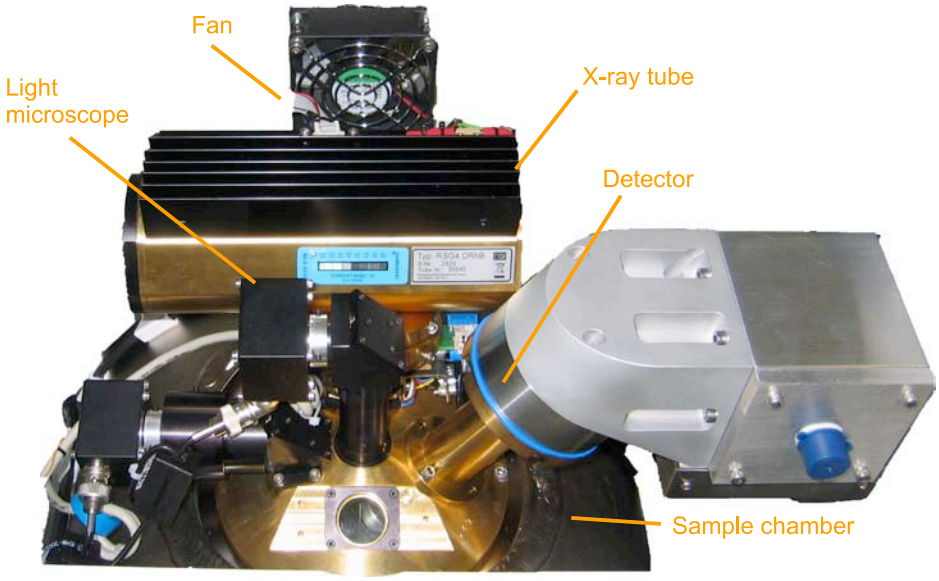

Figure 4.2: Top View of the EDAX Eagle III instrument.

Figure 4.3: Liquid nitrogen vessel with detector.

Figure 4.4: Rhodium X-Ray tube with attached polycapillary.

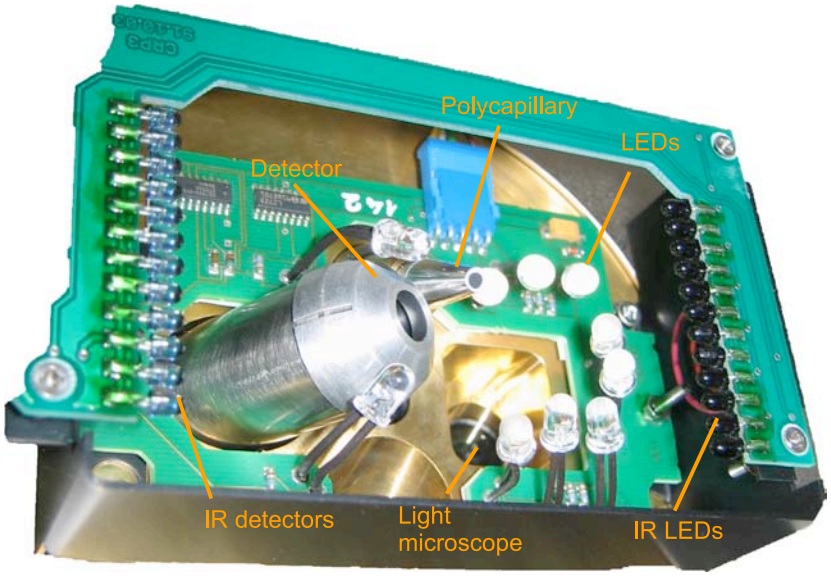

Figure 4.5: Inside view of the EDAX Eagle III instrument.

using the different Varispot settings (defining the polycapillary-to-sample distance) using a live time of 50 s and an adapted step size according to the beamsize. For the first two settings (being closest to the ideal polycapillary focal distance producing the smallest beam sizes), a step size of 5 μm was chosen, for the larger beamsizes 10 and 25 μm respectively. The 25 and 105 μm mode show a clear Gaussian beam profile, resulting in a corresponding deconvoluted beamsize of 25 μm and 112 μm. For the 225 and 315 μm mode, no clear Gaussian profile is present anymore, but a more triangular profile. For determining the FWHM, the maximum of the curve was taken and the resulting interpolated x values at half this maximum value were determined, the difference indicating the beamsize. With this approach, beamsizes of respectively 264 and 372 μm were obtained. It can thus be concluded that for larger beamsizes, larger deviations for the indicated beamsize are present. The results obtained are dependent upon the material of the wire. It must be recognised, however, that the result obtained with this method does not represent the spot size at a particular energy. Instead, the result is the beam size at an effective average energy $\langle E \rangle$ of all the X-rays that can excite the fluorescence of the element the wire is made of. Usually, $\langle E \rangle$ is close to the absorption edge energy of the element considered.

In Fig. 4.8, the results corresponding to a line scan accross a 10 μm thin $Fe - Cr - Ni$ alloy wire are shown, together with the fitted line profiles. The corrected (i.e. deconvoluted) FWHM values for the fitted Cr, Fe and Ni distributions are respectively 33.1, 30.1 and 27.5 μm. The differences in the determined FWHM values can be explained by the energy dependent spatial distribution of photons across the focal spot: higher energy photons are more centered around the optical axis, while lower energy photons will also be present in the outer regions of the beam. In general, the effective beam size decreases with increasing energy, governed by the energy dependence of the critical angle of total reflection. Therefore the low energy (and broader) component of the beam will excite more quickly metals with a lower excitation energy during the line scan, resulting in a lower resolution. The obtained lower resolution for Cr, Fe and Ni compared with the obtained value of 27 μm for Cu is understandable, since the K-absorption edge for Cu is higher than those of all these metals. Fig. 4.9 corresponds to a 200 μm gold wire scan. The $Au - L$ intensity was fitted (squares), after which the derivative was taken (triangles) and a Gaussian profile was fitted. It can be seen that the right edge is much sharper than the left edge, since the right edge was closer to the detector side and therefore less under the influence of sample self-absorption effects.

Since clear differences were observed in the FWHM of the line profiles across different wires, the energy dependent results were summarized in Fig. 4.11. The indicated FWHM values correspond to corrected values, taking into account the finite size of 10 μm of the wires (with the exception of the knife edge scan on the 200 μm thick gold-wire). The data was used from $Mo - L1$ (2.866 keV, pure Mo wire), $Cr - K$ (5.9890 keV, $Fe - Cr - Ni$ wire), $Fe - K$ (7.1120 keV, $Fe - Cr - Ni$ wire), $Ni - K$ (8.333 keV, $Fe - Cr - Ni$ wire),$Au - L1$ (14.353

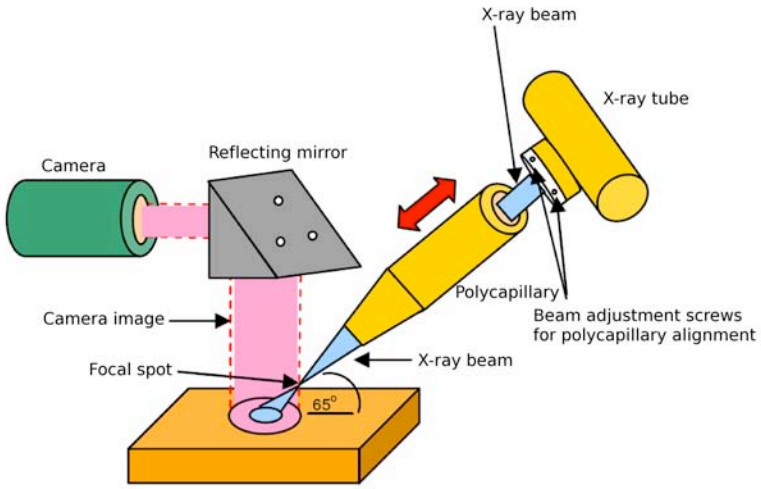

Figure 4.6: Working Principle of the VariSpot option.

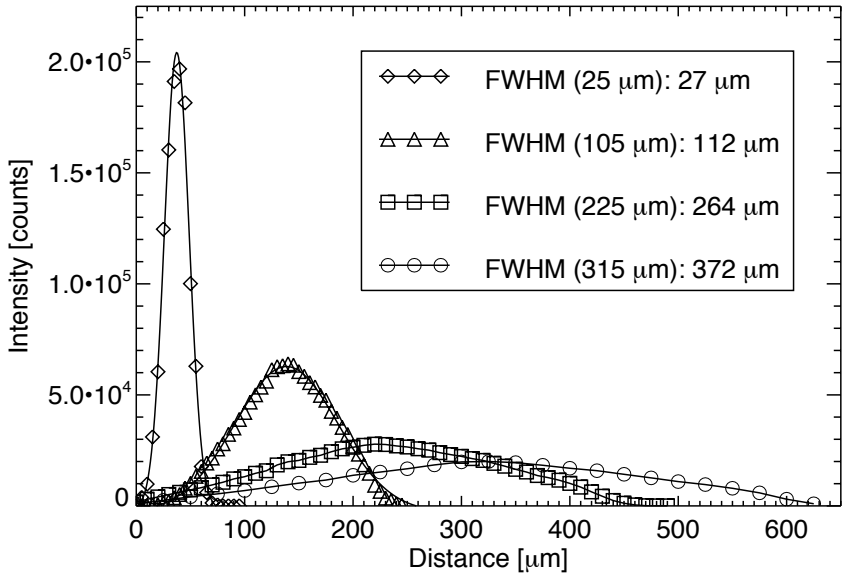

Figure 4.7: Line scan of a 10 μm Cu wire with different Varispot settings.

keV, 200 μm thick Au wire), $Mo-K$ (19.999 keV) and $Pd-K$ (24.35 keV, pure Pd wire). The data was fitted using a third order polynomial, providing the relation:

$$FWHM[\mu m] = 54.0035 - 4.67624E + 0.191550E^2 - 0.00280764E^3 \tag{4.1}$$

where E is the L or K absorption edge energy for a given element measured in keV. Clear differences in beamsizes can be observed as a function of energy. Lower energy photons, which are only able to excite lower-Z elements (or more precisely, lower energy absorption edges), clearly give a lower resolution indicating the increasing beamsize towards lower energies. This clearly demonstrates the chromatic nature of the beam's spatial distribution. Next to the low-energy broad beam components, a high energy halo can also contribute to the measured spatial resolution: at very high energy, X-ray photons can penetrate through the entire body of the X-ray lens. Such a high-energy halo component may reduce the expected spatial resolution considerably if present. As shown in Fig. 4.11, in case of our EDAX Eagle III microprobe, the higher energy photons provide the expected high resolution (and Gaussian beam profiles), indicating an efficient focusing of the high-energy photons and a negligable contribution from high-energy halo effects to the beam profile.

4.4.2 Optimisation of filter application

The EDAX Eagle III has 6 different filters positioned in front of the X-ray tube. These filters absorb certain bands of energy output from the X-ray tube spectrum and excitation occurs from X-rays at higher energies transmitted through the filter. In the detected sample spectrum, scattered background radiation is eliminated or reduced in regions where the filter absorbs the output of the X-ray tube, resulting in higher peak-to-background in the high-sensitivity region of the filter. Usage of a filter for spectral regions obstructed by tube characteristic lines can allow analysis of metals otherwise impossible. In table 4.1, the different filters are shown, together with the element ranges for which they provide increased sensitivity.

Within the scope of this work, the influence of these filters on the fluorescence spectrum of biological materials was investigated in order to be able to perform optimal measurements. As a case study, we studied the XRF spectrum of the NIST (National Institute of Standards and Technology) SRM1577B (Bovine Liver, biological standard reference material) with different filters. It should be noted that inserting a filter reduces significantly the integrated intensity of the radiation impinging on the sample. Increasing the tube current can partially compensate this effect, however this causes a reduced lifetime of the X-ray tube. Whenever possible, the tube current was adapted to achieve a 30 % detector dead time. When the filters were too thick and a 30 % dead time could not be obtained, a full tube current of 1000 μA was applied in order to test the limit capabilites of the instrument. In Fig. 4.12 the results of these measurements are shown. Unfortunately, many of the trace metals present in NIST SRM

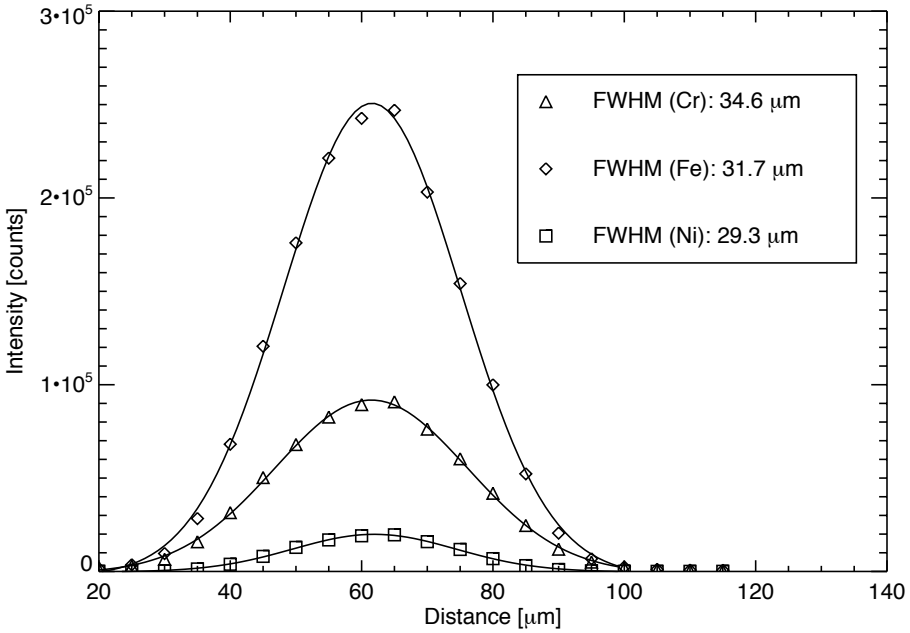

Figure 4.8: Line scan across an Fe-Cr-Ni alloy wire.

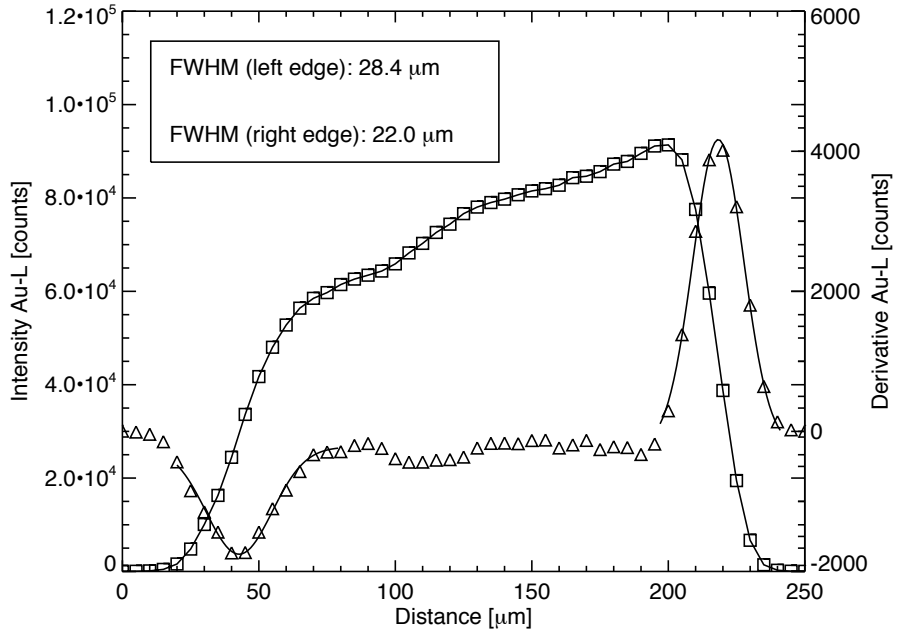

Figure 4.9: Knife edge scan over a 200 μm thick gold wire.

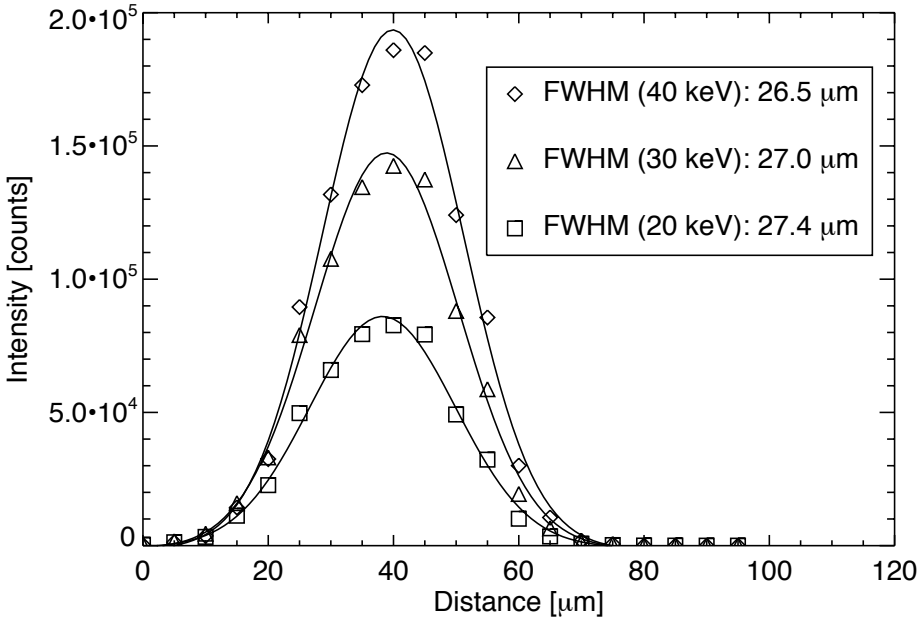

Figure 4.10: Line scan across a Cu wire at different tube voltages.

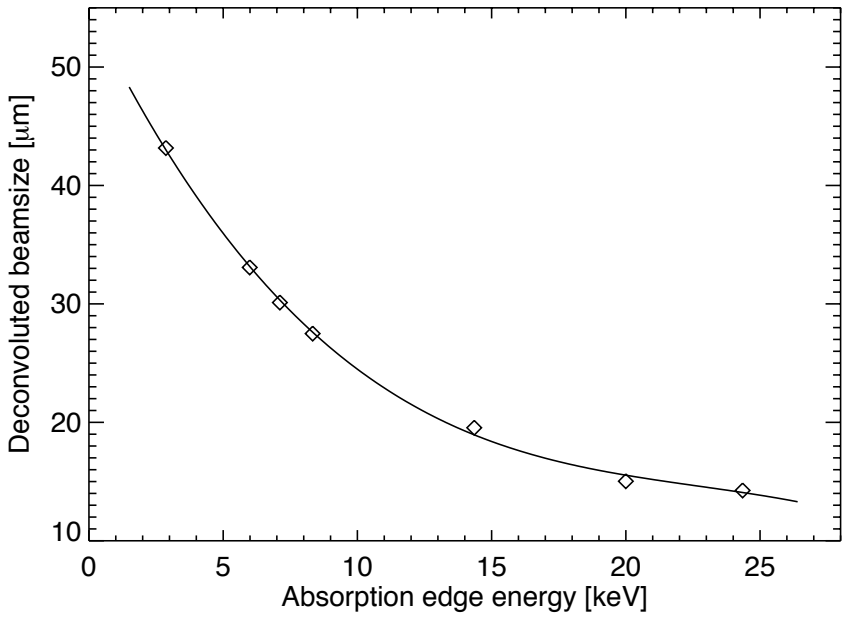

Figure 4.11: Deconvoluted beamsize in function of the energy, determined by line scans over different wires.

	Filter	Thickness	Element Range
1	Tube Shutter		X-rays blocked
2	Open		Na-U
3	Al (thin)	25 μm	S, Cl
4	Ti	25 μm	Cr - Fe
5	Ni	25 μm	Zn - As, Pb, Bi
6	Nb	125 μm	Rh - Cd
7	Al (thick)	250 μm	K - Co
8	Rh	50 μm	Ti - Zr, Pb, Bi

Table 4.1: Standard rhodium tube filter set

1577B are not visible due to the scattered bremsstrahlung of the X-ray tube. Under vacuum conditions, the K-fluorescent lines of the lower Z elements such as P, S provide a much higher count rate. Cl however suffers from a serious overlap with the $Rh - L$ fluorescent lines. Also the lower-Z minor element K provides a high count rate under vacuum conditions. Using a thin Al film primary beam absorber, it is possible to suppress a high amount of this low Z fluorescence. Using a Ti filter or a Ni filter, a clear absorption edge can be observed in the measured XRF spectrum. The rhodium filter delivers an almost monochromatic exitation, however much of the intensity of the beam is lost. It can be seen that for Fe, Cu and Zn the resulting background signal is very low. The Nb filter is more intended for inorganic materials providing high fluorescent intensities and therefore not very useful for biological analysis since most of the analytical signal disappears. The 250 μm thick Al filter seems nevertheless interesting for biological analysis: P and S are still detectable, $Rh - L$ fluorescence is well suppressed in order to detect the Cl and also Ca and K show good detectability. The signals of Fe, Cu and Zn show a very good signal-to-noise ratio. Other filters such as the Ti, Ni and Rh filter and measurement under ambient pressure without filters show no improved detection limits for any metal of interest.

4.4.3 Detection limits

Detection limits in function of time.

In order to evaluate the minimum detection limit in function of time, a repetitive point measurement on NIST SRM1577C was repeated 3000 times (LT=1 s, 200 μA, 40 kV, no filter). Then, for n from 1 to 3000, the first n spectra were summed in order to get sum spectra from 1 s until 3000 s in steps of 1 s. The XRF sum spectra were then fitted and the relative detection limit calculated. Fig. 4.13 shows a lin-log plot of the relative detection limit of P (cross), K (asterisk), Fe (diamond), Cu (triangle) and Zn (square) in function

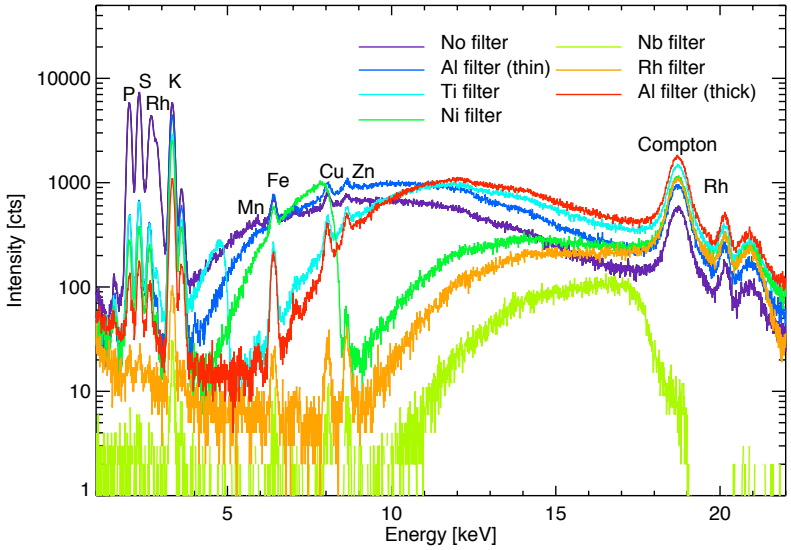

Figure 4.12: NIST SRM 1577B XRF-spectrum under different filter conditions.

of the life measuring time in steps of LT=50 s. An improvement of the relative detection limit with time can be observed. By replacing the net counts N_N and background counts N_B by the product of the measuring time and net intensity I_N and background intensity I_B respectively, the following equation can be obtained from Eq. 2.35:

$$C_{MDL,i} = \frac{3\sqrt{I_B}}{I_N}\frac{1}{\sqrt{t}} \times C_i \tag{4.2}$$

which shows that the relative detection limit improves with $1/\sqrt{t}$. Using this model, the relative detection limits were derived theoretically from a measuring time of 300 s and plotted in a full line, showing a good agreement with the experimental results. For a more detailed analysis of the differences between measured and experimental relative detection limits, a log-log plot was made of the relative detection limit in function of the life measuring time in steps of LT=2 s. More subtle deviations of the experimental detection limits can be observed (e.g. around 20 s for K, 30 s for Fe), probably due to the fitting procedure of the spectra. At low live times however, the experimental detection limits differ significantly from the theoretical estimation. E.g., for LT=10 s, the detection limit is too high in order to still be able to detect Cu in NIST SRM1577C.

Detection limits under different filter conditions.

Using the above measured XRF spectra of NIST SRM 1577B with different primary beam filters, the corresponding detection limits for the different elements of interest could be calculated. The relative detection limits can be seen in Fig. 4.15. For the lower Z elements such

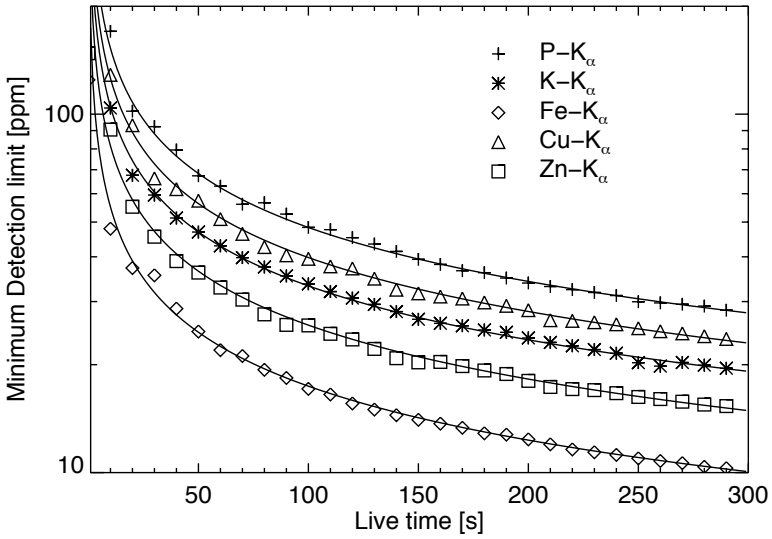

Figure 4.13: Relative detection limit of P, K, Fe, Cu and Zn in function of live time (1-300 s).

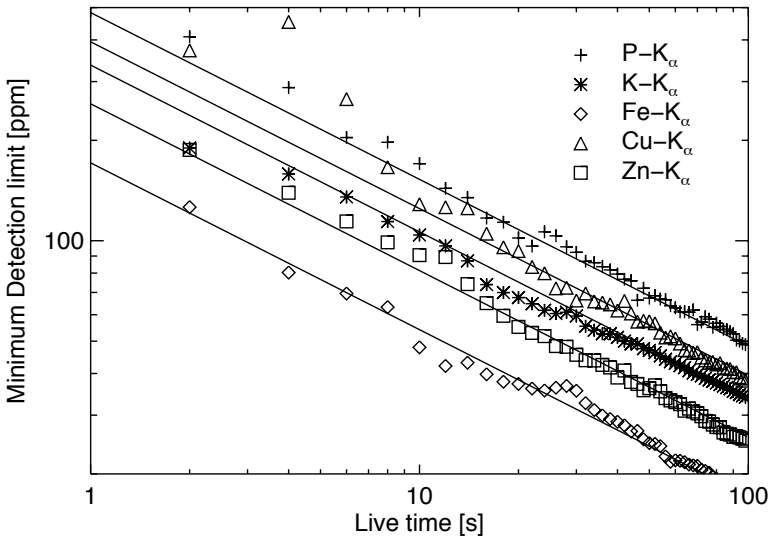

Figure 4.14: Relative detection limit of P, K, Fe, Cu and Zn in function of live time (1-100 s).

as P, S and Cl the vacuum condition using no filters seems to be the best option resulting in detection limits in the 20-30 ppm range. For elements such as K and Ca, the thin Al filter seems to be the best choice, delivering detection limits down to 5 ppm. For the higher Z elements such as Mn, Fe and Zn, a thick Al filter seems the better option resulting in detection limits down to a couple of ppm, with the compromise of using a higher tube current. When converting the relative detection limits to absolute ones, typical absolute detection limits in the 0.1-10.0 pg range can be observed in Fig. 4.16, which are corresponding to areal detection limits in the 0.1-100 $\mu g/cm^2$. An important conclusion is that the vacuum measurement mode delivers good detection limits over a wide range of elements in comparison with others filters in using a low tube current and is therefore the most interesting option for a multi-element analysis of biological samples.

4.4.4 Tube voltage

The EDAX Eagle III also has the possibility to change the X-ray tube voltage. The tube voltage was adjusted to 10, 15, 20, 25, 30, 35 and 40 kV and the corresponding XRF-spectra measured using the NIST SRM 1577B pressed pellet sample. Since a lower tube voltage results in a lower count rate, the tube current was adapted in order to have a constant dead time percentage of 30 %. It can be seen in Fig. 4.17 that below the absorption edge energy of Rh, there should be absolutely no excitation (and scattering) of $Rh-K$ lines and that below 10 kV elements such as Zn are no longer excited. We can conclude from these measurements that no notable difference in excitation efficiency is occuring between excitation energies which are still exciting the element of interest.

4.4.5 Detector shaping time

The EDAX Eagle III instrument also has the possibility to choose the shaping time of the detector. Therefore the shaping time was varied within the different options available. The shaping time can be set to 2.5, 4, 6, 10, 17, 35, 50 and 100 μs. Since a higher shaping time results in a higher dead time, also here the tube current was adjusted in order to have a constant 30 % dead time. The results of this analysis can be seen in Fig. 4.18 and Fig. 4.19. In Fig. 4.18, a shaping time of 4 μs results in a low energy peak and a change in energy calibration. Since most of the detectable elements are in the low energy range, a zoom can be seen in Fig. 4.19. Here it is very clear that a higher signal processing time delivers a better energy resolution for elements such as P, S and K.

4.5 Sample preparation

For the analysis of the entire *Daphnia magna*, dehydration in water/aceton series was applied, followed by fixation in hexamethyldisilazane as discussed in Chapter 3. For the analysis of

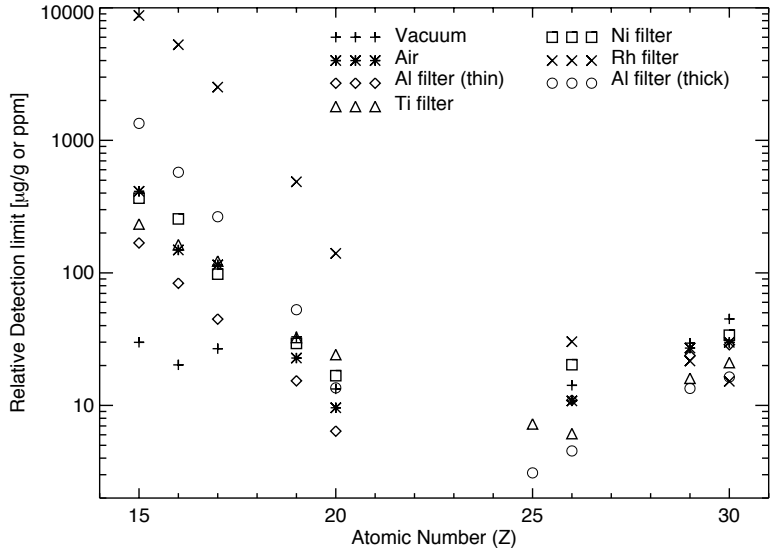

Figure 4.15: Relative detection limits in *ppm* or $\mu g/g$ for NIST SRM 1577B under different filter conditions for a live time of 300 s. The tube current of the instrument was adjusted in order to have a 30 % dead time.

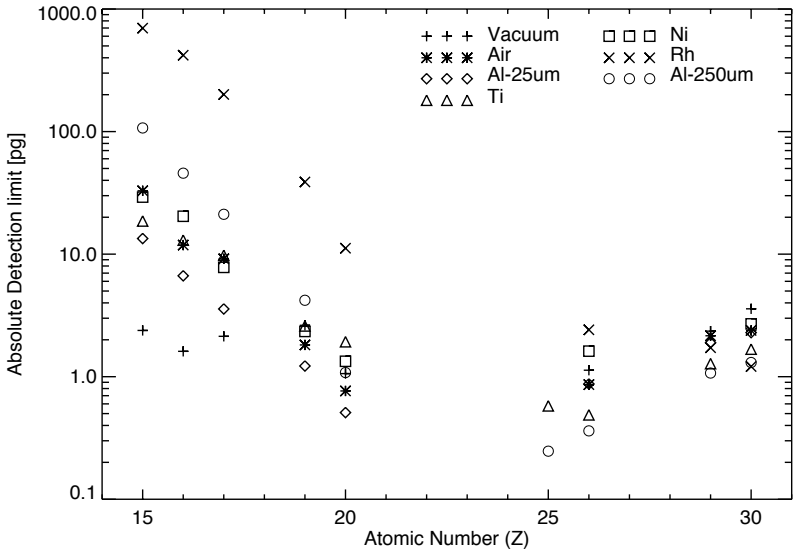

Figure 4.16: Corresponding absolute detection limits in *pg* using a beamsize of approximately 20 μm.

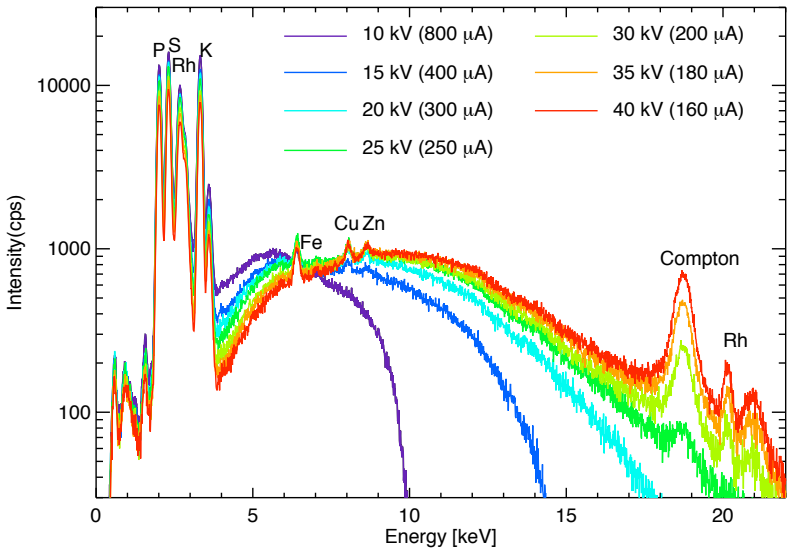

Figure 4.17: SRM1577B under different tube voltages. The conditions were optimised to a 30 percent dead time. The adapted tube current in order to obtain these conditions is also indicated.

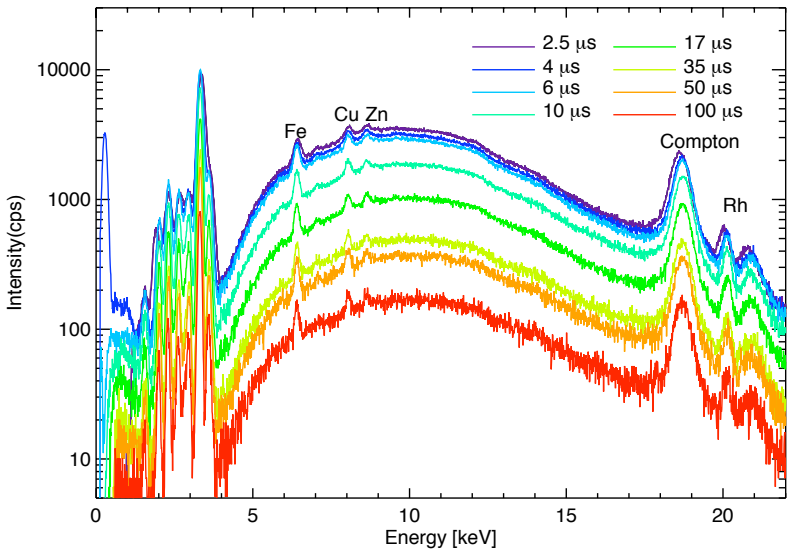

Figure 4.18: NIST SRM 1577B under different detector shaping time values (full energy range).

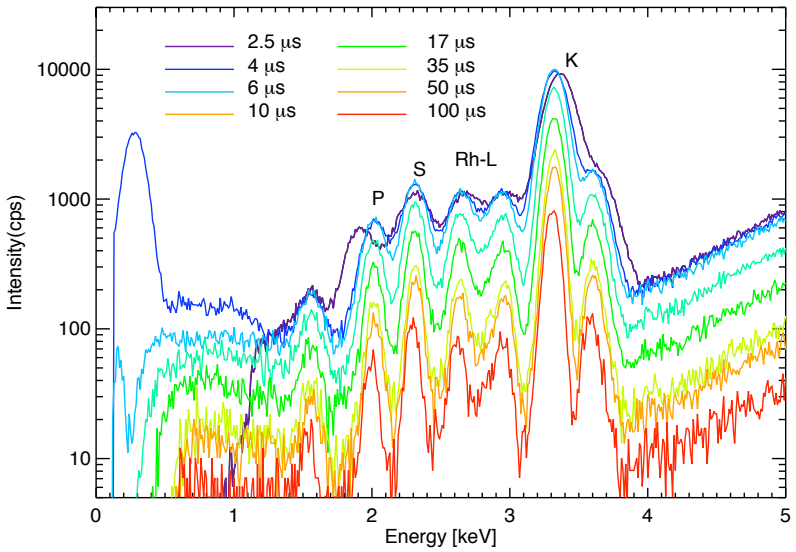

Figure 4.19: NIST SRM 1577B under different detector shaping time values (zoom on the lower energy range).

a sagittal thin section of *Daphnia magna*, the samples were dehydrated in water/aceton and imbedded in paraffin before making sections with a microtome. The sections were then attached with the corners to tape, creating a free standing paraffin slice suitable for micro-XRF analysis. A subsequent thin section was deposited on a glass slide for LA-ICPMS. The dorsoventral thin sections were deposited onto Si_3N_4 supports as described in Chapter 3 in order to allow both micro-XRF and LA-ICPMS analysis.

4.6 Experimental results

4.6.1 Analysis of XRF sum spectra

Taking into account the determined analytical characteristics of the EDAX Eagle III instrument, the vacuum mode was used without any filter between the X-ray tube and the polycapillary optic for providing maximum information on the low Z elements. An X-ray tube voltage of 40 kV was chosen, and the tube current was adapted to provide a suitable dead time. A live time of 5 s allowed the full micro-XRF scanning of the sample within 24 hours with sufficient detectability of P, S and Ca. All samples were analysed with a step size of 25 μm since this is close to the highest resolution of the instrument and smaller stepsizes would significantly increase the measuring time. These scans result in several thousands of XRF spectra, representing several hundred megabytes of data. After the measurements, all individual spectra were converted to a format compatible with the AXIL and MICROXRF2

software. For all different types of samples, a sum spectrum was generated first, which gives an overview of the average detectable element composition of the entire organism. In the sum spectrum shown in Fig. 4.20, normalised to the Compton scattering signal in order to account for differences in illuminated mass, a large continuous scattered bremsstrahlung spectrum can be observed which reveals the presence of Fe and Zn. At higher energies, the scattered characteristic $Rh - K\alpha$ and $Rh - K\beta$ lines can be seen, resulting in two Compton scattering peaks. At lower energies as shown in Fig. 4.21, Si, P, S, K and Ca are clearly present for all sample preparation methods. Unfortunately, the presence of $Rh - L$ lines renders the analysis of Cl impossible. Individual peak fitting was applied which allowed element maps for P, S and Ca with good signal-to-noise ratio.

4.6.2 Analysis of the entire sample

For the analysis of the entire control organism, a tube current of 100 μA was chosen due to the high count rate of this thick sample. The sample was positioned with its carapace perpendicular to the incoming X-ray beam and the X-ray beam was focussed upon the symmetry plane of the sample. It should be noted that due to the high divergence of the polycapillary beam, areas which are lying the furthest away from this symmetry plane, can render more diffuse element map distributions. However, this orientation of the sample yields a lateral view of the element distributions, which was the most informative, given the bilateral symmetry of the organism. Due to the light organic matrix (dry weight of an entire *Daphnia magna* is $\approx$ 100 μg) and the highly penetrating character of the X-ray beam, all trace elements along the beam path within the sample can be considered excited without considerable attenuation of the incident beam. Self-absorption effects for the induced fluorescence radiation can also be considered negligable for all but the lowest atomic number elements detected (e.g. Na, Si).

Fig. 4.22 shows the element maps for the P, S and Ca distribution of the entire control organism. A high contrast pseudocolor scale was applied on the element maps. Pseudocolor scales are arrangements of display colors that are assigned to the input intensity levels in a regular functional manner (often referred to as *look-up tables, LUT*). It can be observed that P and S are highly present in the eggs, gut, gill tissue with the difference that P seems to be present in higher amount in the gill tissue and antennae, whereas S has higher concentrations in the eggs and compound eye. The Ca map reveals a Ca abundance in the exoskeleton, with lower concentrations present in the brood pouch as compared to the antennae and front of the exoskeleton. Using the areal elemental yields for these elements determined from NIST SRM1577B under these experimental conditions, the maxima in the scalebar for P, S and Ca in the maps can be translated to areal concentrations of 600 $\mu g/cm^2$, 350 $\mu g/cm^2$ and 2000 $\mu g/cm^2$ respectively. Although no self-absorption correction is applied, this first order approximation can be considered adequate to obtain semi-quantitative results. Even for these low Z elements, the calculated critical density values, in which so-called thin-sample (linear)

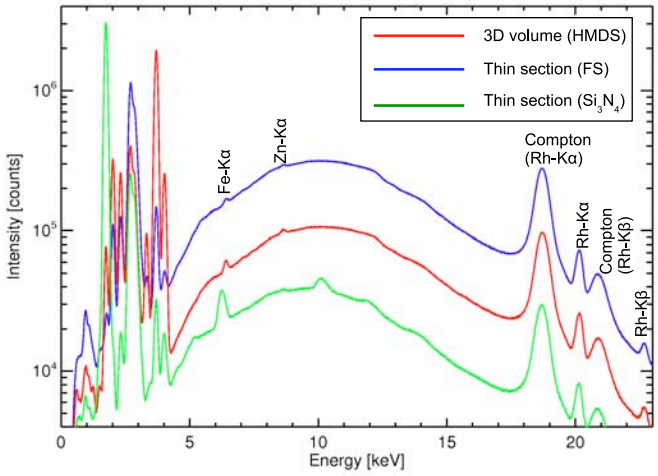

Figure 4.20: Sum spectrum of entire control organism (red), free standing 16 μm paraffin section (blue) and 10 μm paraffin section deposited on Si_3N_4 (green).

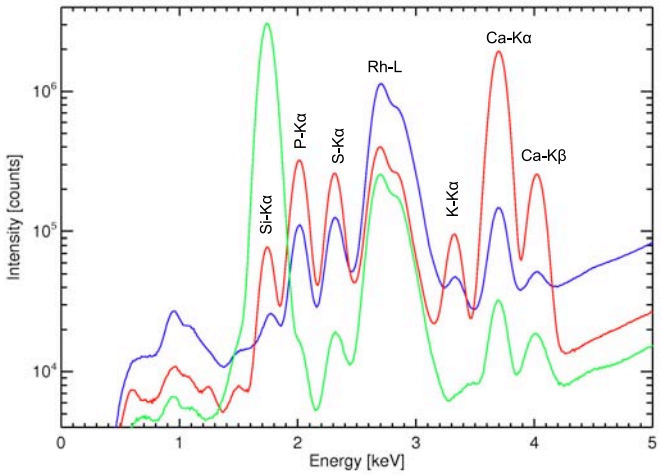

Figure 4.21: Sum spectrum of low energy range of entire control organism (red), free standing 16 μm paraffin section (blue) and 10 μm paraffin section deposited on Si_3N_4 (green).

models can be applied for the considered elements (P, S, Ca) in a biological matrix is well above the maximum values obtained in the element map (e.g. 0.041 g/cm^2 for Ca).

In Fig. 4.23, an RGB combined image is shown where the color bands red, green and blue were associated to the element distributions of Ca, P and Fe respectively. The presence of Fe could be detected in the hepatopancreas and in the supporting glass fibre. The RGB color space is represented as a three-dimensional coordinate system, with the axes corresponding to the red, green and blue contributions, respectively. Each axis ranges in value from 0 (no contribution) to 255 (full contribution). By design, this range from 0 to 255 maps corresponds to the full range of a byte data type. An individual color is encoded as a coordinate within this RGB space. Thus, a color consists of three elements: a red value, a green value and a blue value. Any three element maps from a set of maps can be simultaneously superimposed by assigning each map to one of the three primary colors of the computer display.

4.6.3 Analysis of thin sections

Sagittal thin sections

The sagittal free standing thin section of 16 μm thickness, required a 5 s live time and a 400 μA tube current, since much lower count rates were obtained in comparison with the entire control organism. In Fig 4.24 the element distributions for P, S and Ca are given in counts with the same pseudocolor scale. It can be observed that the P and S distribution are very similar, although some areas show clear differences e.g. in the gut and gill tissue. The Ca distribution seems to be again very apparent in the exoskeleton of the sample revealing higher intensities at the front of the exoskeleton as compared to the back as was already observed in the analysis of the entire organism. Also here, higher concentrations of P in the gill tissue can be observed whereas S has a higher occurence in the embryos. Note that in comparison with the analysis of the entire sample, no diffuse areas in the element map are observed since thin-sections are analysed. By means of the elemental yields derived from an NIST SRM 1577B pressed pellet of known areal mass, the maxima in the scale bars for P, S and Ca in the element maps can be translated to areal concentrations of 75 $\mu g/cm^2$, 40 $\mu g/cm^2$ and 120 $\mu g/cm^2$ respectively. In Fig. 4.25 an RGB image is given of the element distribution of Ca, Fe and Zn. Here, the coinciding presence of the elements of interest can be observed. As in the analysis of the entire organism, the presence of Fe could be detected in the hepatopancreas.

Dorsoventral thin sections

The dorsoventral thin section of 10 μm required a 5 s live time with only a 200 μA tube current due to the higher count rate of $Si - K_\alpha$ which would saturate the detector. In Fig. 4.27, the element distributions for P, S and Ca are given in counts with a pseudocolor scale

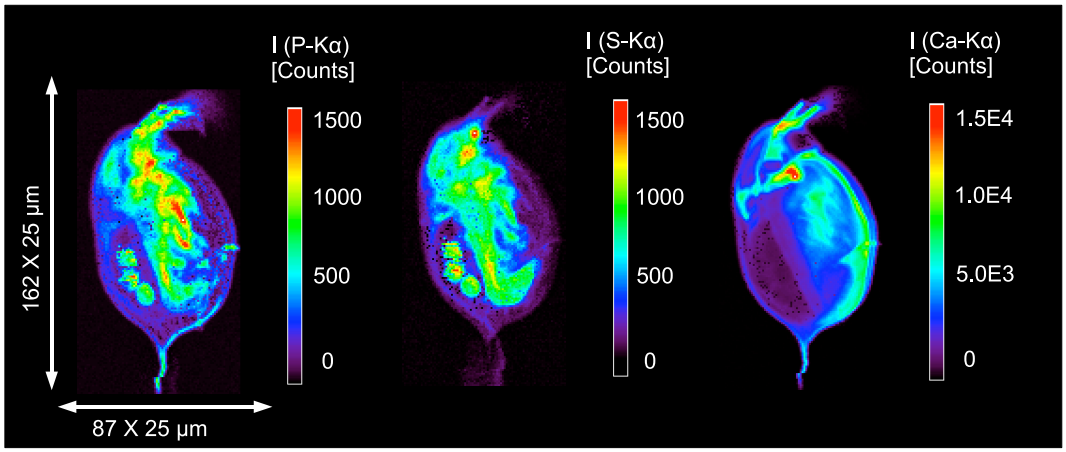

Figure 4.22: Element distributions for P, S and Ca of HMDS fixed control organism.

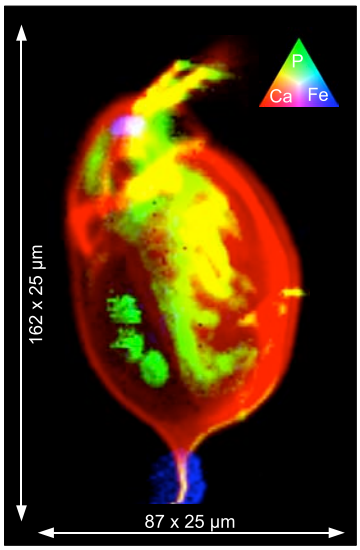

Figure 4.23: RGB image of HMDS fixed control organism. A color triangle is added which shows the different color channels assigned to the scaled element maps.

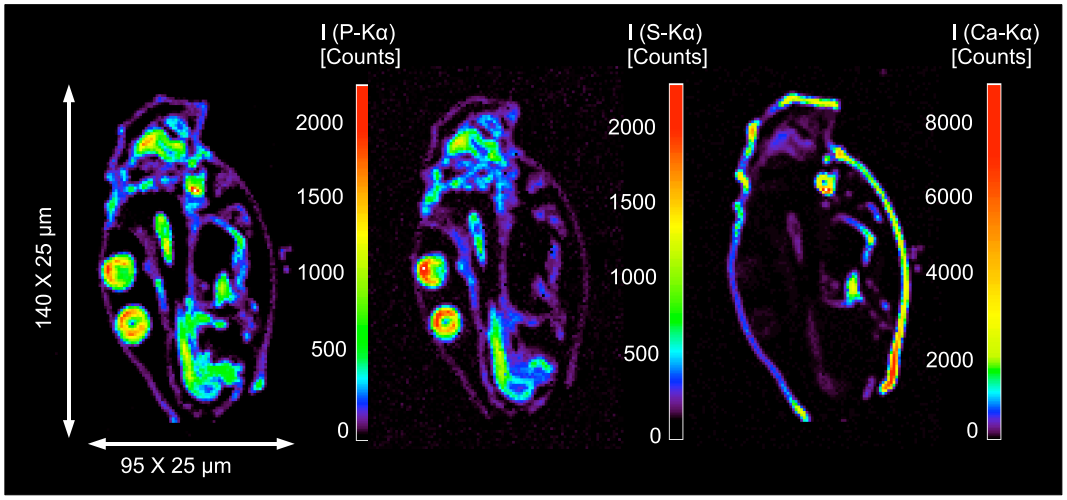

Figure 4.24: Element distributions for P, S and Ca in a 16 μm sagittal free standing paraffin thin section of *Daphnia magna*.

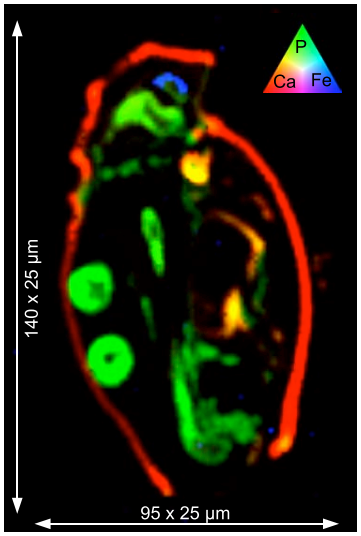

Figure 4.25: RGB composed image of a 16 μm sagittal free standing paraffin thin section of *Daphnia magna*.

bar. The presence of P reveals again maxima in the antennae and gill tissue, whereas S has higher intensities in the eggs and soft tissues around the gut. The higher count rate at the front of the exoskeleton as compared to the back is also clearly visible. Given the fact that the tube current was two times lower, the fluorescence yield is twice as low, which results in maxima in the scalebar for P, S and Ca of 20, 20 and 60 $\mu g/cm^2$. The lower areal concentrations compared to the sagittal section can be explained since this section was twice as thin. Phosphorus appears to be present in the entire section, with higher concentrations in the eggs and antennae. In Fig. 4.26 an RGB image is given of the element distribution of Ca, P and Si. The thin paraffin section normally covers the Si_3N_4 membrane, preventing the fluorescent radiation of silicon reaching the detector. However, areas where Si could be detected reveal areas in the paraffin section where cracks are present.

4.6.4 Cross-validation with LA-ICPMS

Introduction

In order to compare micro-XRF and LA-ICPMS (laser ablation inductively coupled plasma mass spectrometry) in terms of resolution and sensitivity, identical standard reference material (NIST SRM1577B) and histological sections of *Daphnia magna* were subjected to LA-ICPMS at the Analytical Chemistry Laboratory, National Institute of Chemistry, Ljubljana, Slovenia. A laser ablation system ($Nd-YAG$, 213 nm, New Wave Research) coupled to a quadrupole-based ICP-MS (Agilent 7500 cs) was used to determine the element distributions. Once a laser induced aerosol is generated it must be transported from the laser chamber to the ICP spectrometer. The dynamics associated with transporting the aerosol to an inductively coupled plasma will have a significant effect on all subsequent data. For conventional sample cells the time required for complete evacuation of an aerosol generated by a single laser pulse is $>$ 6 seconds. The laser ablation system was therefore equipped with a SuperCell, having a cell volume 10 mL. The geometry and flow characteristics of the SuperCell has been specifically designed to enable rapid evacuation of the laser generated aerosol in a large format cell. Transient signal evacuation is typically complete in $<$ 2 seconds across the entire sample cell working area. The ablated material is then transported to the ICP using helium as the carrier gas and mixed with argon after leaving the ablation chamber.

Comparison of minimum detection limit (MDL)

Minimum detection limits were determined using a pressed powder pellet of NIST SRM1577B. The MDLs for each isotope were calculated as follows:

$$MDL = 3 \times \frac{\sigma_{gasblank}}{I_{standard} - I_{gasblank}} \times c \tag{4.3}$$

with $I_{gasblank}$ and $I_{standard}$ the signal intensities (in cps) of gasblank and standard, respec-

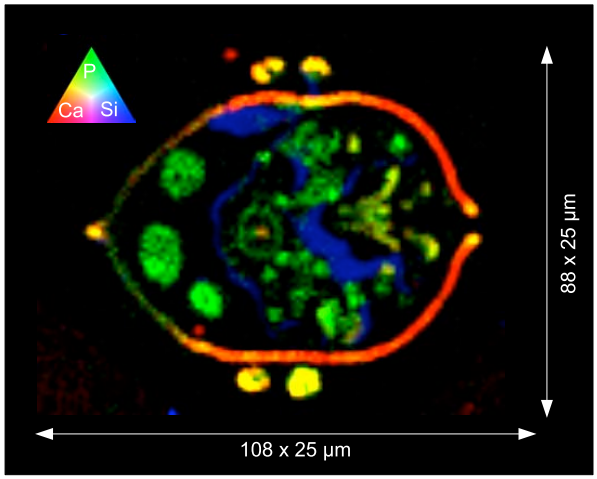

Figure 4.26: RGB composed image of a 10 μm dorsoventral paraffin section of *Daphnia magna* deposited on Si_3N_4. A color triangle is added which shows the different color channels assigned to the scaled element maps.

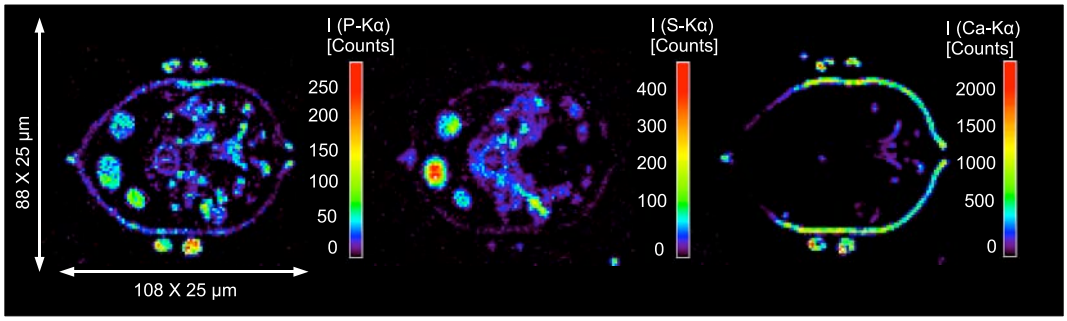

Figure 4.27: Element distributions for P, S and Ca in a 10 μm dorsoventral section of *Daphnia magna* deposited on Si_3N_4.

tively, $\sigma_{gasblank}$ the standard deviation of the gasblank (in *cps*) for 10 replicate measurements and c the certified concentration (in $\mu g/g$). In Fig. 4.28, the MDLs are given as a function of the isotopes measured for different beam sizes. Logically, the MDL increase can be observed when going to smaller beamsizes, e.g. 100, 55, 30 and 15 μm for this specific case. In Fig. 4.29 we can clearly see that the MDL increase with beam size is similar for all isotopes, i.e. when going to beam sizes of 55, 30 and 15 μm the MDLs increase with a factor of 3.6, 15.9 and 95.1 with respect to a beam size of 100 μm.

The MDLs originating from the 15 μm laserbeam are interesting to compare with those obtained with the EDAX Eagle III microprobe on NIST SRM1577B as discussed in section 4.4.3, given the similar spotsize of the X-ray microbeam. Since for XRF the detection limits are dependent on the measuring time as discussed previously, detection limits from Fig. 4.15 were extrapolated towards a 5 s measuring time using Eq. 4.2, which provides 100 $\times$ 100 $pixels$ element maps in $\approx$ 12 h. Interestingly, LA-ICPMS provides reasonable detection limits for isotopes such as ^{23}Na and ^{24}Mg whereas for micro-XRF under vacuum conditions these elements can only be detected when present in the mass percentage level and were consequently below the detection limit for the considered reference material. Phosporus is the first detectable element with micro-XRF in the reference material and provides detection limits of 230 ppm, compared to 600 $\mu g/g$ with LA-ICPMS . However, ^{34}S heavily suffers from spectral overlap in LA-ICPMS, which causes its detection limits to be 100 $\times$ higher than 160 ppm obtained with micro-XRF. Detection limits for ^{39}K are $\approx$ 100 ppm with LA-ICPMS, which is better than the 220 ppm detection limit obtained with micro-XRF, probably due to spectral overlap in the XRF spectrum. Detection limits for ^{44}Ca and ^{55}Mn are similar for both techniques and are respectively $\approx$ 100 and 10 ppm. Although for Fe micro-XRF obtains an $\approx$ 20 ppm detection limit, better than a factor of 5 than LA-ICPMS for the considered beamsize, LA-ICPMS obtains better detection limits for the higher Z elements. E.g. for Cu and Zn, micro-XRF can obtain detection detection limits of $\approx$ 100 ppm, whereas the detection limit for LA-ICPMS dives down to $\approx$ 10 ppm. For other trace elements present in the SRM, such as Se, Rb, Sr, Mo, Ag and Pb, LA-ICPMS continues to obtain detection limits in the (sub)ppm level, whereas the concentration of these elements is below the detection limit for the micro-XRF system.

Comparison of element distributions

For the LA-ICPMS imaging measurements, similar experimental conditions were used as those for the determination of the MDLs. Simulation software developed at the National Institute of Chemistry, Ljubljana was used to predict various possible images that might be obtained by using different laser parameters (e.g. spot size, gas flow rate, fluence, chamber volume and acquisition time) by means of a digital image of the section to be ablated. The parameters providing the best resolution given the time frame available are then selected for

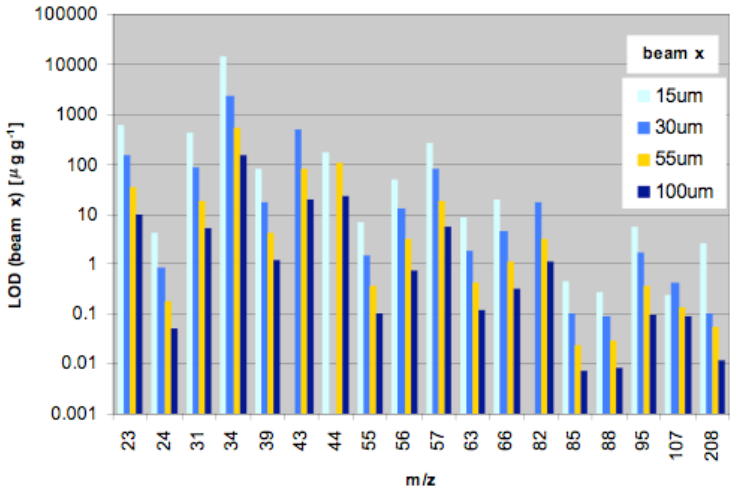

Figure 4.28: MDLs as a function of the isotopes measured for different beamsizes.

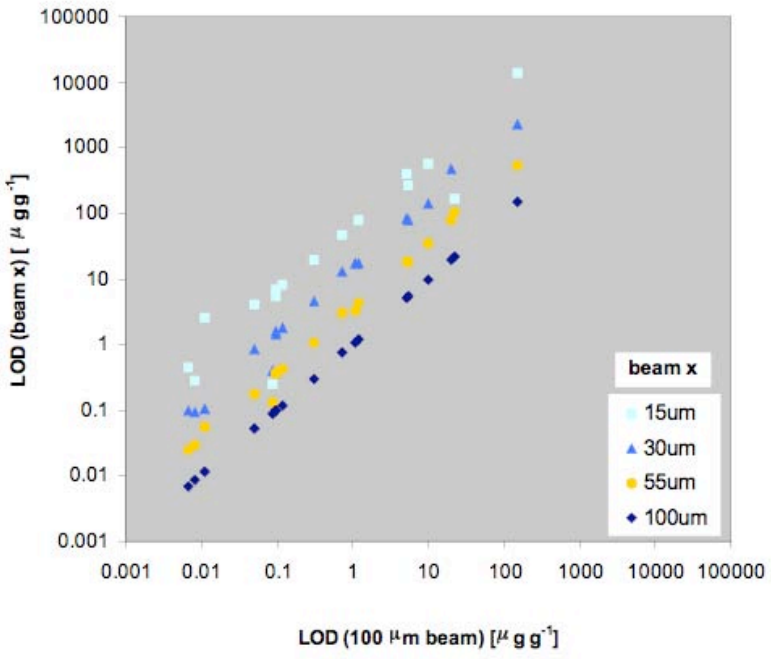

Figure 4.29: MDL increase with respect to the beamsize used.

the actual laser ablation process. Further image processing for the comparison of the LA-ICPMS and micro-XRF element distributions was done with the IDL software (Interactive Data Language).

ICP-MS	Agilent	LA	New Wave Research
Rf power (W)	1500	Spot size (μm)	15/30/55/100
Carrier gas flow rate, Ar (L/min)	0.8	Scanning speed ($\mu m/s$)	30
Optional gas, He (L/min)	1.0	Frequency (Hz)	10
Sample depth (mm)	6.0	Laser energy (J/cm^2)	0.13-0.20
Torch - H (mm)	0.8		
Torch - V (mm)	0.6		
Acquisition time (s)	108		
Sampling period (s)	0.5		

Table 4.2: Optimised experimental parameters for LA-ICP-MS

An important aspect for an optimal comparison of element distributions obtained by micro-XRF and LA-ICPMS is optimal scaling of the image. For visual comparison, all pixel intensities are scaled within the same interval (e.g. from 0-255). However, in our case, an informative comparison was hampered due to high intensities (spikes) and a high background signal in the element distributions obtained by LA-ICPMS. Therefore, for an optimal comparison, all pixel intensities were rescaled between a lower and higher threshold value within the original dataset. An objective manner to determine the new lower and higher threshold value for rescaling of the original dataset is by means of a histogram. The new lower and higher threshold value within the original dataset can be adjusted in such a way that the histograms of the element distributions of a certain element obtained by both techniques are similar. Fig. 4.30 and Fig. 4.31 show a comparison between the histogram of the P and Ca element distribution respectively obtained by micro-XRF (black) and LA-ICPMS (red) in which the lower and higher threshold value was adjusted until a good agreement was obtained.

Fig. 4.32 shows the element distributions of P and Ca (XRF/ICPMS), S (XRF) and Zn (ICP) within a dorsoventral section of *Daphnia magna*. The analysis was performed on the very same sample deposited on silicon nitride. Even though the micro-XRF data represents the element contents along the entire depth of the sample whereas the LA-ICPMS maps provide information of an ablated volume of the surface, element maps generated from both techniques are very similar. The tissue structures seem to be smaller in the LA-ICPMS maps which could be due to the better resolution of the laser beam or due to the low penetration depth of the laser as compared to the X-rays. The LA-ICPMS images are nevertheless also suffering

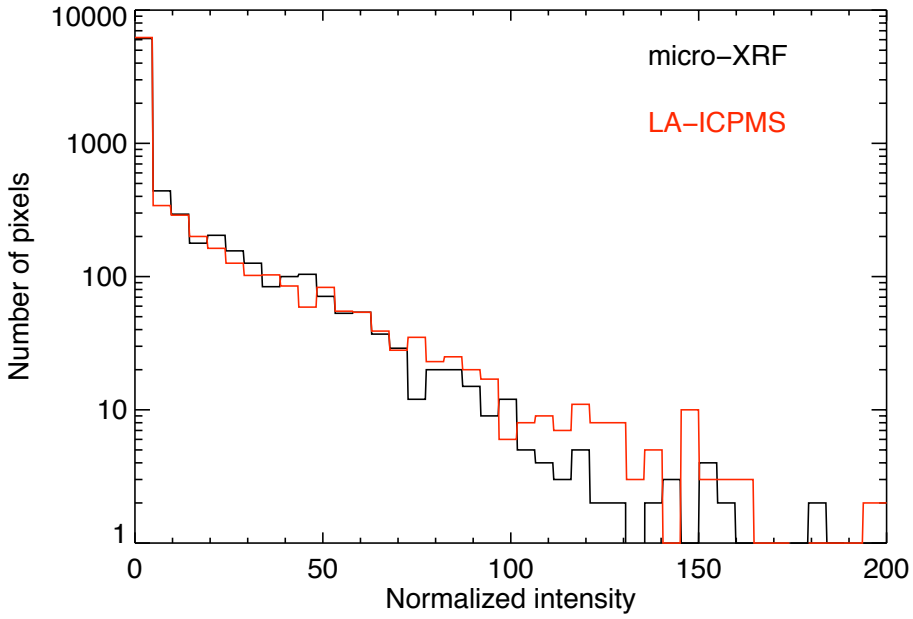

Figure 4.30: Histogram of the element distribution of P for micro-XRF (black) and LA-ICPMS (red).

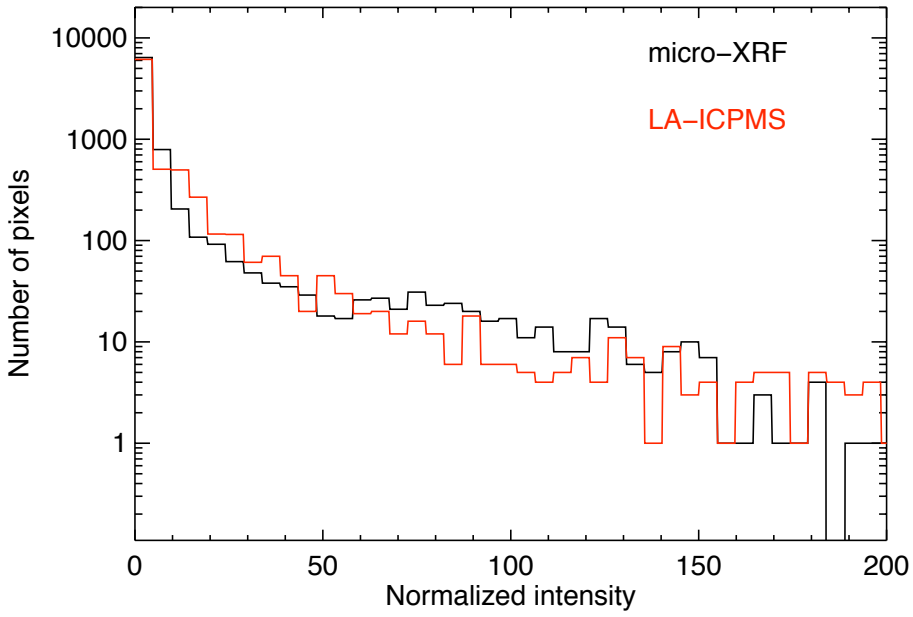

Figure 4.31: Histogram of the element distribution of Ca for micro-XRF (black) and LA-ICPMS (red).

from horizontal distortions, probably due to wash-out effects. The element distributions also seem to be distributed in a less homogeneous manner as compared to the micro-XRF maps, probably due to slight changes in the ablation volume. The element maps of P seem to show a very good correlation and reveal its presence in nearly all tissues of the sample, e.g., eggs, gut, gill and exoskeleton. Interestingly, the presence of Ca could only be observed in the exoskeleton and not in the soft tissues, as shown by micro-XRF. As already discussed in the previous section, it is also interesting to note that each technique has a superior sensitivity in order to generate an element map with sufficient signal-to-noise ratio, S in the case of micro-XRF and Zn in the case of LA-ICPMS, showing that both techniques can be used in a complementary manner.

Fig. 4.33 shows the element distributions of P and Ca (XRF/ICPMS), S (XRF) and Zn (ICPMS) within a sagittal section of *Daphnia magna*. Two subsequent sections separated by 100 μm were analysed. The micro-XRF analysis was performed on a free standing thin section whereas the LA-ICPMS analysis was performed on a glass substrate. A better resolution in the LA-ICPMS maps is observed, which could be explained by the glass sample support or due to the more hydrated state of the sample since it was not analysed under vacuum conditions for micro-XRF analysis. Again, P is present in nearly all tissues of the sample whereas Ca is mainly observed in the exoskeleton. Zinc seems to be present in the internal softer tissue of the organism. Interestingly, an egg present in the brood pouch could only be observed on the micro-XRF scan, probably since the section from LA-ICPMS was taken 100 μm deeper within the sample. Fig. 4.34 visualises the colocalisation or complementary presence of different elements of interest, e.g., Ca, P (both techniques), Fe (micro-XRF) and Zn (LA-ICPMS). This way of visualisation reveals the complementary presence of Ca/P in parts of the gill tissue using micro-XRF and P/Zn in parts of the gut using LA-ICPMS.

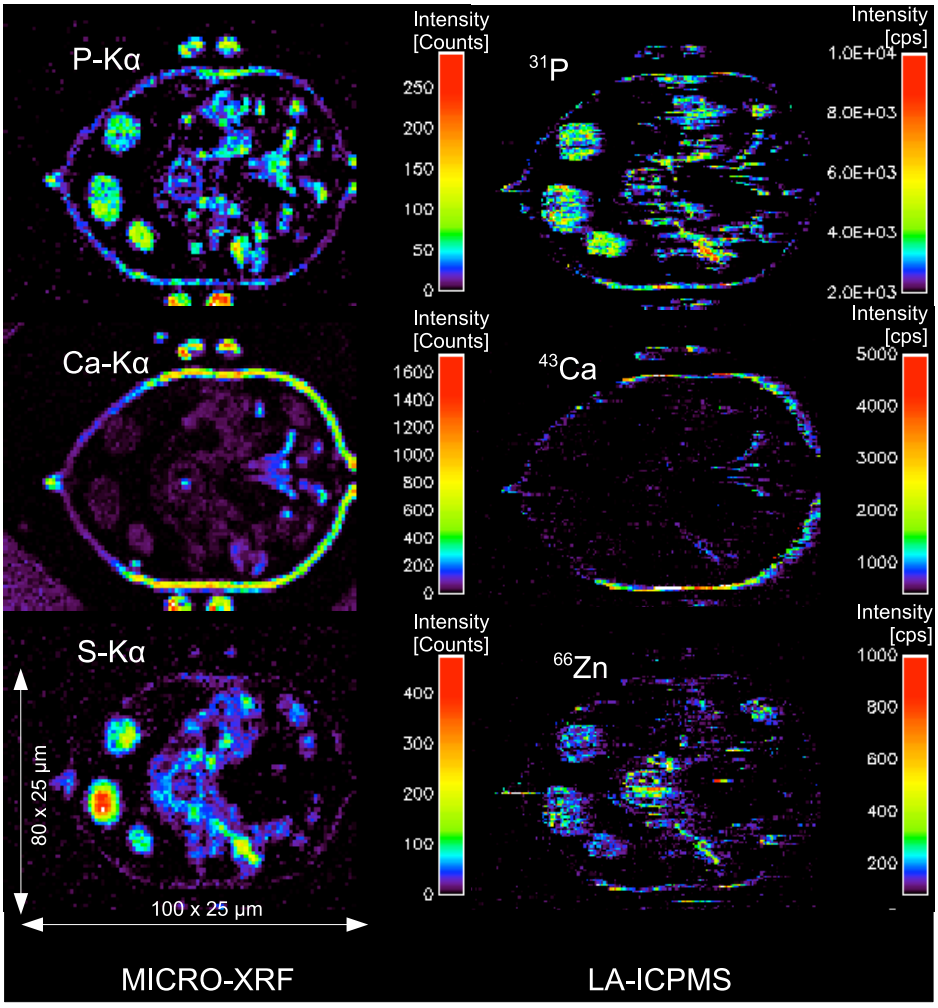

Figure 4.32: Element maps obtained by micro-XRF (left) and LA-ICPMS (right) of a dorsoventral section of *Daphnia magna*.

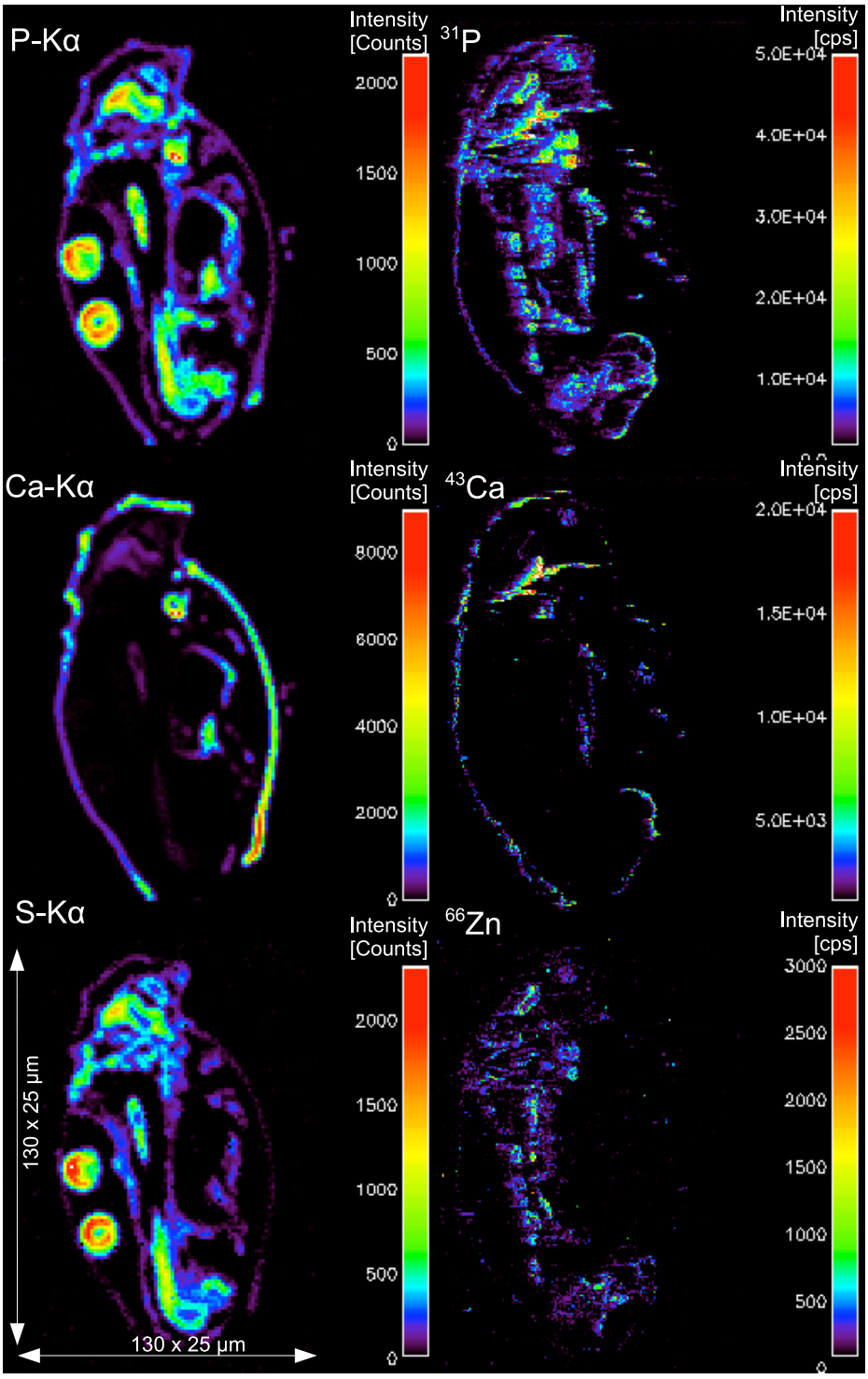

Figure 4.33: Element maps obtained by micro-XRF (left) and LA-ICPMS (right) of a sagittal section of *Daphnia magna*.

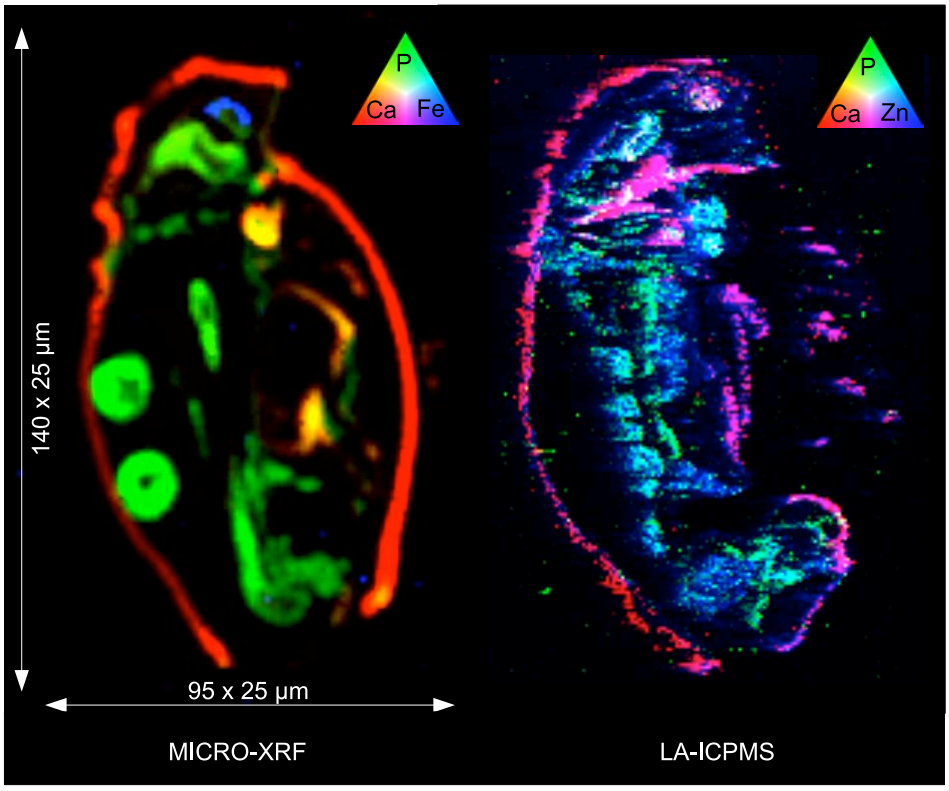

Figure 4.34: RGB representation of respectively Ca, P and Fe (micro-XRF) and P, Ca and Zn (LA-ICPMS).

Chapter 5

2D and CT micro-XRF on *Daphnia magna*

5.1 Introduction

In Chapter 4, laboratory micro-XRF was applied on *Daphnia magna*, which provided valuable information on the distribution of P, S, Ca and Fe. However, due to its lower sensitivity as compared to SR micro-XRF, no element information could be obtained with respect to the target element Zn. For the analysis of trace level Zn, the superior sensititivies of a synchrotron XRF microprobe, Beamline L at the Hamburger Synchrotronstrahlungslabor (HASYLAB) were necessary. The technical details and recent developments are discussed in section 5.2. Section 5.3 discusses the experimental conditions of Beamline L for the experiments on *Daphnia magna*. Section 5.4 details the sample preparation for the 2D/CT micro-XRF experiments. In section 5.5, differences in tissue specific spatial distribution of Zn between control organisms and Zn exposed organisms using advanced data processing tools such as K-means clustering and Principal Component Analysis (PCA) will be highlighted. A disadvantage of 2D micro-XRF is that it provides no depth information of the element distributions within a sample. At HASYLAB Beamline L, micro X-ray fluorescence computed tomography (micro-XRF CT) is available, which allows the determination of trace level metal distributions within virtual cross-sections of the sample. This is illustrated on *Daphnia magna* in section 5.6. During the initial investigations, a chemical fixation was used for 2D/CT micro-XRF analysis on *Daphnia magna*. In order to study the degree of alteration of chemical composition, we also investigated in section 5.7 possible changes between the element distributions within a frozen hydrated specimen and a dehydrated chemically fixed *Daphnia magna* using a dual detector 2D/CT micro-XRF configuration. As previously mentioned, the 2D/CT micro-XRF data visualising the accumulation of various metals should be correlated with the different tissue structures of *Daphnia magna* with high accuracy. The micro-XRF studies were coupled with absorption micro-CT in order to visualise the tissue

structure of *Daphnia magna* in a non-destructive manner. The UGCT facility at Ghent University was used to acquire the 3D tissue structure of *Daphnia magna*. Its possible coupling with the previously obtained 2D/CT micro-XRF results is highlighted in section 5.8.

5.2 Beamline L, a synchrotron XRF microprobe

5.2.1 General purpose

All synchrotron radiation micro-XRF experiments discussed in this chapter were performed at Beamline L of the DORIS-III storage ring at HASYLAB (Hamburg, Germany). The primary X-ray beam is generated by a 1.2 T bending magnet source which, given the machine energy of 4.45 GeV provides a polychromatic spectral distribution with a critical energy of 16.6 keV. A lay-out of the optical components of Beamline L is shown in Fig. 5.1: after initial low-energy filtering and collimation, the beam can be monochromatized by a multilayer or a silicon crystal monochromator. The monochromator can also be removed from the beam path, in which case the beamline provides a polychromatic (white-beam) excitation. Before the X-ray focusing stage, various absorption filters can be applied to modify the spectral distribution according to the requirements of the experiment. The filtered/monochromatised beam is focused by a (poly)capillary optic onto the sample, down the microscopic dimensions. Beamline L was originally designed and mainly used as a hard X-ray microprobe. Thanks to the versatile monochromator and experimental table, different optics and detectors, it is now also used for a variety of experimental techniques such as micro-XANES, micro-EXAFS, micro-XRF and micro-TXRF. In this section, we discuss the different hardware components of the beamline and illustrate its possibilities to perform 2D/CT micro-XRF experiments on biological materials.

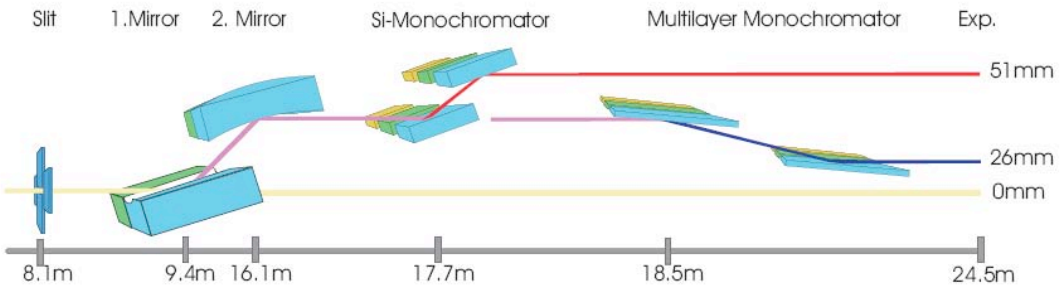

Figure 5.1: Optical components of Beamline L. Reproduced from Falkenberg *et al.* (2001).

5.2.2 Monochromator system

Several different monochromators are available at Beamline L (Falkenberg *et al.*, 2001). $Si(111)$ and $Si(311)$ double crystal monochromators are employed for applications demanding high energy resolution such as microscopic X-ray absorption spectroscopy (XAS). Multilayer double monochromators are used for high flux applications, including 2D and 3D trace element imaging by microscopic X-ray fluorescence analysis. The different multilayer monochromator optics available are given in Table 5.1. The ratio of metal to total layer thickness d is $\Gamma = 0.5$ for all multilayers in order to suppress the second order Bragg peaks. The energy resolution and (energy dependent) ratio of photon fluxes of several monochromators have been determined experimentally under normal working conditions at beamline L and are shown in Table 5.2. The results may help to select the most appropriate monochromator for the particular measurement (Falkenberg *et al.*, 2007b).

Fig. 5.2 shows the opened monochromator vessel in which synchrotron radiation is entering from the lower right side. The experimental table is located at the higher left side of the photograph. Both the Si perfect crystal monochromator and the multilayer monochromator are present in the vessel. The silicon double monochromator consists of two independent units. Both crystal holders are water cooled and equipped with $Si(111)$ and $Si(113)$ crystals. The multilayer double monochromator is also composed of two independent units. The relative position of the monochromator systems is given in Fig. 5.1. The system is a fixed exit monochromator, which means that during a change in energy, the beam remains at the same vertical position. During alignment, a fluorescent screen is inserted in the beam path between the monochromator crystals and the experimental table. The horizontal and vertical position is then adjusted until the beam is visible on a fluorescence screen. In the case of the perfect crystal monochromator, the rotation angle of the first crystal is adjusted until optimal flux is obtained in the first ionisation chamber. This is achieved by performing a so called rocking curve measurement. For the multilayer monochromator, the second crystal needs to be moved forward at low energies since there is the possibility that the crystals collide. When sealed, a He flushed pipe is going from the monochromator tank towards the experimental table, where a motorised cross-slit system and an absorber wheel is present, followed by the focusing optics stage. Fig. 5.3 shows the operational monochromator vessel.

Ni/C	d = 3.34 nm	100 layer pairs
Mo/Si	d = 2.98 nm	200 layer pairs
W/B4C	d = 1.5 nm	500 layer pairs

Table 5.1: Different multilayer monochromator optics available at Beamline L.

	Ni/C	W/B4C	Mo/Si
8 keV	1.65	0.46	0.96
12 keV	1.70	0.49	0.89
15 keV	1.78	0.56	0.92
18 keV	1.83	0.61	0.95
21 keV	2.13	0.66	1.07

Table 5.2: Spectral resolution of the beam after passing the double multilayer monochromator determined by a $Si(111)$ channel-cut analyser.

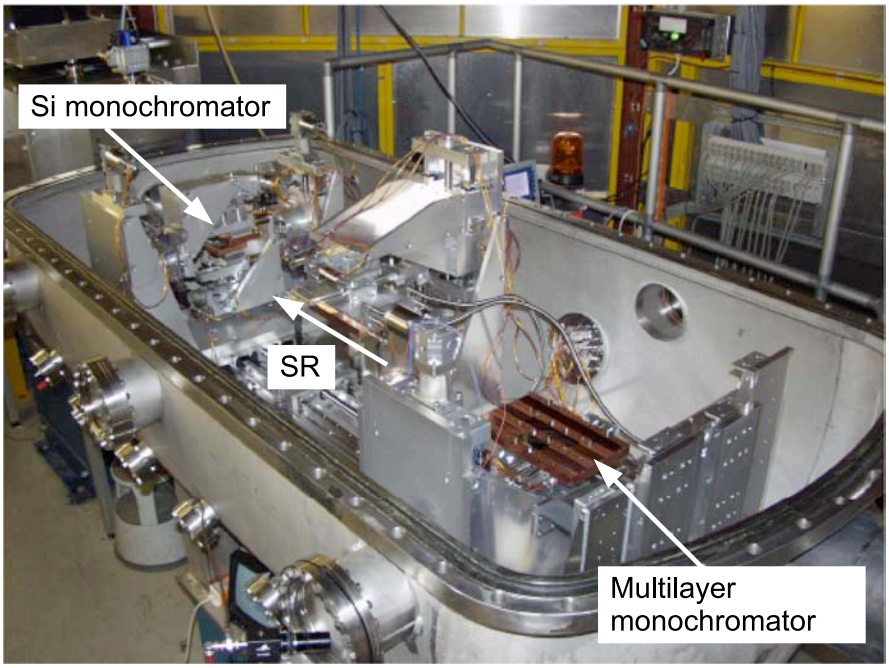

Figure 5.2: View into the open monochromator vessel. The Si monochromator is shown in the upper left and the multilayer monochromator in the lower right part of the photograph. Reproduced from Falkenberg *et al.* (2001).

Figure 5.3: View of the operational monochromator. The shielded horizontal tube exiting the monochromator is the He-flushed X-ray beam-pipe, which extends towards the experimental table.

5.2.3 focusing Optics

As previously mentioned, Beamline L has a variety of capillary based X-ray focusing optics available which are all based on the principle of single or repeated total external reflection of X-rays on glass surfaces. Each type of capillary optic has its own unique specifications adapted to different user needs. Fig. 5.4 shows the different polycapillaries available together with their transmission, focus size, flux density gain and working distance in Table 5.3 (Falkenberg, 2007a).

Figure 5.4: Different types of XOS polycapillary half-lenses which are available at beamline L. From top to bottom: conventional polycapillary, strongly-focusing polycapillary, high-energy polycapillary, detector polycapillary. The conventional polycapillary is 100 mm long. Reproduced from Falkenberg (2007a).

Polycapillary	Transmission	Focus Size	Gain	Working distance
conventional	30 %	15 μm	3000 (17 keV)	4.8 mm
strongly-focusing	4.7 %	7 μm	2000 (17 keV)	2.0 mm
high-energy	6 %	5 μm	2000 (30 keV)	2.5 mm
detector	5.5 %	6 μm	2000 (17 keV)	2.1 mm

Table 5.3: Summary of some basic parameters of the polycapillaries derived from wire scan and edge scan measurements. Reproduced from Falkenberg (2007a).

The conventional polycapillary shows the highest transmission, meaning that 30 % of the incoming photons are transmitted through the capillary at the X-ray energy of 17 keV. This particular polycapillary also features the highest gain, meaning the gain in flux density in the focal spot as compared to the flux density of the unfocused incoming beam. This polycapillary has the additional advantage of having a relatively large working distance, which results in a lower risk to hit the sample during alignment. Due to these properties, this

polycapillary is mainly used for traditional moderate energy micro-XRF experiments with medium resolution (15-20 μm) and for confocal micro-XRF experiments requiring a high incoming flux. When requiring higher resolution, the strongly-focusing polycapillary can be used with the disadvantage of having a lower transmission and gain. At higher energies a specific polycapillary is available which produces a spotsize of 5 μm at 30 keV. A polycapillary with a small working distance and low focal size is also available, which serves as a detector optic for confocal micro-XRF (Falkenberg, 2006). A vertical scan of a thin Fe structure with a well-defined edge generated by the different capillaries at different energies is shown in Fig. 5.5

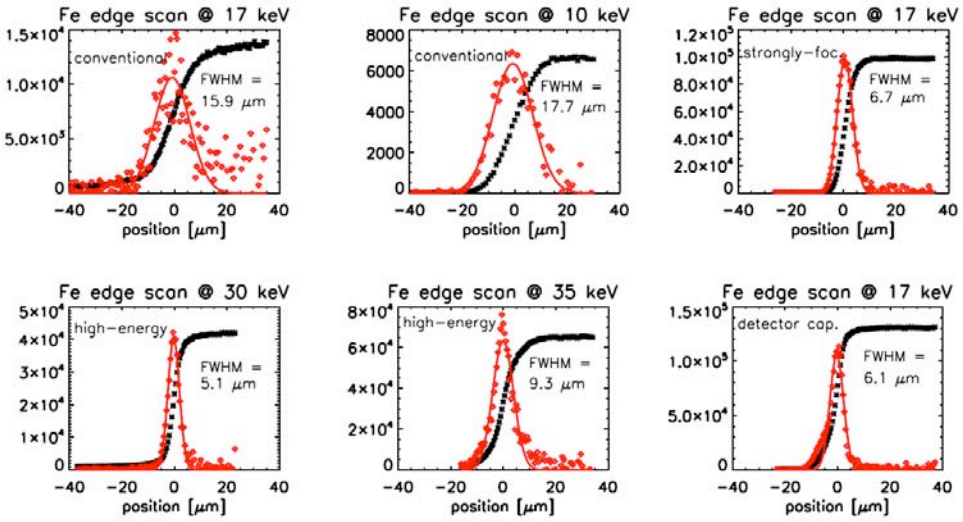

Figure 5.5: Vertical scan of a thin Fe structure with a well-defined edge generated by different capillaries at different energies. The Fe intensity detected by a drift detector is shown in black; red diamond symbols represent its derivative, and the line the Gaussian fit of the derivative. Beam sizes derived from edge-scans are indicated. Reproduced from Falkenberg (2007a).

Next to polycapillary optics, also a single bounce ellipsoidal capillary (SBC) is available, which was specifically designed and drawn at Cornell University (Falkenberg *et al.*, 2003). This single bounce ellipsoidal capillary requires a micro-beam stop and features an exceptional large working distance (50 mm) and low divergence ($\leq$ 4 $mrad$), not characteristic for polycapillaries. The low beam divergence provided by this optic makes it ideally suited for XRF micro-tomography on larger samples in which a pencil beam throughout the sample is required. Also, experiments involving complex sample environments (e.g. a cryostream set-up), require this focusing optic due to the large working space needed around the sample. One disadvantage of this optic is the lower focused intensity provided when compared to polycapillary optics, due to its considerably smaller input aperture. This makes the single

bounce capillary less suitable for confocal micro-XRF experiments.

5.2.4 Continuous Scanning Mode

Recently, more and more users are requesting large overview micro-XRF maps within a short amount of time. Therefore, a continuous scanning mode implemented in the online data acquisition and motor control software for collecting MCA spectra was used which provides a fast scanning capability in the sub-second per pixel regime with minimum time loss due to sample positioning. The concentration of elements relevant to our investigations are typically above the detection limits even for collection times of 1 s or less if the experimental conditions are optimised on sensitivity. Reducing the measuring time per point enables to measure larger areas of the sample without loss of spatial resolution. Relevant areas are often as large as several square millimeters. Keeping the spatial resolution at 10-20 μm, which currently is the lower limit at beamline L using capillary optics, results in several 10.000 points per scan and (sub)-second measuring time per point. In the continuous scanning mode the sample is moved continuously across the beam and not stepwise as in the conventional scanning mode. During continuous sample scanning, the spectrum is integrated in the MCA for a pre-defined time interval (sample time) at a pre-defined scanning speed, depending on the required pixel-size. Subsequently, the spectra are read out from the MCA and written to the hard disc. In addition, counter signals needed for normalisation (ionisation chamber signal, detector dead time, DORIS ring current, detector count rate) are saved. During readout, computing and writing, the spectrometer is blind: photons are not detected and signals are not counted. However, this time interval (0.02 s) is almost negligible compared to a typical sample time. Fig. 5.6 illustrates the principle of conventional scanning versus continuous scanning micro-XRF. The left panel illustrates the non-continuous movement of the stepping motors and the discrete points (white) measured on the sample, while the right panel reveals a continuous movement of the software with integrated areas being measured on the sample (Falkenberg *et al.*, 2005).

Figure 5.6: Principle of conventional (left) and continuous (right) scanning mode for 2-dimensional arrays of MCA spectra. Reproduced from Falkenberg *et al.* (2005).

The user may specify a sample time and integrated pixel size. Based on these input parameters, the scanning software adjusts the motor sweep-speed and displays scan parameters such as time per sweep, total time before the sequence is started. The crucial requirement for the application is that the MCAs are almost always active while the sweeping motor moves. This is achieved by an MCA board that has two memory banks. One is read out while the other is active. The observed coverage is in the order of 98.5%. If needed, the user may disable the sweep mode and measure MCA spectra while the motors stand still (Kracht & Núnez, 2007). The user may also specify limits for three different motors, an inner, a middle and an outer loop motor. The third loop motor is for e.g. 3D confocal micro-XRF measurements, which will be illustrated in Chapter 6.

5.2.5 Implementation of a high resolution CCD camera

A high resolution X-ray camera developed at Photonic Science has been installed and tested by our group at Beamline L. The X-ray sensitive camera is based on a $YAG : Ce$ thin-film scintillator (20 μm thickness) deposited on a 300 μm thick undoped YAG single crystal substrate which generates visible light when irradiated with X-rays. The visible image from the scintillator is then magnified and imaged by a 10× magnification microscope objective onto a Peltier cooled 1004 × 1002 CCD chip (8 μm pixel size) with 12 bit digitization, resulting in an effective pixel-size of 0.8 μm and a field-of-view of 800 μm (De Samber *et al.*, 2006). The camera is based upon a CCD image sensor that includes up to approximately 2000 times on-chip amplification of the acquired image signal. Such amplification provides many of the benefits of an image intensified CCD, and allows the CCD to provide usable video images in much lower lighting conditions than conventional CCDs. In addition, this technology has benefits over ICCDs, as the CCD cannot be damaged by overexposure to high light levels, which can occur with image intensified devices. A fully automatic Digital Gain Management System (DGMS) exposure control circuit is used to cope with a large range of input light levels. CCD integration period, on-chip amplification and video gain are controlled within a single feedback loop to regulate the video amplitude. The camera is driven with Image Pro software which makes operations such as background subtraction, sensitive integration, multi-image capturing and applying enhancement filters convenient. The coolview EM 1000 includes features such as software and hardware triggering (via an RS232 interface). The hardware triggering of the camera has recently been optimised to work with the TTF-triggering signals (sent from the workstation) which controls the movement of the different motors at the sample stage. In this way, a synchronised movement of a motor during scans can be coordinated while automatically acquiring images with the camera (Coolview, 2005).

Images of the set-up and a detail of the camera itself are shown in Fig. 5.7. The camera has been mounted on a double motorised stage. The first linear-stage allows the camera to move easily out of the beam and switch quickly with other analysing tools such as the ionisation

chamber or a diffraction camera. The second linear-stage allows to move the camera closer to the sample stage. Next to high-resolution radiography, the camera can be used for sample positioning, for selecting areas of interest for analysis with the microbeam, and for aligning the microbeam optics. Fig. 5.8 shows a transmission image of a foraminefere, which is an ideal test sample since its size fits perfectly into the field of view of the CCD camera. The radiograph reveals a multispherical structure with internal channels, which perfectly matches what can be seen in a SEM image of the structure.

Next to micro-radiography, another interesting application of the high-resolution CCD camera is the characterisation of monocapillary optics. When a single bounce capillary is inserted in the primary beam, its beam forming characteristics can be studied in detail by the CCD camera. Fig. 5.9 shows the working principle of the single bounce capillary (SBC): the ellipsoidal capillary (green) focuses the photons into a focal spot. The direct beam is blocked by means of a micro beam-stop. Further away from the focus, a far field ring of photons is created. In Fig. 5.10 this far field ring was observed using the CCD camera with (left) and without (right) the micro beam-stop blocking the direct beam. Since the SBC is a thin-walled glass capillary, the ellipsoidal profile is very sensitive to mechanical stress. It should be positioned onto a holder which imposes minimal stress. Using the CCD camera, the influence of different capillary holders was investigated. Fig. 5.10 also shows the far field ring of photons with the conventional and a prototype capillary holder. It can be clearly seen that the far field ring is much more circular using the new prototype holder, which should also result in a better focal spot. A line profile through the centre of the far field ring with and without the beam-stop is shown in Fig. 5.11, the irregularities in the far field ring can clearly be observed. The same is shown for the new holder in Fig. 5.12, revealing a more homogeneous intensity for the far field ring.

One interesting aspect of combining the SBC and the CCD camera is the enhanced knowledge of the position of the microbeam on the sample. When the SBC is moved out of the beam, the sample can be investigated by means of radiography. When an interesting radiographic image of the sample is obtained, the SBC can be put into position again. This generates a blocking of the field of view of the CCD camera. However, when the micro beam-stop is not aligned with the SBC, it becomes possible to see where the microbeam will hit the sample and adjust the position of the beam in greater detail. An image of organic tissue which can be seen through the aligned SBC (with the micro beam-stop out of the beam path) is given in Fig. 5.13. These aspects are also very useful for determining the boundaries of the sample to be scanned, or for determining left/right boundaries of the cross section of interest to be scanned by micro-XRF CT.

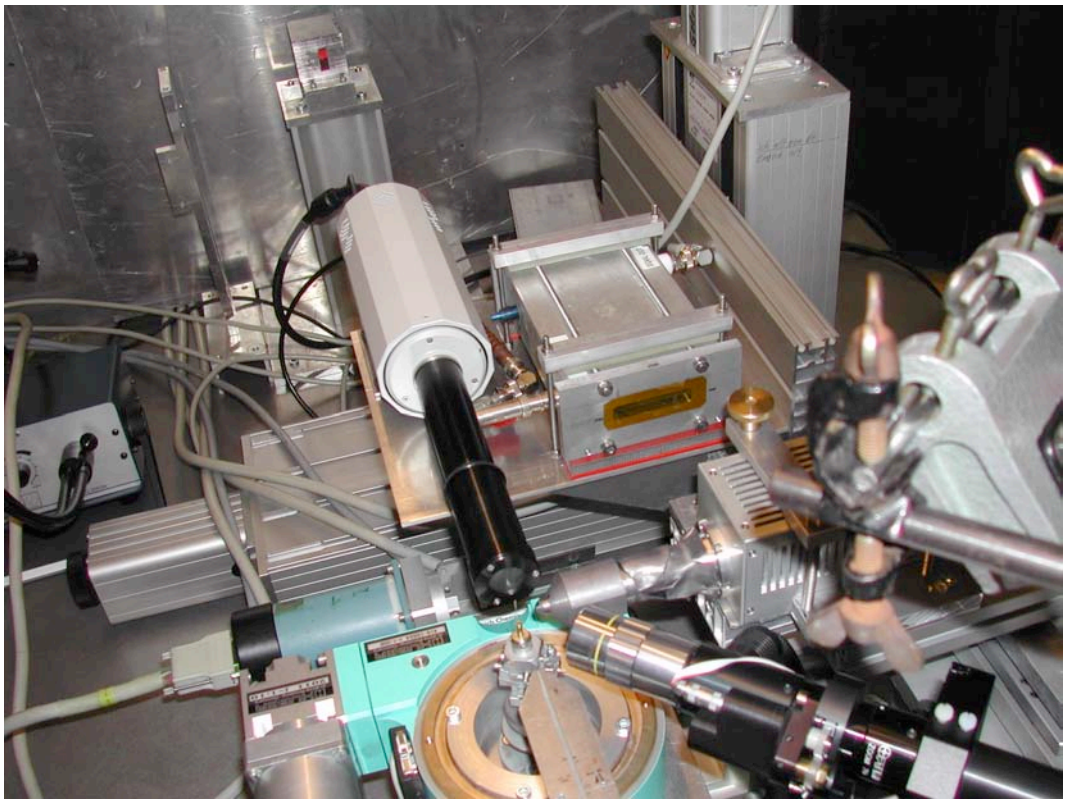

Figure 5.7: Experimental set-up with high resolution CCD camera. Reproduced from De Samber *et al.* (2006).

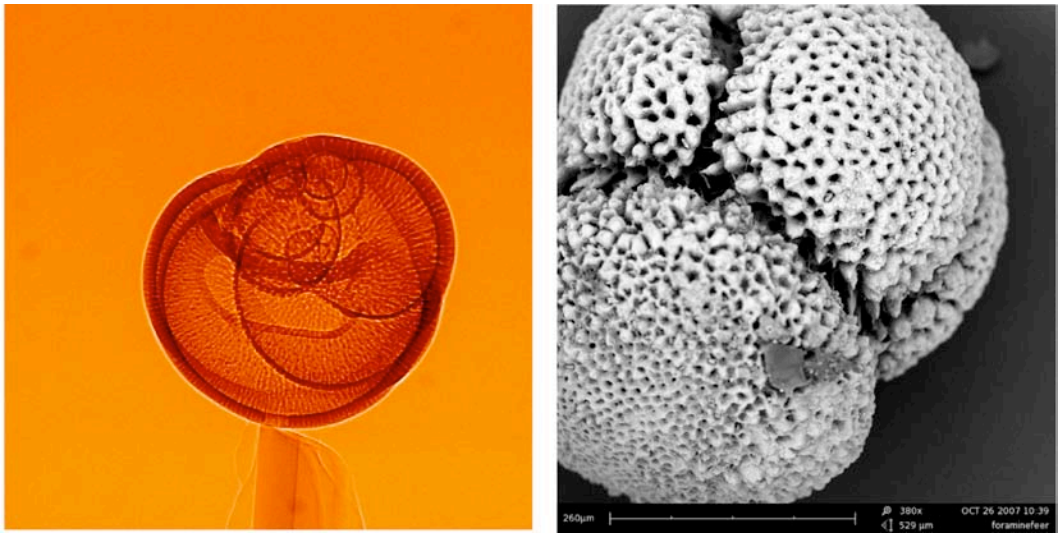

Figure 5.8: Radiograph of Foraminefere (left), SEM of Foraminefere (right). Reproduced from De Samber *et al.* (2006).

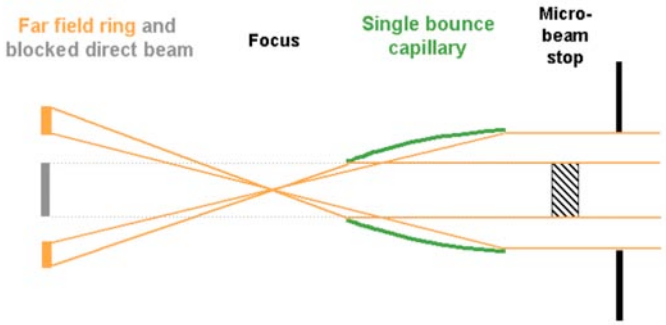

Figure 5.9: Schematic drawings illustrating the X-ray optical path of a single-bounce capillary. Reproduced from Falkenberg *et al.* (2003).

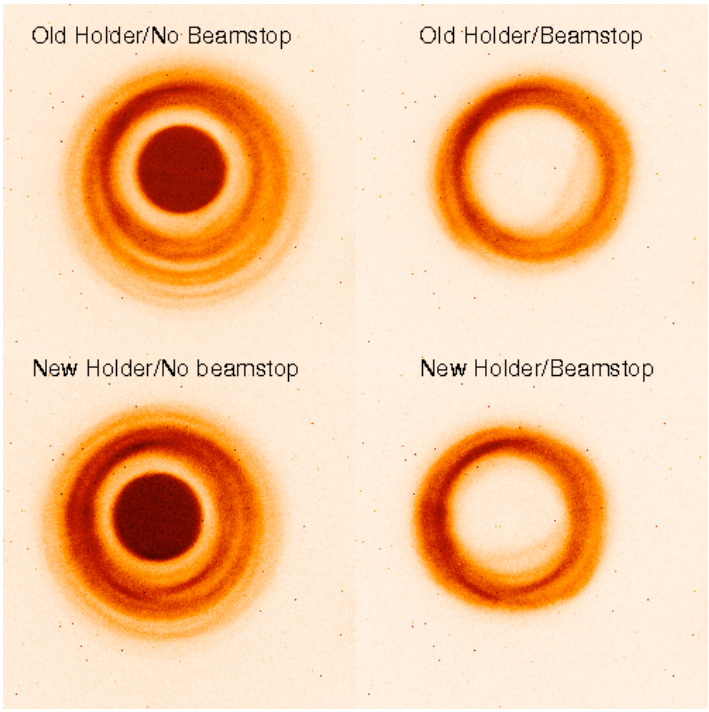

Figure 5.10: Influence of the single bounce capillary holder.

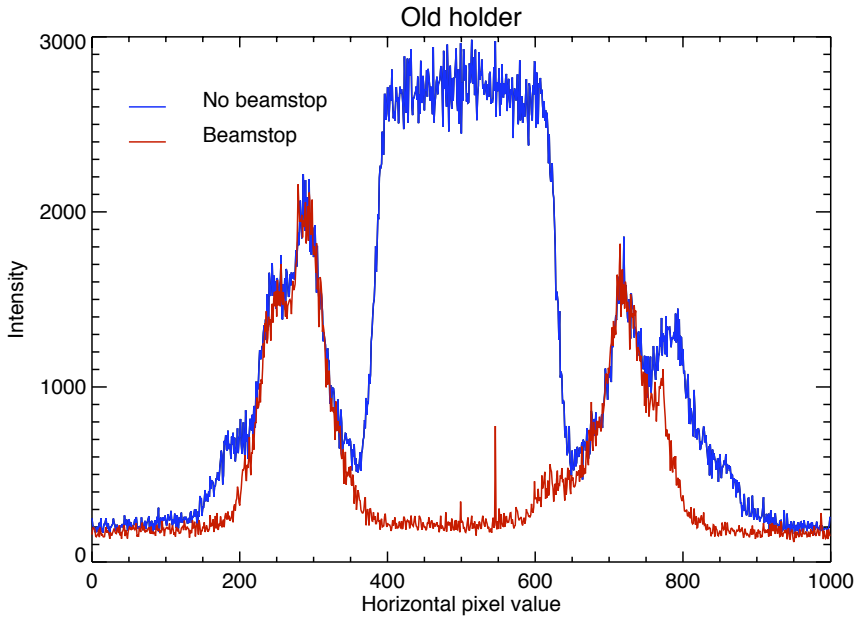

Figure 5.11: Line profile through old single bounce capillary holder.

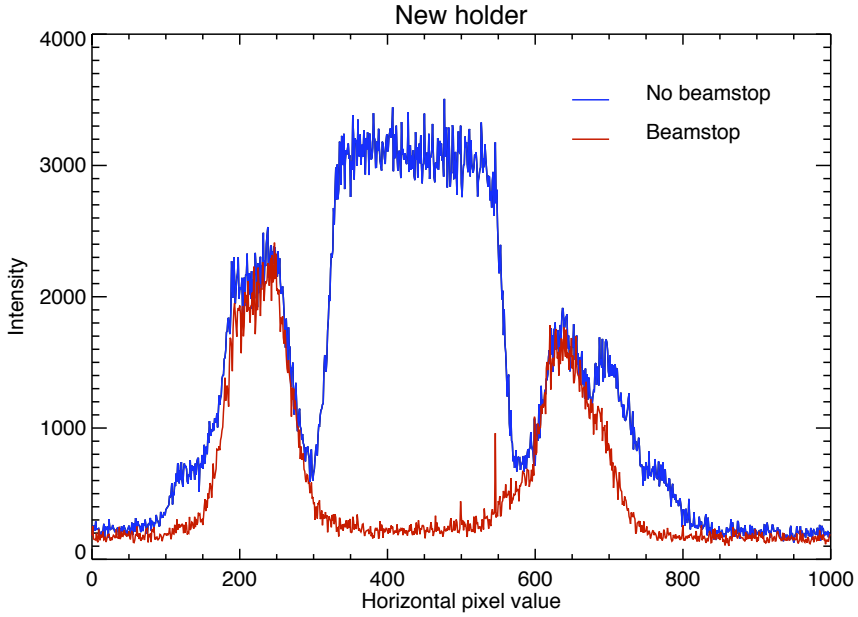

Figure 5.12: Line profile through new single bounce capillary holder.

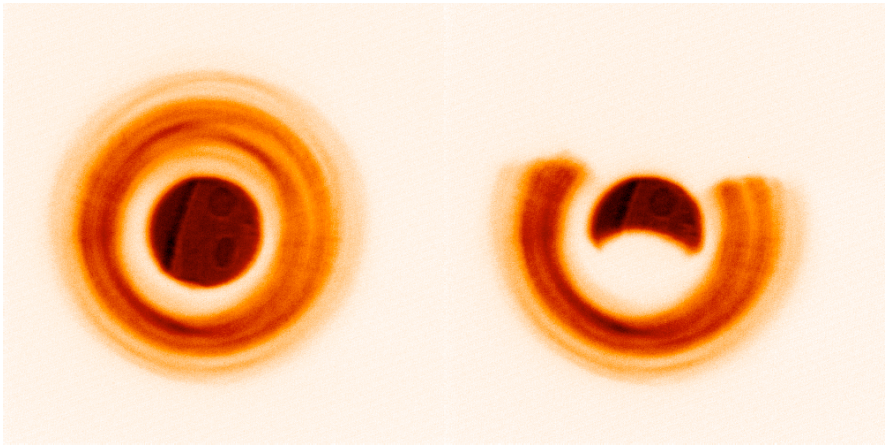

Figure 5.13: Organic tissue seen through the single bounce capilllary without a beamstop and while moving in the beamstop.

5.3 Characterisation of the 2D/CT micro-XRF set-up

Fig. 5.14 shows the experimental set-up in which the synchrotron radiation is monochromatised using the multilayer monochromator for optimal flux, after which a single bounce capillary focusses the photons into a focal spot of approximately 15 μm. A single bounce capillary was chosen since it produces a micro beam with low divergence and large depth of focus compared to polycapillary optics. This is particularly useful when sharp images are desired of a rather thick sample such as *Daphnia magna* in which a divergent beam could blur the projection image. Also when tomography is envisaged on these thick samples, a pencil beam is necessary so that a clear line integral through the sample is obtained. Moreover, using a CCD camera it is very useful to perform radiography on the sample. Fig. **??** shows a top view of the experimental set-up in which the synchrotron radiation is coming from the left side of the image. It shows the optimised single bounce capillary holder attached to a hexapod stage. The sample itself is positioned upon a goniometer-head which is attached to a rotation stage, below which a XYZ stage is present. The combination of goniometer, rotation stage and XYZ stage allows full flexibility in sample positioning. A light microscope is positioned under 45° angle with respect to the central axis of the micro-beam. For a larger sample such as *Daphnia magna*, a low-magnification (10 ×) microscope objective was used. A Vortex Silicon Drift Detector (SDD) is positioned under 90° with respect to the incoming beam for minimizing Compton/Rayleigh scattering. Fig. 5.16 shows a side overview image of the set-up in which the synchrotron radiation is emerging from the right side. The beam passes through the first ionisation chamber (which signal is used for normalisation purposes) and is then focused by the SBC. Behind the sample, the above described Photonic Science CCD camera is present which can be used for radiography. The CCD camera is changed with

a second ionisation chamber during a micro XRF scanning experiment, the information from both ionisation chambers can then be used to obtain information regarding the absorption of the sample. Along the optical axis of the of the microscope and behind the sample, a transmission light is positioned which is very useful when studying thicker organic samples in which reflection light is insufficient to visualise the sample region of interest.

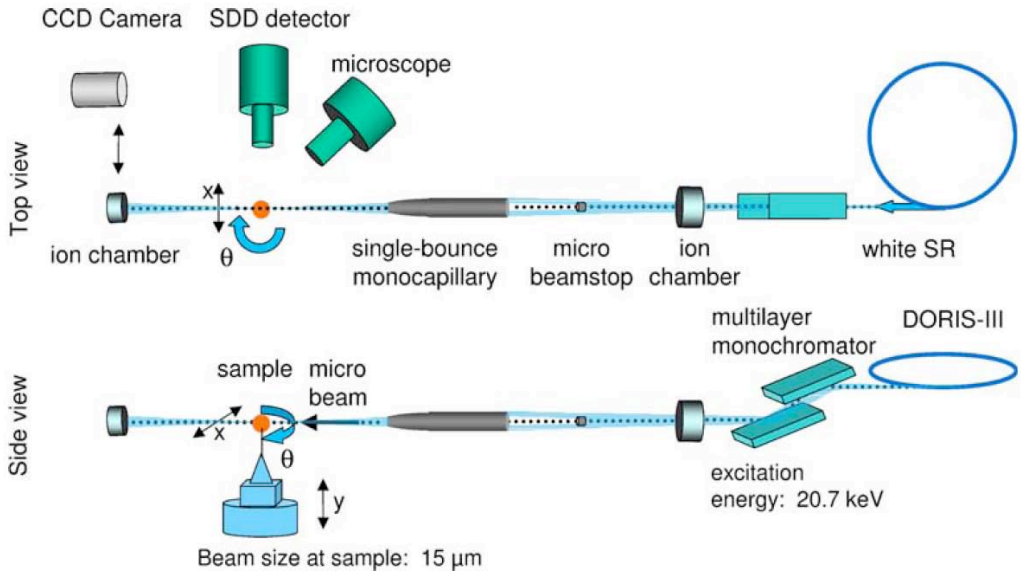

Figure 5.14: Schematic experimental set-up.

In order to quantify the scanning micro-XRF measurements, a carefully determined amount of NIST SRM 1577B (Bovine liver) powder was pressed to a pellet of 13 mm internal diameter resulting in an areal density of 19.7 mg/cm^2. A line scan of 25 measuring points with individual live time of 200 s was performed in order to verify the homogeneity of the obtained pressed pellet. The homogeneity of the reference material was within statistical uncertainty (3-5 %) for Ca, Fe and Zn. Fig. 5.17 shows the first ionisation chamber signal in function of the DORIS current which was used for the normalisation procedure. Fig. 5.18 shows a XRF-spectrum of the SRM with a live time of 300 s, normalised to 100 mA DORIS current. Based on the obtained sum spectrum from the line scan on the standard and assuming the certified concentration values, the relative and absolute detection limits and elemental yield curve were calculated as shown in Fig. 5.19. The detection limits and elemental yields were fitted with a 2^{nd} degree polynome in order to 'guide the eye'. Deviations from the curve can partly be explained by statistical uncertainty due to Poisson counting statistics, but are probably caused by other factors, e.g. discrete behaviour of the photo-electric cross-section, systematic errors in the fitting process, absorption effects for lower Z elements and uncertainty of the concentration in the SRM. Absolute detection limits for the elements of interest are in

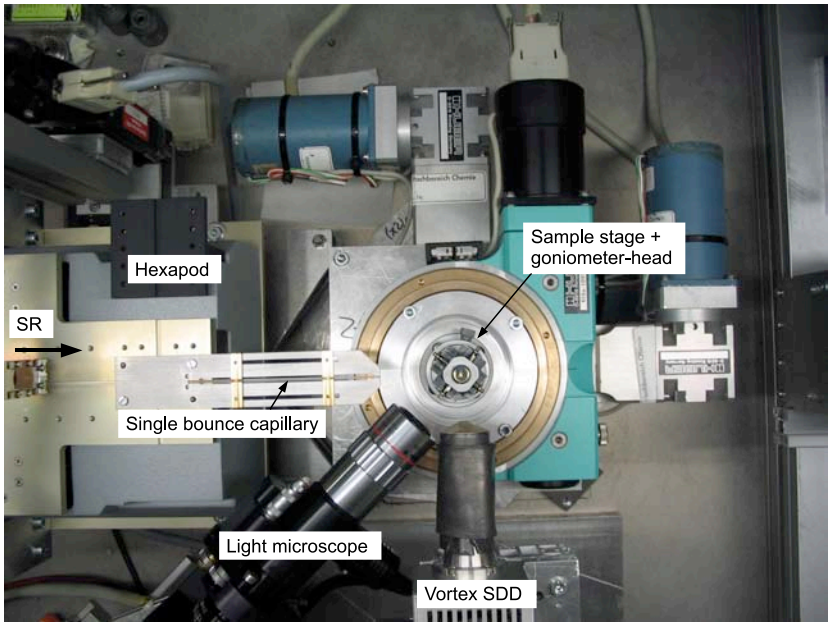

Figure 5.15: Top view experimental set-up.

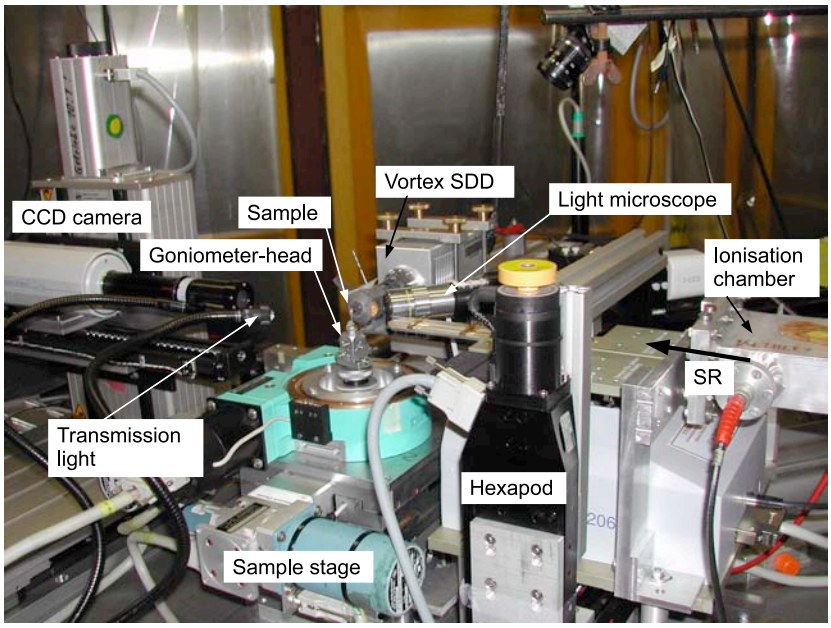

Figure 5.16: Side view experimental set-up.

the 1-10 fg range. These values correspond to relative detection limits in the 0.01-0.10 $\mu g/g$ for the most efficiently excited/detected elements assuming a beam size of 15 μm (FWHM), which was available during the experiment. The same experimental conditions were used for the measurements on the *Daphnia magna* samples.

5.4 Sample preparation

For the 2D/CT micro-XRF experiments, adult *Daphnia magna* were taken from the stock culture at the Laboratory of environmental toxicology, of which the details are described in (Muyssen *et al.*, 2006). The Zn concentration in the case of this culture is 5-7 mg/L Zn, which is near-optimal for promoting Zn dependent biochemical processes in *Daphnia magna*. This sample is termed the unexposed *Daphnia magna* in what follows. In order to obtain insights into the possibility of determining tissue-specific element uptake and distribution following exposure to metal pollution, an adult *Daphnia magna* was selected that was exposed for one week to 120 mg/L Zn, a concentration at which toxic effects started to appear in an earlier study (Muyssen *et al.*, 2006). The exposure was carried out in a test medium, with the exception that dissolved organic carbon was not added. This sample is further on termed the exposed *Daphnia magna*. It should be noted that, since the culture medium (corresponding to unexposed *Daphnia magna*) and the test medium (corresponding to exposed *Daphnia magna*) are not the same, definitive biological/ physiological inferences should preferably not be made with respect to the differences in element distributions between these two samples, with the exception of differences in Zn contents and distributions. The samples underwent dehydration and fixation with HMDS as described in Chapter 3

For the comparison between micro-XRF experiments performed under ambient and cryogenic temperature, adult living *Daphnia magna* were harvested from the culture medium, rinsed with deionised water and glued on top of a polymer fibre, which was subsequently attached to a goniometer-head and immediately inserted into the cryostream, which induced a fast freezing of the sample. In order to make a comparison possible between chemical fixation and cryo-fixation, other *Daphnia magna* control organisms were harvested immediately after the first sample was inserted into the cryostream. The samples were dehydrated in water/aceton series and immersed in HMDS and dried overnight in a desiccator under anhydrous conditions as described in Chapter 3. After completion of the scanning micro-XRF experiment under cryogenic conditions, the cryostream flow was stopped, while keeping the analytical characteristics of the set-up unchanged. Then the scanning micro-XRF experiment was repeated under ambient temperature using a chemically fixed *Daphnia magna* as described in Chapter 3.

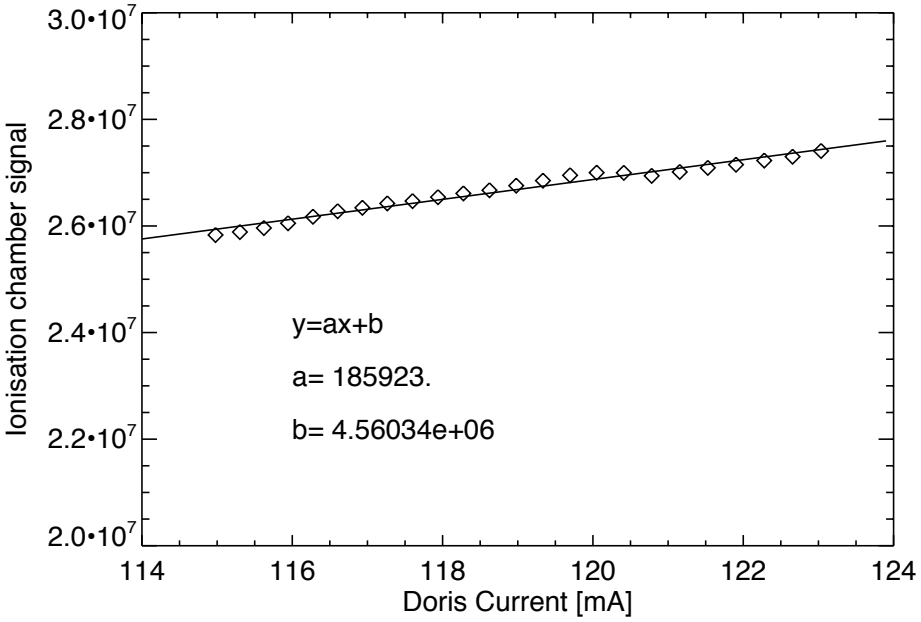

Figure 5.17: Determination of the offset of the first ionisation chamber in order to normalise each obtained spectrum by the variation in incoming intensity (a line scan of 24 points was measured across the SRM).

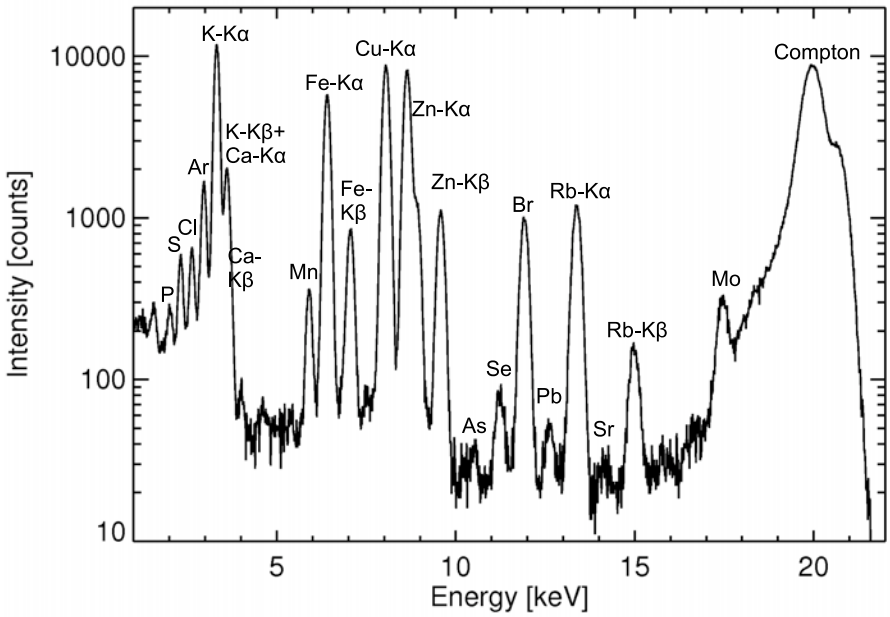

Figure 5.18: Sum spectrum of NIST SRM1577B Bovine liver (LT=300 s).

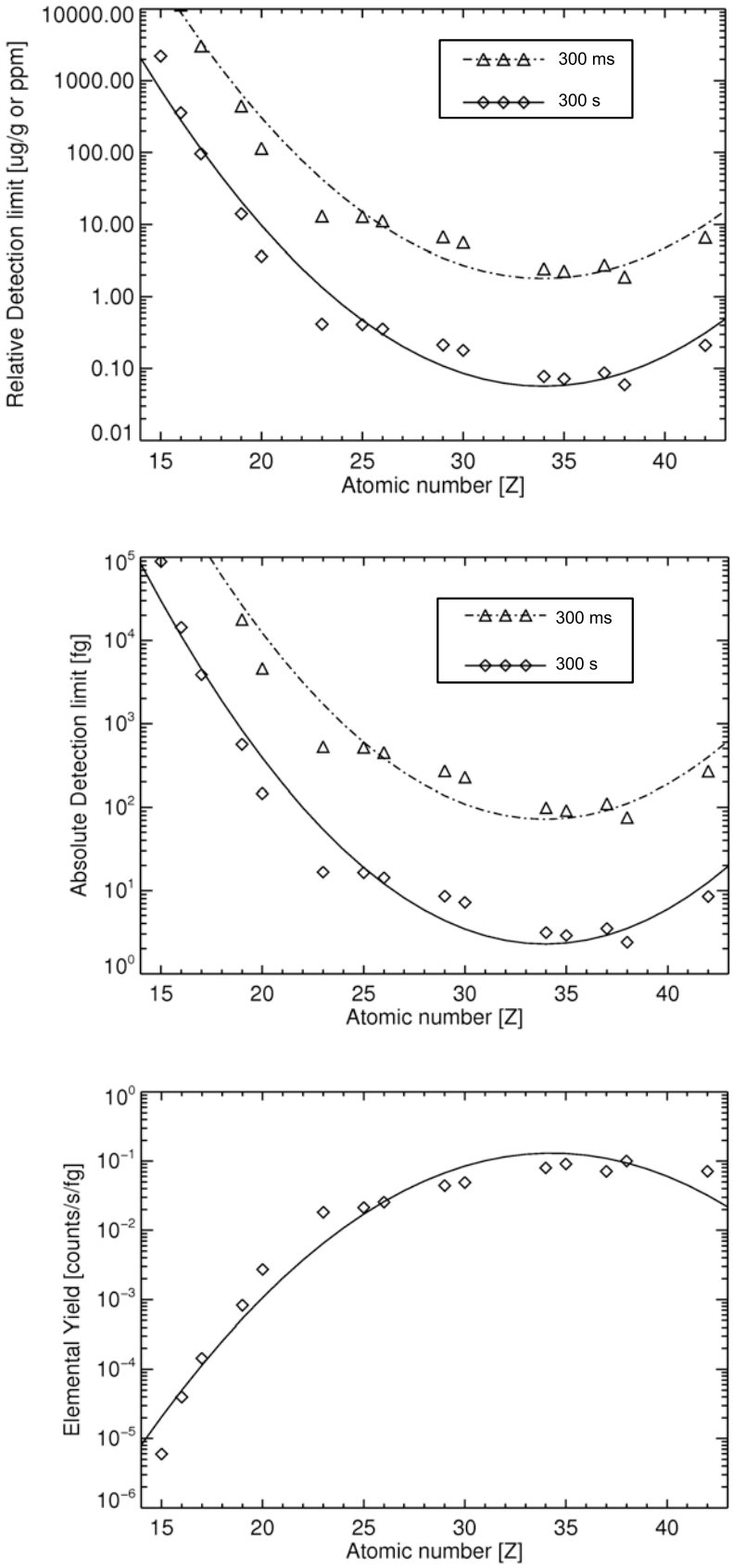

Figure 5.19: Relative and absolute detection limits (LT=300 ms and LT=300 s) with corresponding absolute elemental yield curve for NIST SRM 1577B.

5.5 2D micro-XRF on *Daphnia magna*

5.5.1 Normalisation procedure

Unlike laboratory micro-XRF as described in Chapter 4, which has a constant X-ray flux and automatic correction for detector dead time, element maps obtained at a synchrotron XRF microprobe require careful normalisation. All element maps were normalised to a live time of 1 s and a DORIS-III current of 100 mA and were corrected for detector dead time. In order to achieve this, several additional signals are monitored during a measurement which can be seen in Fig. 5.20. A pseudocolor thermal scale was used for displaying these signals. The first ionisation chamber signal shows a clear decrease in intensity throughout the 2D scan, minor irregularities can be seen in the signal, probably due to instability of the positron bunch or thermal effects on the monochromator. Also the second ionisation chamber features very similar effects, but with the superposition of the sample due to additional absorption of X-rays within the sample. The DORIS signal shows a very homogeneous decrease in intensity, proving that it is very important to correct for the change in incoming intensity when analysing micro-XRF maps. The DORIS signal differs from the displayed DORIS current in a way that the DORIS signal features a higher accuracy than the displayed DORIS current on the monitors. Also the total count rate renders very informative information, the sample can be clearly recognised in this signal. Interestingly, the dead time signal is very similar, confirming that high count rates result in a proportional change in the recorded dead time signal. Note that the the scale is inverted, meaning that a higher dead time signal corresponds to a lower dead time. A first normalisation can be applied to the 2D maps, namely the dead time correction $N_D^{(1)}$. If S_d represents the dead time signal and T_s represents the sample time, then the dead time correction is given by (Falkenberg, 2007b):

$$N_D^{(1)} = \frac{100}{100 - 100 \times (1 - \frac{2.6E^{-6} \times S_d}{T_s})} \tag{5.1}$$

Taking into account the previous remarks, the first ionisation chamber together with the detector dead time seem to be the ideal signals to normalise the 2D maps and generate a so called normalisation matrix. However, the first ionisation chamber is not an absolute value to correct for: between various synchrotron runs it may vary considerably, depending on the alignment and configuration of the experimental set-up. A signal which is reliable throughout runs is the DORIS current in the storage ring, which is in principle proportional to the ionisation chamber current value. Fig. 5.21 shows the signal of the first (blue) and second (red) ionisation chamber as a function of the DORIS current, in which a clear proportional behaviour can be observed. More deviations can be seen for the second ionisation chamber, since additional absorption from the sample causes a (relative) beam position dependent decrease of signal from the second ionisation chamber. Due to the non-zero ionisation chamber current, an offset is present. This means that even when the DORIS current is 0 (e.g. during

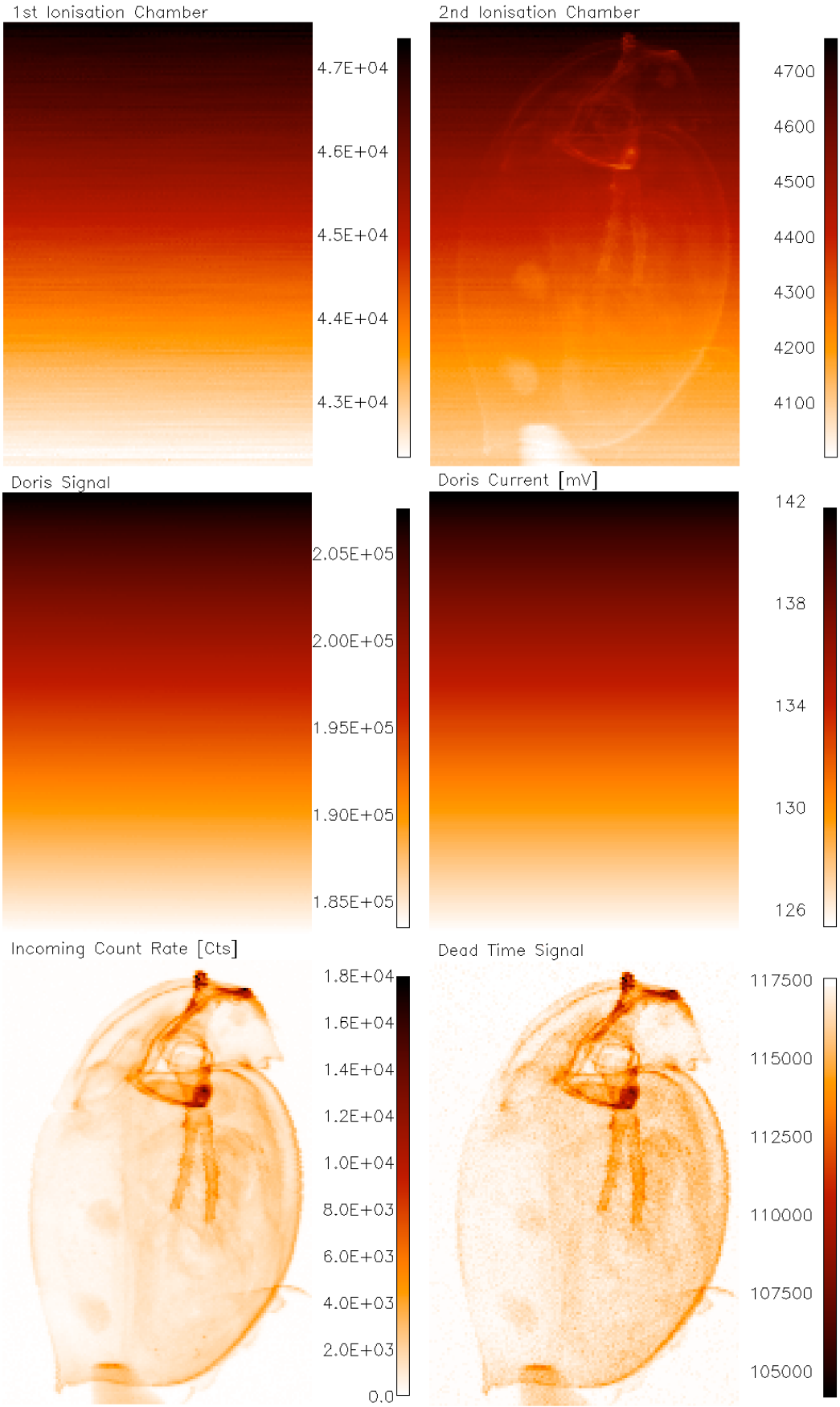

Figure 5.20: 6 scaled maps of incoming signals during a scan. First Row: First and second ionisation signal, Second Row: Doris signal and current, Third Row: Incoming Count Rate and Dead time signal.

an injection), the ionisation chamber measures a value different from 0. Therefore, before the ionisation chamber signal can be used for normalisation, this offset has to be determined. If the influence of the monochromator can be neglected, the relation between the ionisation chamber current C_{ion} and the DORIS current C_{doris} is described by the following equation:

$$C_{ion} = a + b \times C_{doris} \tag{5.2}$$

This makes it possible to perform a second normalisation $N_c^{(2)}$, the doris current normalisation, making use of Eq. 5.3

$$N_C^{(2)} = \frac{b}{C_{ion} - a} \tag{5.3}$$

A 2D map also has the important property that the individual points are measured for a specific measuring time. Therefore, it is also important to normalise the 2D maps to a predefined measuring time, e.g. 1 s. This symbolises the last normalisation, the sample time normalisation $N_T^{(3)}$. If the sample time is given by T_s (measured in seconds) then the sample time normalisation is given by:

$$N_T^{(3)} = \frac{1}{T_s} \tag{5.4}$$

The three derived normalisation procedures can then be used to create the normalisation factor matrix N_{matrix}. A simple multiplication with the 2D maps, representing the net fluorescent line intensity maps of the elements of interest then creates the normalised datasets. The normalisation factor matrix is given in Eq. 5.5. The calculated normalisation factor matrix for the previous dataset is also shown in Fig. 5.22, in which several interesting trends can be observed. The first apparent trend is the linear decrease in the signal, due to the decrease in the DORIS current signal. Subtle irregularities can be observed within this slope, probably due to irregularities in the positron orbit or thermal effects in the monochromator. A second trend superimposed on the slope are the sharp peaks, being dead time corrections for the exoskeleton of the sample due to high count rates. Along the Z axis, a multiplication factor of almost 3 can be seen, correcting for the fact that the sample was only measured for 0.3 s.

$$N_{matrix} = N_D^{(1)} \times N_C^{(2)} \times N_T^{(3)} \tag{5.5}$$

5.5.2 Experimental results

Both *Daphnia magna* samples (exposed and unexposed) were positioned with their carapaces perpendicular to the incoming X-ray beam. The 2D dynamic scanning XRF maps from the unexposed (175 × 122 pixels) and exposed (175 × 142 pixels) were recorded using a step size of 20 μm and a data collection time of 0.3 s per pixel. During the post-processing

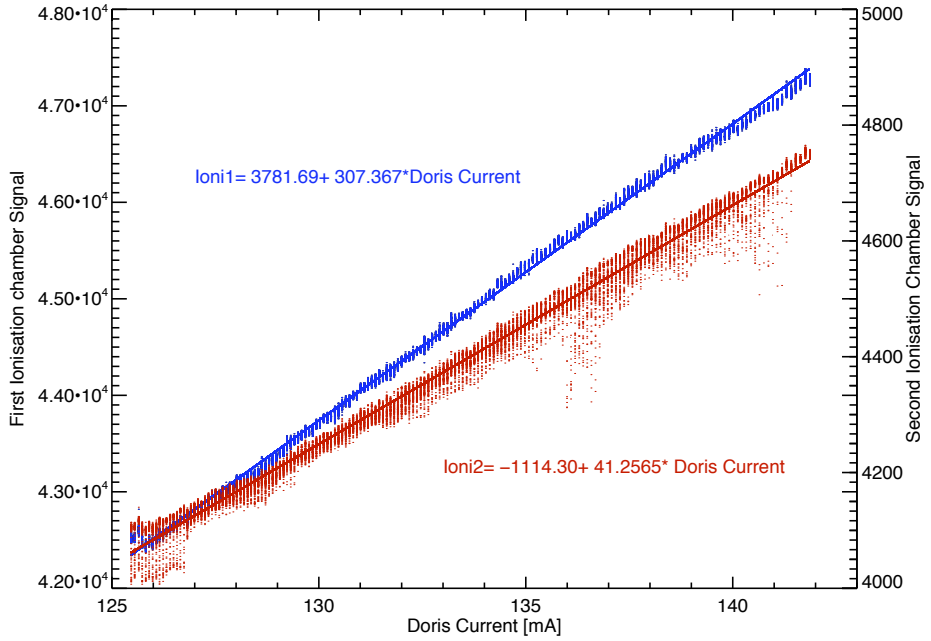

Figure 5.21: First and second ionisation chamber in function of the DORIS current in order to determine the offset.

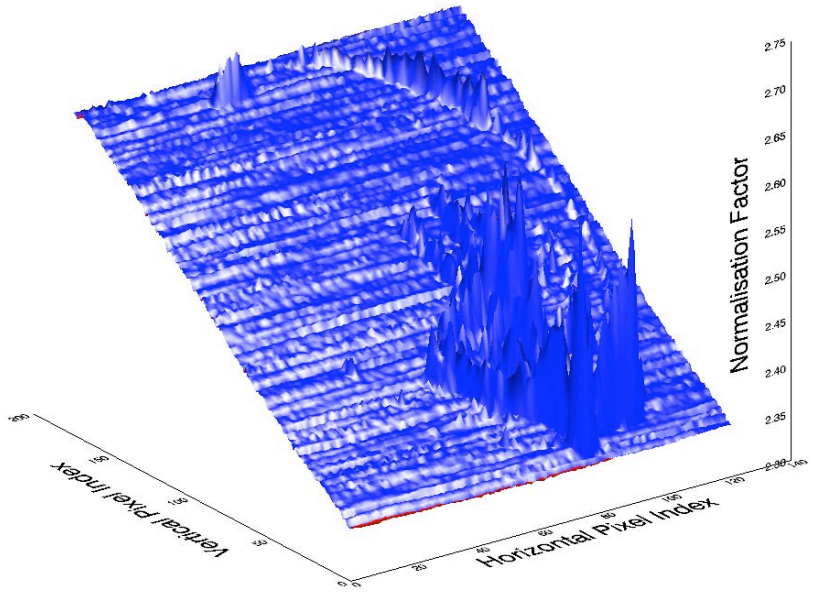

Figure 5.22: Typical normalisation matrix for an XRF map: three superimposed signals can be seen: statistical noise in the ionisation chamber, linear decrease due to the DORIS current and sudden increases due to dead time correction.

procedure, for both daphnids, a sum spectrum was generated first, which gives an overview of the (overall) detectable element composition of the entire organism. The sum spectrum of both samples, normalised to the Compton scattering signal in order to account for differences in illuminated mass, is shown in Fig. 5.23. As expected, one can immediately observe that the Zn exposed *Daphnia magna* exhibits a higher total Zn content than the unexposed specimen, which was previouly observed by Zn detemination on the basis of total organism digestion followed by AAS analysis (Muyssen *et al.*, 2006). It can clearly be seen that the exposed *Daphnia magna* appears to contain lower amount of Br and Sr, however, it is not clear if this difference is linked with the elevated Zn exposure or caused by differences in Br and Sr concentrations in the culture vs. exposure medium. Additional experiments, in which *Daphnia* are exposed to a range of Zn concentrations in a test medium with the same Br and Sr concentrations are needed to resolve this uncertainty. Some unexpected elements, such as Y, Ti and Pb are also present in the sum spectra. As shown below, individual analysis of the sum spectra of the areas of interest within *Daphnia magna* reveals that the Ti was present in the glue on the support capillary and not within the organism. The Pb signal is probably originating from scattering/fluorescence effects from beamline (shielding) components, whereas the Y signal is due to fluorescent radiation originating from the Y-containing YAG crystal, present in the CCD camera positioned near the sample. Within the sum spectra the elements $P, S, Cl, Ar, K, Ca, Mn, Fe, Ni, Cu, Zn, Se, Rb, Sr$ and Pb could be identified and were included in the fitting model of the spectrum evaluation software AXIL.

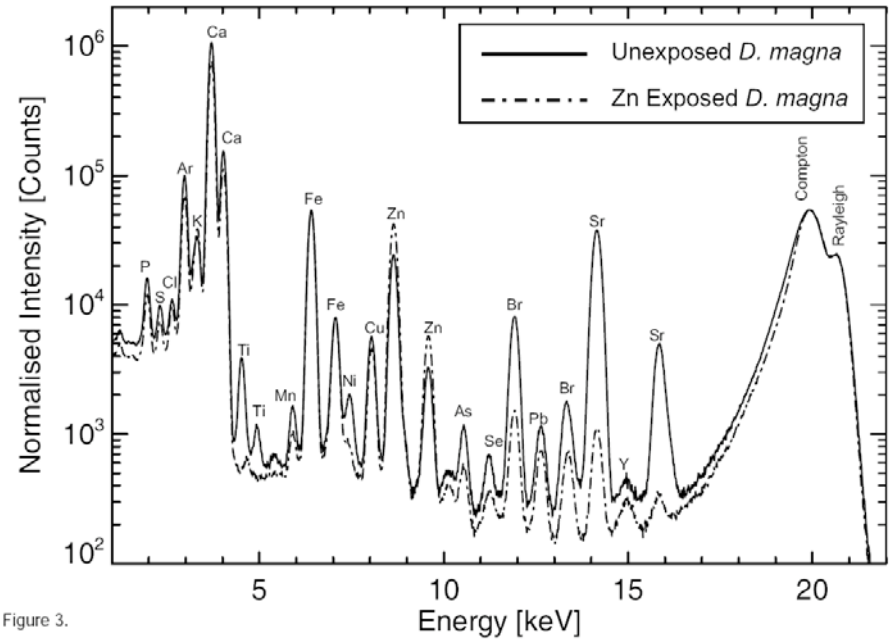

Figure 5.23: Sum spectra of the exposed and unexposed *Daphnia magna*.

By using the elemental yield curve shown in Fig. 5.19, an estimation of the areal concentrations of the elements Zn, Fe and Ca of both *Daphnia magna* was performed. Although no self-absorption correction is applied, this first order aproximation can be considered adequate to obtain semi-quantitative results for direct comparison between the exposed and unexposed case. The calculated areal concentration maps for Ca, Fe and Zn in this first order approximation for both *Daphnia magna* samples are shown in Fig. 5.24

When comparing the Zn distribution of the non-exposed and the exposed daphnid, a distinct enrichment of Zn can be observed in (A) the gill-like osmoregulatory tissue, (B) the gut and (C) the digestive gland. The latter two are part of the digestive system of *Daphnia magna* and are involved in nutrient absorption as well as the holocrine secretion of digestive enzymes (Schultz & Kennedy, 1976). The accumulation in gills may suggest that Zn accumulation may interfere with osmoregulation, as in fish (Hogstrand *et al.*, 1996). The accumulation in the digestive system may suggest that nutrient assimilation from food is a possible target of Zn toxicity. It has indeed recently been shown that gene expression related to digestive processes in *Daphnia magna* was altered following Zn exposure (Poynton *et al.*, 2007). Alternatively, Zn accumulation in the digestive gland could also be the result of a detoxification strategy, whereby secretory vesicles are used to eliminate metals from the body, a process which is commonly observed in mussels (Marigomez *et al.*, 2002). However, having obtained these data, some questions still remain unsolved. First, using only the 2D micro-XRF data, it remains unclear whether elevated levels of Zn in the gut region are located in the gut or in the gut epithelium. In order to answer this question, virtual cross-sections need to be obtained using micro-XRF CT (or confocal micro-XRF) to get a better insight in the internal structure and element distribution of the sample. Second, there is a need to analyse the average element concentrations of different substructures of interest within these element maps based on e.g., K-means clustering. Third, the metal accumulations should be correlated with the different tissue structures which can be visualised using absorption micro-CT.

5.5.3 K-Means clustering

Introduction

K-Means clustering is an iterative technique that is used to partition an image into K clusters. The process is composed of the following steps:

- Pick K cluster centers, either randomly or based on some heuristic
- Assign each pixel in the image to the cluster that minimizes the variance between the pixel and the cluster center (centroid)
- Re-compute the cluster centers by averaging all of the pixels in the cluster
- Repeat steps 2 and 3 until convergence is attained (e.g. no pixels change clusters)

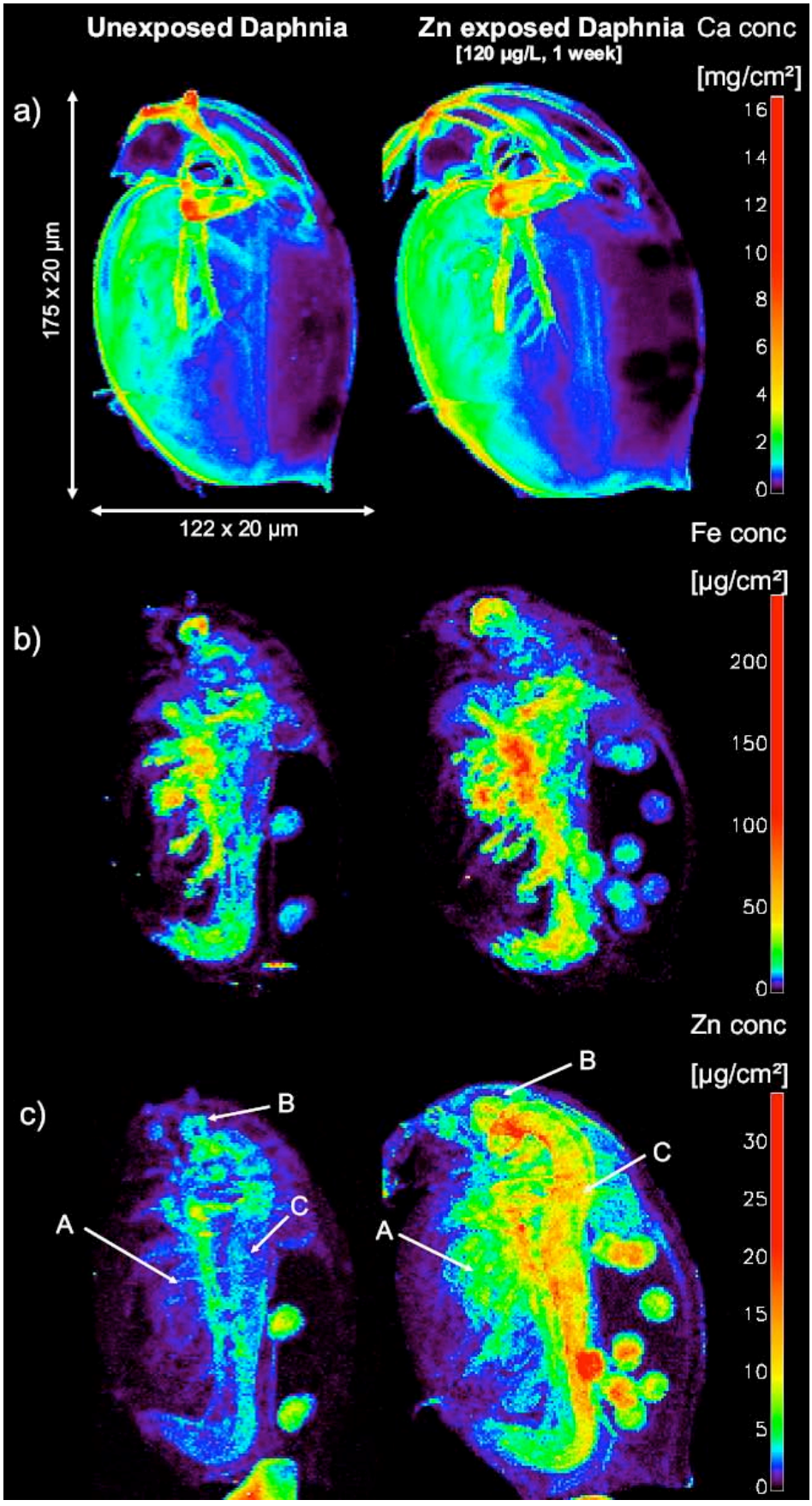

Figure 5.24: Comparison between the *Ca*, *Fe* and *Zn* element distributions of the unexposed and exposed *Daphnia magna*.

In this case, variance is the squared or absolute difference between a pixel and a cluster center. The difference is typically based on pixel color, intensity, texture, and location, or a weighted combination of these factors. K can be selected manually, randomly, or by a heuristic. This algorithm is guaranteed to converge, but it may not return the optimal solution. The quality of the solution depends on the initial set of clusters and the value of K. The procedure quite often automatically creates different clusters which, dependent on the element and cluster number selection, generates the substructures wanted. Anomalies such as very pronounced concentrations of unexpected elements due to contamination can be easily isolated and removed. The subsequently generated sumspectra are very often of better quality and are better suited for semi-quantitative analysis.

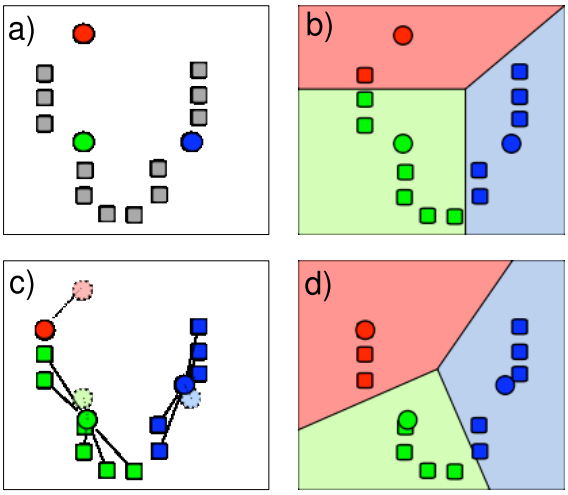

Figure 5.25: a) Shows the initial randomized centroids and a number of points b) Points are associated with the nearest centroid c) Now the centroids are moved to the center of their respective clusters d) Steps 2 and 3 are repeated until a suitable level of convergence has been reached. Reproduced from Wikipedia (2009a).

Application to *Daphnia magna*

In order to obtain a better understanding on the variation of element concentrations between different organs of the organism *Daphnia magna* and to compare the determined element concentrations of organs between different samples, the K-means clustering method was explored. In this way, one can overcome the problem of only evaluating the sum spectra of the entire 2D micro-XRF scan, which averages out the element distribution of an area of interest with other areas (which can even contain contamination). The generated sum spectra corresponding to the different clusters are also of considerably better quality than individual (point) spectra due to their improved statistics, and are better suited for (semi-)quantitative analysis.

In order to make comparison possible, there is the need to find a suitable clustering method which generates similar tissue structures on both datasets. Different elements were used to obtain satisfying clusters. It should be noted that noisy element images render noisy clusters. On the other hand, element maps with good counting statistics allow to obtain clusters of good quality. The amount of clusters is also an important aspect to be explored: choosing a low amount of clusters often results in the fact that structures which need to be separated are often grouped together whereas choosing a high amount of clusters results in a too high subdivision of the element maps. Although these clusters can then be manually again grouped together, this additional type of data handling should be avoided. Also different types of data pretreatment can generate clusters of better quality.

Fig. 5.26 shows the K-means clustering of a control *Daphnia magna* XRF data set when requesting 10 clusters using the Ca, Fe and the Compton scattering maps. Using these signals, the clusters were best coinciding with the different tissue structures/organs of interest. Note that before the actual clustering a square-root data pre-treatment is necessary in order to compensate for the Poisson counting statistics and a normalisation is performed in order to give equal weight to each element. Next to the air (CLR1) and clusters constituting the paraffin/support capillary (CLR3, CLR9, CLR10), we observe the brood pouch (CLR2), the gut (CLR4), the front exoskeleton (CLR5), the antennae (CLR8), the gill tissue (CLR7), and the eggs/eye (CLR6). The corresponding sum spectra of the different clusters obtained are shown in Fig. 5.27. For clarity, only the clusters of scientific importance are shown, such as the brood pouch, the front of the exoskeleton, the antennae, the gill tissue and hepatopancreas, eggs and eye and the gut. Moreover, in order to compare the presence of elements in the different clusters, all sum spectra were normalised to the average density of CLR7 by using the Compton scattering signal. Normalisation using the Compton scattering means normalising to the amount of sampled mass targeted by the X-ray beam. From these results, it can be concluded that the different tissues indeed show different metal enrichments. For instance, the antennae (CLR 6) and the front exoskeleton (CLR5) have a higher Ca and Sr concentration than other tissues. The occurence of high amounts of Ca in the exoskeleton is often reported for crustaceans as well as other species with a calcified exoskeleton. In the carapax of Daphnia, Ca is suggested to be mainly associated with carbonate and phosphate minerals, which renders it a rigid structure as protection against predators (Alstad *et al.*, 1999; Waervagen *et al.*, 2002). The gill tissue (CLR7) has the highest Fe concentration of all tissues. The enrichment of Fe in the gill tissue is most likely related to the gill's respiratory function and, hence, to the presence of haemoglobin which is the most important oxygen transport molecule in *Daphnia* (Pirow *et al.*, 1999a,b). The Zn content is highest in eggs/eye (CLR8), although differences with the antennae (CLR6), gill (CLR7) and gut (CLR 4) are less pronounced. Note, that the Ti signal in these clusters completely disappeared in comparison with the sum spectrum, since this contamination is not present in the clusters of interest.

Also note, that valuable information is obtained regarding the element content of clusters from which the element maps were too noisy, e.g., for Mn, As, Se.

By applying a similar K-means clustering procedure on the exposed *Daphnia magna*, it is also possible to isolate structures of interest such as the gut, gill tissue and eggs/eye for the exposed *Daphnia magna*. In Fig. 5.28, the tissues of interest such as the gut, gill tissue and eggs are compared between both samples. For clarity, only the energy range for the elements Mn up to Sr was selected. Br, Sr, As, Se and Pb are present to a higher extent in the unexposed *Daphnia magna*, but it is unclear if this is due to differences in the Zn concentration in the water or due to other differences between culture and exposure medium. It is, however, more interesting to focus on the comparison between the Zn contents and tissue distribution of non-exposed vs. exposed *Daphnia magna*. First, no increased Zn accumulation is observed in the eggs of the exposed *Daphnia magna*, which may suggest that Zn transfer from mother to offspring is tightly regulated. Furthermore, the proportional increase of tissue-specific Zn accumulation after Zn exposure is the highest in gut tissue, followed by a smaller difference in the gill tissue. The higher Zn accumulation in the digestive tract after Zn exposure, compared to the gills, is interesting because this tissue is only subjected to an indirect Zn exposure, after ingestion of algal food that has become contaminated by Zn from the water. The occurence of high Zn amounts in the gut epithelium and/or lumen could have an influence on the production and secretion of digestive enzymes (Poynton *et al.*, 2007), and/or on the biochemical activity of these enzymes themselves (Chen *et al.*, 2002). Thus, impaired nutrient assimilation could be a toxicological target of Zn exposure. The accumulation of Zn in the gill tissue can disturb osmoregulatory processes (Hogstrand *et al.*, 1996) and impair the influx of Ca^{2+}, which in turn can lead to hypocalcaemia (Spry & Wood, 1985). Further work, e.g. whereby Zn accumulation and physiological effects are investigated simultaneously for a range of different Zn concentrations, is needed to establish causal links between tissue specific Zn accumulation and disturbance of physiological processes.

5.5.4 Principal Component Analysis (PCA)

Introduction

A micro-XRF dataset consisting of a series of X-ray maps, each corresponding to one chemical element, may contain images which are highly correlated or images that do not convey any information. PCA is a multivariate statistical technique which is aimed towards highlighting the variance-covariance structure of experimental multivariate datasets, essentially through reduction of the dimensionality of the data, and as such, its general objectives are data reduction and interpretation. Since PCA is a mathematical procedure that operates on (two-dimensional) data matrices, the three-dimensional (e.g. $N_{el} \times N_{row} \times N_{col}$) micro-XRF data set Z first needs to be unfolded to a two-dimensional ($N_{pix} \times N_{el}$) matrix V.

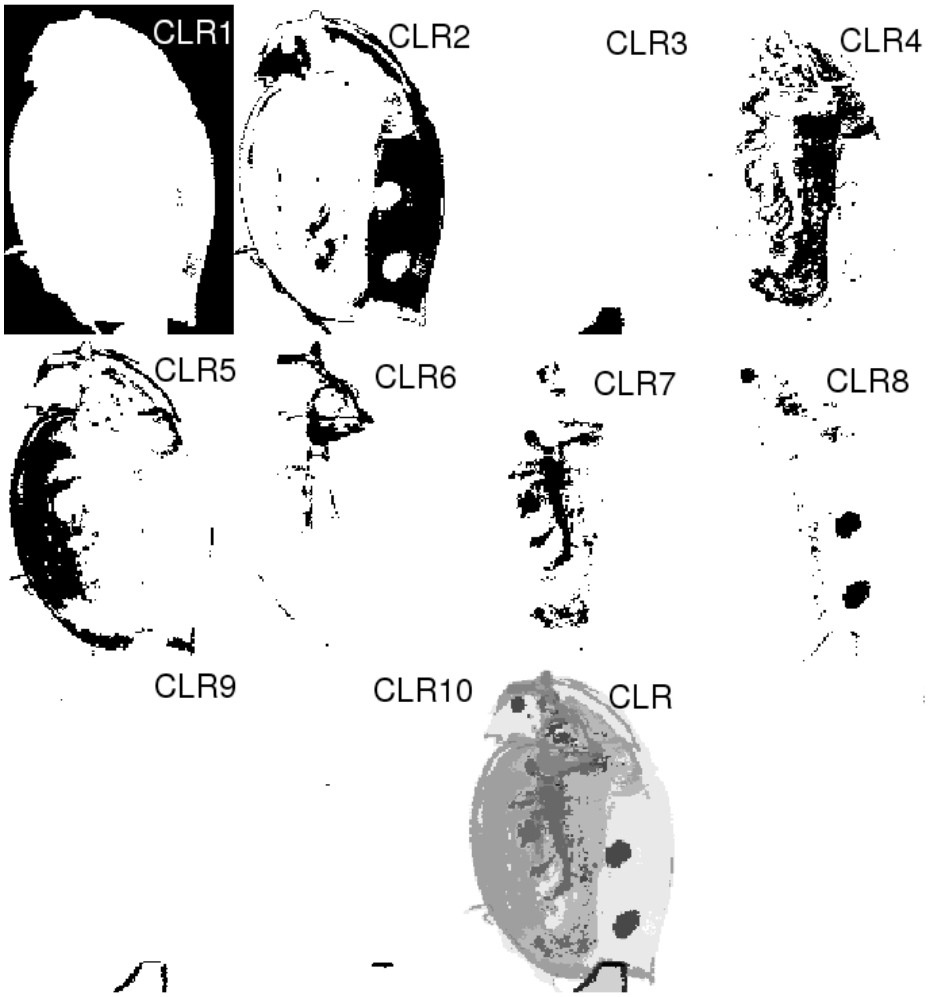

Figure 5.26: 10 clusters obtained by K-means clustering on the unexposed *Daphnia magna*. An extra image is added showing the clusters instantaneously, using different grey scales per cluster.

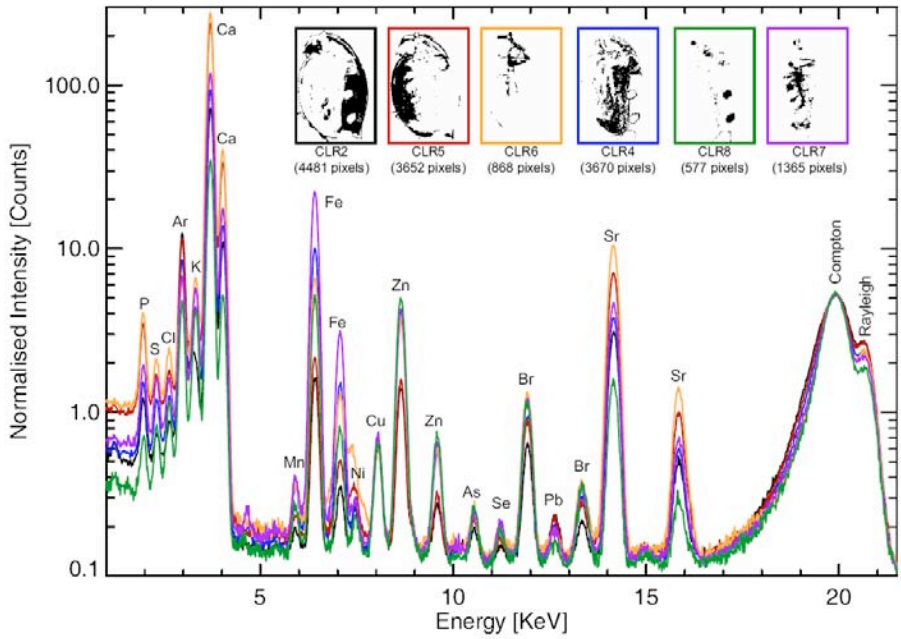

Figure 5.27: 6 sum spectra of the clusters obtained by K-means clustering on the unexposed *Daphnia magna*. All the sum spectra were normalised to the Compton scattering.

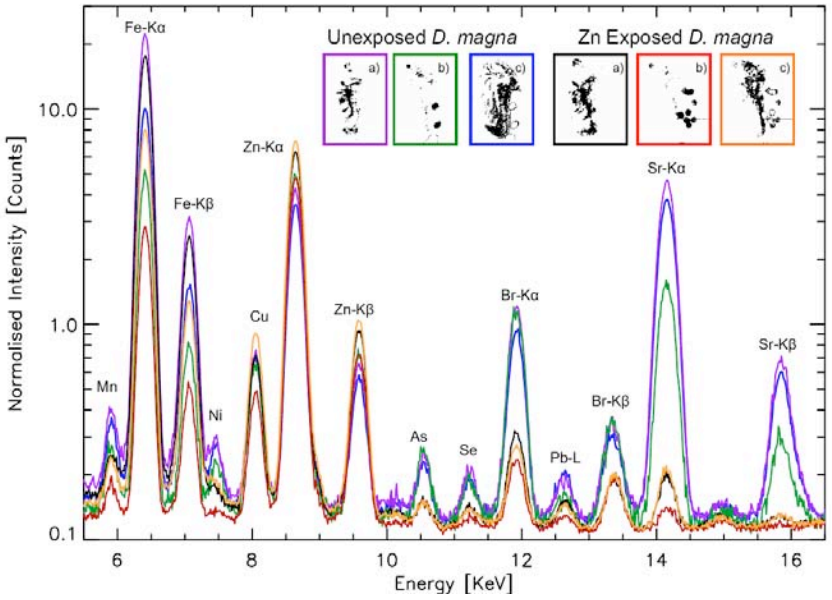

Figure 5.28: Comparison of the 3 clusters of interest of the exposed and unexposed *Daphnia magna*. All the sumspectra were normalised to the Compton scattering.

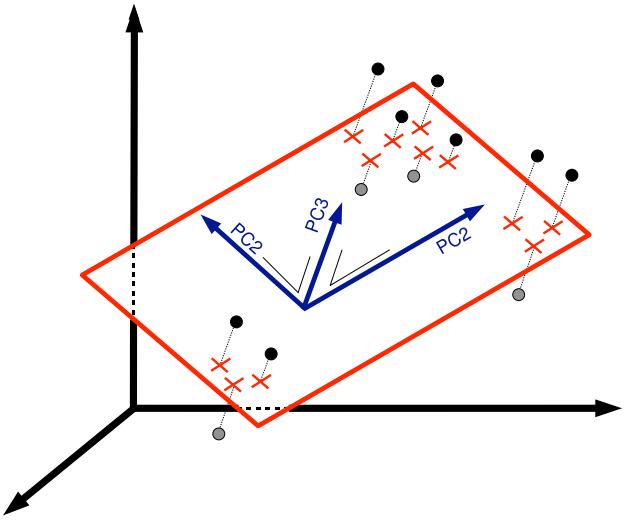

Figure 5.29: The principle of Principal Component Analysis (PCA): in the hyperspace of the original variables (or objects), new principal component axes are defined, which are better suited to decribe the variation in the set of datapoints considered. Score (or loading) plots are derived by the orhogonal projection of the data points onto planes defined by pairs of PC axes. Reproduced from Vekemans (2000).

Mathematically, PCA corresponds to a decomposition of the two-dimensional multivariate data matrix V of rank R into R matrices of rank 1:

$$V = t_1 p_1' + t_2 p_2' + \ldots + t_k p_k' + t_R p_R' = TP' \tag{5.6}$$

where matrix element V_{ij} is the value of the i^{th} case (pixel) and j^{th} variable (e.g. chemical element) and column vectors t_k and p_k are respectively called the score vector and loading vector of the k^{th} principal component (PC). It can be shown that the vectors p_k are the eigenvectors of the symmetric matrix $V'V$ and that the vectors t_k are equal to the eigenvectors of the symmetric matrix VV' multiplied by its corresponding eigenvalue a_k:

$$a_k p_k = V'V p_k \tag{5.7}$$
$$a_k t_k = VV' t_k \tag{5.8}$$
$$a_k = t_k' t_k \tag{5.9}$$
$$\tag{5.10}$$

Since $P\prime P$ is equal to the identity matrix, we may write:

$$T = VP \tag{5.11}$$

where T_{ik} and P_{jk} are respectively the score value of the t^{th} data point/pixel and the loading value of the j^{th} original variable of the k^{th} PC. This equation expresses the working method of PCA: replacement of the original variables of the data matrix (in this case, the chemical elements) by mutually orthogonal (i.e. uncorrelated) linear combinations of the latter. Graphically, in the hyperspace (of dimension N_{el}) subtended by the original variable axes, in which each data point (pixel i) is represented by a point at a location defined by its corresponding cordinates V_{ij}, the PCs are a new set of mutually orthogonal axes that are better suited to describe the structure of the clouds of data points (the pixels) which are present in this space. The score value T_{ik} is then the orthogonal projection of the i^{th} data point/pixel on the k^{th} PC axis. The orthogonal projection of the data points onto planes defined by pairs of PC axes (the equivalent of plotting columns of matrix T against each other) gives rise of so-called score plots, which reveal relationships between data points/pixels. Refolding the column vectors that constitute T, a set of N_{el} score images is obtained, also called pricipal component or eigenimages. Analogeous data manipulation in the hyperspace subtended by the objects/pixels results in loading plots, which hold variable specific information. Since the eigenvalue a_k corresponding to the k^{th} PC is a measure of the fraction of the total variance in the data set which is explained by that PC, the corresponding eigenvectors should be sorted accordingly, and as a result, the first PCs define the directions along which the data points vary the most. Usually one plots $CVE_k = a_k / \sum a_k$ (CVE = contribution to the variance explained) vs. the PC index to obtain an idea of how many of the PCs are necessary to explain most of the variance of the data set. Also, usually the first few PC images (associated with large eigenvalues) will show a high contrast and a low noise level while the remaining ones will convey less and less information. Discarding irrelevant PC images is equivalent to reduction of dimensionality of the data set, thereby facilitating the data analysis.

Fig. 5.30 shows the scheme of the decomposition of the multivariate image set. Prior to the actual decomposition, the raw intensity data set X can optionally be transformed. The resulting three-dimensional data set Z is then unfolded to the corresponding (two-dimensional) matrix V as explained before. As a next step, the set of eigenvectors are extracted in two steps: the set of loading vectors are calculated by reducing the $(N_{el} \times N_{el})$ real symmetric matrix $V'V$ to tridiagonal form by using the Householder's method of which the N_{el} ($\leq N_{pix}$) eigenvalues and eigenvectors are calculated applying the QR algorithm. The loading vectors are sorted accordingly (eigenvectors with largest eigenvalues first), resulting in the loading $(N_{el} \times N_{el})$ matrix P, the score matrix T is computed by means of Eq. 5.11. As can be seen in the scheme, this working method provides the analyst following tools for interpretation of data sets: CVE plots and the sets of eigenimages for the determination of the relevant PCs, score and loading plots for the analysis of relationships between respectively pixels and chemical elements. The score matrix T may be used as input to cluster analysis.

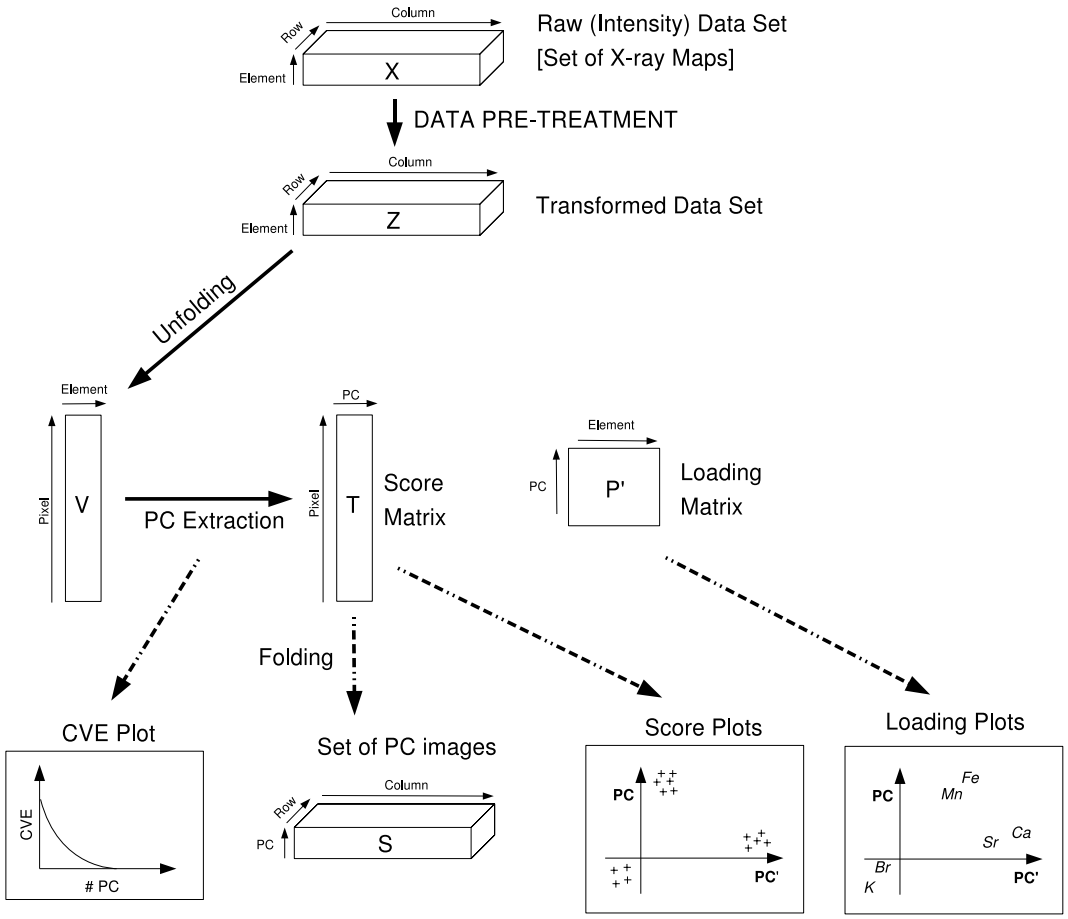

Figure 5.30: Decomposition of multivariate image set X into loading and score vectors, constituting respectively matrices P and T.

Application to *Daphnia magna*

Although PCA analysis is often performed before K-means clustering in order to reduce the dimensionality and thus perform calculations on smaller datasets, this approach was not followed here. The reason is that clusters of ecotoxicological meaningfulness could only be obtained while performing K-means clustering on the original dataset and not on the principal component maps. As previously discussed, PCA analysis is a powerful analysis tool to investigate the (co)variance of different element maps. However, when performed on large overview element distributions obtained on *Daphnia magna* interpretation of the loading and score plots are cumbersome since too many datapoints are visualised. However, PCA analysis can also be performed on the mean element intensities of the different clusters obtained. This has the advantage that (1) interpretation of the loading and score plots is simplified since less data points are visualised and (2) information on elements with previously insufficient signal-to-noise ratio can now be obtained since K-means clustering improves on the dataquality of the XRF-spectra.

$PC\#$	1	2	3	4	5	6	7	8
CVE (%)	0.579	0.316	0.079	0.021	0.003	0.001	0.000	0.000
$K - K_\alpha$	0.381	-0.324	-0.030	0.565	-0.370	0.447	0.138	0.271
$Ca - K_\alpha$	0.325	-0.397	0.397	-0.256	0.188	0.338	-0.406	-0.447
$Mn - K_\alpha$	0.449	0.001	0.301	0.006	0.492	0.521	0.143	0.416
$Fe - K_\alpha$	0.375	0.071	0.714	0.236	0.478	0.195	0.135	0.062
$Cu - K_\alpha$	0.310	0.457	0.075	0.342	0.226	0.145	0.474	0.525
$Zn - K_\alpha$	0.340	0.385	0.199	0.586	0.523	0.223	0.169	0.049
$Sr - K_\alpha$	0.351	0.362	0.369	0.250	0.135	0.472	0.368	0.413
$Compton$	0.270	0.494	0.244	0.192	0.122	0.287	0.624	0.317

Table 5.4: Loading and the average score values resulting from PCA and K-means operation on the mean element intensities

In Table 5.4, the corresponding loading values of the average element intensities together with the CVE for each PC is given. Clearly the first PCs explain most of the total variance in the data set. Also in Fig. 5.31 it can be observed that the CVE becomes more insignificant with increasing PC number. The score plots of the average element intensities are given in Fig. 5.34 and Fig. 5.36. By constructing the corresponding loading scatter plot of the chemical elements involved as in Fig. 5.35 and Fig. 5.37, it is also possible to associate high element signals with clusters. The justification of these associations can be derived by recalculating the mean intensities of elements for the clusters applying Eq. 5.6 with the data of Table 5.4. Since there seems to be a close connection between pixel groups and elements in the same

quadrant or even on the same relative position in the corresponding scatter diagrams, it is evident to superimpose the two plots, displaying both pixels (objects) and elements (variables) which is a common practice in correspondence analysis. However, since we are dealing with large data sets, the score and loading plots are kept separately to improve clarity.

From the comparison between the 1st and 2nd principal component shown in Fig. 5.34 and Fig. 5.35, it can be observed that the clusters containing organic tissue are well separated from the clusters containing the clusters of the capillary. The inorganic material is characterised by a higher Compton scattering signal, indicating a higher density and a higher Zn and Cu signal, whereas the organic tissue is characterised by a higher Ca, Sr and K contents. The increase in Ca and Sr in the different organic clusters can clearly be observed: there is an increase in the Ca contents or density in the series of clusters: air, brood pouch, front exoskeleton and antennae. By comparing the 2nd and 3rd principal component shown in Fig. 5.36 and Fig. 5.37, a correlation between Ca and Sr is present, but also between Zn, Cu and the Compton scattering signal. We also see that Fe does not correlate with any of the other elements, although a (minor) correlation with Mn seems possible. This explains why an efficient K-means clustering on the *Daphnia magna* could only be obtained by using only the Ca, Fe and Compton map. By association with the corresponding score biplot, we can also easily relate the antennae (CLR6) and the front exoskeleton (CLR5) with Ca and Sr, the gill tissue (CLR7) and the tip of the capillary (CLR10) and to a lesser extent the gut (CLR4) and eggs (CLR8) with Fe, the capillary tip (CLR9+10) and eggs with Zn.

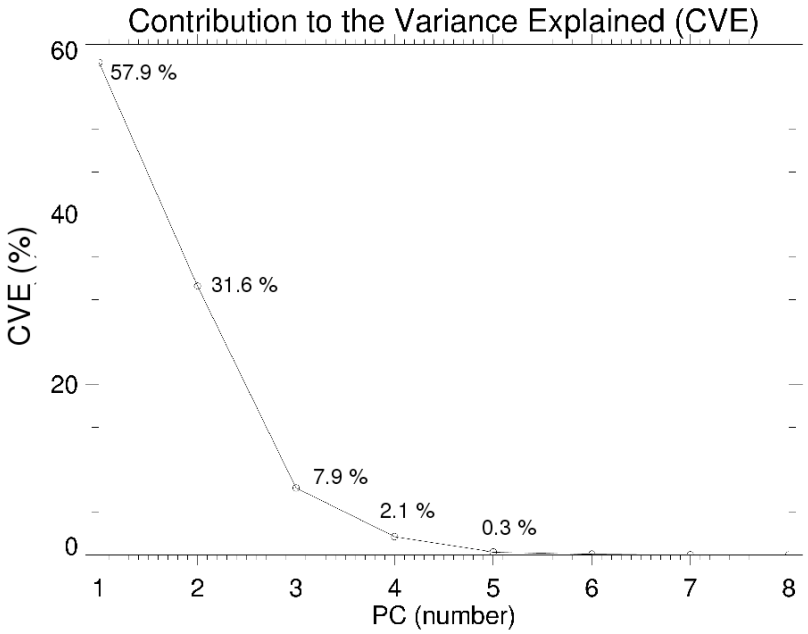

Figure 5.31: Contribution to the variance explained (CVE).

A very illustrative way to visualise the simultaneous/complementary presence of elements as investigated by means of PCA can be obtained by creating RGB images of the elements lying the furthest away from each other in the score plot of interest. For effective scaling, a histogram was used to select the range of scaling as shown in Fig. 5.33. From the resulting RGB image shown in Fig. 5.32, it can be deduced that the carapace is rich in Ca, eggs and gut in Zn and the osmoregulatory tissue in Fe.

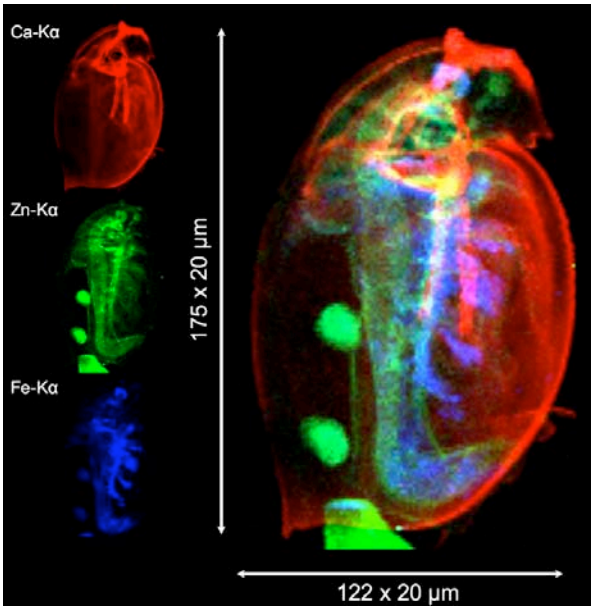

Figure 5.32: 2D element map of Ca, Zn and Fe respectively.

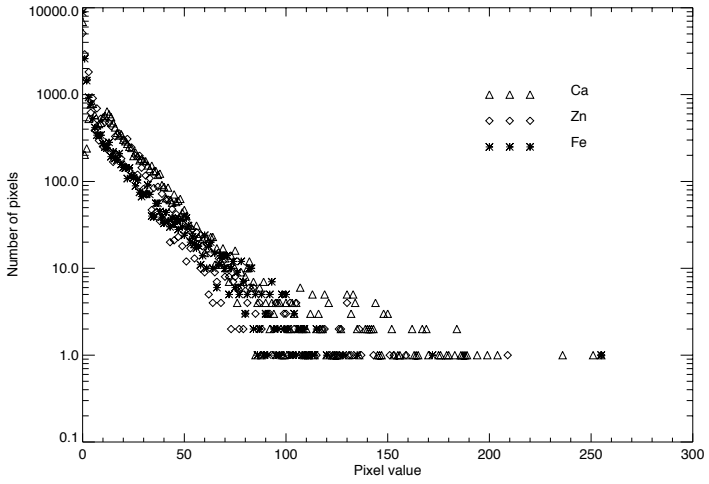

Figure 5.33: Histogram of the composite 2D dataset.

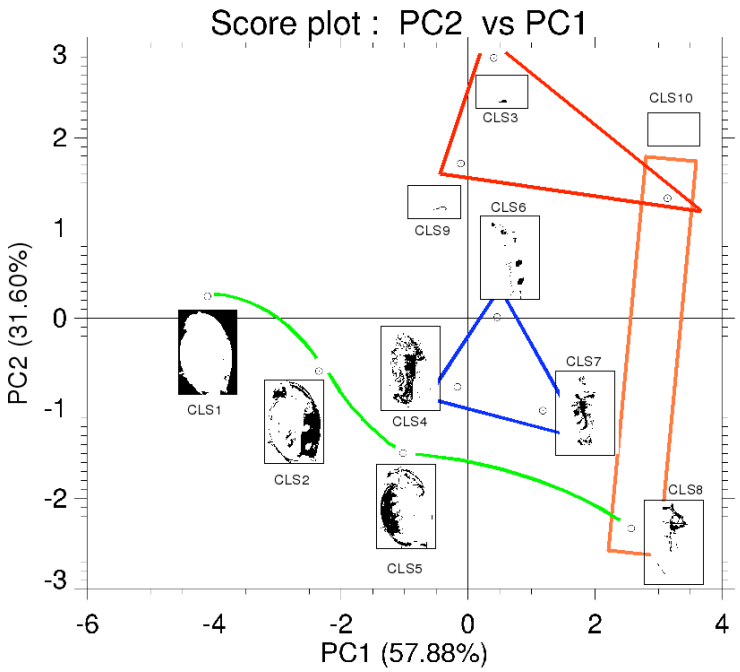

Figure 5.34: Score plot 2nd PC versus 1st PC.

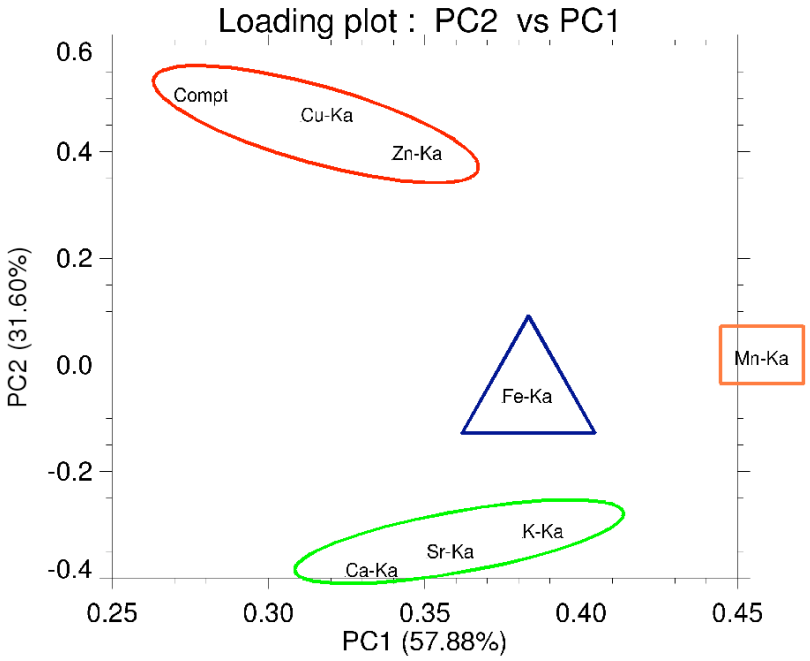

Figure 5.35: Loading plot 2nd PC versus 1st PC.

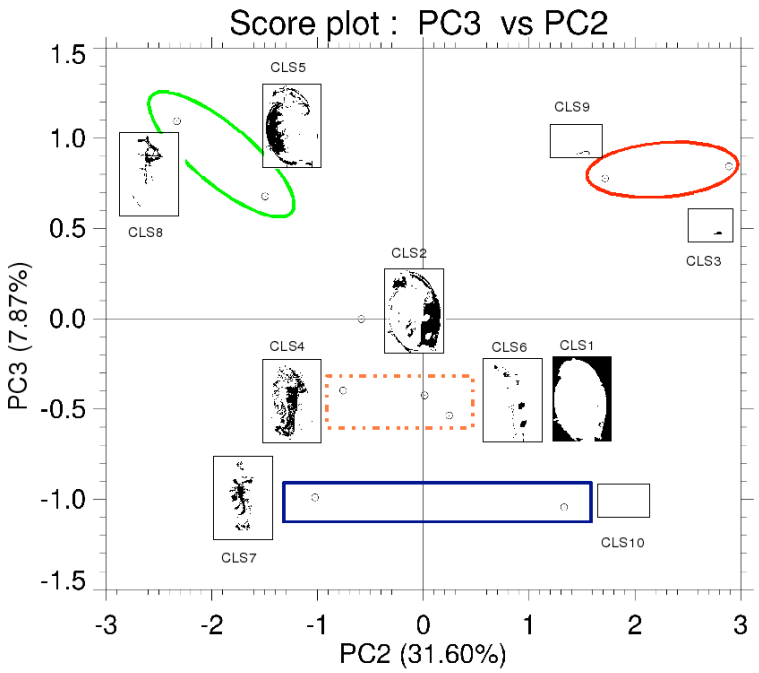

Figure 5.36: Score plot 3rd PC versus 2nd PC.

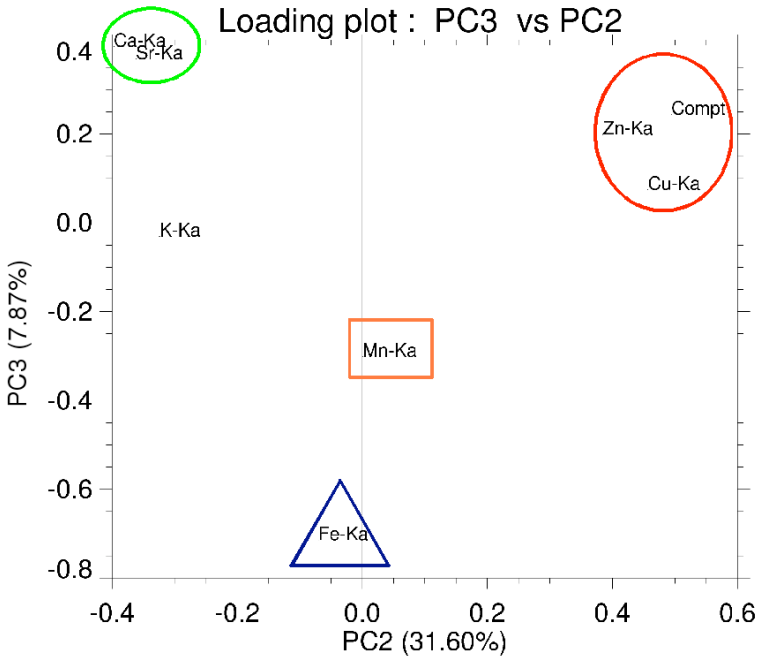

Figure 5.37: Loading plot 3rd PC versus 2nd PC.

5.6 Micro-XRF CT on *Daphnia magna*

5.6.1 Theoretical aspects

By combining micro-XRF with tomographic techniques, the element distribution on an arbitrary virtual section through the sample can be obtained without the need for destructive sample preparation (Schroer, 2001). In a simple model, the incident microbeam excites fluorescence radiation inside the sample along its path as shown in Fig. 5.38. The position of the microbeam with respect to the sample is given by the coordinate r in the (s, r) coordinate system. The origin of this coordinate system coincides with that of the (x, y) coordinate system that is fixed with respect to the sample and follows the rotation of the sample by ϕ. To obtain a single tomographic projection, the sample is scanned through the hard X-ray microbeam in translation along r. After each projection, it is rotated by an integer fraction of 360° and the next projection is recorded. The procedure is repeated until a full rotation is completed. At each step, the X-ray fluorescence that is excited along the microbeam is recorded by the energy-dispersive detector. Two ionisation chambers, one before and one after the sample, are used for normalisation and to measure the transmission, respectively.

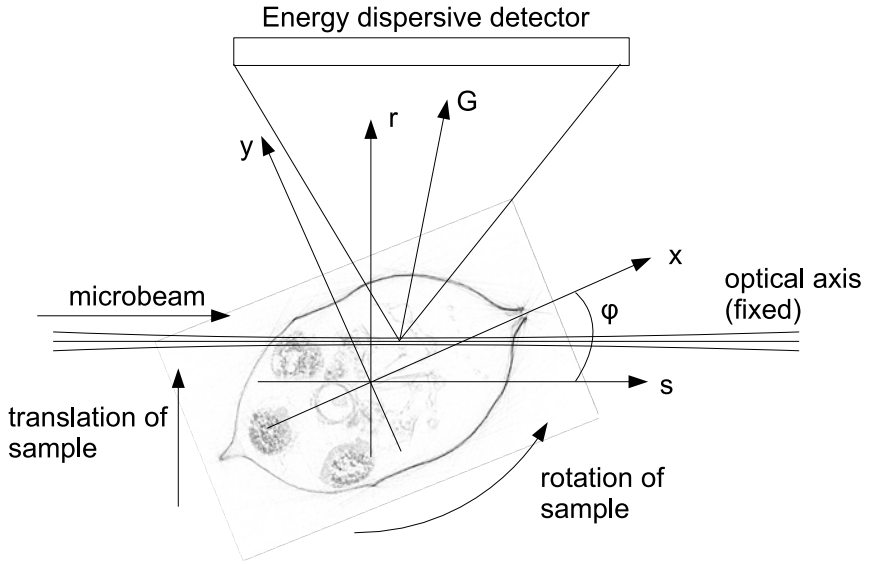

Figure 5.38: Experimental geometry for micro-XRF CT on *Daphnia magna*.

Neglecting all influences of absorption inside the sample, the detector signal is given by the line integral of the fluorescence coefficient $p(x, y)$ of the element under consideration:

$$I(r,\phi) = I_0 \frac{\Omega}{4\pi} \int \mathrm{d}s p(x(s,r), y(s,r)) \tag{5.12}$$

By neglecting absorption effects $I(r,\phi)$ is a Radon transform of $p(x,y)$ (Kak & Slaney, 1988). Usually, $p(x,y)$ can be found using standard tomographic reconstruction techniques, such as filtered backprojection. In general, however, the incident microbeam as well as the fluorescence radiation are attenuated inside the sample. Therefore, the previously shown Eq. 5.12 needs to be modified:

$$I(r,\phi) = I_0 \int \mathrm{d}s f(\phi,s,r).p(x(s,r),y(s,r)).g(\phi,s,r) \tag{5.13}$$

where

$$f(\phi,s,r) = exp(-\int_{-\infty}^{s} \mathrm{d}s' \mu_I(s',r)) \tag{5.14}$$

accounts for the absorption of the incident beam up to the point (s,r) and

$$g(\phi,s,r) = \frac{1}{4\pi}\int_{\Omega} \mathrm{d}^2\gamma exp(-\int_{G(\gamma,\phi,s,r)} \mathrm{d}g \mu_F(x,y,z)) \tag{5.15}$$

determines what fraction of the fluorescence radiation produced at the point (s,r) reaches the detector. $\mu_I(x,y)$ and $\mu_F(x,y,z)$ are the attenuation coefficient distributions inside the sample at the incident and fluorescence energy, respectively. For each direction γ inside the solid angle Ω spanned by the detector, the attenuation along the straight path $G(\gamma,\phi,s,r)$ from the point (s,r) pointing towards the detector in the direction γ is integrated. The attenuation coefficients $\mu_I(x,y)$ can be reconstructed from the transmission data collected by the ionisation chambers. Unfortunately, $\mu_F(x,y,z)$ is specific for each fluorescence line recorded and is not directly accessible by the experiment. Moreover, even when $\mu_I(x,y)$ and $\mu_f(x,y,z)$ are known, the modified Eq. 5.15 is more complicated than the inverse Radon problem. Biological samples have an advantage concerning this issue since they are composed of a low density matrix of lower Z elements and therefore it can be verified by the ionisation chamber values that the sample is practically transparent for the incident radiation. Therefore $f(\phi,s,r) = 1$ to very good approximation and may be neglected in Eq. 5.15. $g(\phi,s,r)$ on the other hand is not negligable for elements with low fluorescence energy (e.g. $Ca - K_\alpha$), even in a low density matrix with low absorbing elements. However, for elements with higher fluorescence energies (e.g. $Sr - K_\alpha$), no attenuation toward the far side of the detector is observed in the biological matrix. Therefore, also $g(\phi,s,r)$ can be neglected and the standard filtered backprojection may be used to reconstruct element distributions of elements which do not suffer from self-absorption effects.

5.6.2 Experimental results

Making use of the experimental set-up as previously described for the 2D micro-XRF measurements, micro-XRF CT was performed on *Daphnia magna*. The element analysis of a single dorsoventral (virtual) slice was envisaged. The height of the tomographic section was chosen

according to ecotoxicological relevance, namely at the height where gill tissue, gut, eggs and ovaria are coinciding. By using the single bounce capillary and the CCD camera without the micro beamstop, it was possible to accurately track the position of the microbeam on the tissue of interest. During a full fast rotation, the camera was also used to check whether the sample did not move out of the field of view of the CCD camera. If so, the goniometer was adjusted so that the sample stayed within the field of view. The data sets obtained from the tomographic (x,θ) scans (sinograms) were fitted and normalised in an identical manner as the data sets obtained from 2D micro-XRF on *Daphnia magna* and can be seen in Fig. 5.39. The recorded sinograms (see left column and upper right) correspond to 165 translation steps of 20 μm and 180 rotation steps of 2 °, with a measuring time of 1 s through the region of gut, gill tissue and eggs. The reconstruction of the displayed tomographic data sets was done via a filtered back-projection algorithm, without using self-absorption corrections (Russ, 1995). Self-absorption effects are negligable due to the low density matrix of the organic material, even for low energy lines such as $Ca-K_\alpha$ (E_{K_α}=3.69 keV). Several methods exist to correct for the attenuation of both primary and fluorescent X-rays within the sample matrix, but the use of these algorithms was not explored in this work (Golosio *et al.*, 2003). The distributions in the reconstructed cross-section (middle column) agree with the previously measured conventional 2D micro-XRF scanning results: a Ca-rich exoskeleton, Zn enrichment in eggs and gut and Fe enrichment in the osmoregulatory tissue (epipodites). The Zn cross-sectional data also clearly show that the Zn concentration in the gut epithelium of the non-exposed *Daphnia magna* is higher than the concentration in the gut lumen, an observation that could not be made using conventional 2D micro-XRF (projection) maps. It would be instructive to apply the same computed tomography technique to the Zn exposed *Daphnia magna* to determine whether the Zn enrichment detected in the gut region is actually due to accumulation in gut epithelial tissue or whether it is due to Zn that is present in the gut lumen. Fig. 5.39 also confirms the lower concentration of Ca in the back of the carapax as compared to the front part, which was already concluded from the cluster spectra obtained from laboratory and synchrotron 2D micro-XRF.

Fig. 5.40 shows the histogram of the sinograms shown in Fig. 5.39. A clear peak for Ca can be observed indicating an average value for the exoskeleton, whereas the distribution for Zn and Fe seems to be more diffuse. Interestingly, when the sinograms are reconstructed and the histogram of the single cross sections are visualised (Fig. 5.41), three maxima can be observed. One would think that these correspond to the average intensity of Ca, Fe and Zn fluorescent lines within the different tissues, but these maxima represent the noise within the reconstruction and the actual information on the element distribution is hidden deeper in the histogram. By setting the display threshold above these maxima, the reconstruction seen in Fig. 5.39 show a tremendous increase in quality.

As shown earlier by the loading plots of the PCA analysis, the 2D element distributions

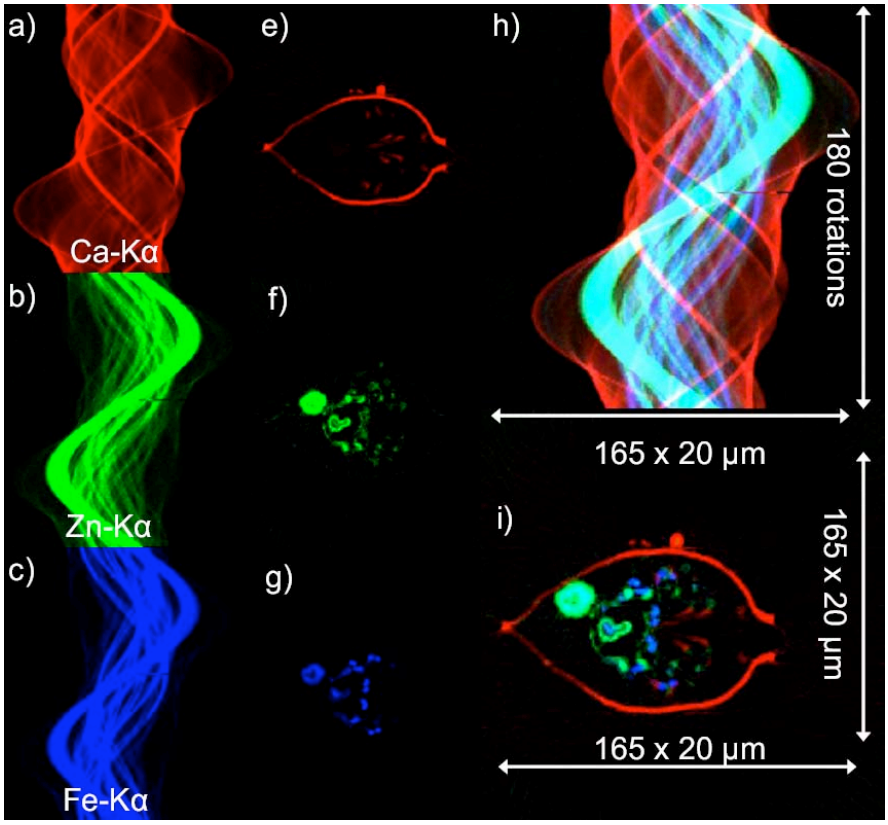

Figure 5.39: element sinograms and reconstructed element distributions corresponding to Ca, Zn and Fe, respectively.

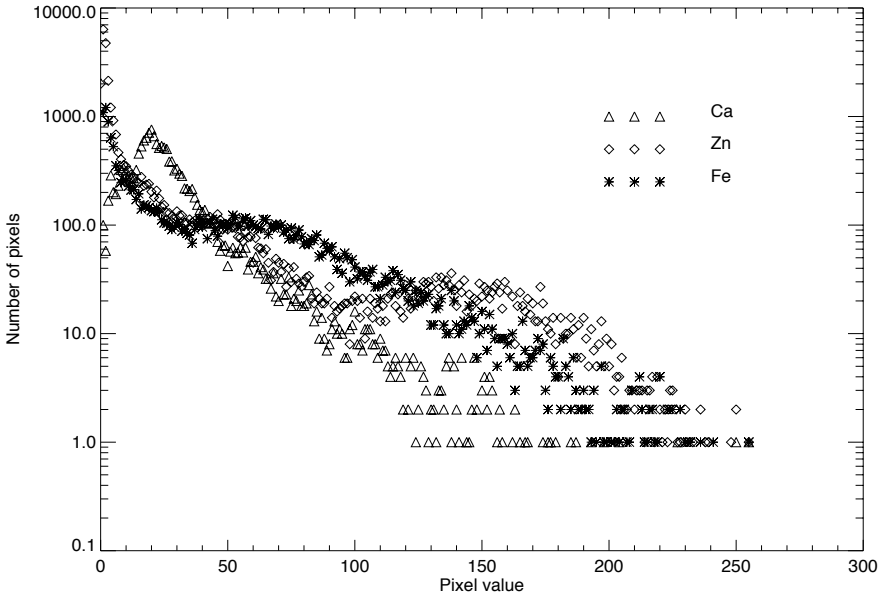

Figure 5.40: Histogram of the composite sinogram dataset.

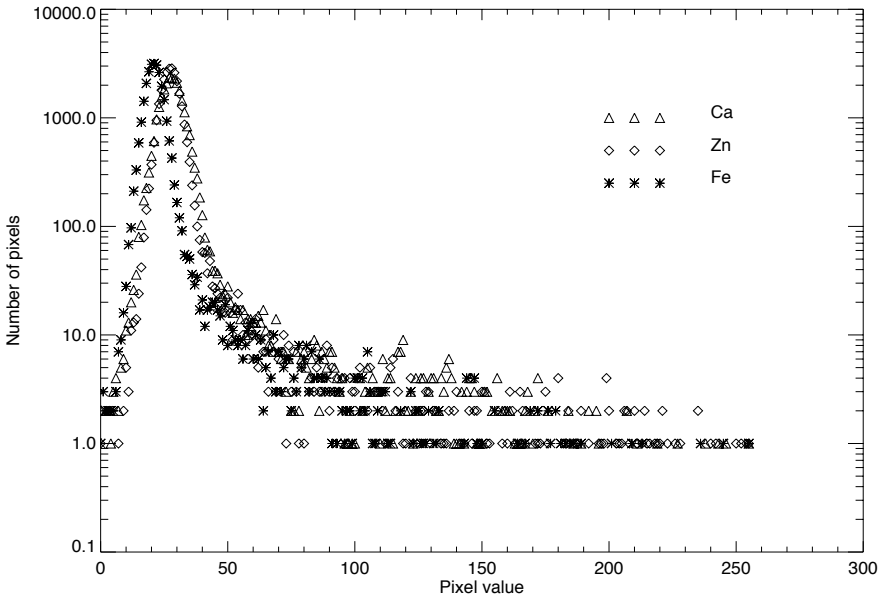

Figure 5.41: Histogram of the composite CT dataset.

of Ca and Sr are closely correlated, as expected. A basic way to explore such element correlations in greater detail is to plot the X-ray intensity pertaining to one element against the intensity obtained for another throughout the series of pixels that constitute the image. In case two elements follow the same distribution throughout the sample, a linear correlation becomes visible in such correlation plots. However, even in case of homogeneous samples, self-absorption effects of the fluorescent radiation in the sample cause these correlation graphs to differ significantly from straight lines as described in Somogyi *et al.* (2000). In this aspect, a comparison between the correlation plot of the 2D element distributions and the CT results for Ca and Sr provide us with a valuable tool to verify to which extent the absorption effects are present. Fig. 5.42 illustrates such a scatter plot of the square root of the $Ca-K_\alpha$ intensity (in order to correct for the Poisson counting statistics) versus the square root of the $Sr-K_\alpha$ intensity for the 2D element distributions and the CT element distribution. One can observe a similar slope for both curves, although a slightly higher slope for the 2D element distributions occurs at higher count rates, indicating only a minor presence of self-absorption effects for the $Ca-K_\alpha$ lines, thus strengthening the hypothesis that a first order approximation for quantifying the element maps shown in Fig. 5.24 is justified.

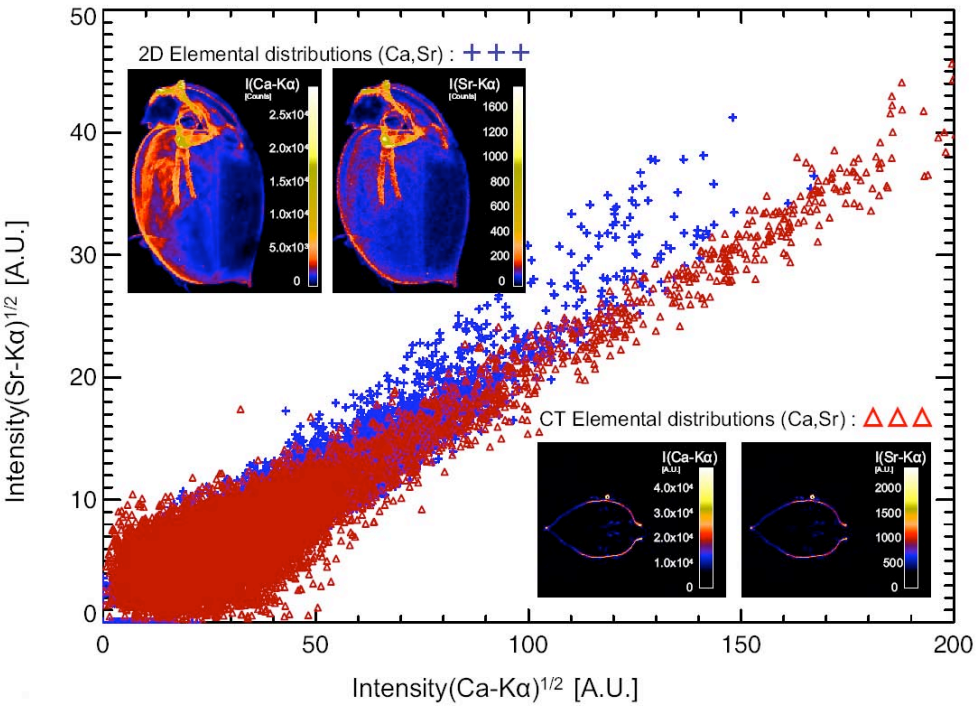

Figure 5.42: Correlation between the $Ca-K_\alpha$ and $Sr-K_\alpha$ signals of the unexposed *Daphnia magna*. Correlation plot was generated for the 2D integration maps and for the CT reconstructed maps.

5.6.3 Improved dataquality of tomography XRF scans using FFT

When performing XRF tomography scans on larger samples, the sample time often has to be limited in order to avoid experiments with too long duration. These small measuring times, often in the sub-second time range, result in considerable noise in the sinograms, which after tomographic reconstruction give rise to line artefacts. The possibility of removing this background noise in the sinograms with image filters is discussed in this section. Many image filters, applied to remove noise (or to sharpen, extract features) are based upon transformations of the original image into another domain. These domain transformations have different advantages: they may avoid very computationally expensive processes performed on an image in the original spatial domain, provide additional information about an image (determine which pixels contain more important information and whether repeating patterns occur) and offer compression benefits. The Fast Fourier Transform (FFT) process is such a domain transformation process and the basis for many filters used in image processing. It transforms an image between spatial and frequency domains. The original and most common representation of a pixel's value and location is spatial, where it appears in three dimensions (x, y and z). Pixel value and location in this space is usually referred to by column (x), row (y), and value (z), and is known as the spatial domain. The FFT decomposes an image into sines and cosines of varying amplitudes and phases. In this domain, pixel location is represented by its horizontal x- and vertical y-frequencies and its value is represented by an amplitude. This image information in the frequency domain shows how often patterns are repeated within an image. Low frequencies represent gradual variations in an image: they tend to contain the most information because they determine the overal shape or pattern in the image. High frequencies correspond to abrupt variations in the image. They provide detail in the image, but they are often contaminated by the spurious effects of noise. Masks can be easily applied to the image within the frequency domain to remove noise. When the image is not manipulated while it is in the frequency domain no information is lost when using the FFT. Unlike some domain transformations, all image information is retained when transforming data to and from the frequency domain.

The example shown in Fig. 5.43 uses IDLs (Interactive Data Language, ITT Visual Information Solutions) FFT function to remove noise from a sinogram using a mask as filter upon an image in the frequency domain. The sinogram corresponds to the $Mn - K_\alpha$ signal of the unexposed *Daphnia magna*. The first display contains the original image and under the original image its forward Fourier transform is given. The data type of the array returned by the FFT function is complex, which contains real and imaginary parts. The real part is the amplitude, and the imaginary part is the phase. In image processing, we are more concerned with the amplitude, which is the only part represented in the surface and displays of the results of the transformation. However, the imaginary part is retained for the inverse transform back into the spatial domain. In most cases though, the imaginary part will look the same as the

real part. The results of the FFT function are shifted to move the origin $(0, 0)$ of the x and y frequencies to the center of the data. Frequency magnitude then increases with distance from the origin. If the results are not centered, then the negative frequencies appear after the positive frequencies because of the storage scheme of the FFT process. If the image does not contain any background noise, the rest of the data frequencies are very close to zero. However, the results of the FFT function have a very wide range: the range of values from the peak to the high frequency noise is extreme. An inititial display may not show any variations from zero, but a smaller range will show that the image does actually contain background noise. We used a logarithmic scale to retain the shape of the surface, but reduce its range. Since the logarithmic scale only applies to positive value, the power spectrum was computed, which is the absolute value squared of the transform. The noise is very evident in the transform of the sinogram. The transformation in Fig. 5.43 shows the log-scaled power spectrum as an image. The most colored pixels near the center of the display represent the low frequency peak of information-containing data. The noise appears as random lighter pixels within the image. A surface representation of the power spectrum is shown in Fig. 5.45 and helps to determine the threshold necessary to remove the noise from the image. In the surface representation, the noise appears random and below a ridge containing the spike. The ridge and spike represent coherent information within the image. A mask is applied to the transform to remove the noise: the image is shown next to the fast Fourier transform of the original image in Fig. 5.43. In the upper right corner of Fig. 5.43 the inverse transform is applied, resulting in an improved sinogram. The filtered backprojection algorithm is applied to the original sinogram and to the Fourier filtered sinogram at the lower part of Fig. 5.43 which reveals a significantly improved reconstructed element distribution of *Daphnia*.

In order to verify whether the principle is generally improving on the quality of reconstructed sinograms, the same procedure was repeated for different element sinograms. The most important observed trends can be seen in 5.44. For P, the quality of the exoskeleton structure is improved. The presence of Cl in the egg is more clear to observe, also small improvements of the presence of Cl in the gut can be seen. For K, an element with much better statistics than all other presented elements in Fig. 5.44, the ray artifacts are removed, although a blurring of the image is more present. Similar behaviour is observed for elements with good statistics (Ca, Fe, Zn). The best results were obtained for the elements Br and Mn, elements with better elemental yields than S, Cl but present in much lower concentration. Ray artifacts are again well removed, for Mn a marked presence is seen in the gut and egg as for Br a marked presence is observed in the egg and in the softer tissues.

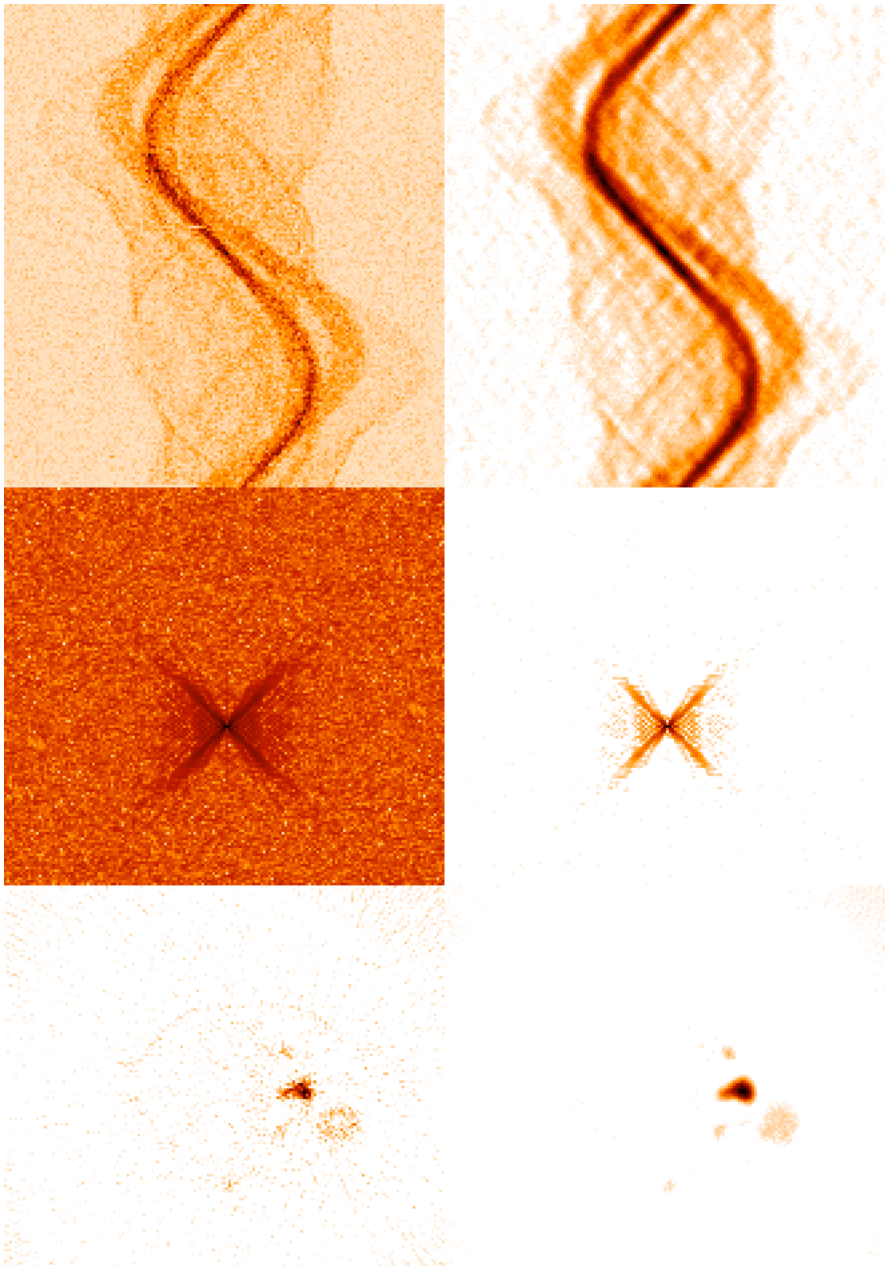

Figure 5.43: Illustration of the Fourier-filtering procedures. From left to right: original sinogram, filtered sinogram, frequency domain of original sinogram, filtered frequency domain of original sinogram, backprojection of original sinogram, backprojection of filtered sinogram.

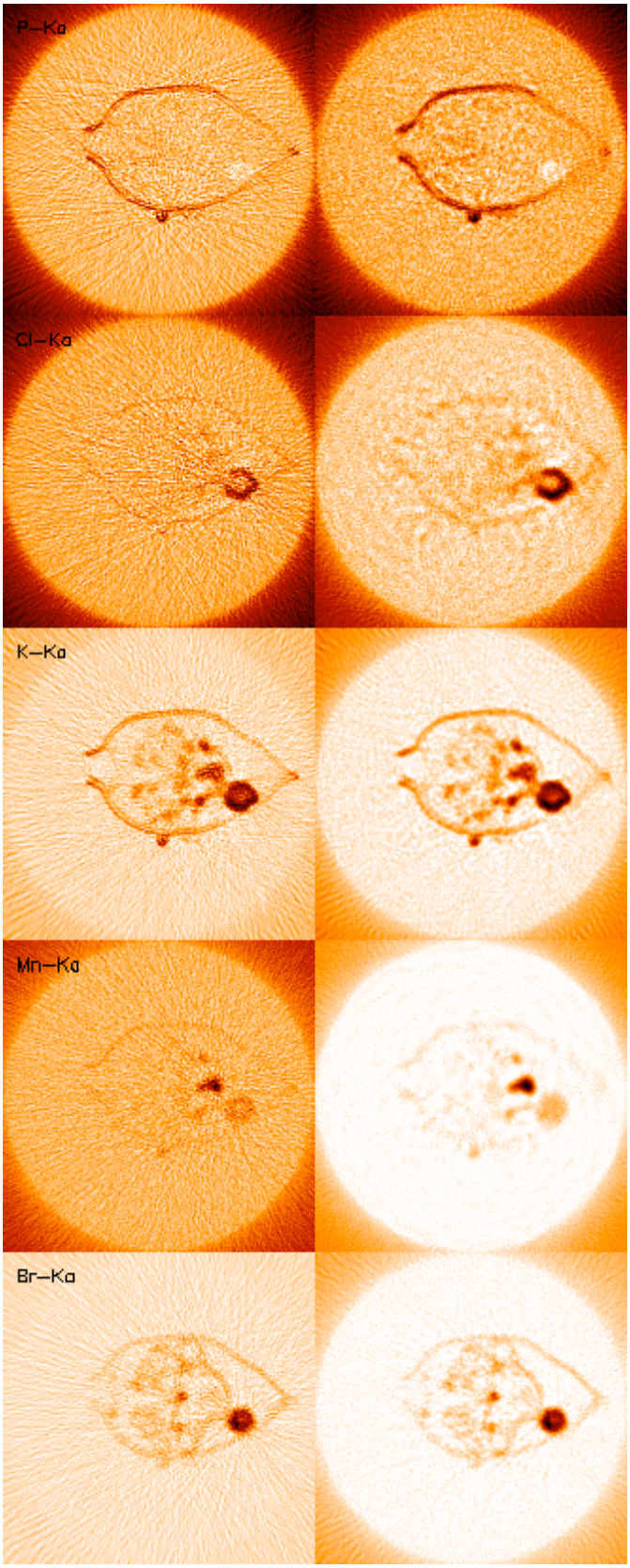

Figure 5.44: Reconstructed element distributions of P, Cl, K, Mn and Br within *Daphnia magna*. The left column is a backprojection from the raw element sinograms whereas the right column is a backprojection of the Fourier filtered element sinograms.

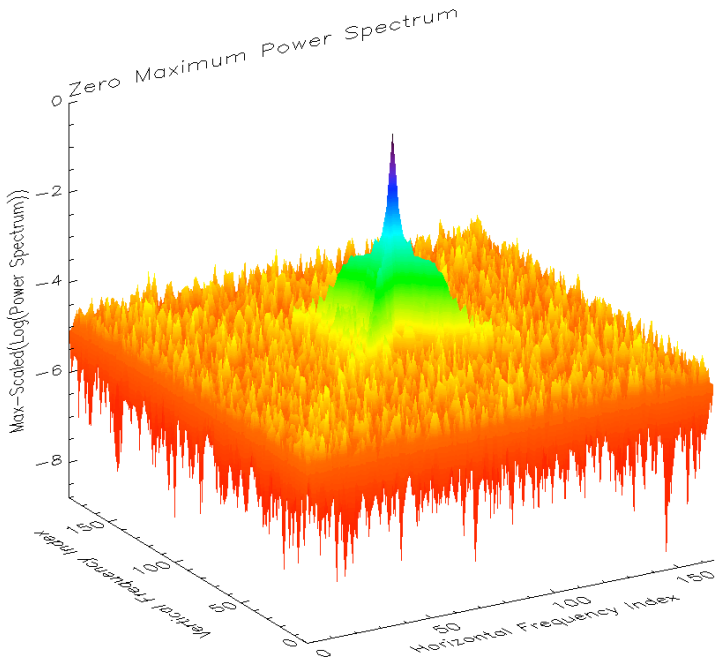

Figure 5.45: 3D visualisation of the frequency domain of the original sinogram.

5.7 Cryogenic 2D/CT micro-XRF on *Daphnia magna*

5.7.1 Introduction

As mentioned earlier, a potential risk of element redistribution during the sample preparation is difficult to verify experimentally and therefore cannot be excluded in previous experiments. The use of a cryostream in protein crystallography in which the sample is shock frozen and maintained at a temperature of about 80 K during the measurement is very common at synchrotron sources. Surprisingly, even though such cryostream equipment is mobile, it has rarely been installed at beamlines aiming at micro-XRF on biological samples. In this section, we demonstrate the use of a cryostream set-up installed at beamline L for 2D/CT micro-XRF.

Since frozen hydrated samples show higher absorption of low energy fluorescent lines (e.g. K, Ca, Fe) and tomography experiments can benefit from a reduced scanning time, the potential of a dual detector detector set-up was explored to reduce scanning time, study self-absorption effects and provide new insights on an ecotoxicological experiment studying *Daphnia* with different metal tolerance. During these experiments, dual detector XRF cryotomography was illustrated at Beamline L as a proof of principle, revealing the element distribution within a virtual cross-section of a fully hydrated *Daphnia magna*.

5.7.2 Implementation of cryostream and detectors

The experiments were performed at Beamline L of the DORIS III storage ring as previously described. Fig. 5.46 shows an image of the experimental set-up with cryostream (Oxford Cryosystems, 700 series). The SR-XRF spectra were measured under a 90° detection angle relative to the incident beam using 2 Radiant Vortex-EX silicon drift detectors (SDD), coupled with a XIA digital signal processor for pulse processing. Silver detector collimators of sufficient solid angle were used in order to detect the fluorescent radiation emerging from the full beam path within the sample. Both detectors were covered with ultralene foil to protect them from ice deposition originating from the cryostram nozzle. Both detectors were gain optimised and their sample distance was adjusted to provide an identical element spectrum using NIST SRM 1577B (Bovine liver). Since icing can occur on objects outside the path of the laminar flow, a single bounce capillary was again used as focusing optic with a long working distance of 5 cm.

The working principle of the cryostream is illustrated in Fig. 5.47. Liquid nitrogen is drawn up from an unpressurised dewar by the action of a diaphragm pump. By using a diaphragm pump in the nitrogen gas circuit, the gas pressure at the sample is the same as in the dewar. This means that it is safe to replenish the supply of liquid nitrogen in the dewar at any time without any fluctuations in gas temperature. The liquid passes through a flexible vacuum insulated transfer line, into the cryostream coldhead. Once inside the cryostream coldhead, the liquid nitrogen passes through a heater, which evaporates most of the liquid into vapour. This vapour then flows along one path of the heat exchanger. The flow rate of the gas from the pump is then regulated by a variable flow controller. This gas flows back into the cryostream coldhead where it is re-cooled along the second path of the heat exchanger. The gas temperature is then regulated before entering the nozzle of the cryostream. The gas then flows along the isothermal nozzle and out over the sample. A laminar gas flow of 5 L/min insures a temperature of 100 K at an obligatory 8 mm distance from the cryostream nozzle. This means that a 60 l dewar will last for up to 4 days, so it can easily be run over long measuring times without refilling. The temperature range is available from 80-400 K with a stability of 0.1 K. The typical gas temperature in function of the sample distance from the nozzle is given in Fig. 5.48. Within a range of 20 mm, the temperature remains very close to 100 K (Oxford Cryosystems, 2009a; OxfordCryosystems, 2009; Oxford Cryosystems, 2009b).

5.7.3 Experimental results

Comparison between chemically fixed and frozen samples

Fig. 5.49 shows a comparison between element distributions of Zn, Cu, Br and Compton scattering of a cryofrozen (left) and a chemically fixed (right) *Daphnia magna* using a single detector. Deformations of the tissue strucure in the chemically fixed sample are present,

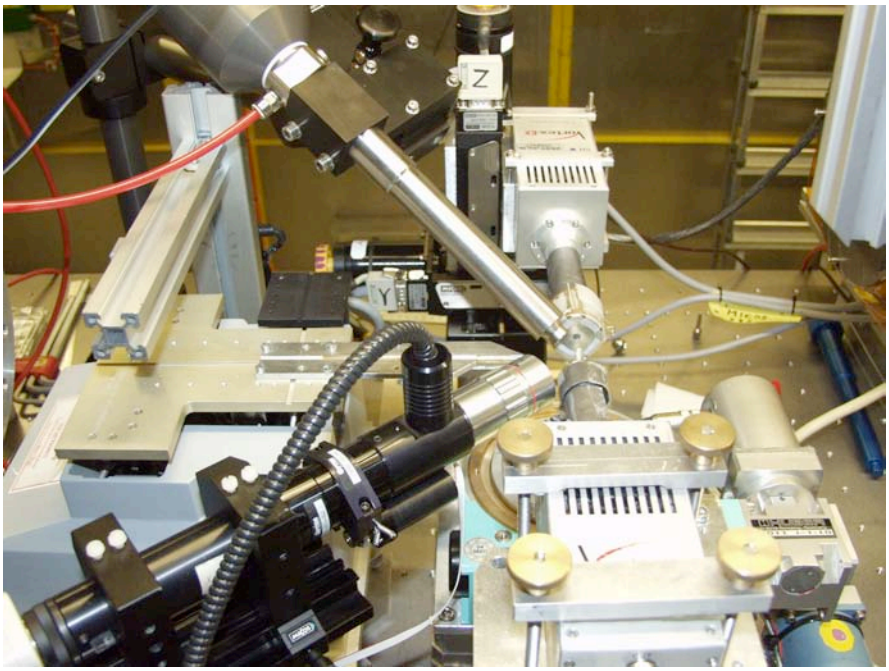

Figure 5.46: Detail on the experimental table of the dual detector set-up with cryostream. Reproduced from Oxford Cryosystems (2009a).

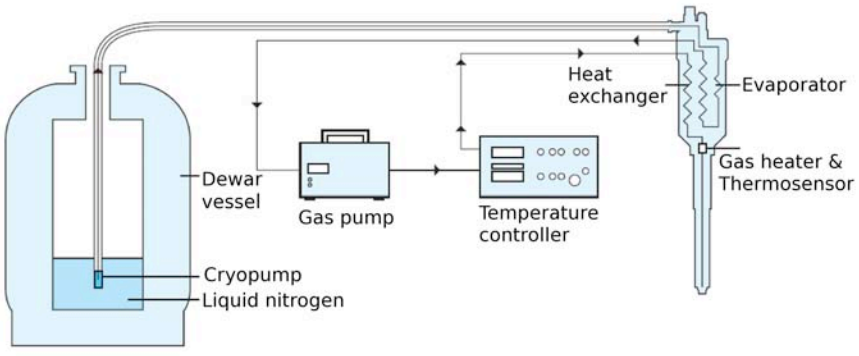

Figure 5.47: Working principle of the 700 series cryostream cooler. Reproduced from Oxford Cryosystems (2009a).

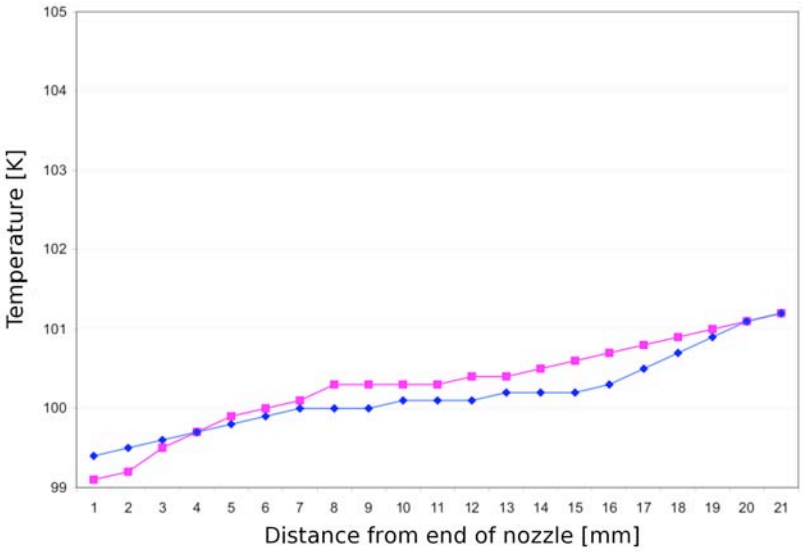

Figure 5.48: Gas temperature versus distance from end of nozzle (at a set point of 100 K). Reproduced from Oxford Cryosystems (2009a).

such as a more opened exoskeleton and less clearly resolved tissue structures. However, the measured Zn intensities appear to be comparable for both samples, with exception from upper gut and exoskeleton borders. The direct comparison between cryogenic (approximating the native state of the organism) and HMDS based sample preparation methods confirms the validity of our earlier measurements with respect to the target element Zn. Cu however, seems to show a significant leaching from the upper and lower part of the gut. A possible explanation could be the displacement and accumulation of metals at specific sites during the drying procedure. The Br distribution features very similar count rates in the regions of the antennae and egg, although a higher intensity can be noted for the gill tissue of the dried sample. A higher Compton scattering in the frozen sample can be observed due to the fact that the cryofrozen sample contains mainly water, having a higher density in comparison with the dried sample. An interesting finding is that the Compton map for the cryomapping shows a very uniform distribution suggesting that metals are distributed in a mainly water containing matrix with a uniform density. In the Compton map of the dried sample, tissues become identifiable and are also revealing a very similar density, whereas areas within the sample which were mainly liquid are replaced by air, e.g. the brood pouch and gill tissue, given the low Compton scattering of these areas. Metals present in this liquid could have been relocalised and/or removed during the fixation procedure. Since the changes in metal distribution between chemical fixation and cryogenic conditions are only studied at a resolution level of 10-20 μm, problems which likely to occur at the submicron level are not encountered: (1) due to the size of *Daphnia magna*, a real vitrification is not possible,

given the fact that amorphous ice can only be formed until a depth of approximately 300 μm. However, ice crystal formation during insertion of the sample into the cryostream should not have an effect on the metal distributions on the scale which is resolved by a microbeam (2) vibrations and temperature drift issues induced by the use of the cryostream are less critical during scanning type of analysis on the 10-20 μm level. Because of these problems, cryogenic analysis on the submicron level would require the use of dedicated cryostat set-ups.

Dual detector XRF cryomapping

Fig. 5.50 shows the results when performing dual detection 2D micro-XRF analysis under cryogenic conditions. The left column shows the element maps built from the spectra collected by the SDD located on the left with respect to the incident beam (looking at the front part of the sample), while the middle column shows the element maps built from the spectra collected from the SDD on the right (looking at the back part of the sample). The element maps are composed of 158 $\times$ 130 pixels corresponding to a step size of 20 μm and a real time of 0.6 s. The dynamic scanning mode in which the sample is continuously moving across the microbeam resulted in a reduced scanning time. One clear advantage of the dual detector set-up is the partial compensation of self-absorption effects which strongly influence the lower-Z elements. For example, $Ca - K_\alpha$ fluorescent photons originating from the edge of the sample are unable to travel through the entire organism towards the detector on the far-side, however, they do escape from the sample towards the other detector. Surprisingly, also $Fe - K_\alpha$ fluorescence is partially absorbed, e.g. in the region of the eggs for the left detector and in the region of the gut for the right detector. For elements such as Cu, Zn, Rb and Sr no obvious self-absorption could be observed. However, also these elements benefit from a dual detector set-up since the collected fluorescent signal is effectively doubled, which in turn allows the reduction of scanning time by a factor of 2 per sample. The element distributions originating from the left and right SDD detectors can be summed to provide element maps for metals with low fluorescent energies (e.g. K, Ca), which are to a large extent corrected from self-absorption effects occurring in the sample.

Fig. 5.51 shows the element distributions of Zn from several *Daphnia magna*. Individual point spectra were collected from both SDD detectors. All individual element maps were scaled with respect to the same color bar, indicating the Zn intensity in $counts/s$. A histogram of the dataset was used to remove hot spots from the element maps which prevented an adequate scaling and comparison of the samples. Per exposure condition and genotype of organism, two replicates were measured (replicate A and replicate B). It can be observed that the variation in metal distributions between differently exposed samples is higher than the variation between replicates of the same exposure. A higher Zn concentration could be observed in the region of gut, eggs, gill tissue and hepatopancreas when comparing all exposed organisms with the organisms from the control medium. Interestingly, the metal sensitive clone $O22$ reveals a

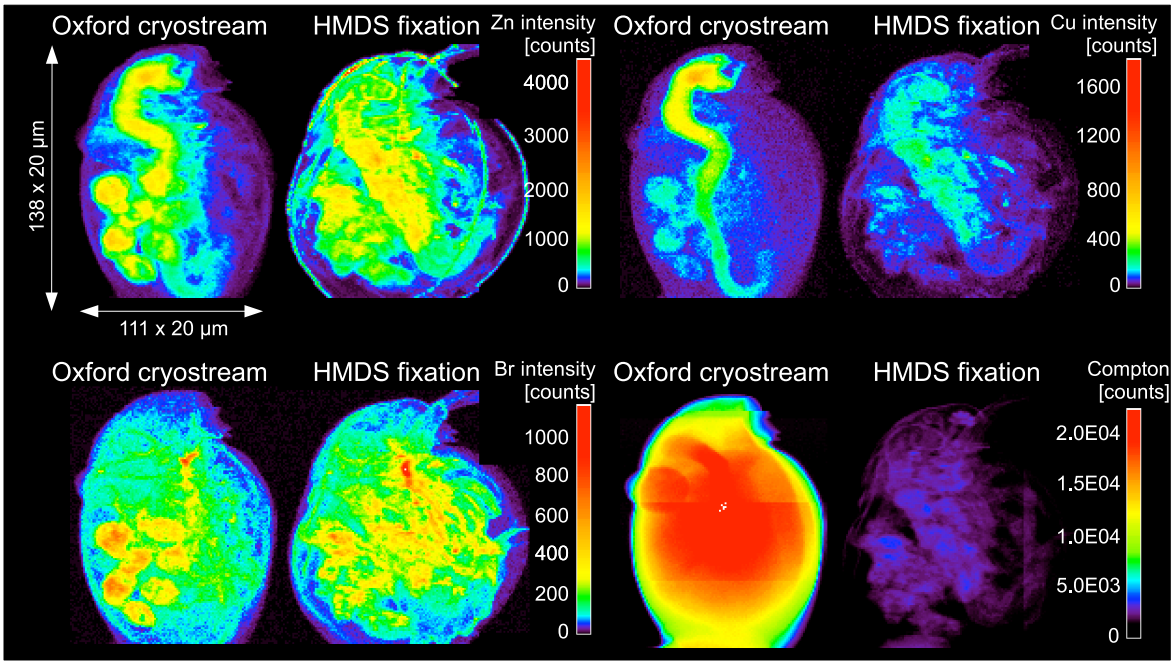

Figure 5.49: Element distribution of Zn, Br, Cu and Compton scattering. Comparison between a chemically fixed sample and a sample under cryogenic conditions.

higher concentration of Zn in these areas, which can be explained by a higher uptake of Zn or a lower elimination of Zn from the more metal sensitive clone $O22$.

Dual detector XRF cryotomography

Fig. 5.52 shows element sinograms obtained from performing dual detector cryotomography on *Daphnia magna*. When only a single detector is available, rotation of the sample is necessary over the full 360°. However, for a symmetric dual detector arrangement shown in Fig. 5.52, a rotation angle of 0-180° is sufficient, decreasing either the measuring time, or improving the reconstructed resolution due to the finer angular step size that can be chosen for a given total analysis time. In our experiment, a line scan of 120 steps of 20 μm was repeated for 180 views with a rotation step size of 1°. The first row shows the element sinograms obtained from the left detector, whereas the second row shows the sinograms obtained from the right detector. Similar to the 2D cryomaps performed on *Daphnia magna*, $Ca - K_\alpha$ fluorescence could not reach the detector when the signal originates from a position further than halfway in the sample. However, these element sinograms can be summed, thus providing an element sinogram which is to a large extent corrected for this self-absorption effect, as can be seen in the last row of Fig. 5.52. An RGB representation reveals to a large extent complementary element distributions of Ca, Cu and Rb within a single glance. After applying a conventional filtered backprojection algorithm on the element sinograms,

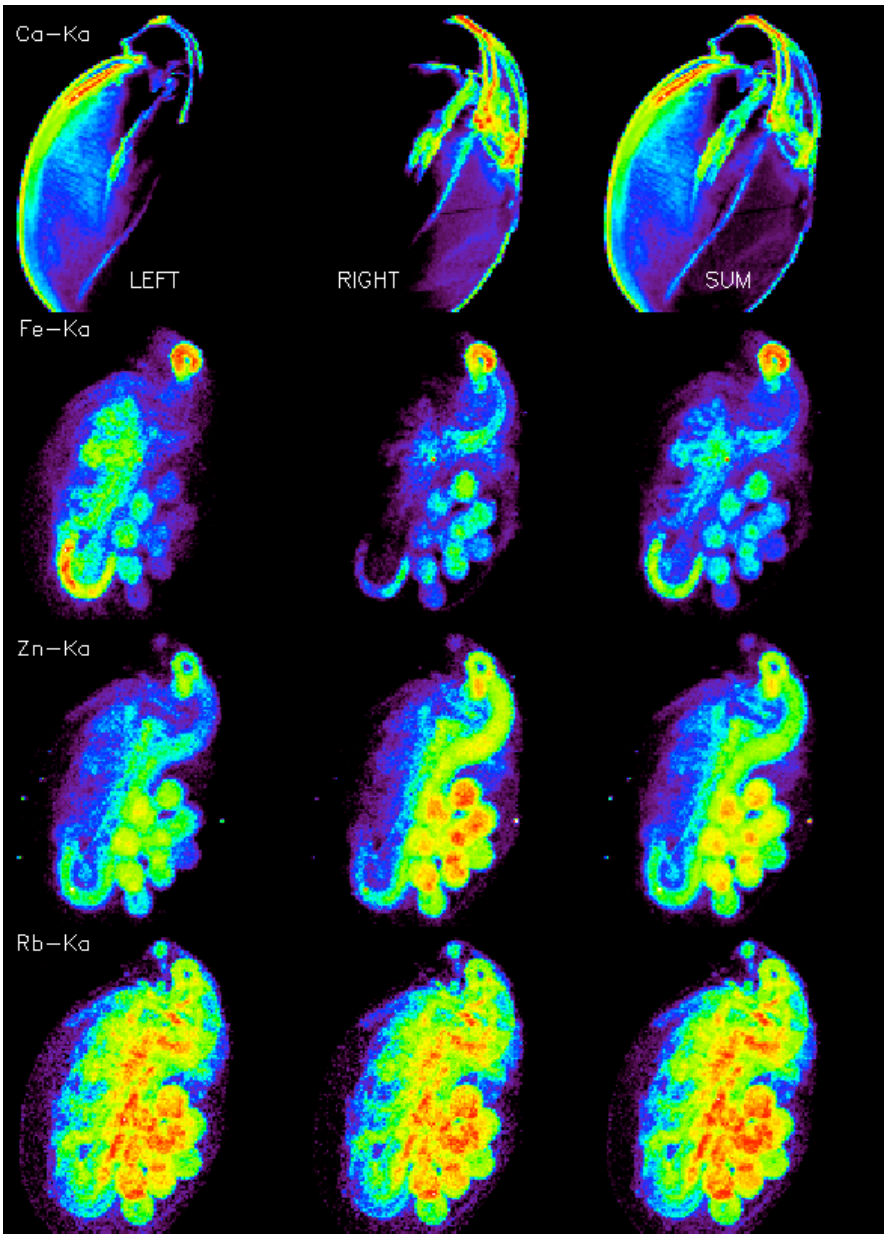

Figure 5.50: Separate and summed element distributions within a cryogenic frozen *Daphnia magna* as collected by both silicon drift detectors.

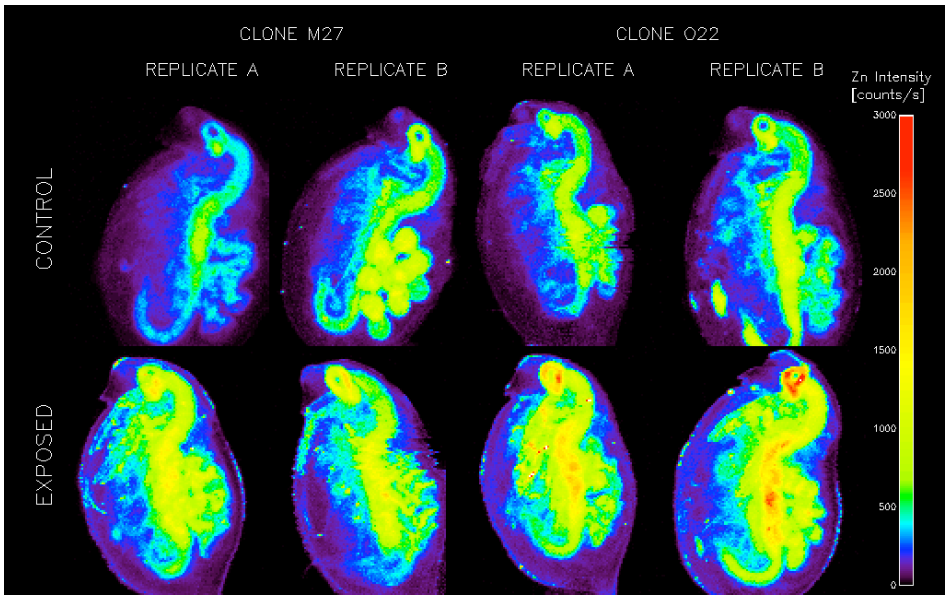

Figure 5.51: Element distributions of different metal sensitive *Daphnia magna* genotypes (M27 and O22) under different exposure conditions (control medium and 200 $\mu g/L$ Zn) obtained under cryogenic conditions.

the element distributions within a single virtual cross-section through the sample could be reconstructed, as shown in Fig. 5.53. When the sinograms originating from the individual detectors are reconstructed, approximately only half of the Ca containing exoskeleton can be reconstructed. However, the summed sinograms provide a full reconstruction for the Ca distribution within the sample. Also here, some absorption effects can be observed for the virtual cross-section of Cu and Zn which disappear when using the information originating from both detectors.

5.8 Absorption micro-CT on *Daphnia magna*

5.8.1 Theoretical aspects

In case of absorption micro-CT experiments, the physical parameter which is providing the information about the internal micro-structure of the sample is the X-ray linear attenuation coefficient μ. This coefficient is the product of the photon mass attenuation coefficient $\mu/\rho(cm^2/g)$ and the mass density $\rho(g/cm^3)$. The attenuation coefficient μ depends on the local composition of the material of the sample. Furthermore the mass attenuation coefficient depends on the energy of the X-rays: the higher the energy of the photon, the smaller the attenuation in the sample (Masschaele *et al.*, 2007). The resolution of a CT-system is ultimately defined by the size of the X-ray source and the resolution by the detection system.

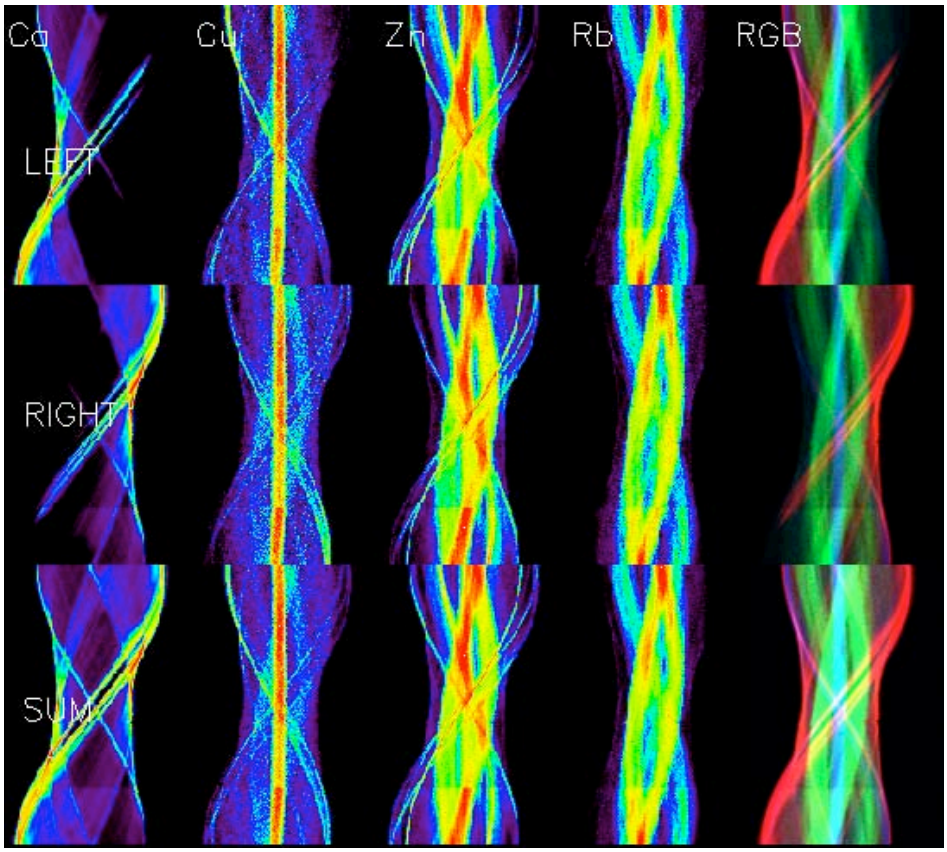

Figure 5.52: Separate and summed element sinograms of Ca, Cu, Zn and Rb obtained from a cryogenically frozen *Daphnia magna*. An RGB representation reveals the combined presence of Ca, Cu and Rb respectively.

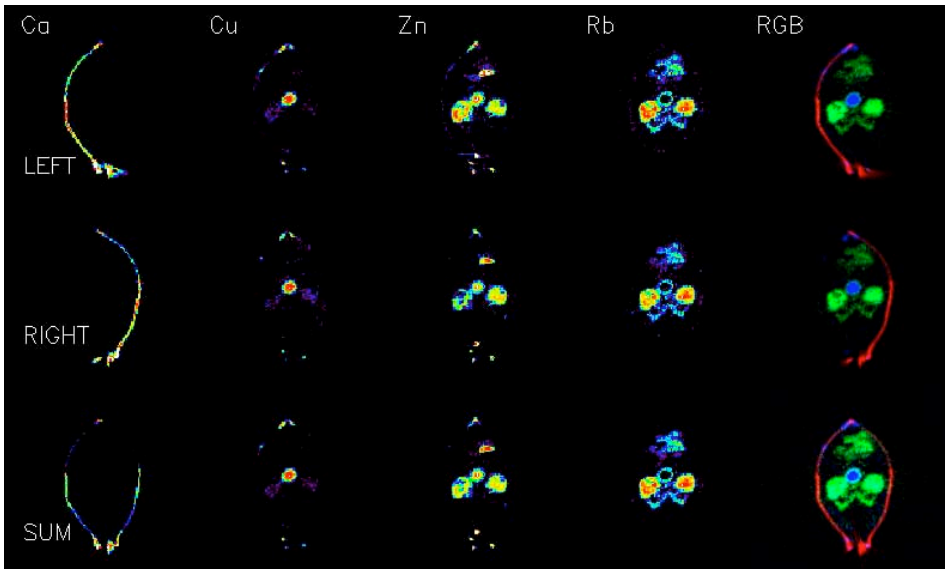

Figure 5.53: Reconstructed cross section of the separate and summed element sinograms from both detectors. An RGB representation shows the complementary presence of Ca, Cu and Rb respectively.

Because these components have a finite size/resolution, the resolution of the imaged object is limited. Eq. 5.17 expresses the resolution that can be achieved within the image (Cnudde, 2005):

$$R = \frac{d}{M} + (1 - \frac{1}{M})s \tag{5.16}$$

with R the achievable resolution in the object, s the spot size of the X-ray source, d the resolution of the detector and M the magnification, which is related to the position of the object:

$$M = \frac{d_s + d_d}{d_s} \tag{5.17}$$

where $d_s + d_d$ represent the total source-detector distance, with d_s being the source-object distance and d_d the object-detector distance. Consequently, the higher the d_d/d_s ratio (i.e. the achieved magnification), the higher the achievable instrumental resolution for a given detector resolution and source size. Since typically $d >> s$, large magnification (M) values are necesssary, in which case the ultimate limiting factor in resolution becomes the source size s. However, optimal resolution can only be achieved when the object can be positioned very close to the X-ray source and is consequently limited to small objects.

5.8.2 Laboratory micro-CT set-up at UGCT

The entire set-up is built on a large optical table to obtain the highest possible stability. Due to the flexible set-up (e.g. various detectors and X-ray tubes are available), it is possible to obtain the highest quality and best signal-to-noise ratio of the reconstructed images for each type of sample. The experimental set-up is shown in Fig. 5.54. The X-ray tube is a state-of-the-art FXE-160.50 dual head open type source from Feinfocus. Open type means that one can open the tube to clean it or to replace filaments or targets. The dual head means that two tube heads are available, a high power (150 W) directional head and a nanofocus transmission head. For the nanofocus transmission head, the power is adapted according to the scan type: 1 W for nanofocus, max. 3 W for microfocus and max. 10 W for high power. The minimal sample distance is 0.2 mm and a cone angle of 170 ° is present. A resolution of down to 0.3 μm can be achieved.

The sample manipulator is an XYZ-θ CT system. The linear spindle modules are using Berger-Lahr Intelligent Compact Drives. The controller is integrated inside the stepper motor housing. The rotation motor is an ultra precision rotation stage from MICOS (UPR-160F AIR). To reach sub-micron resolution CT scans, the rotation stage requires low wobble ($<$ 2.5 μrad) and eccentricity ($<$ 0.1 μm) which can be guaranteed by high precision toroid air bearings. The load capacity is 5 kg. The air pressure is 4.5 bar and is filtered for oil, particles and humidity. For nano-CT a PI miniature XY piezo stage is used in order to place the sample exactly on the rotation axis. The XY stage has remarkable features: its resolution is 50 nm, travel range 20 mm, acceleration of 20 g and a load capacity of 500 g.

X-ray detectors are used to record the attenuation information along lines through the object. To detect the transmitted X-rays they have to be converted to visible light with scintillation materials like Gadoliniumoxysulphide ($GdOS : Tb$) or CsI crystals. The visible light from the scintillator is in turn registered by CCD camera's, CMOS-flat panels or amorphous Si-flat panels. Biological samples are typically scanned at low kV settings to obtain high contrast projections.

5.8.3 Experimental Results

Digital radiographs of *Daphnia magna* were taken from different orientations by rotating the sample along the scan axis from 0 to 360°. The laboratory μ-CT experimental set-up was composed of the RadEye HR CMOS Gadox screen (1200 $\times$ 1600 pixels, 22 μm pixel size) and a Feinfocus transmission tube (160 kV, 900 nm focal spot size). In Fig. 5.55, a single radiograph of *Daphnia magna* is shown. During the tomographic scan, 800 projections, 20 flat field images and 10 dark current images were processed into a stack of CT-slices with the Octopus package. In Fig. 5.56, one of the individual slices is shown. The 3D rendering was realised with VGstudioMAX (Volume Graphics GmbH, Heidelberg, Germany). Fig.

Figure 5.54: Absorption Tomography set-up at UGent.

5.57 shows a final reconstructed dataset. The different internal organs such as intestine, gill tissue, eggs, compound eye and muscle fibers are clearly visible. Unlike SEM, the complete 3D morphology of the sample can be investigated. This reveals not only a good surface quality in our case, but also an excellent preservation of the internal structure/morphology of the sample due to the HMDS based preparation method at a resolution level of $\approx 3\ \mu m$. Since the laboratory micro-CT measurement was performed after SEM and SR micro-XRF analysis, it should be noted that the morphology of the sample remained intact as a result of these experiments.

5.8.4 Combination with 2D/CT micro-XRF

For one *Daphnia* sample, the 2D composite RGB (Ca, Fe, Zn) element maps were overlayed onto a 3D generated absorption image as shown in Fig. 5.58. Since the format of the images is different, first a technique described in IDL as warping was used. In image warping, corresponding control points (selected in the input and reference images) control the geometry of the warping transformation. The arrays of control points from the original input image, X_i and Y_i, are stretched to conform to the control point arrays X_0 and Y_0, designated in the reference image. Image warping in IDL is a three-step process. First, control points are selected between two displayed images. Second, the resulting arrays of control points, X_i, Y_i, X_0 and Y_0 are then input into one of IDL's warping routines. Third, the warped image resulting from the translation of the X_i, Y_i points to the X_0, Y_0 points is displayed. A blended

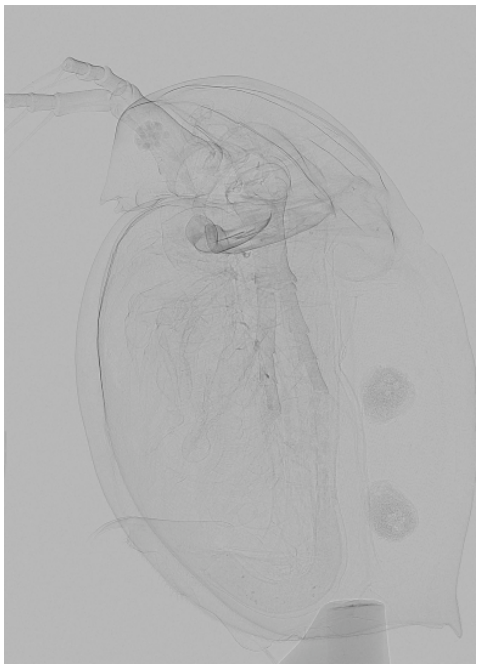

Figure 5.55: Single radiograph of *Daphnia magna*.

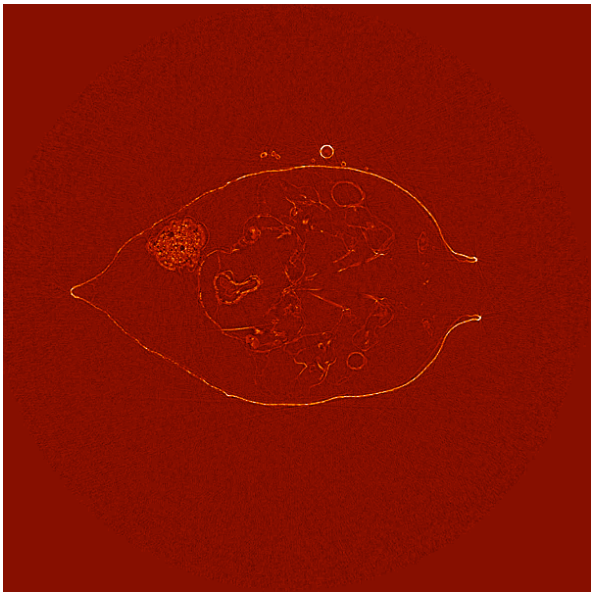

Figure 5.56: Single reconstructed slice of *Daphnia magna*.

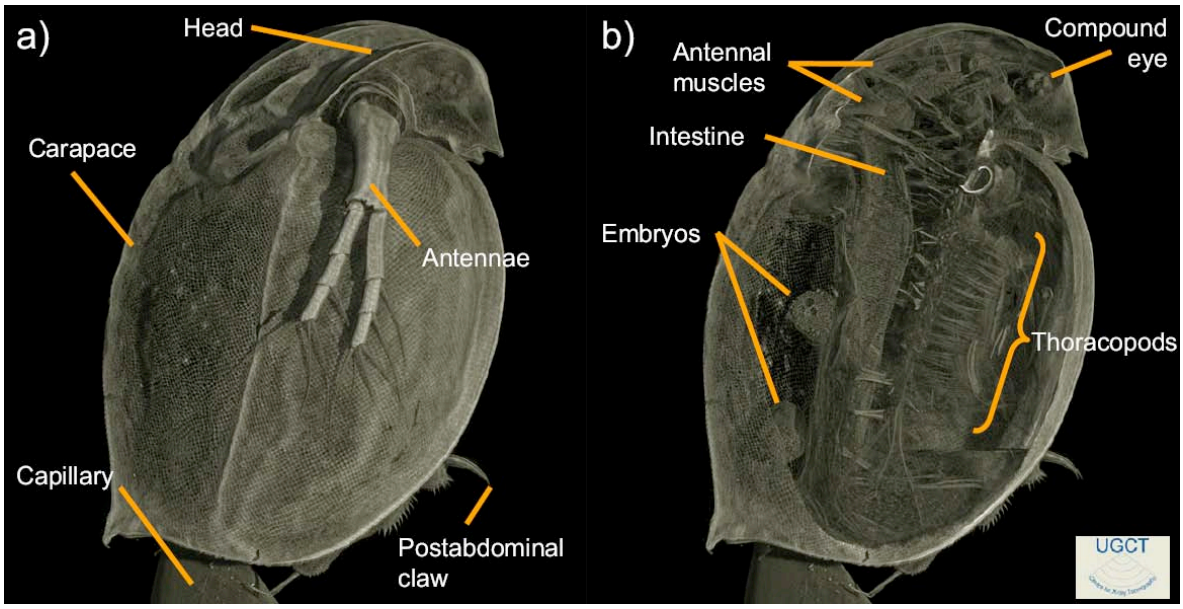

Figure 5.57: 3D rendered reconstruction in VGStudioMax. Inner and outer structure of *Daphnia magna*.

image is then displayed by adding half of the bytescaled intensity of the absorption image to the RGB channels and fill the other half of these RGB channels with respectively half of the bytescaled intensity of the Ca, Fe and Zn XRF maps. By using the software package VGSTUDIOMAX, it was possible to combine the SR micro-XRF results from given slices and the absorption micro-CT data in a single 3D dataset, illustrated in Fig. 5.59, using typical reference markers (e.g. support capillary, sample boundaries).

The combination of X-ray fluorescence and absorption tomography has until now rarely been illustrated. Currently, a compact dual modality laboratory scanner is being developed, which uses a full field X-ray camera. Two X-ray sources symmetrically illuminate an object. A full field X-ray camera for XRF imaging is placed in between of excitation sources. An X-ray camera for transmission imaging uses radiation from one X-ray source. By object rotation the scanner acquires all necessary angular two-dimensional views in transmission and fluorescence modes for following 3D reconstruction. The system acquires data in such a way that micro-CT scans and micro-XRF scans match each other exactly in position, magnification and spatial orientation. However, the samples were purely metallic, consequently the system lacks sensitivity for visualising the trace level metal distributions (Sasov *et al.*, 2008).

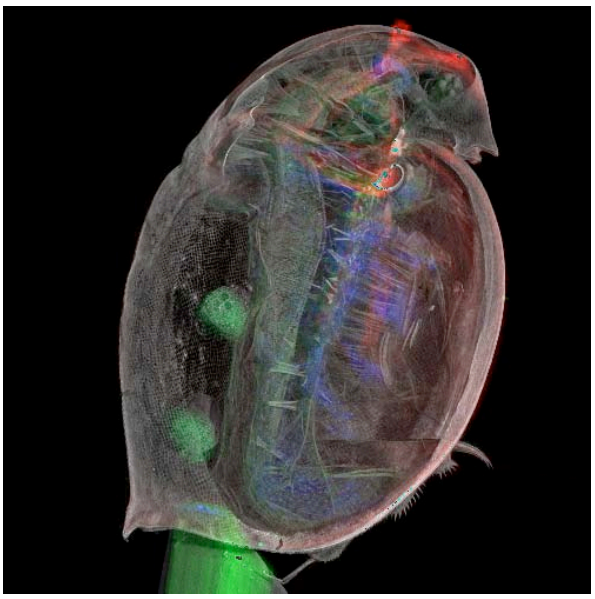

Figure 5.58: 3D rendered image of the unexposed *Daphnia magna* obtained by absorption micro-CT warped onto an RGB composed image of the scaled 2D Ca, Zn, Fe element distributions.

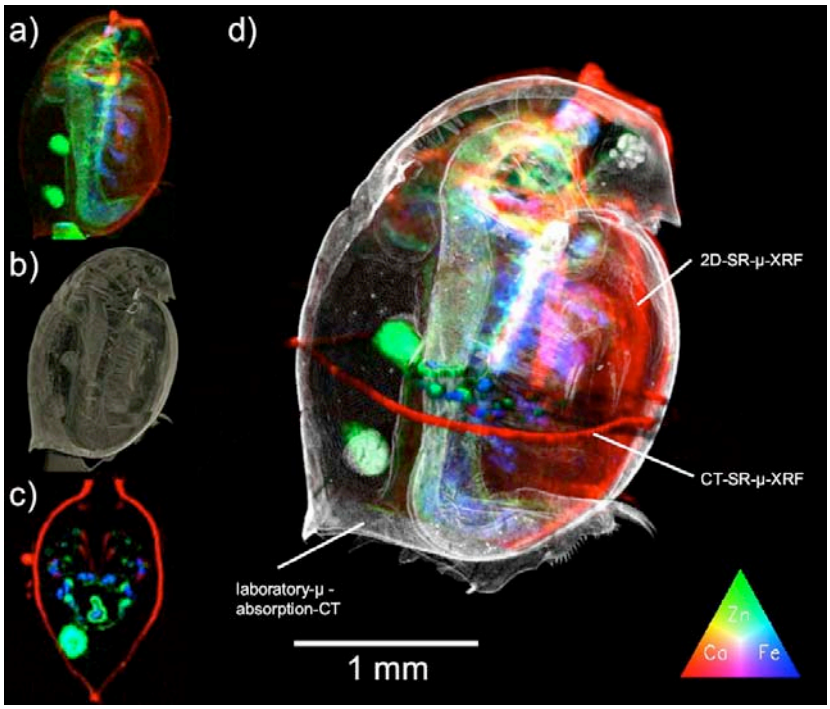

Figure 5.59: (a) RGB composed image of the scaled 2D Ca, Zn, Fe element distributions of the unexposed *Daphnia magna*. (b) 3D absorption micro-CT rendering of the inner structure of *Daphnia magna*. (c) RGB composed image of the scaled Ca, Zn, Fe element cross-sections within the unexposed *Daphnia magna*. (d) 3D rendered image of the unexposed *Daphnia magna*, combining laboratory absorption micro-CT and synchrotron 2D/CT micro-XRF data.

Chapter 6

Confocal micro-XRF on *Daphnia magna*

6.1 Introduction

In the previous chapter, synchrotron radiation 2D/CT micro-XRF on *Daphnia magna* was illustrated to detect differences in tissue-specific metal distributions. As a consequence of the penetrating character of X-rays, the detected analytical information obtained by 2D micro-XRF represents the full line integral along the path where the microbeam penetrates the organism. The introduction of micro-XRF CT allowed the visualisation of elemental distributions in a selected virtual cross section through the organism. The disadvantages of micro-XRF CT involve a more difficult alignment of the sample, extended measuring times, the need for an extra tomographic reconstruction step and challenging quantification. When different virtual sections of samples are necessary, this approach can be rather cumbersome. Therefore, we highlight the theoretical aspects of a new approach for scanning micro-XRF, confocal micro-XRF in section 6.2. In section 6.3, we illustrate how a confocal micro-XRF set-up was optimised and characterized at Beamline L, HASYLAB, Hamburg.

One toxicological aspect which has been studied intensively is the importance of different exposure routes of metals on *Daphnia magna*. Analysing a sufficient number of samples with systematically varied exposure routes/levels using micro-XRF CT is not feasible within a single beamtime and therefore quantitative comparison is cumbersome. Section 6.4 details the sample preparation methods applied during these experiments, while in section 6.5, we illustrate how confocal micro-XRF can be used to investigate the different uptake routes of metals by *Daphnia magna*. In order to investigate the quantitative character of these measurements, self-absorption effects were estimated. In analogy with the previous chapter, we explored the feasibility of analysing subregions of interest and the coupling of confocal micro-XRF with absorption micro-CT datasets. Finally, we illustrate 3D confocal micro-XRF

on a *Daphnia magna* egg resulting in elemental isosurfaces which can be directly correlated with absorption micro-CT datasets.

6.2 Theoretical aspects of confocal micro-XRF

Recently, a new approach for scanning micro-XRF has been illustrated, confocal micro-XRF, in which a polycapillary is attached to the energy-dispersive detector (Vincze *et al.*, 2004). The polycapillary detector lens represents a significant modification to the regular scanning micro-XRF spectrometer, i.e., defining a specific microvolume from which the XRF signal is detected in the coinciding focii of the detection-side polycapillary and the incoming microbeam as illustrated in Fig. 6.1. The detection-side polycapillary, which acts as an efficient detector collimator, accepts an energy dependent segment from the incoming beam path as it intersects the sample: this defines a microscopic volume element of detection within the investigated object. The combination of polycapillary half-lens coupled with an energy-dispersive detector for 3D-XRF was first proposed in the early 1990s by Gibson and Kumakhov (Gibson & Kumakhov, 1992). However, no experimental demonstration was given in this work for the proposed principle. As a result of the rapid development of monolithic polycapillary optics in recent years, the principle was recently applied in practice by several authors (Proost *et al.*, 2002; Kanngieser *et al.*, 2003; Janssens *et al.*, 2004). The local character of confocal micro-XRF carries several inherent advantages: (1) the 2D/3D data collection from the sample requires no rotation (2) the elemental distributions are directly obtained without reconstruction (3) comparison and quantification of the obtained elemental distributions is easier compared to micro-XRF CT (4) fast overview scans are possible, which can be followed by detailed scans (5) an internal point or small sub-volume of interest can be re-analyzed using longer measuring times. All these aspects result in lower measuring times and higher sample throughput.

6.3 Characterisation of the confocal micro-XRF set-up

6.3.1 Confocal alignment procedure

In order to align the focii of the X-ray focusing and confocal optics used for the confocal set-up at Beamline L, the following optimisation procedure was applied. In order to have a high flux necessary for confocal micro-XRF, a multilayer monochromator was used and adjusted to an excitation energy of 19.8 keV. A microspot was obtained by optimising the orientation of a conventional polycapillary half lens of beamline L (5 mm working distance). A fluorescent single-crystal emitting visible light upon X-ray irradiation was used to obtain a minimal beamsize. Subsequently, a novel strongly-focusing polycapillary half lens (2 mm working distance) was mounted onto the detector. The excitation side polycapillary was

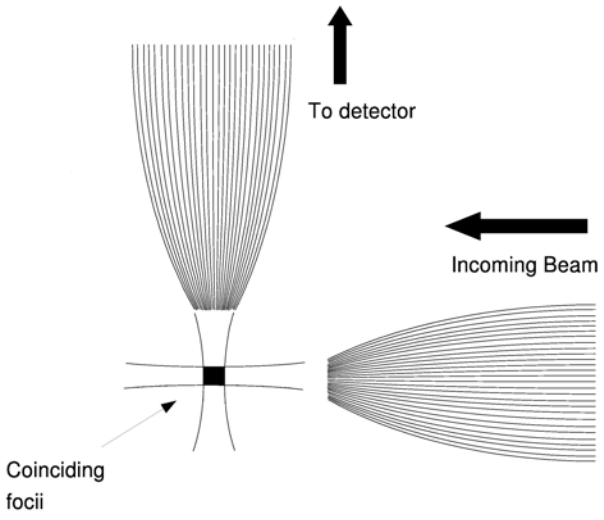

Figure 6.1: Principle of confocal detection, showing the top-view of the applied excitation-detection geometry.

lowered outside the beam path and the motorised detector moved until the tip of the detection side polycapillary enters the field of view of the CCD camera. Afterwards, the excitation polycapillary is moved back to its position defined by its nominal working distance and a 1 mm thick glass standard (NIST SRM 611) is placed into the beam with its surface positioned in the focal spot of the exciting polycapillary, which coincides with the focal-plane of the optical microscope.

In Fig. 6.2, the first alignment procedure of the exciting (cap_e) and detector (cap_d) polycapillary optic is illustrated. Although the focus of the exciting polycapillary is positioned on the surface of the standard, the diverging beam behind the focal spot generates a cylindrical path from which fluorescence is emitted. This emission of fluorescence is used in a first alignment procedure of the detector capillary: by performing a vertical scan with the detector capillary cap_d, the correct height h_i at which the focii of both capillaries coincide, can easily be determined corresponding to the maximum detected count rate (position h_2). In the second alignment step, the thick glass SRM is removed from the sample stage and replaced by a thin Au foil (thickness $<<$ 1 μm) of which the surface is again sharpened on the microscope image, so that the focal spot of the exciting capillary coincides the thin Au foil. The detector capillary cap_d is then moved horizontally toward a position p_i until the highest count rate is observed (position p_2). In this way, one can be sure that the focii of the capillaries coincide exactly in the focus of the microscope image. In the third alignment step (Fig. 6.4), the detector polycapillary cap_d is moved along the axis of the detector in order to maximize the

$Au - L$ intensities, which correspond to the smallest excitation volume. This step represents the fine tuning of the working distance d_i of the detection side polycapillary corresponding to its focal distance (position d_2). After this step, another vertical and horizontal alignment of the detector capillary is performed since it is always possible that the detector is not perfectly positioned along its axis, resulting in a vertical and/or horizontal shift during the third alignment step.

6.3.2 Acceptance Determination

The acceptance of the detection side polycapillary in a confocal micro-XRF set-up is energy dependent and can be determined experimentally by scanning a thin wire or foil (infinitely thin compared to the dimensions of the detection volume) through the detection volume with a linear motor scan. As the X-axis of the sample stage assembly is oriented under 45° with respect to the incoming beam and detector axis, also the sample is scanned under 45° through the detection volume. As a result of this particular set-up geometry, the FWHM of the fluorescence intensity scan can be retrieved by the following considerations. If b represents the FWHM of the beam of the excitation side polycapillary and s represents the FWHM of the linescan through the thin foil, then the energy dependent acceptance of the detection side polycapillary a is determined by taking into account the convolution of the excitation side and detection side capillary beam profiles when the confocal volume moves through a thin film sample, using the following equation:

$$a = \sqrt{2s^2 - b^2} \tag{6.1}$$

A very interesting approach to determine the energy dependent acceptance of a polycapillary optic is to use a so-called free standing thin film (FSTF) standard, a thin multilayer structure composed of a series of pure element thin films on a polymer support. This type of thin multilayer/multi-element standard makes it possible to obtain the energy dependent acceptance using the characteristic fluorescent radiation from the different elements deposited on the surface. In general, FSTFs are very well suited as reference samples for the calibration and characterisation of experimental micro-XRF set-ups. They are particularly useful for the determination of elemental sensitivities under given experimental conditions, and also for establishing the energy/element dependent depth resolution of confocal micro-XRF set-ups. A main advantage of the FSTF is that X-ray absorption can be neglected or has only a minor influence due to its sub-micron thickness so that uncertainties due to absorption effects do not influence the calibration.

Fig. 6.8 shows the prototype FSTF prepared by AXO Dresden Gmbh. (Heidenau, Germany), which was used for characterising the acceptance of the confocal set-up at Beamline L. Elements such as Ca, Fe, Cu, Pb, Mo, Pd and La were deposited on thin polymer foils by physical vapour deposition (PVD) techniques like magnetron sputtering, ion beam sputtering

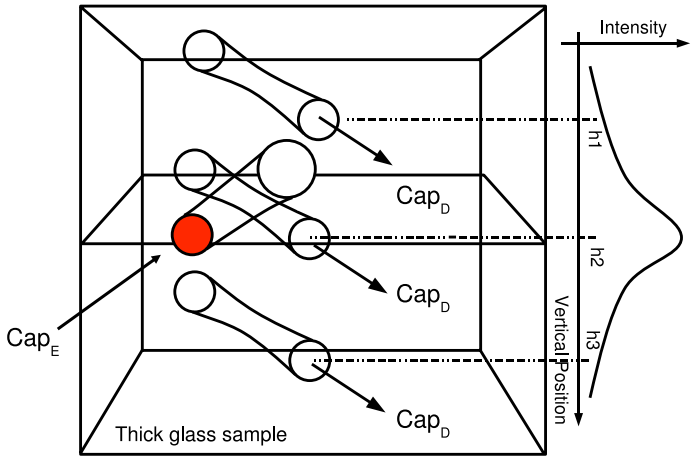

Figure 6.2: First step of the confocal alignment procedure.

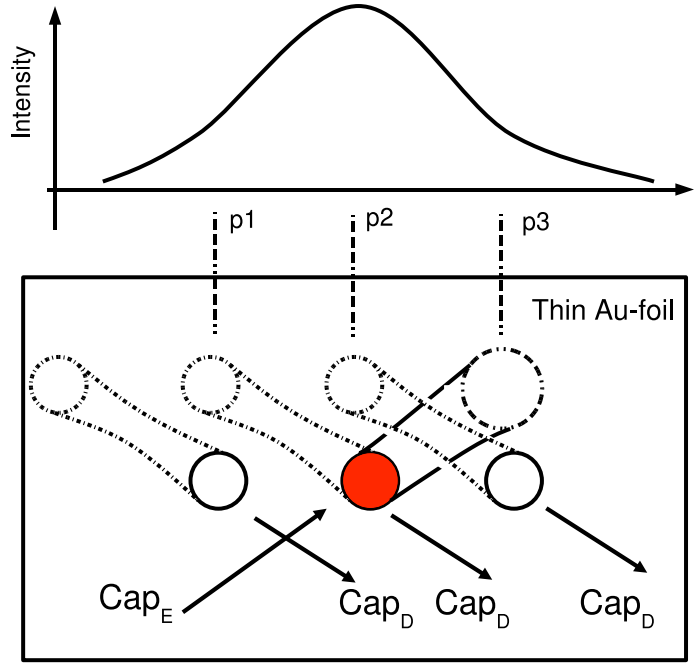

Figure 6.3: Second step of the confocal alignment procedure.

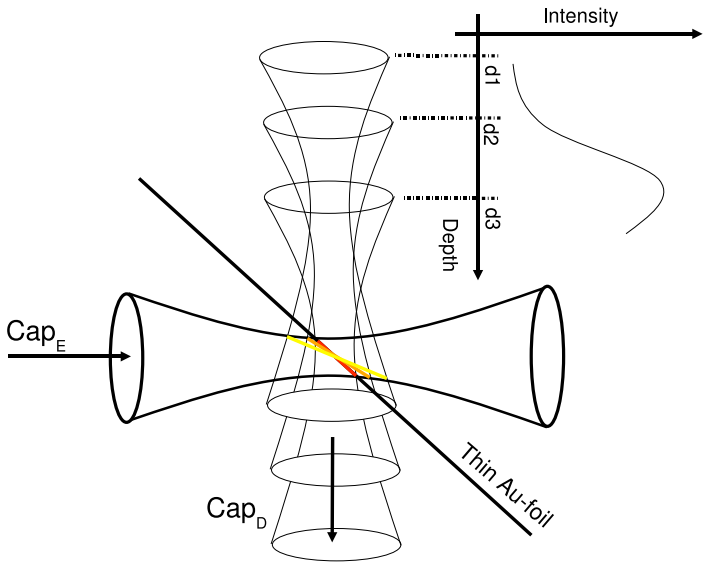

Figure 6.4: Third step of the confocal alignment procedure.

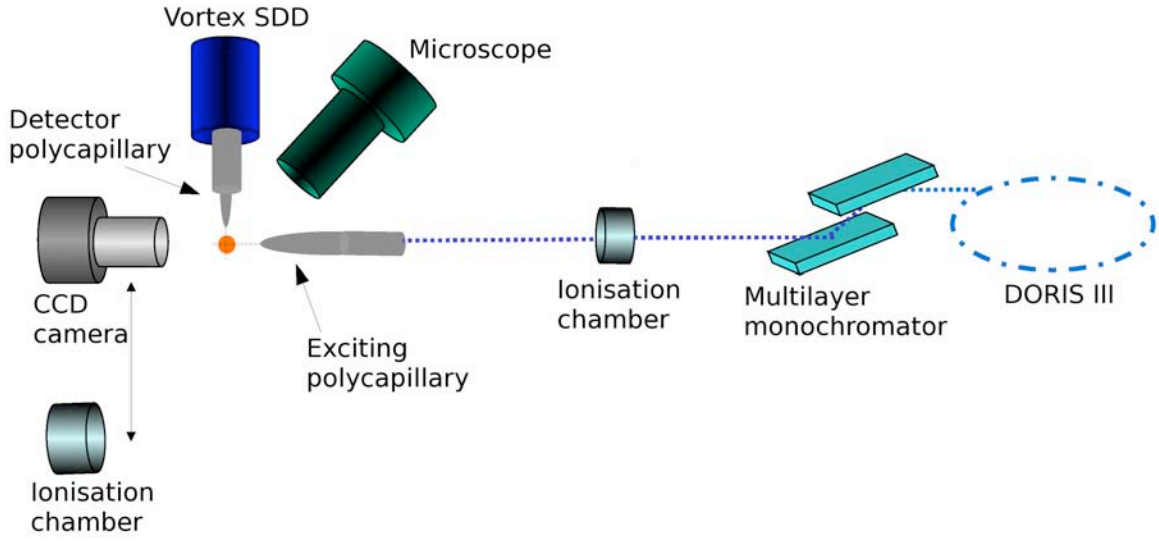

Figure 6.5: Schematic of the experimental confocal set-up.

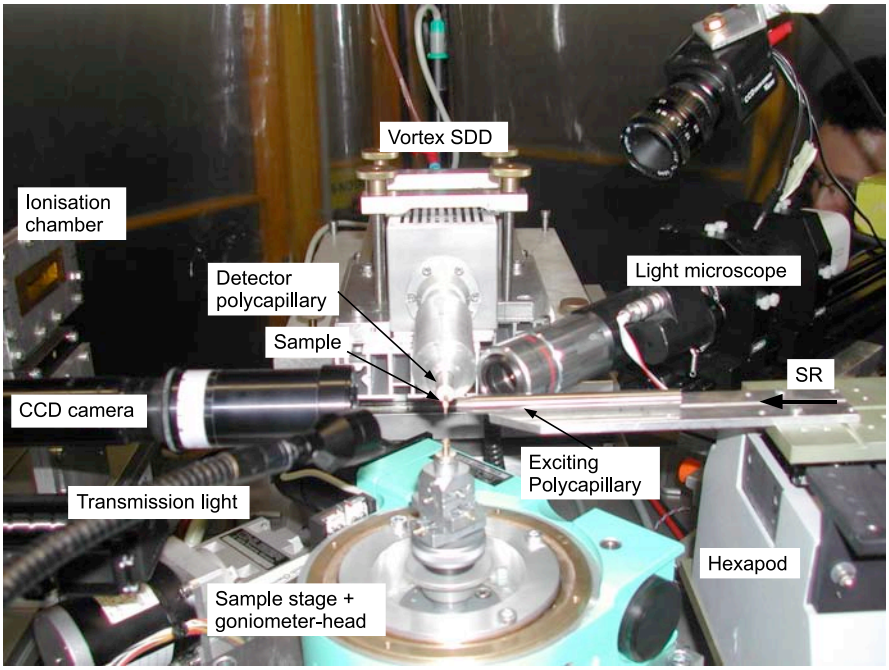

Figure 6.6: Lateral view of the experimental confocal set-up.

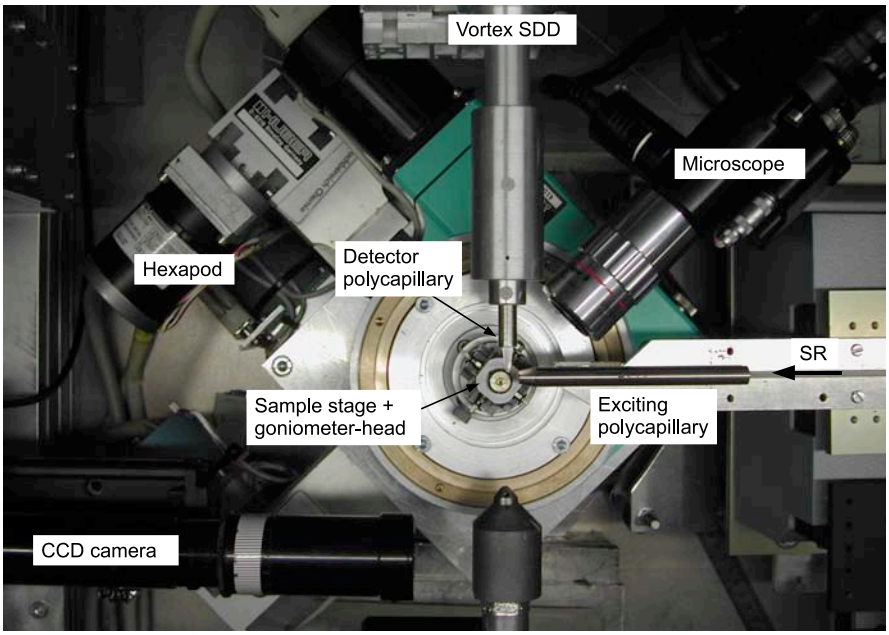

Figure 6.7: Top view of the experimental confocal set-up.

and pulsed laser deposition (Falkenberg *et al.*, 2007a). The elements deposited were chosen in such a way that their characteristic lines cover a broad energy range without giving rise to spectral overlap, as can be seen on a spectrum in Fig. 6.9. The substrate is a 6 μm foil clamped in a frame with 50 mm diameter, thickness 3 mm. The coated area of the FSTF has a diamter of 30 mm. After alignment of the confocal set-up, a depth scan was performed through the FSTF, using a step size of 5 μm and a live time of 10 s per scan point. The measured XRF point spectra were fitted using an appropriate input model based on the sum spectrum (accumulated spectrum corresponding to the sum of all individual point-spectra of the full scan), shown in Fig. 6.9. The net elemental intensities obtained by fitting the individual point-spectra were plotted versus scan position, as shown in Fig. 6.10. The FWHM of each elemental line profiles (obtained by Gaussian fits to the meausured profiles) was then converted to the corresponding energy dependent acceptance of the detection side polycapillary using Eq. 6.1 of which the results are shown in Fig. 6.11.

6.3.3 Operational Elemental Yields and Detection Limits

Operational elemental yields, absolute and relative detection limits were determined using an NIST SRM1577B (Bovine Liver) pressed pellet standard at the excitation energy of 19.8 keV. A total amount of 0.0187 g from the NIST SRM 1577B powder was carefully pressed into a first pellet of 13 mm diameter, corresponding to an areal density of approximately 14.09 mg/cm^2. A depth scan through a second pressed pellet of NIST SRM1577B was made, from which the thickness could be estimated to be approximately 149 μm. This resulted in a density 0.612544 g/cm^3 of pressed bovine liver powder. Since both pellets were pressed in an identical manner, the determined density of the first pellet was used to determine the required volume concentration for each certified element in first pellet. Relative and absolute detection limits and elemental yields can be observed in Fig. 6.13 which were calculated from a point measurement of 300 s just below the surface of the SRM. Relative detection limits

Figure 6.8: Prototype Free Standing Thin Film (FSTF).

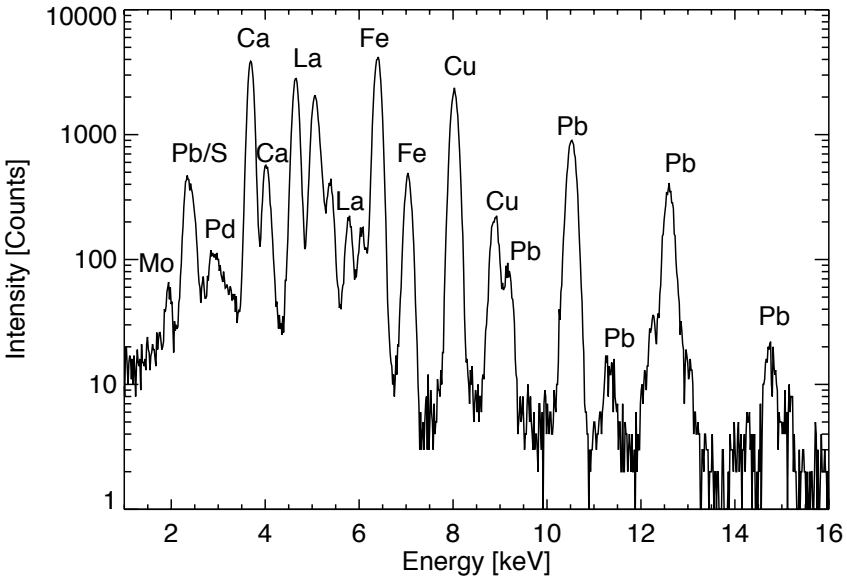

Figure 6.9: Sum spectrum of the multi-element standard.

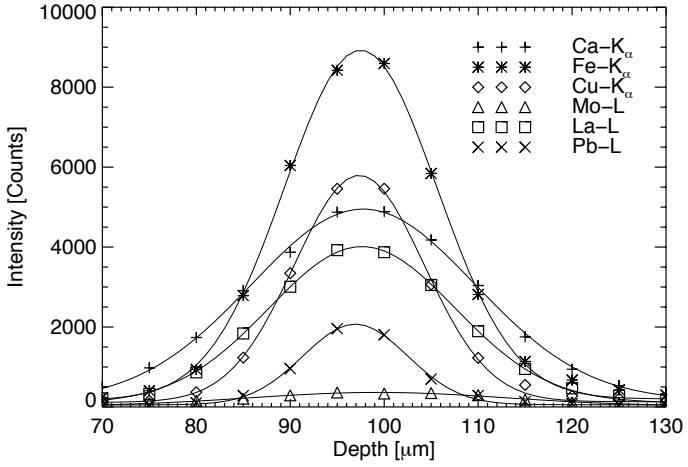

Figure 6.10: Depth scan through the multi-element standard.

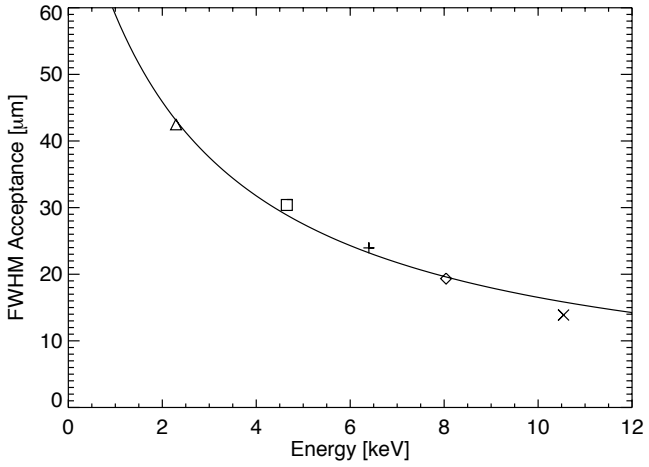

Figure 6.11: Acceptance as a function of the energy of the fluorescent lines.

are in the 0.1-1 *ppm* range, corresponding to absolute detection limits in the 1-10 fg range taking into account the energy dependent acceptance of the detection side polycapillary.

6.4 Sample preparation

Fig. 6.15 shows the results of a chronic Zn exposure experiment from which the samples were used. *Daphnia magna* were taken from the stock culture at the laboratory of environmental toxicology of Ghent University of which the details are described in Muyssen *et al.* (2006). The background Zn concentration in the culture water is about 5-7 $\mu g/L$ Zn. From the experiment, it can be observed that reproduction is maximal at 80 $\mu g/L$ and that a lower or higher concentrations results in a lower reproduction (number of juveniles). However, when the samples are additionally exposed to Zn contaminated algae, another decrease in reproduction is occuring. In order to correlate these findings with the tissue-specific metal distributions, confocal micro-XRF was used to obtain quantitative dorsoventral sections through the region of gut, gill tissue and brood pouch. Samples from this experiment were taken, indicated in Fig. 6.15 as D2/D3/D4/D5/D6, and underwent dehydration in a water/aceton series and subsequent fixation with HMDS as described in Chapter 3. The samples were then fixed on a polymer fibre attached to a brass holder used for mounting in the goniometer-head of the experimental set-up.

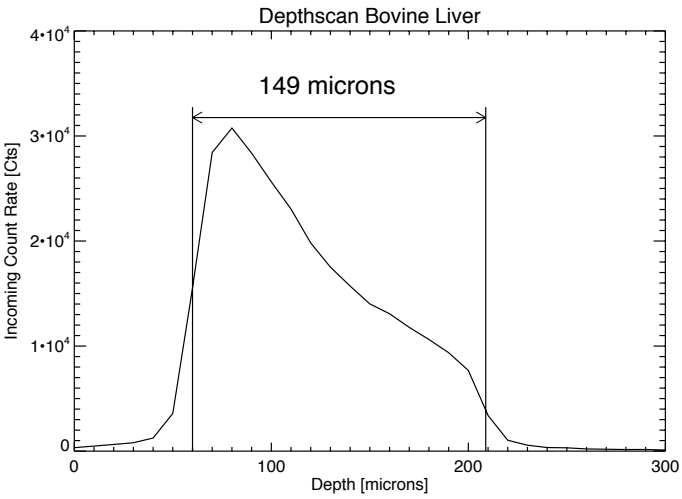

Figure 6.12: Estimation of the thickness of a bovine liver NIST pellet by means of a confocal depth scan.

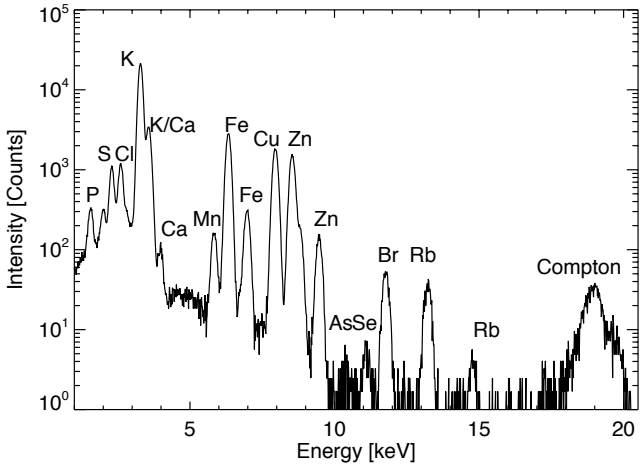

Figure 6.13: Point spectrum obtained from a pressed pellet of NIST SRM 1577B (Bovine Liver) corresponding to a live time (LT) of 300 s. Sample depth was adjusted to yield maximum count rate, when the analysed volume is just below the surface of the sample.

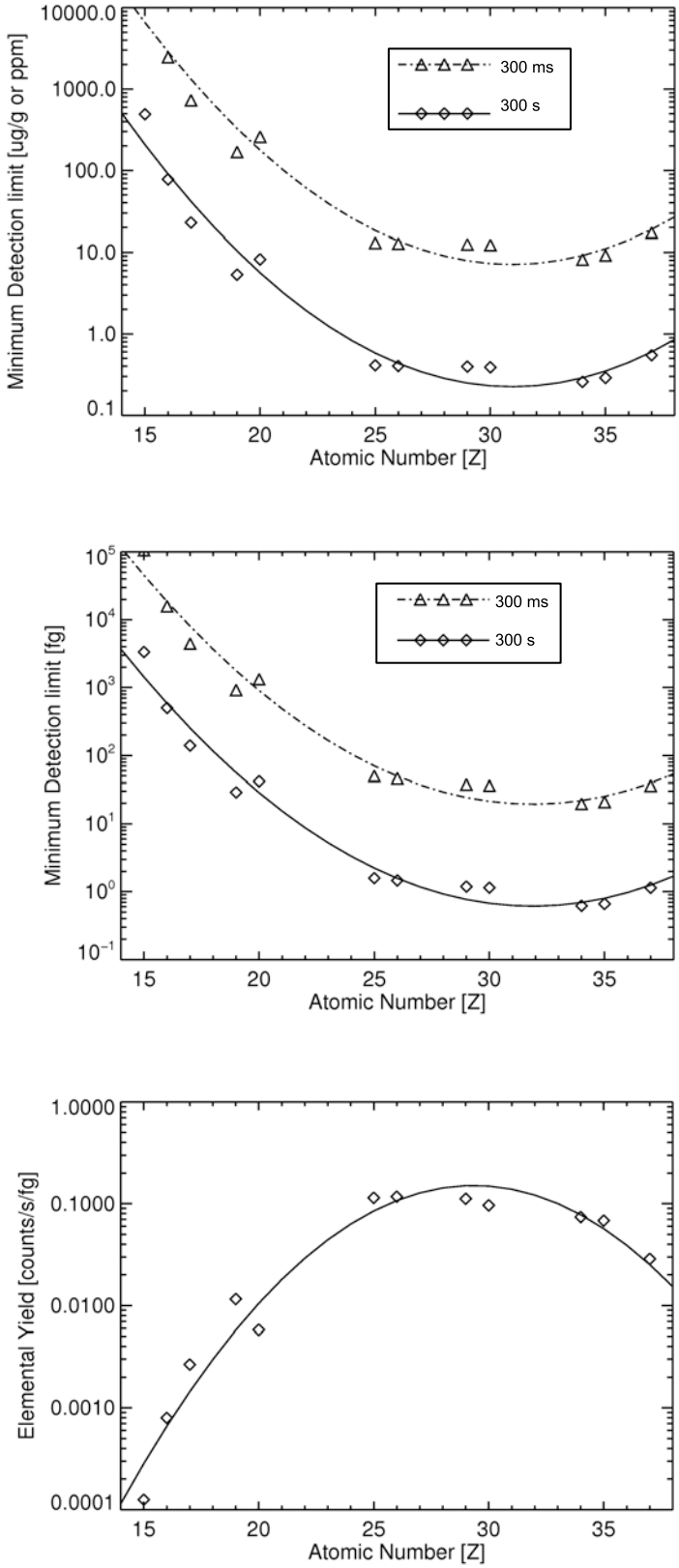

Figure 6.14: Measured relative (a) and absolute detection limits (b) for biological materials corresponding to respectively LT=300 *ms* and LT=300 *s* as determined from the point spectrum shown in Fig. 6.13. The corresponding absolute elemental yield curve is shown in (c).

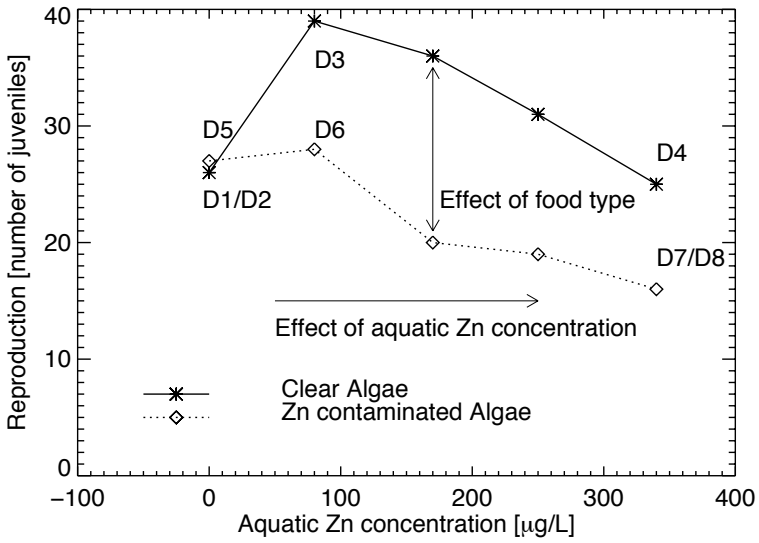

Figure 6.15: Ecotoxicological data from a full factorial exposure experiment on *Daphia magna*.

6.5 Experimental results

6.5.1 2D confocal micro-XRF

All *Daphnia* were mounted on the experimental set-up in such a way that the side part of the exoskeleton was perpendicular to the microscope view and the head looking away from the detection side polycapillary. The scanning boundaries of each sample were determined by taking a depth scan through the center of a sample (we use the microscope view as a reference axis system). The motors were then moved to the average value of these boundaries. Then a left-right scan was taken in order to determine the outer left and right boundary of the sample. Moving the sample to a corner of the bounding box, followed by a linear sweep in depth or in left/right should reveal no jump in count rate, otherwise the boundaries were expanded. Care should be taken since due to the confocal geometry a lower count rate is present which makes the observation of intensity changes during line scans more cumbersome. For each scan, a sum spectrum was made and a common suitable fitting model was made with AXIL. The element maps were corrected for dead time and normalised to the doris current using the first ionisation chamber. Making use of the previously determined elemental yields, the element maps were converted to a volume concentration ($\mu g/cm^3$), providing a first general overview of differences in Zn distribution between the differently exposed *Daphnia*. These values could in principle be converted to a concentration on a $\mu g/g$ basis by taking into account the density of the sample. Comparison of *Daphnia magna* in a medium containing a background concentration level of 5 $\mu g/L$ Zn (unexposed *Daphnia magna*) and also in a

medium with elevated Zn of 340 $\mu g/L$ (exposed *Daphnia magna*) shows distinct accumulation in several tissues: i.e. in the eggs, gut epithelium, ovaries, gills and the carapace. It should be noted, however, that subtle changes in intensity are difficult to reveal by this comparison only. Therefore, further data treatment will be exploited in a next section to tackle this problem.

6.5.2 Data treatment using 'Growing Regions of Interest'

In order to further interpret the data, it was preferred to investigate certain subregions of the sample in closer detail. However, traditional K-means clustering on the data proved to be more difficult as compared to the traditional 2D experiments performed on *Daphnia* in the previous chapter. Due to the lower and very subtle differences in count rate, K-means clustering provided clusters which did not correspond to the tissues of interest. The XROI utility in IDL was used to select specific regions of interest for elemental analysis. The tool enables the interactive definition of single or multiple regions from an image using the mouse. The REGION GROW routine enables the programmable definition of ROIs to deal with the problem in a more reproducible manner. It expands an initial region to include all connected, neighboring pixels that meet given conditions. These conditions are imposed by either a threshold range (minimum and maximum pixel values) or by a multiplier of the standard deviation of the original region. The neighboring pixels search method can be set to 4 neighbor (which searches only the four neighboring pixels that share a common edge with the current pixel), or to 8-neighbor (which searches all eight neighboring pixels, including those that are located diagonally relative to the original pixel and share a common corner). Once a ROI is defined, it can be displayed or subjected to further analysis (e.g. the geometric area, perimeter of each region, the number of pixels making up each region when it is displayed, histogram of pixel intensities). Fig. 6.17 illustrates the region growing process performed on a given *Daphnia magna* dataset obtained by confocal micro-XRF. The left column of images shows the Ca distribution within the sample while the right column column the Zn distribution. In the vertical direction, one can follow the procedure for region growing. First, a simple geometrical shape is selected as an initial ROI and then the region is grown from this shape. On the left, one can see a grown region of the exoskeleton, while on the right, different individual eggs were selected. Once the ROIs have been selected, further data treatment can be performed, as shown in Fig. 6.18. The histograms displayed in this figure indicate the number of pixels with a certain Zn concentration within three different eggs of an unexposed and an exposed *Daphnia magna*.

The REGION grow function allowed to differentiate the carapax from the internal tissues and in a next step the eggs, gill tissue and gut within the internal tissues. An overview of the sum spectra from the carapax and from internal tissues of the different *Daphnia magna* can be seen in Fig. 6.19 and in Fig. 6.20. Although the detection side polycapillary causes a strong reduction of XRF intensity at higher energies, it was nevertheless possible to normalise the

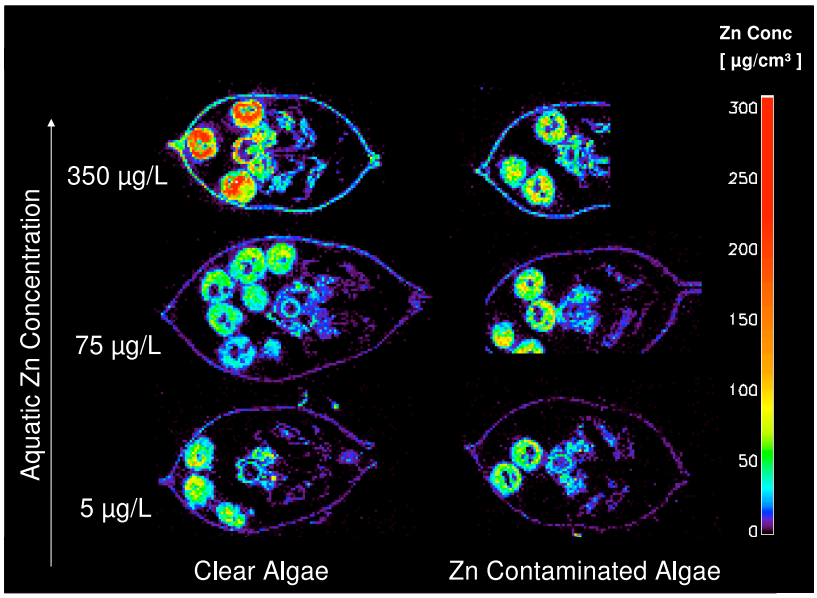

Figure 6.16: Overview of the different quantified confocal sections for the six differently exposed *Daphnia magna*.

spectra to the Compton signal, which is a requirement to correct for the amount of illuminated mass. At first sight, the spectral intensities seem very similar for a certain element, but very quickly some slight differences can be observed. Because comparison of the peak intensities for different organs between different organisms is cumbersome within these graphs, the peaks were fitted separately and for each organism a diagram was made from the normalised relative intensities of an element corresponding to its different organs. The results of this analysis are given in Fig. 6.21 and Fig. 6.22.

In Fig. 6.21, it can be observed that Zn is present in similar ratios between the different organs. Zinc seems to be present in lowest concentration in the carapax, followed by the gills, gut and eggs. Gut and eggs though feature similar concentration levels which fluctuate depending on the exposure conditions. When looking at the carapax and gills, a clear increase in the Zn concentration can be seen with increasing Zn exposure, for both series. The relatively high increase of Zn accumulation in the gills, in comparison with other tissues, is likely due to its function as primary site for ion uptake and as the main site for active ion transport involved in osmoregulation of the body fluids (Kikuchi & Matsumasa, 1997). The increased accumulation in the carapace is probably the result of the employment of this tissue as a metal sink in the detoxification process of this element. Previous research has shown that on average 38 % of total Zn can be incorporated into the exoskeleton when *Daphnia magna* was exposed to 600 $\mu g/L$ Zn, and that the element is lost by shedding the carapace during the molting process (Muyssen & Janssen, 2002). The comparable concentration levels of Zn

in the gut/ovarium and eggs, as well as their similar proportional increase after Zn exposure, are supporting the assumption that the main part of Zn accumulation in the eggs is not due to ventilation of the broodpouch with culture water after disposal of the eggs (Seidl *et al.*, 2002), but most probably mainly due to a transfer of Zn vitellogenin from the ovaries via the haemolymph to the developing embryos. It has been demonstrated that in this way on average 18 to 30 % of total body Zn contents could be transferred from the mother organism to its developing (embryonal) offspring in the broodpouch (Guan & Wang, 2004).

Fig. 6.22 summarises the information for the tissue-specific distribution of Ca. Since the carapax is mainly composed of Ca, the scale is logarithmic to make comparison between the different tissues possible. It can be seen that the Ca concentration in the carapax is more or less stable and does not reveal any trend, indicating that Ca present in the carapax could serve as an internal reference. Besides the carapax, the Ca concentration is higher in gills, gut and eggs respectively. With the exception of one measurement, Ca concentration seems to drop with higher Zn concentration in the gill tissue, possibly confirming its antagonist role. Physiological research suggests that Zn uptake in fish from the water mainly occurs via the gill tissue, where it interferes with Ca homeostasis which ultimately leads to toxicity (Hogstrand *et al.*, 1996, 1995; Barron & Albeke, 2000). It is possible that this is also the case in *Daphnia magna* and that Zn first enters the gill tissue, interferes with Ca homeostasis and is then further distributed into other tissues of possible toxicological relevance (Muyssen *et al.*, 2006).

6.5.3 Combination with absorption micro-CT

Since confocal micro-XRF is essentially a local technique, it can investigate smaller regions of interest in an efficient manner. This is illustrated in Fig. 6.23, where a dorsoventral overview scan was taken using a stepsize of 20 μm. For clarity an RGB scale was used to visualise the data. When performing XRF microtomography such local analysis is not possible: the full sample cross-section needs to be analysed though the sub-feature of interest may be much smaller, resulting in longer measuring times. Using confocal micro-XRF, an egg was scanned with a stepsize of 5 μm and relatively long measuring time (5 s per scan point, resulting in elemental distributions with more detail and better statistics (part 1). The same was done to investigate the substructure of the gut, this time with a step size of 10 μm (part2). An interesting aspect of such confocal scans is that since the confocal volume is fixed in space, the sample can be moved through it in any possible way, as far as the sample stage allows. For example, by scanning the sample in the YZ-plane (while keeping the depth coordinate X fixed), a sagittal section through the sample can be obtained (part3). Using XRF tomography, the sample would need to be placed on another rotation axis, loosing the coordinate reference frame. Also, since the sample is less symmetrical in this plane, a lot of measuring time would be spent with measuring air.

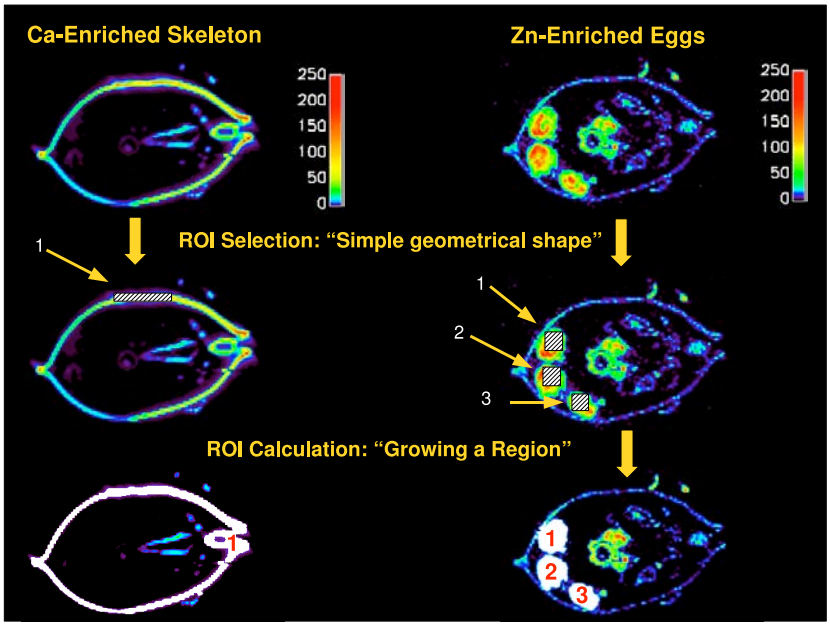

Figure 6.17: Principle of growing Regions of Interest.

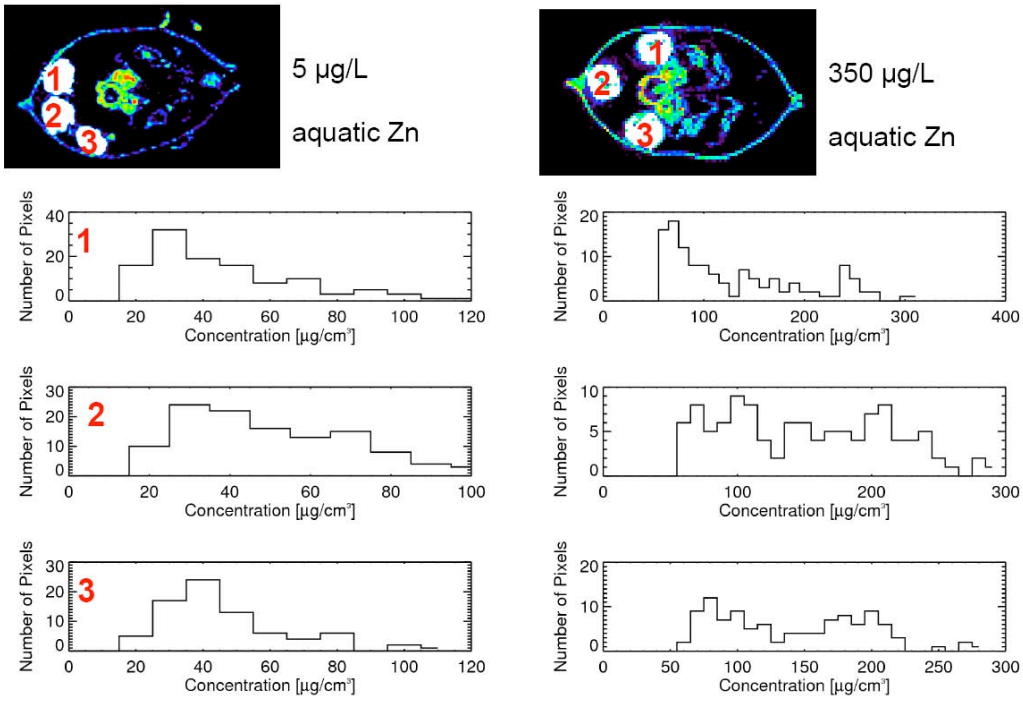

Figure 6.18: Histograms of ROIs of *Daphnia magna* (corresponding to the eggs) in culture medium of 5 and 350 μg/L aquatic *Zn* respectively.

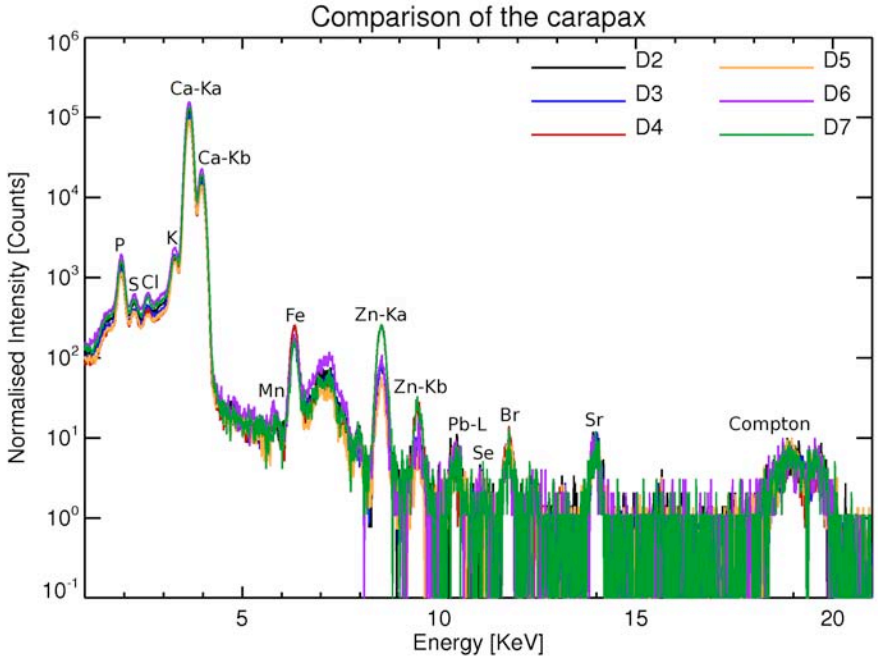

Figure 6.19: Sum spectra of the carapax.

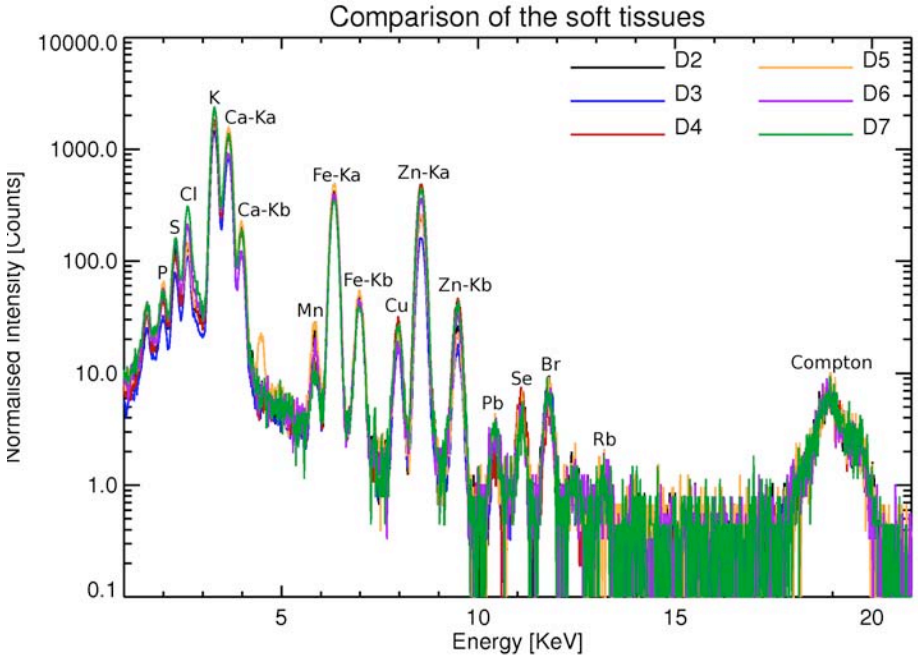

Figure 6.20: Sum spectra of the soft tissues.

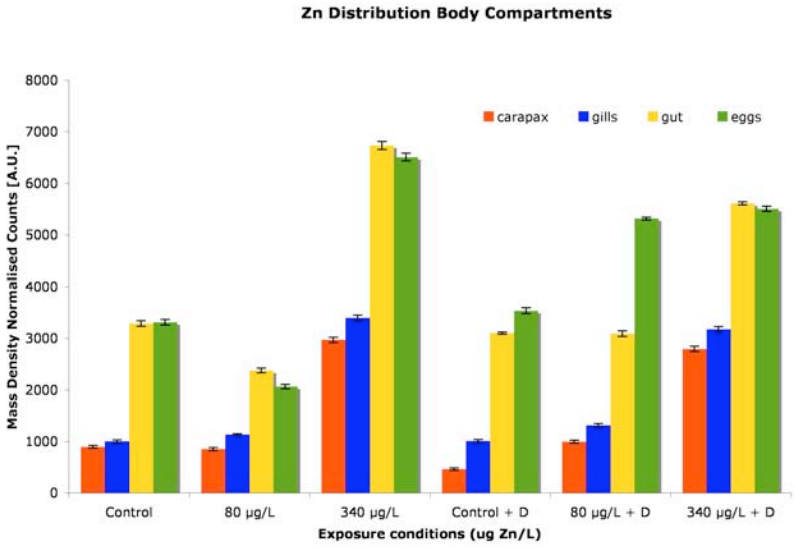

Figure 6.21: Mass density normalised Zn counts for the carapax, gut, eggs and gill tissue.

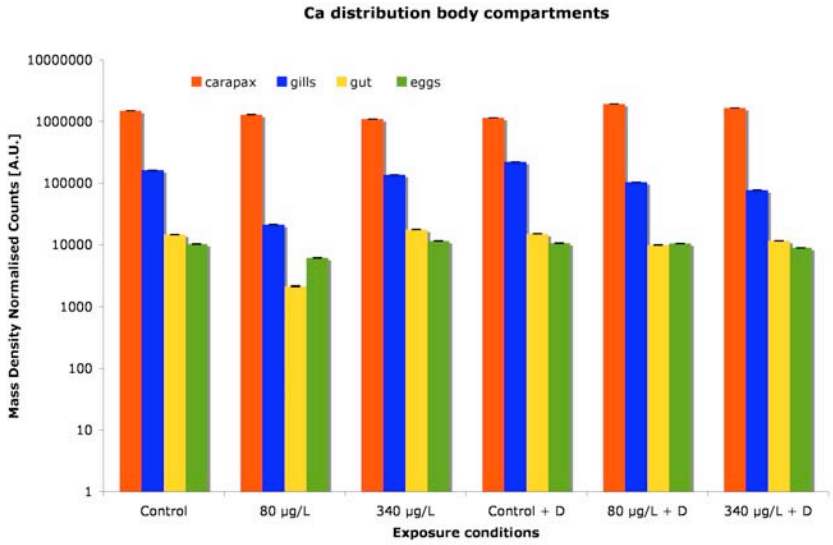

Figure 6.22: Mass density normalised Ca counts for the carapax, gut, eggs and gill tissue.

In the dorsoventral and sagittal section, Fe is present in the spine. The Fe distribution matches the main sites of haemoglobin concentration in the circulatory system of the organism. Haemoglobin is a porphyrin-Fe complex which can capture oxygen from the surrounding medium and acts as an oxygen-transport molecule throughout the tissues. Different haemoglobin currents inside the organism become confluent at the median dorsal ridge of the carapace before returning to the pericardium around the heart (Pirow *et al.*, 1999a,b). The Fe detected at the base of the sample is due to the trace level presence of Fe in the glass support capillary.

As pointed out in the previous chapter, the combination of absorption tomography datasets and XRF datasets is a very powerful method. However, when performing conventional 2D micro-XRF scans, the resulting dataset cannot be fully overlaid with the 3D absorption tomography dataset. However, confocal elemental distributions are local measurements in well-defined planes within the sample, and can be overlaid with the absorption datasets, providing valuable complementary information. In Fig. 6.24 this overlay is visualised with the saggital and dorsoventral XRF confocal scans incorporated in the 3D reconstruction of sample $D4$.

6.5.4 Estimation of sample self-absorption effects

Due to the confocal principle, local fluorescence is collected from a well-defined volume within the sample. For a specific element, both K_α and K_β lines are collected. The ratio of these K_α and K_β lines can be calculated for each atomic number by using their corresponding radiation rates, as shown in Fig. 6.25 and Fig. 6.26 by using the XrayLib database (Brunetti *et al.*, 2004). Since the attenuation coefficient for a K_α line is higher than for K_β (Trojek *et al.*, 2008), their corresponding intensity I_{K_α} / I_{K_β} will be reduced if absorption is occuring, which is the case when the confocal volume is extracting information from deeper regions within the sample. Therefore, the intensity of the K_α and K_β lines gives an estimate of the importance of absorption effects in the sample as the analysing confocal volume moves deeper into the sample. Note, that the K_α/K_β intensity ratio can only increase for a given element with increasing sample absorption, if an element is present having an absorption edge between the two XRF lines with sufficiently high concentration.

In order to verify possible self-absorption effects on the previously discussed dorsoventral sections on *Daphnia magna* which could interfere with the interpretation of the results, the $Ca-K_\alpha$ and $Ca-K_\beta$ peaks were fitted separately for all individual measuring points. In Fig. 6.27, the $Ca-K_\alpha/Ca-K_\beta$ ratio is visualised, together with the orientation of the excitation and detection side polycapillary. A clear gradient in the ratio can be observed: the $Ca-K_\alpha$ / $Ca-K_\beta$ ratio drops from 8.8 at the side of the carapace closest to the detection side polycapillary to 4.7 at the side of the carapace furthest from the detection side polycapillary,

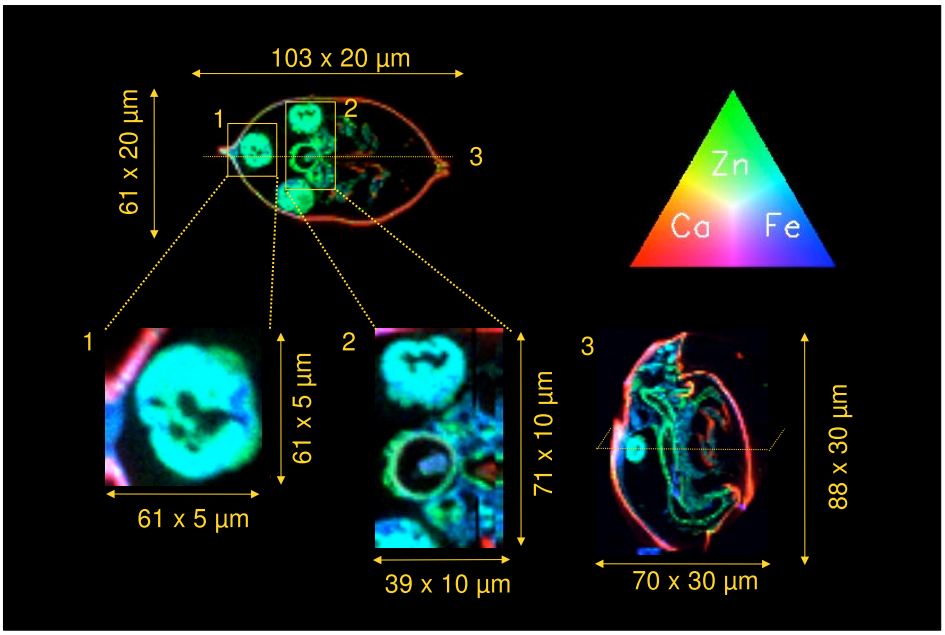

Figure 6.23: Dorsoventral section through D4. Detailed scan of egg (1), gut (2), sagittal section through D4(3).

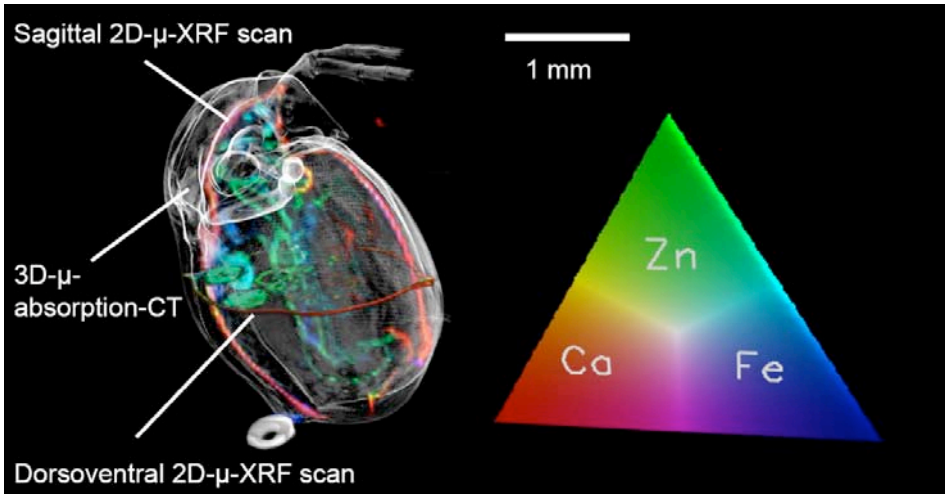

Figure 6.24: Two Confocal XY and XZ slices loaded into a 3D rendered absorption micro-CT model of *Daphnia magna D*4.

which is in perfect agreement with what one would expect on the basis of self-absorption effects. Also note that the maximum value is in good agreement with the theoretical values for Ca shown in Fig. 6.26

The $Ca - K_\alpha / Ca - K_\beta$ ratio can also be handily used to predict absorption for the other elements. If we consider R as the K_α / K_β ratio, we can apply the X-ray attenuation law as follows:

$$\begin{aligned} R &= \frac{I_{K_\alpha}}{I_{K_\beta}} && (6.2)\\ &= R_0 e^{-(\mu_{K_\alpha} - \mu_{K_\beta})d} && (6.3)\\ &= R_0 e^{-\Delta\mu_{\alpha,\beta} d} && (6.4) \end{aligned}$$

The difference in mass absorption coefficient coefficients can be estimated by using the E^3 relationship between the K_α / K_β fluorescent lines.

$$\begin{aligned} \Delta\mu &= \mu_{K_\alpha} - \mu_{K_\beta} && (6.5)\\ &= \mu_{K_\alpha} - \mu_{K_\alpha} \left(\frac{E_{K_\alpha}}{E_{K_\beta}} \right)^3 && (6.6)\\ &= \mu_{K_\alpha} \left(1 - \frac{E^3_{K_\alpha}}{E^3_{K_\beta}} \right) && (6.7)\\ &= \mu_{K_\alpha} (1 - k^3) && (6.8) \end{aligned}$$

From this, the mass absorption coefficient for the $Ca_{K\alpha}$ fluorescent lines can be estimated:

$$\begin{aligned} \ln\left(\frac{R}{R_0}\right) &= -\mu_{K_\alpha} d(1 - k^3) && (6.9)\\ \mu_{K_\alpha} d &= \frac{\ln\frac{R_0}{R}}{1 - k^3} && (6.10)\\ &= 1.738 && (6.11) \end{aligned}$$

This ratio corresponds to a transmission of about 17 % of the Ca fluorescent lines for the highest measured K_α / K_β ratio. We can then therefore also calculate the mass absorption coefficient for the Zn fluorescent lines by using the above mentioned E^3 approximation. From this can be calculated that the transmission of the Zn fluorescent lines is 87 %, from which we can conclude that the sample is virtually transparent for Zn fluorescent radiation. This means that the obtained semi-quantitative results for the Zn concentrations are not influenced significantly by self-absorption effects.

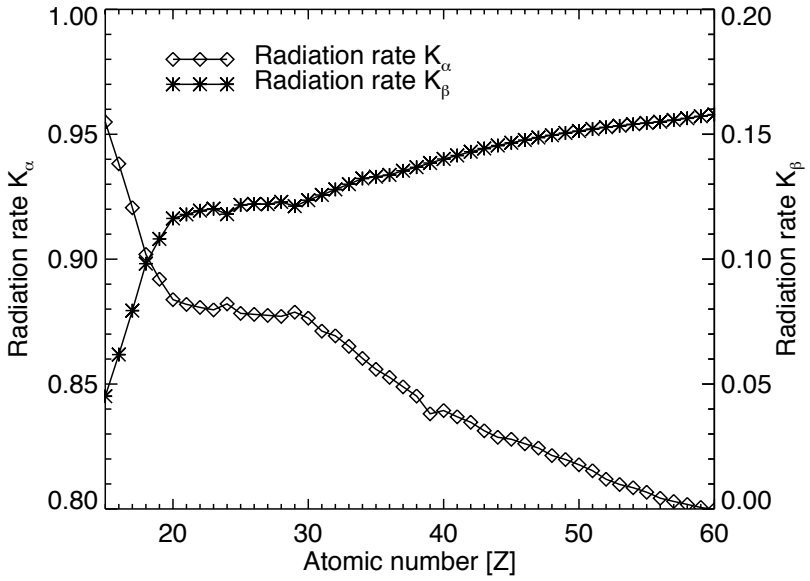

Figure 6.25: K_α and K_β radiation rates as a function of the atomic number.

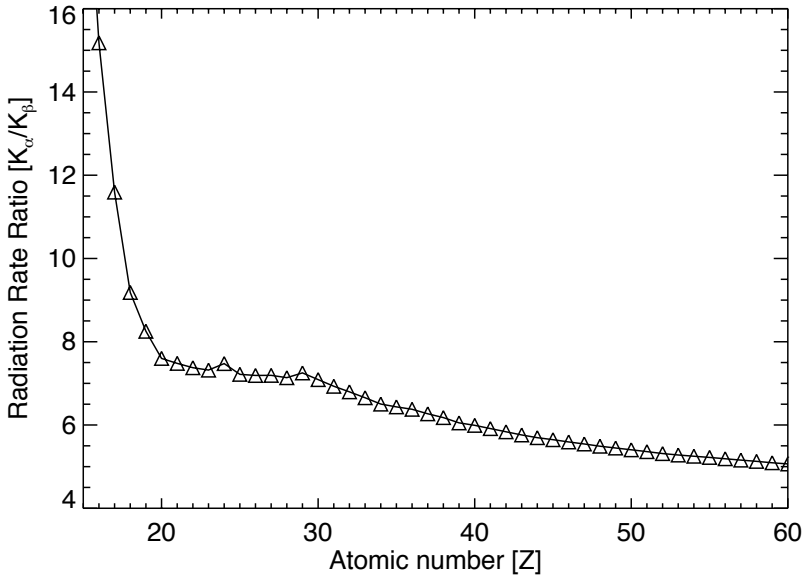

Figure 6.26: K_α and K_β ratio as a function of the atomic number.

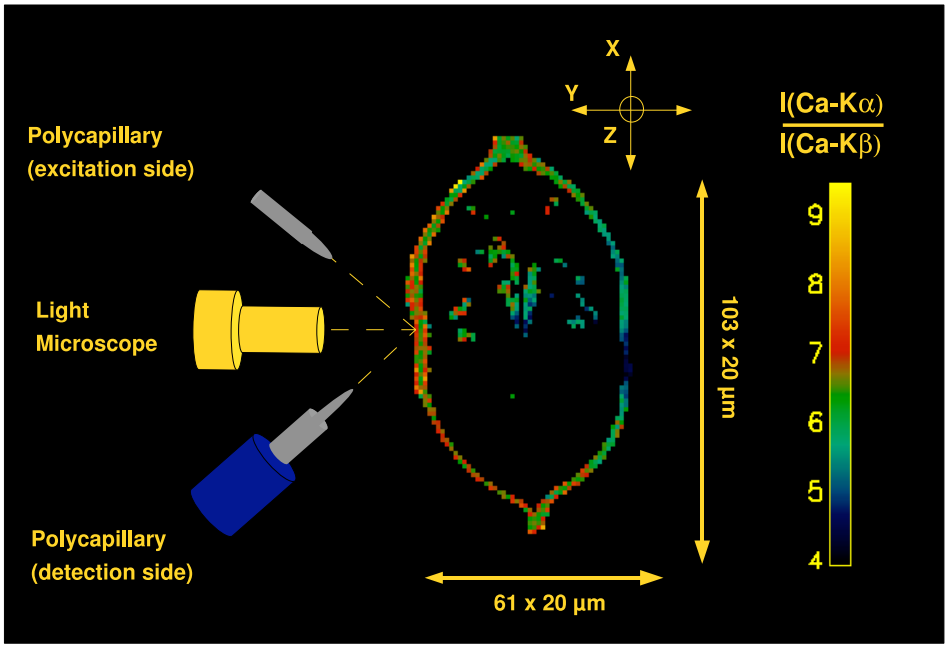

Figure 6.27: Experimental set-up which explains the changes in K_α / K_β intensity.

$$\mu_{Zn-K_\alpha} d \approx \mu_{Ca-K_\alpha} d \left(\frac{E_{Ca-K_\alpha}}{E_{Zn-K_\alpha}} \right)^3 \tag{6.12}$$

$$\approx 1.738 \times 0.078 \tag{6.13}$$

$$\approx 0.135 \tag{6.14}$$

$$\ll 1 \tag{6.15}$$

6.5.5 3D confocal micro-XRF

In the previous sections, 2D elemental distributions of *Daphnia magna* were obtained using confocal micro-XRF. However, due to the local principle of confocal micro-XRF, the scanning times for virtual sections is drastically reduced as compared to micro-XRF CT, allowing the visualisation of elemental distributions in three dimensions. In this section we demonstrate a three-dimensional elemental analysis of a single egg of *Daphnia magna*. An individual egg was extracted from *Daphnia magna* which underwent chemical fixation with HMDS as described in Chapter 3. Then, the extracted egg was glued on the tip of a carbon capillary. The sample was precharacterised at the X-Ray Tomography facility at Ghent University. A 3D visulation of the sample is shown in Fig. 6.28. The image clearly shows a spherical structure of about 300 μm in diameter. The glue and the carbon capillary can clearly be distinguished.

The 3D confocal micro-XRF analysis was performed at Beamline L, HASYLAB, Hamburg,

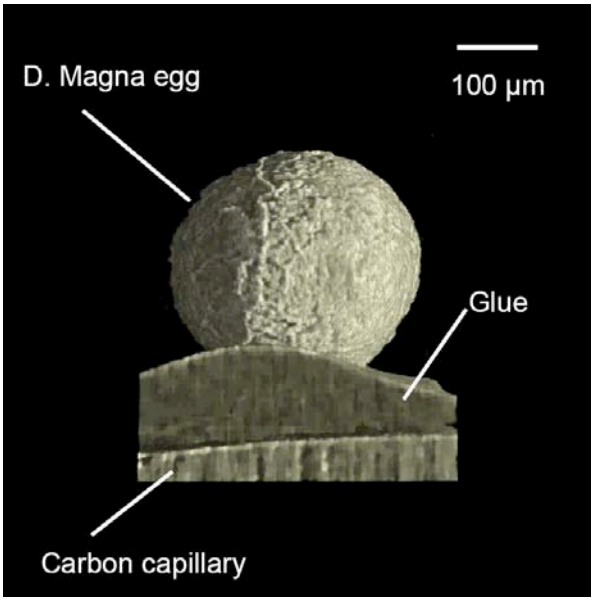

Figure 6.28: Absorption micro-CT of an egg of *Daphnia magna*.

Germany. The confocal set-up as described in previous sections was used. By means of three subsequent line scans the centre of the sperical sample was determined. In order to limit the amount of voxels measured which contain air, only the central part of the egg was measured. A total of 16 vertical parallel planes through the central part of the egg were measured with a spacing of 10 μm between the subsequent images. The planes were measured by dynamic (continuous) scans with a pixel size of 5 μm, which resulted in elemental maps of 295 μm by 335 μm. A total amount of 63248 spectra were afterwards fitted using AXIL and MICROXRF2. Elemental maps of Ca, Fe and Zn of a single slice through the sample are shown in 6.29. Three cavities are clearly present within the spherical structure of the egg. A strong overlap between the elemental distributions of Ca, Fe and Zn is present. Minor differences can be observed among these distributions: (1) self-absorption effects can be seen for the Ca distribution. (2) Fe shows some extra cavities as compared to the Zn distribution, and some additional hot-spots can be observed at the positon of the glue. A striking difference is observed when comparing distributions corresponding to Compton scattering. The first hollow cavity, which is present for the Zn, Fe and Ca distributions, clearly generates a Compton scattering signal, which is comparable to the rest of the bulk matrix in terms of counts. This is an indication for a non-metal containing low Z matrix comparable to the rest of the sample. Moreover, these results correspond perfectly to the absorption micro-CT results: a comparison of both measurement is shown in Fig. 6.30. In the absorption micro-CT data even a slight difference in density can be observed between the 3^{rd} cavity and the bulk composition, which is an indication that the material has indeed a different composition.

A possible explanation could be that the HMDS fixating solution entered into this cavity. Interestingly, this could mean that very little leaching of metals from the sample towards the fixating polymer HMDS occurs, as described in Chapter 3.

As described in the introduction, one of the aims of this scan was to illustrate the full 3D abilities of confocal micro XRF. Also, having a full 3D elemental distribution is very interesting to compare with the full 3D density distribution. In Fig. 6.31, the sixteen different confocal slices are visualised. Here, the need for full 3D imaging is demonstrated, the hollow structures are visible in every slice, but unfortunately no thorough 3D information is present in these data. Therefore, in a second data processing procedure, the data was transformed into a properly scaled data matrix and visualised with IDLs XVOLUME utility, used for viewing and interactively manipulating volumes and isosurfaces. Since the scanning resolution was 10 μm in depth and 5 by 5 μm in the scanning plane, an appropriate transformation of the datamatrix was necessary. Also, the threshold value of the isosurface was optimised in order to obtain a clear visualisation of the data. Finally, color and opacity were adjusted in order to obtain a good visual image. With IDLs XVOLUME ROTATE procedure, the volume displayed in XVOLUME was rotated. Fig. 6.32 shows the Fe isosurface under 4 different angles rendered in this way. In this image the threshold value was chosen just at the interface solid gas in order to visualise the different cavities in the egg. It is now possible to image the 5 different cavities at once, which could not be observed from the series of images in Fig. 6.31. Moreover, if with the XVOLUME ROTATE procedure, isosurfaces are rendered at each degree and the specified image array can be stored at the specified frame index in an MPEG sequence using IDLs MPEG PUT procedure.

However, the data shown in the previous image is only concerning a single element. Only one isosurface of a certain element can be interpreted. For visualizing 3D multi-element isosurfaces, a similar procedure was used as previously discribed. The isosurfaces for Compton scattering, Fe and Zn were generated and each assigned a color channel red, green and blue. The RGB composed image was then generated. In Fig. 6.33, the isosurfaces for Compton scattering, Fe and Zn are assigned respectively the colors blue, green and red which can be seen on the left. The combined RGB image can be observed on the left. From the image it can be seen that the Zn, Fe and Compton isosurfaces coincide at the external part of the egg, seen from the white color. This is also the case for three cavities, which tells us that these cavities are indeed hollow. However, the other two cavities show a yellow collor, which indicates that besides a density similar to the bulk, no Fe nor Zn are present inside these cavities. This is in perfect correspondence with the previously shown results from the absorption micro-CT datasets. Additionally one can also see some Fe and Zn grains present in the glue and the blue Compton isosurface, indicating the boundaries of the glue on the capillary. As previously mentioned, also these images can be combined into a full 3D multi-element animation.

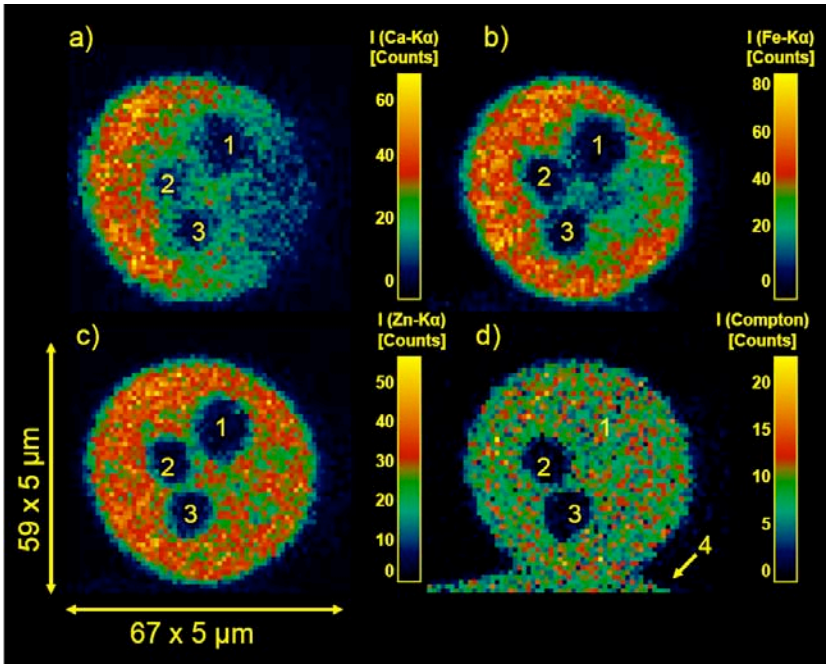

Figure 6.29: Distributions of Ca, Fe, Zn and Compton scattering within a single slice through the egg obtained by confocal micro-XRF. Area **1** contains virtually no trace elements and has a density similar to the bulk matrix, area **2** and **3** also contain few trace elements, but appear to be hollow. Also the capillary **4** shows Compton scattering but no Ca, Fe or Zn fluorescence.

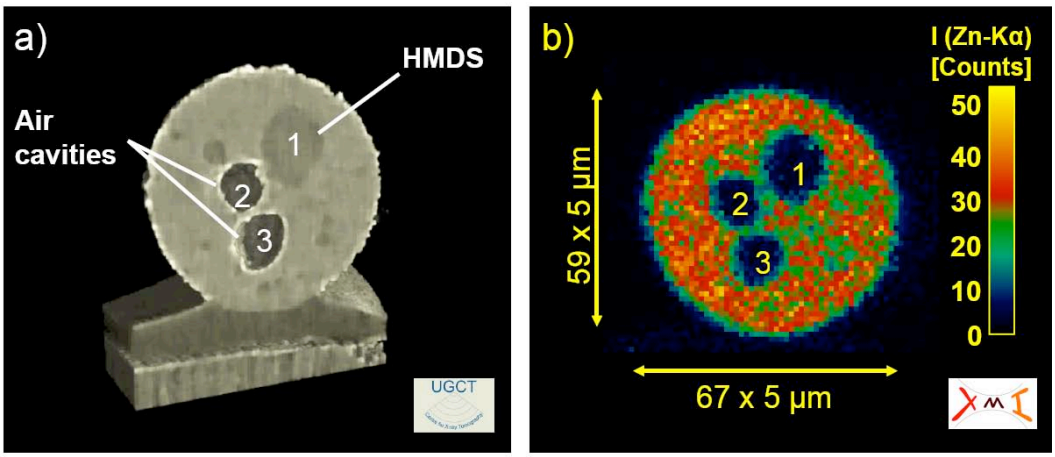

Figure 6.30: Comparison of the absorption micro-CT and micro-XRF element map. Areas **2** and **3** are indeed hollow cavities, whereas area **1** seems to be a hollow area filled up with HMDS.

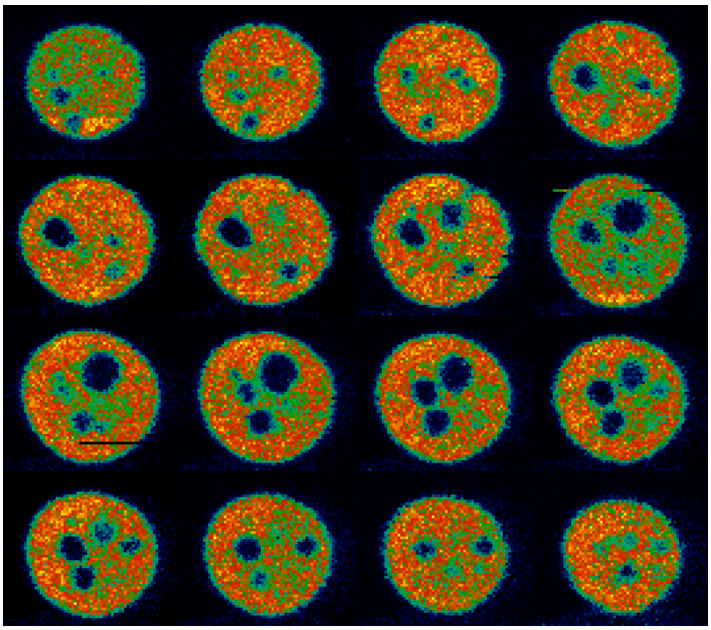

Figure 6.31: 16 subsequent confocal element slices of the *Zn* distribution in a *Daphnia magna* egg.

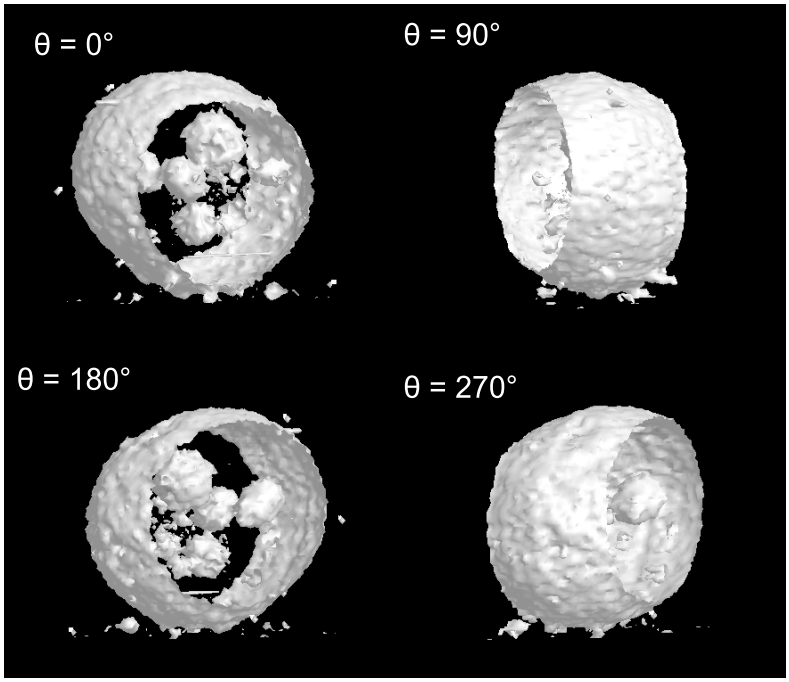

Figure 6.32: *Fe* isosurface visualised under 4 different angles.

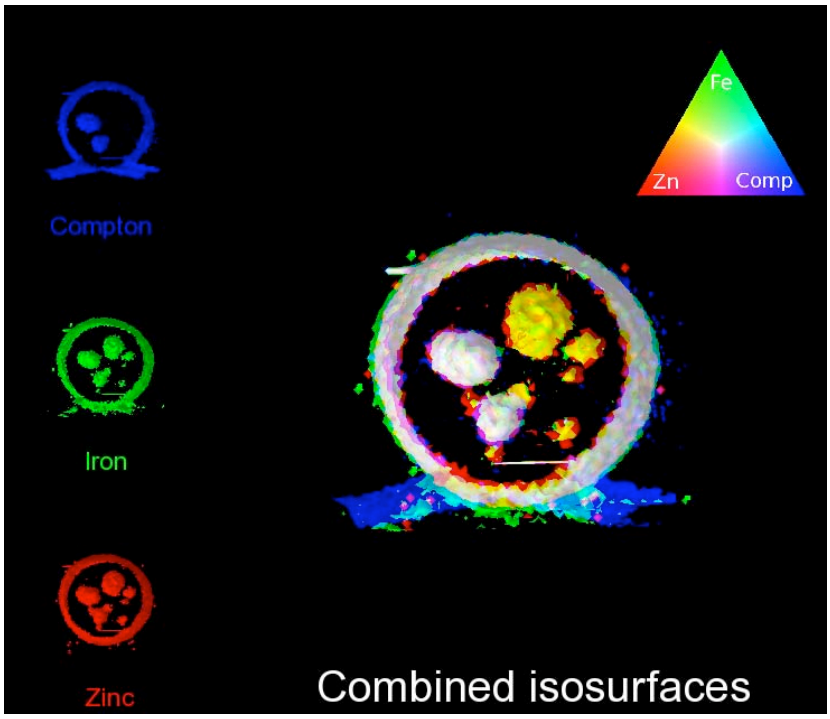

Figure 6.33: 3D multi-element rendering of a single egg of *Daphnia magna*.

Chapter 7

Micro-XAFS on *Daphnia magna*

7.1 Introduction

In the previous chapters, we investigated the tissue-specific differences in metal accumulation for *Daphnia magna* samples, subjected to various levels/routes of Zn-exposure by means of laboratory and synchrotron based 2D/3D micro-XRF methods. The energy tunability of synchrotron radiation allows to investigate how X-rays are absorbed by an atom at energies near and above the core-level binding energies of the atoms of an element of interest. X-ray Absorption Fine Structure (XAFS) represents the modulation of an atom's X-ray absorption probability due to the chemical and physical state of the atom. Since all atoms have core level electrons, XAFS spectra can be measured for essentially every element on the periodic table. Importantly, measurements can even be performed on minor and trace level elements and crystallinity is not required for XAFS measurements, making it one of the few structural probes available for biological samples. With the use of sophisticated focusing optics (e.g. Fresnel zone plates, KB-mirrors, compound refractive lenses and dispersive sagittal focusing) micro-XAFS can be performed, providing information of the chemical state of an element within an area of interest. With the use of polycapillary lenses confocal-XAFS can be performed, providing information of the chemical state of an element within a well-defined volume of interest (Silversmit *et al.*, 2009). A more detailed description of the theoretical aspects of XAFS is given in 7.2. In section 7.3, the conventional and confocal micro-XAS set-up used at the Dutch Belgian Beamline (DUBBLE) at the European Synchrotron Radiation Facility (ESRF) in Grenoble, France are described. As discussed in Chapter 3, an important research topic is to gain information of the chemical state of the metal accumulations of interest within *Daphnia magna* since they determine to an important extent their bioavailability. Metals can bind physiologically inert binding sites used for detoxification of an excess of metals, e.g. metallothionine, membrane limited vesicles, precipitated Ca/Mg or Ca/S granules. They can also bind physiologically active binding sites, e.g. metallo-enzymes, resulting in damage to the cell metabolism. Therefore, the experimental set-up was used to perform conventional

and confocal micro-XANES on *Daphnia magna* in Section 7.5.

7.2 Theoretical aspects of XAFS

The theoretical aspects of X-ray Absorption Fine Structure (XAFS) spectroscopy are discussed in detail by Newville (2009). For XAFS, the absorption μ is measured as a function of energy, near and at energies just above the absorption edges. When the incident X-ray has an energy equal to that of the binding energy of a core-level electron, there is a sharp rise in absorption: an absorption edge corresponding to the promotion of this core level to the continuum. A XAFS measurement probes the energy dependence of μ just below and above the binding energy of a known core level of a known atomic species. Since every atom has core-level electrons with well-defined binding energies, in principle we can select the element to probe by tuning the X-ray energy to an appropriate absorption edge. The absorption edge energies are well-known and tabulated. The edge energies vary with atomic numbers approximately with Z^2, but both K and L levels can be used in the hard X-ray regime (in addition, M edges can be used for heavy elements), which allows most elements to be probed by XAFS with X-ray energies between 5 and 35 keV. In case of hard X-ray microprobes working in air sample environment, a practical limitation is encountered due to X-ray absorption by the sample environment gas, as well as limitations in reaching X-ray excitation below ≈ 5 keV. This limits the elements to be studied at these beamlines by XAFS to $Z \geq 22$. XAFS on lighter elements requires specialised low-energy beamlines operating in vacuum.

For concentrated samples, the energy dependence of the linear attenuation coefficient $\mu(E)$ is measured in transmission mode. In transmission mode, two ionisation chambers are used: an ionisation chamber before the sample registers the incident X-ray intensity I_0, while the other registers the transmitted intensity I_t. A sufficient transmission through the sample to get a detectable signal for I is necessary. Therefore, the sample thickness t is adjusted so that $\mu t \approx 2 - 2.5$ above the absorption edge. The measured linear attenuation coefficient can then be determined according to the following formula:

$$\mu(E)t = ln\frac{I_0}{I_t} \tag{7.1}$$

For lower concentrations (down to the *ppm* level), monitoring the X-ray fluorescence is the preferred technique. In fluorescence mode, only one ionisation chamber before the sample registers the incident X-ray intensity I_0. An energy dispersive detector can then be used to register the X-ray fluorescence intensity I_f. In this case, the linear attenuation coefficient can be approximated according to:

$$\mu(E)t = \frac{I_f}{I_0} \tag{7.2}$$

XAFS occurs because the photo-electron can scatter from a neighboring atom. The scattered photo-electron can return to the absorbing atom, modulating the amplitude of the photo-electron wave-function at the absorbing atom, as shown schematically in Fig. 7.1. This in turn modulates the absorption coefficient $\mu(E)$, causing the EXAFS. Typically, the X-ray absorption spectrum is divided into two regimes: X-ray absorption near-edge spectroscopy (XANES) and extended X-ray absorption fine-structure spectroscopy (EXAFS). Fig. 7.2 shows the normalised absorption μ around the $Zn - K$ edge, indicating the XANES and EXAFS region.

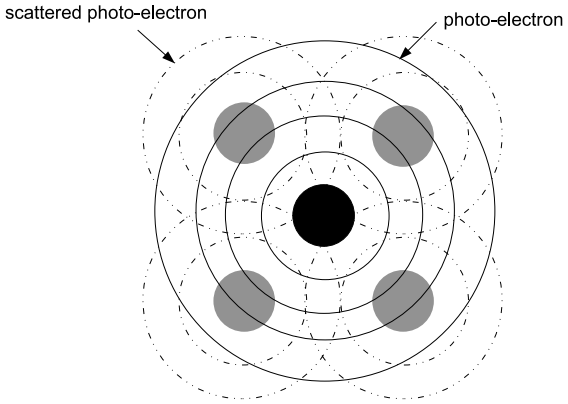

Figure 7.1: Scattered photo-electron waves from neighboring atoms which return to the absorbing atom.

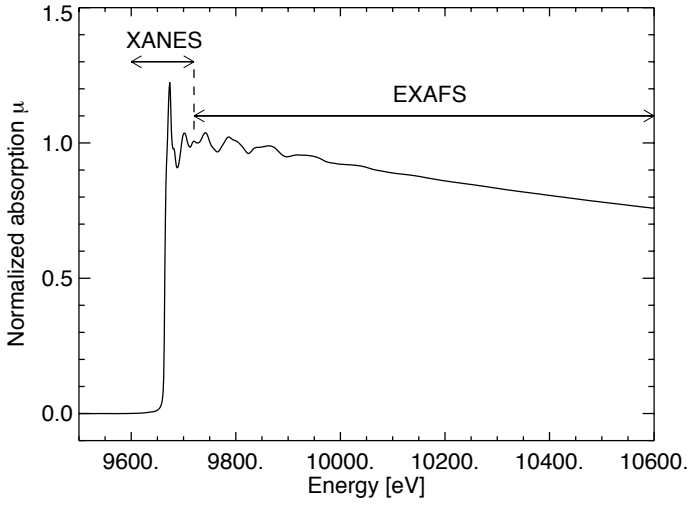

Figure 7.2: Normalised absorption μ around the $Zn - K$ edge recorded in transmission mode on a thin Zn foil, indicating the XANES and EXAFS region.

There is a wealth of chemical information which can be obtained by the analysis of the XANES region. The edge position and shape is sensitive to the formal valence state, ligand type, and coordination environment. XANES can be used as a fingerprint to identify molecular phases. An important and common application of XANES is to use the shift of the edge position to determine the valence state. With good model spectra, valence state ratios can be determined with very good precision and reliability. The heights and positions of pre-edge peaks can also be reliably used to empirically determine oxidation states and coordination chemistry. These approaches of assigning formal valence state based on edge features and as a fingerprinting technique make XANES somewhat easier to crudely interpret than EXAFS, even if a complete physical understanding of all spectral features is not available.

For the EXAFS, oscillations well above the absorption edge are of importance and therefore the EXAFS fine-structure function $\chi(E)$ is defined as:

$$\chi(E) = \frac{\mu(E) - \mu_0(E)}{\Delta\mu_0(E)} \tag{7.3}$$

where $\mu(E)$ is the measured absorption coefficient, $\mu_0(E)$ is a smooth background function representing the absorption of an isolated atom, and$\Delta\ \mu_0$ is the measured jump in the absoption $\mu(E)$ at the threshold energy E_0.

However, EXAFS is best understood in terms of the wave behavior of the photo-electron created in the absorption process. Because of this, it is common to convert the X-ray energy to k, the wave number of the emitted photo-electron, which has dimensions of 1/distance and is defined as:

$$k = \sqrt{\frac{2m(E - E_0)}{\hbar^2}} \tag{7.4}$$

where E_0 is the absorption edge energy and m is the electron mass. The primary quantitity for EXAFS is then $\chi(k)$, the oscillations as a function of photo-electron wave number. $\chi(k)$ is oscillatory and decays quickly with k. In order to enhace the oscillations towards larger k-values, $\chi(k)$ is often multiplied by a power of k typically K, k^2 or k^3.

The different frequencies apparent in the oscillations in $\chi(k)$ correspond to different near-neighbor coordination shells which can be described and modeled according to the EXAFS equation:

$$\chi(k) = \sum_j \frac{N_j f_j(k) e^{-2k^2\sigma_j^2}}{kR_j^2} sin(2kR_j + \delta_j(k)) \tag{7.5}$$

where $f(k)$ and $\delta(k)$ are the backscattering amplitude and the phase-shift respectively (scattering properties of the atoms neighboring the excited atom). N represents the number of neighboring atoms, R is the distance to the neighboring atom, and σ^2 is a measure for the

disorder in the neighbor distance. Though somewhat complicated, the EXAFS equation allows us to determine N, R, and σ^2 knowing the scattering amplitude $f(k)$ and phase-shift $\delta(k)$ from reference structures or calculations. EXAFS can thus be used to determine the distances, coordination number, and species of the neighbors of the absorbing atom.

7.3 DUBBLE, a synchrotron XAFS beamline

The micro-XAFS test experiments on *Daphnia magna* were performed at the Dutch-Belgian beamline (DUBBLE), a collaborative research group (CRG) beamline at the European Synchrotron Radiation Facility (ESRF). The DUBBLE beamline has an incident energy range with a reasonable flux from 4.9 to 30 keV of about $1\times10^{11} photons/sec$. In order to accurately determine $\mu(E)$, a monochromator with a high energy resolution and stability is required. The $Si(111)$ monochromator installed at the DUBBLE beamline has an energy resolution $\Delta E/E = 2 \times 10^{-4}$. For transmission measurements two ionisation chambers are already sufficient for adequate measurements: for this DUBBLE has low noise ionisation chambers from Oxford instruments. For fluorescence measurements it has a 9 element monolithic Ge detector with a maximum count rate per element of 150 kHz and an energy resolution of 250 eV at 5.9 keV. If no optics are used to focus the beam, the beamsize upon the sample can be modified from 0×0.2 mm^2 until 30×3 mm^2.

7.4 Characterisation of the micro-XAS set-up

The micro-XAS set-up was characterised in detail in Silversmit *et al.* (2009). Microfocusing was achieved using a large-acceptance polycapillary lens with an entrance diameter of 5 mm, an optic length of 50 mm, an exit diameter of 1.6 mm and a focal distance of 3.6 mm manufactured by XOS, specifically designed for the beam characteristics of DUBBLE (i.e. with respect to source size/divergence, source-sample distance, bending magnet energy range). In order to characterise the microbeam size and the depth of focus, the vertical FWHM of the focused beam was recorded as a function of the distance from the polycapillary tip at an X-ray energy of 11.6 keV by means of a Au knife-edge scan. As shown in Fig. 7.5, the optimal beam size is reached at a distance of 3.6 mm from the polycapillary exit. The optimal X-ray beam size at this distance was determined by horizontal and vertical knife-edge scans to be 14.8 μm (V) $\times$ 15.7 μm (H) (incident energy = 11.6 keV). The variation of the vertical beam size as a function of X-ray energy is given in Fig. 7.6. For these measurements the beamline optics was optimized for an X-ray energy of 11.6 keV, and at each new energy value the height of the polycapillary was re-optimized towards a maximum transmitted signal. For an X-ray energy of 11.6 keV a smaller value compared with Fig. 7.5 is now obtained, owing to a re-alignment of the polycapillary.

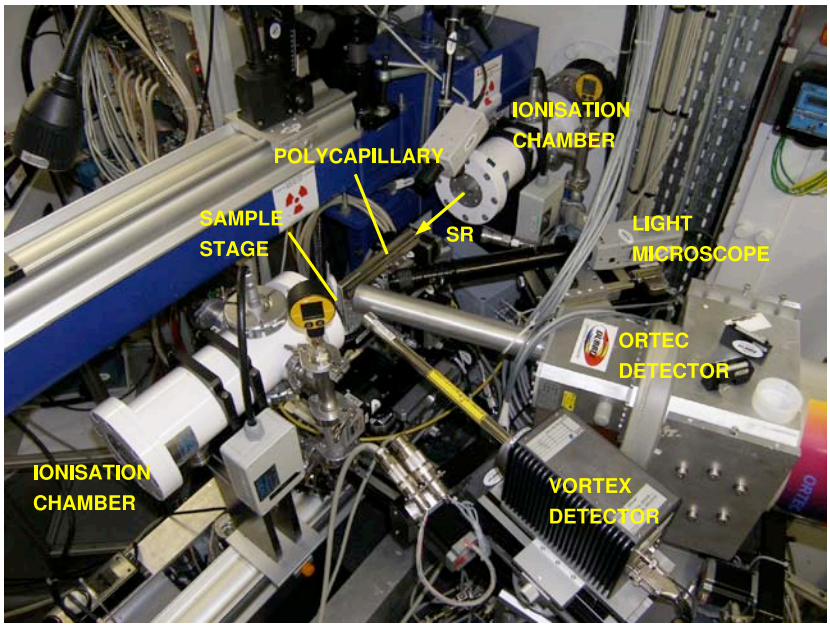

Figure 7.3: Overview of the experimental set-up at DUBBLE.

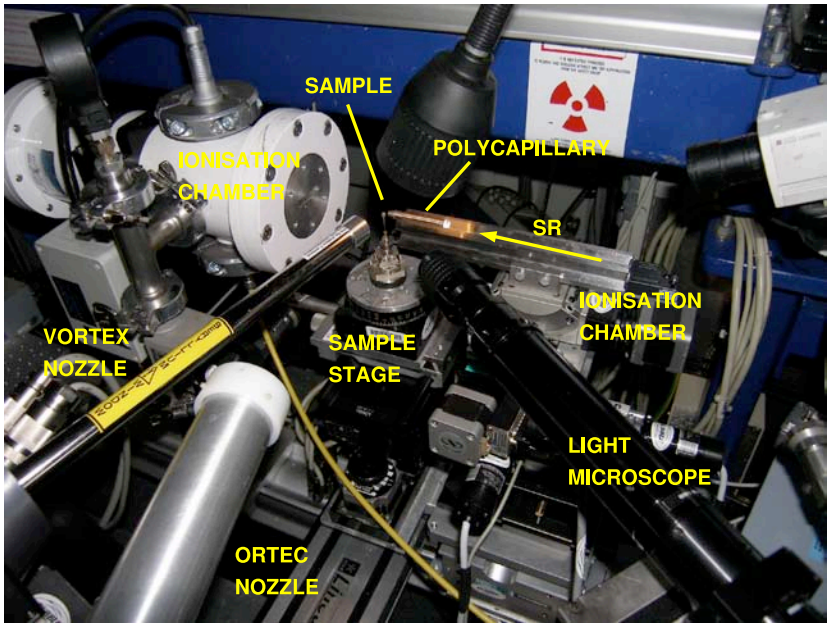

Figure 7.4: Zoom of the experimental set-up at DUBBLE.

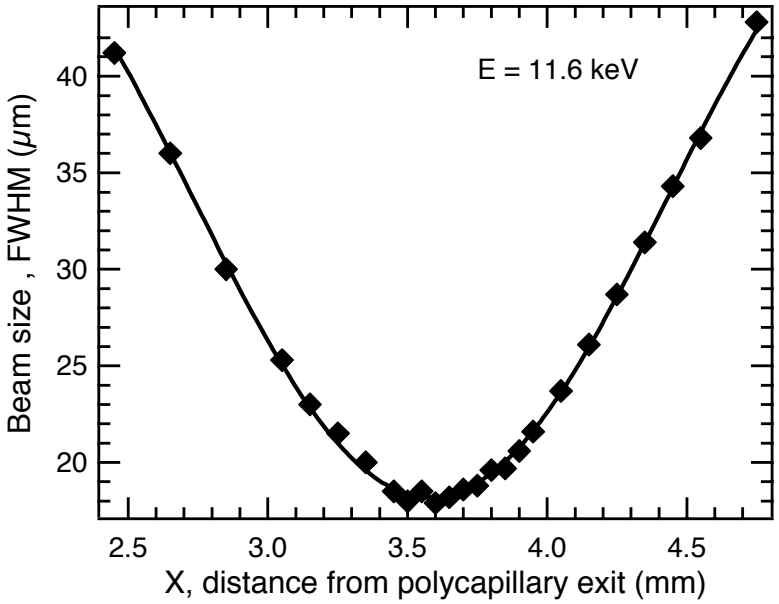

Figure 7.5: Measured vertical FWHM (μm) of the polycapillary focused microbeam as a function of the distance from the polycapillary exit window for an incident X-ray energy of 11.6 keV.

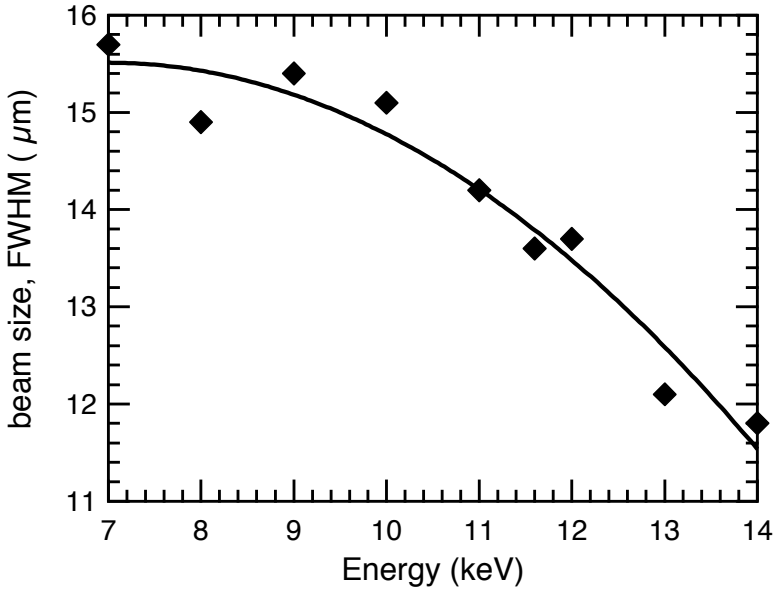

Figure 7.6: Measured vertical FWHM (μm) of the polycapillary focussed microbeam as a function of incoming X-ray beam energy, determined by vertical Au knife-edge scans in the focal plane of the polycapillary.

The $Si(111)$ double-crystal monochromator at DUBBLE is operated in a non-fixed-exit mode, implying that the height of the monochromated beam changes with energy. The vertical movement of the incoming beam on the polycapillary can thus influence the position of the focused beam spot. After optimisation of the beamline optics at 9.6 keV, X-ray images of the microbeam in the focal plane for different X-ray energies ranging from 7 to 12 keV were taken. From these images, vertical and horizontal beam profiles and positions were obtained by summing the total intensity in each data-row or column respectively, providing Gaussian distributions of the microspot. Fig. 7.7 shows the resulting vertical and horizontal profile positions as a function of the incoming X-ray beam energy. A constant horizontal beam position with energy (between 7 and 12 keV) can be assumed. The vertical position slightly changes with increasing energy, from 7 to 12 keV this shift was ≈ 2.7 μm. This figure also shows, that in case of a typical EXAFS experiment (scanned energy range ≈ 1 keV), the vertical movement of the focused beam is ≤ 1 μm. Taking into account that the focused beam size is > 10 μm, this vertical shift is considered acceptable.

The energy dependence of the polycapillary lens transmission efficiency (ϵ) is shown in Fig. 7.8. The efficiency decreased as a function of energy from 45 % to 25 % in the 7-14 keV energy range. The flux-density or intensity gain factor (G) of the polycapillary lens can be calculated based on the measured transmission efficiency and the corresponding beam size as $G = \epsilon S_{input}/S_{focal}$, where S_{input} and S_{focal} are the beam cross sections at the entrance of the polycapillary and in the focal plane. Since with increasing energy, both the polycapillary lens transmission efficiency (ϵ) and the size of the microbeam decrease, the flux density gain varies only slightly in the energy range 7-14 keV, showing an average value of approximately 2000.

7.5 Experimental results

7.5.1 Conventional micro-XAFS

Transmission and Fluorescence micro-XAFS on SRMs

Transmission XAFS spectra of a Zn foil, ZnO and $Zn_3(PO_4)_2$ powder were recorded with and without a focusing polycapillary for an incoming beam size of 0.5×2 mm. Generally, the spectra taken with the polycapillary focusing have different slopes in the pre- and post-edge region. This is due to the smoothly changing transmission efficiency of the polycapillary with X-ray energy. The transmission function $\epsilon(E)$ of the polycapillary can be used to correct for this effect. If $\mu x' = ln(I_0/I_t')$ applies for the focused case and the relation $I_t' = I_t\epsilon(E)$ gives the relation between the transmission for the focused and non-focused case, then the corrected absorption spectrum is given by $\mu x_{corr} = ln(I_0\epsilon(E)/I_t')$. After correction, the slopes of the pre-edge and post edge regions are very close to the transmission spectrum without focusing.

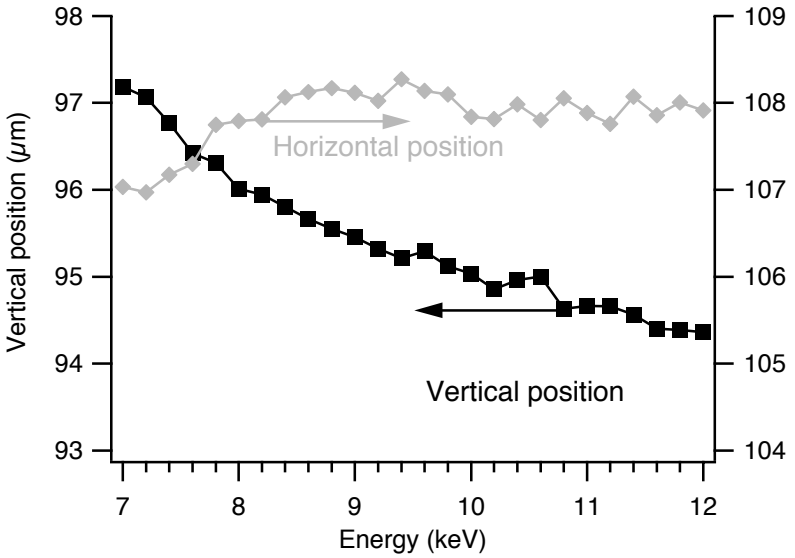

Figure 7.7: Vertical and horizontal beam positions in the focal plane as a function of incoming X-ray energy.

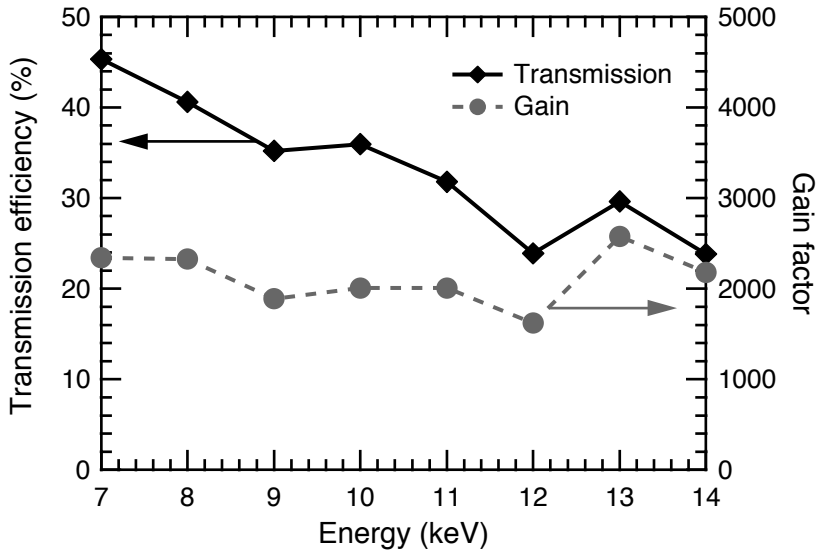

Figure 7.8: Polycapillary transmission efficiency and gain factor as a function of incoming X-ray energy.

It should be noted that there is no need to correct the EXAFS spectra for the polycapillary transmission function, as for all samples the corrected EXAFS spectra and Fourier transforms are identical with the uncorrected polycapillary spectra (Silversmit *et al.*, 2009).

A micro-XRF spectrum of a pellet of NIST SRM 1577B (18.7 mg, 6.5 mm diameter), excited with a focused beam of 11.61 keV was recorded with the ORTEC detector using a measuring time of 300 s. For Zn, an absolute detection limit for the fluorescence emission of about 4 fg (0.2 ppm) can be deduced. $Zn-K$ XAFS spectra were taken in fluorescence mode with a beam spot $FWHM$ of about 15 μm at the $Zn-K$ edge (9.6 keV) as shown in Fig. 7.9. This results in a probed Zn mass of about 3 pg (if no self absorption is assumed, so the real probed mass will be lower). The $Zn-K$ EXAFS spectra $k^1 * \chi(k)$ and corresponding $FT(k^2 * \chi(k))$ of the NIST SRM 1577B pellet recorded in fluorescence mode with the focusing polycapillary are given in Fig. 7.10 and Fig. 7.11. Both spectra are identical with and without the focusing polycapillary optic, since no effect of the polycapillary optic is present on the EXAFS spectra in the fluorescence mode.

Fluorescence micro-XANES on *Daphnia magna*

On a chemically fixed *Daphnia magna* exposed to 360 $\mu g/L$ of Zn as described in Chapter 3, a full 2D micro-XRF mapping was performed, in order to locate the Zn rich regions. Map dimensions were 121 μm × 20 μm (H) by 126 μm × 20 μm (V). During the mesh scan, ROIs of Zn, Ca en ICR (total count rate) windows were recorded, which are given in Fig. 7.12. $Zn-K$ micro-XANES spectra in fluorescence mode were taken on two eggs and in the digestive channel of which the spectra are given in Fig. 7.13 and compared to Zn, ZnO, $Zn_3(PO_4)_2$ and NIST SRM1577B. The local Zn environment in the two eggs appears to be identical, while the spectrum taken on the digestive channel has significant changes compared to the eggs, indicating that Zn reveals a tissue-specific local environment. The XANES spectrum in the eggs also matches very well with that obtained from NIST SRM1577B. In order to completely identify the spectra, more reference materials are required, which was not within the scope of this explorative study. Since detoxified Zn is often chelated with metallotheonin or condensed in granules, compounds such as Zn-cysteine, Zn-oxalate, $ZnPO_4$, ZnS and $ZnCl_2$ could represent important reference materials.

7.5.2 Confocal micro-XANES

In the previous section, micro-XANES recorded spectra represent delivered information concerning the tissue-specific local environment of Zn. However, these spectra still represent the full line integral along the beam penetrating the sample and could therefore also include the local environment before or behind the target tissue. Therefore, the possibility of confocal micro-XANES was explored, which could allow the determination of the local environment of Zn within a specific subvolume within a target tissue. On the same *Daphnia magna* sample

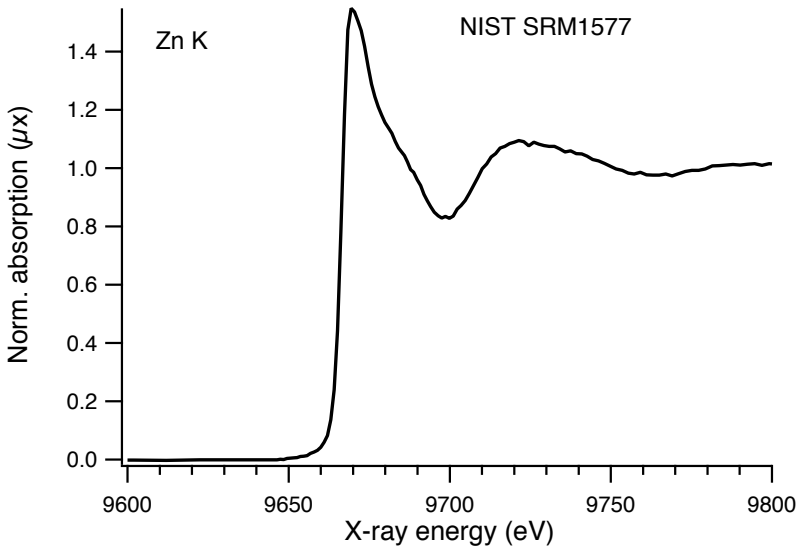

Figure 7.9: Normalised $Zn-K$ fluorescence spectra of NIST SRM 1577B recorded with polycapillary focusing.

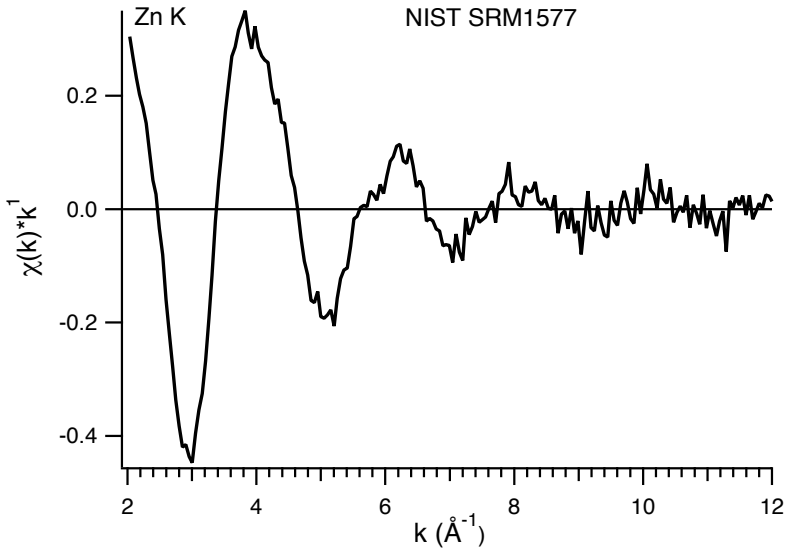

Figure 7.10: $Zn-K$ fluorescence $k^1 * \chi(k)$ EXAFS spectrum measured from NIST SRM 1577B recorded with polycapillary focusing.

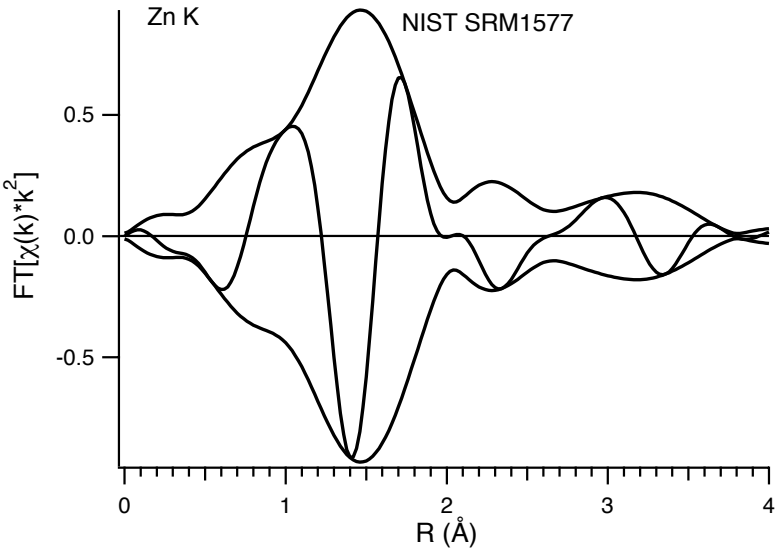

Figure 7.11: $Zn-K$ fluorescence $FT(k^2 * \chi(k))$ EXAFS spectrum measured from NIST SRM 1577B recorded with polycapillary focusing.

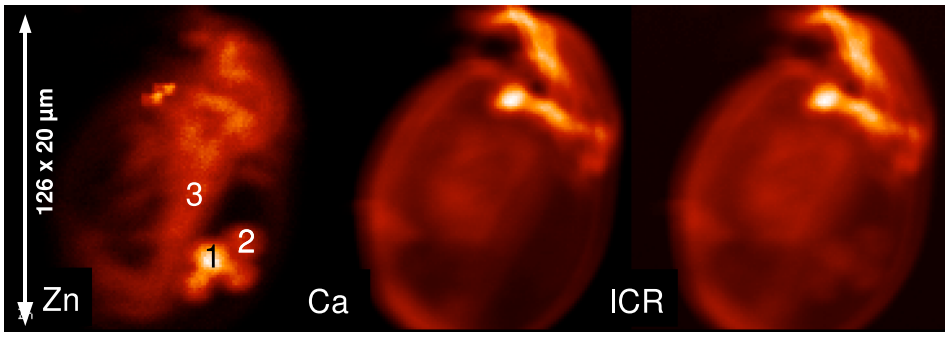

Figure 7.12: Element maps corresponding to the measured Ca and Zn intensities (derived from simple ROI integration) and incoming count rate (ICR) map. The locations analysed by micro-XANES are indicated by 1-3.

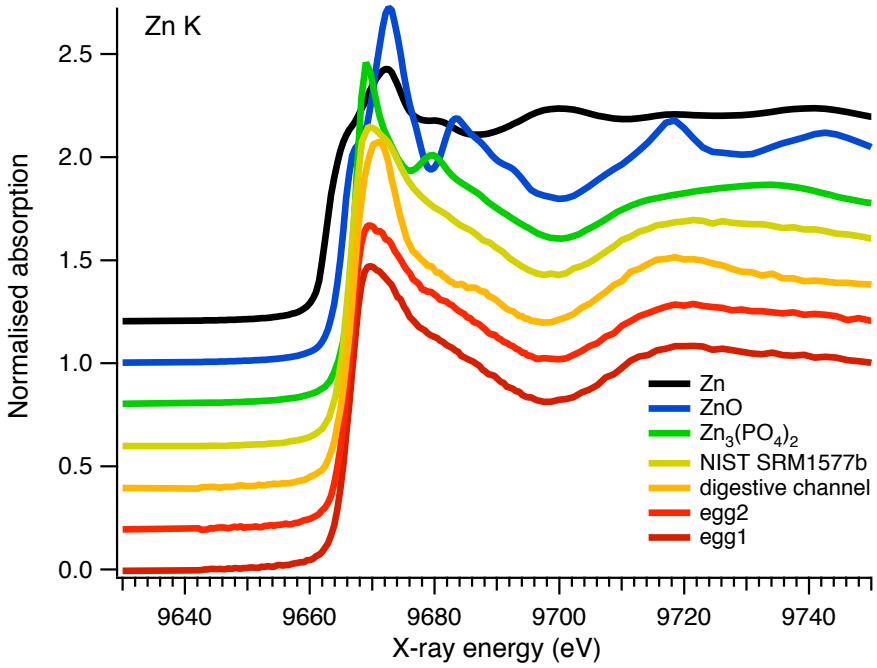

Figure 7.13: Normalised $Zn-K$ fluorescence XANES spectra of different reference materials and different regions measured on *Daphnia magna*.

used for the conventional micro-XANES, a dorsoventral section (vertical size: $134 \times 15\ \mu m$, horizontal size: $80 \times 15\ \mu m$) was performed in order to locate the Zn rich regions, which are shown in Fig. 7.14.

A $Zn-K$ micro-XANES spectra in confocal mode was obtained within a single egg (lower right in Fig. 7.14) as shown in Fig. 7.15. The confocal micro-XANES spectrum shows good agreement with the conventional micro-XANES spectrum of a single egg, showing that the confocal detection does not introduce significant artefacts in the XANES spectrum.

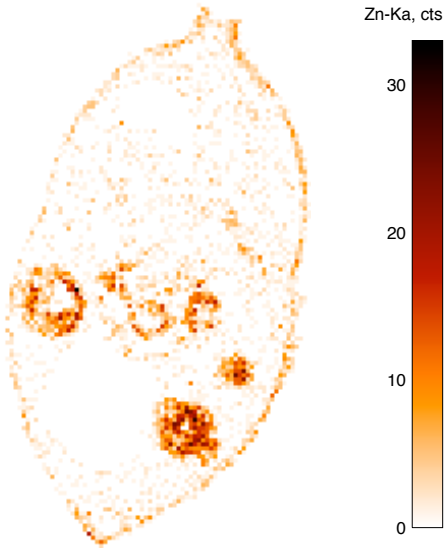

Figure 7.14: *Zn* distribution within a virtual dorsoventral section of *Daphnia magna*, obtained by confocal micro-XRF

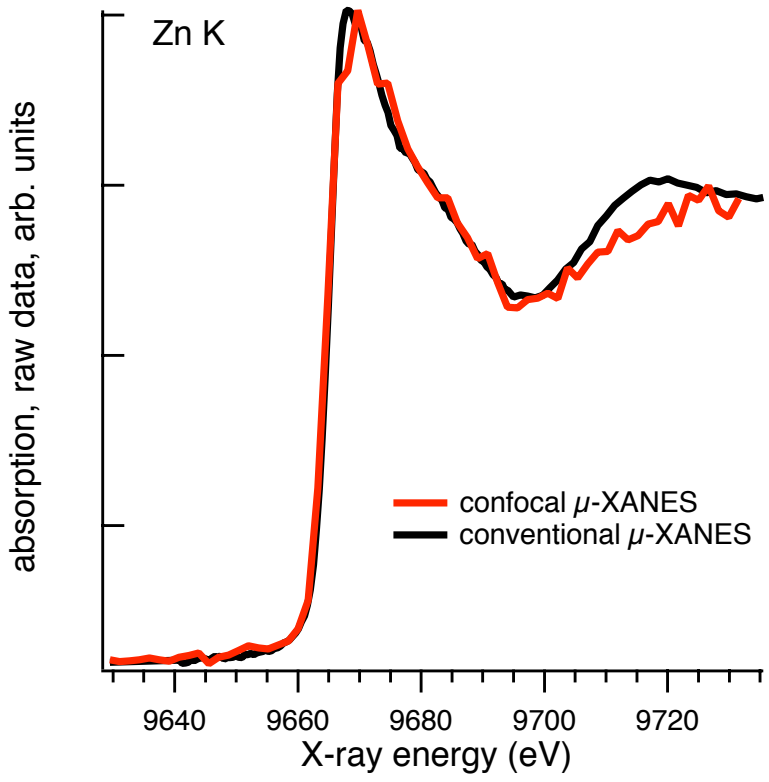

Figure 7.15: Conventional and confocal micro-XANES on *Daphnia magna*.

Chapter 8

Nano-XRF on *Daphnia magna*

8.1 Introduction

In the previous chapters, we discussed the chemical distribution and speciation of Zn using respectively synchrotron radiation based micro-XRF and micro-XAFS. Another point of interest concerns the non-destructive intra- and intercellullar determination of toxic metal distributions within *Daphnia magna*. Recently, nanobeams of hard X-rays providing unprecedented spatial resolutions are being obtained at synchrotron facilities allowing the visualisation of the intra- and intercellullar distribution of trace level metals. In what follows, a nano-XRF experiment on *Daphnia magna* is described, exploiting the unmatched combination of submicroscopic resolution and world leading X-ray nanobeam intensity, available at the ESRF ID22NI nanoprobe. A technical description and analytical characterisation of the employed nano-XRF setup are given in Section 8.2 and 8.3. Conventional and confocal nano-XRF is finally applied on respectively thin sections of *Daphnia magna* and the entire organism in Section 8.5 in order to investigate the accumulation of Zn at the subtissue level.

8.2 ID22NI, a synchrotron XRF nanoprobe

The ID22NI end-station is dedicated to hard X-ray nanoanalysis allowing nano-XRF, nano-XRD and absorption/phase-contrast tomography. The end-station is installed at a high-β straight section equipped with two different undulators covering an energy range of 6-70 keV. The optical layout of the associated ID22NI beamline is shown in Fig. 8.1, including several pairs of slits, a flat vertical mirror and a monochromator. The optical elements are moveable in such a way that any of the various beam modes (white, pink, monochromatic, monochromatic + reflected) can reach the experimental hutch. The role of the first optical element of the beamline, a flat horizontally deflecting Si mirror, is twofold: as a low-pass filter it reduces the higher harmonic content of the X-ray beam and moderates the heat load on the monochromator crystals. The Si crystal itself and two different coatings, Pd and Pt,

are available for choosing the cut-off energy of the primary beam (Somogyi *et al.*, 2004).

When operated in pink beam mode it uses a perpendicularly crossed elliptical *Rh*-coated mirror-pair in the Kirkpatrick-Baez (KB) geometry for achromatic nanofocusing in the 6-18 keV energy range. The two elliptical-shaped mirrors collect and focus X-rays in both vertical and horizontal axis at glancing angle (3.5 $mrad$). Total-reflection mirrors are particularly attractive because of their achromaticity, broad bandpass, long working distance and high efficiency. The first mirror, coated with a graded multilayer plays both the role of vertical focusing device and monochromator selecting a given undulator harmonic from the incident pink beam, resulting in a very high flux ($2 \times 10^{11} photons/s$) and medium monochromaticity ($\Delta E/E$ 10^{-2}). Evaluation of the error contributions shows that the vertical focus is presently limited by the mirror figure errors, while the horizontal focus is limited by the horizontal extension of the X-ray source. The relatively large working distance ensures enough free space around the sample for the installation of beam monitors and various sample environments. Owing to the low divergence of the high-β source, a submicrometer horizontal spot size of relatively high intensity can still be achieved by creating a small ($<$ 100 mm) secondary horizontal source by closing the primary slit situated at 21 m from the focusing device (Hignette *et al.*, 2005).

The ID22NI XRF-nanoprobe is based on a Kirkpatrick-Baez system shown in Fig. 8.2, which is installed in Experimental Hutch 2. This KB-system consists of two invar benders, for the vertical and horizontal planes respectively, coated with a graded multilayer to increase the usable numerical aperture, crucial for the spatial resolution and photon flux. Invar as material choice improves the thermal stability, and in particular, the stability of the curvature of the elliptically shaped mirrors. The KB mirror-pair is enclosed in a He chamber to protect the mirrors from chemical surface damage and to ensure their thermal stability. To reduce temperature drift and/or hutch contamination, the standard in-hutch air conditioner was replaced by a complete air-exchange system, producing a thermal stability of 0.1 $^{\circ}C$. In order to avoid amplification of the mechanical vibrations, all instrumentation is mounted on

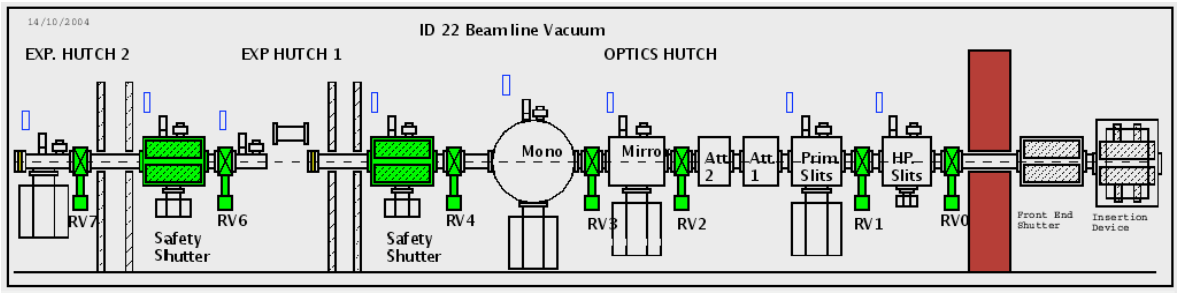

Figure 8.1: Optical layout of ID22NI.

a single table consisting of a concrete base and a 4.4 m long granite bed as shown in Fig. 8.3. Vibration measurements performed and experimental results indicate that this solution gives the required stability. The table has only one degree of freedom that allows adapting the height of the complete instrument to the pink or monochromatic beam mode.

The sample stage shown in Fig.8.4 combines a maximum of precision with excellent rigidity by means of a high resolution YZ nanopositioner (Physik Instrument) equipped with integrated capacitive sensors mounted on medium resolution XYZ stages. A standard positioning and retaining ring system, using the kinematic 3 balls & 3 vees principle was used. This standard ring provides a common base into which various holders can be housed to cater for a wide variety of samples and environmental conditions ranging from cryogenic to high temperatures or sealed cells for aqeous samples under vacuum. The design provides fast, accurate and dependable sample alignment and repositioning (Susini *et al.*, 2006). Since the nanopositioner is under normal incidence with respect to the incoming beam, a video microscope with pierced mirror looking along the beam allows for the precise determination of the focal plane, easy alignment of the sample followed by scanning a sub-cellular region of interest. Moreover, this mode is also compatible with transmission imaging modes. A Vortex SDD coupled with a XIA digital signal processor was used for detection and processing of the fluorescent signals. The convenient normal incidence positioning of the sample has the drawback that the SDD can not be placed under 90° angle, resulting in a higher Compton scattering. However, when placed under 75° angle, the detector nozzle can still approach the irradiated area providing a sufficient solid angle while still heavily suppressing Compton scattering (Cloetens, 2009).

8.3 Characterisation of the nano-XRF setup

8.3.1 Beamsize estimation

A high-resolution and calibration standard test pattern for calibrating and evaluating the spatial resolution and performance of X-ray imaging systems has been used for determining the beamsize available at the ID22NI nanoprobe. A high resolution image of such a test pattern is shown in Fig. 8.5. The test pattern has a variety of structures that enable resolution tests, modulation transfer measurements, length scale calibration and field distortion measurements. The finest feature size on the pattern is 50 nm. The gold test pattern is fabricated on a free standing, low stress Si_3N_4 membrane with a thickness of 330 nm (XRadia, 2009c). The size of the nanobeam was determined by means of a horizontal and vertical line scan along the Xradia test pattern as shown in Fig. 8.6 and Fig. 8.7 respectively, providing a deconvoluted beamsize of 177 nm (vertical) by 180 nm (horizontal).

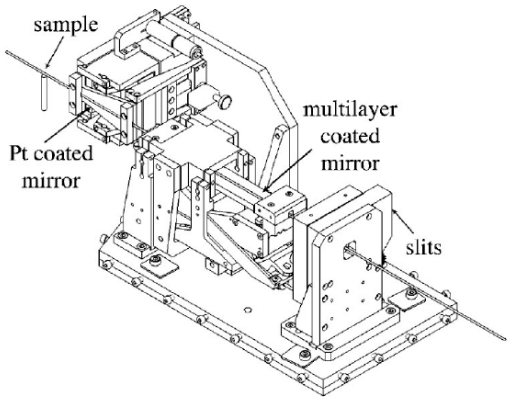

Figure 8.2: Kirkpatrick-Baez focusing device. Reproduced from Hignette *et al.* (2005).

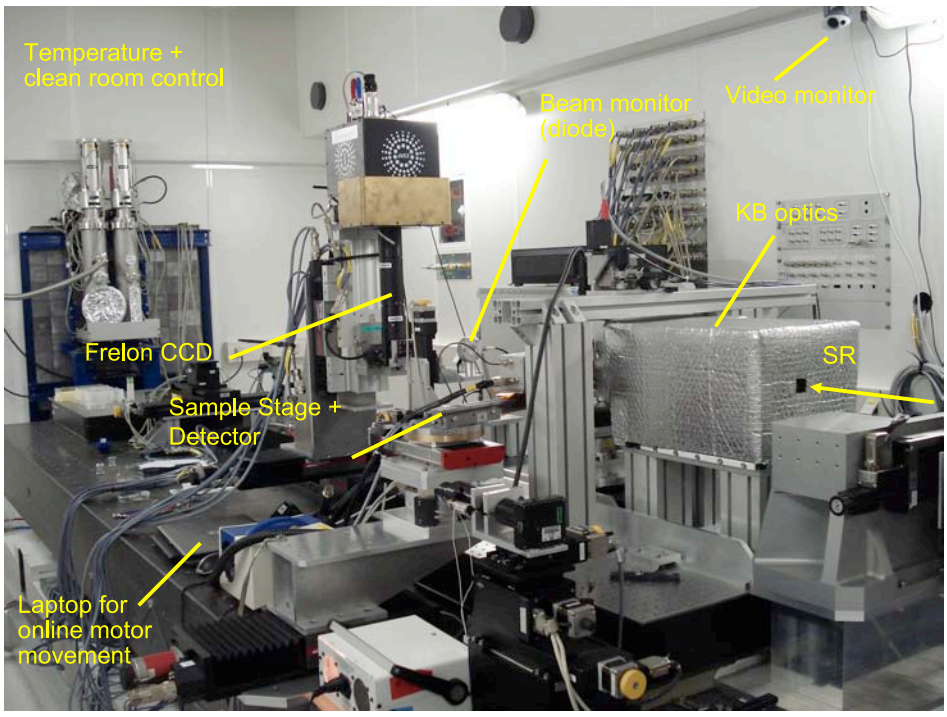

Figure 8.3: Overview of the experimental setup at ID22NI.

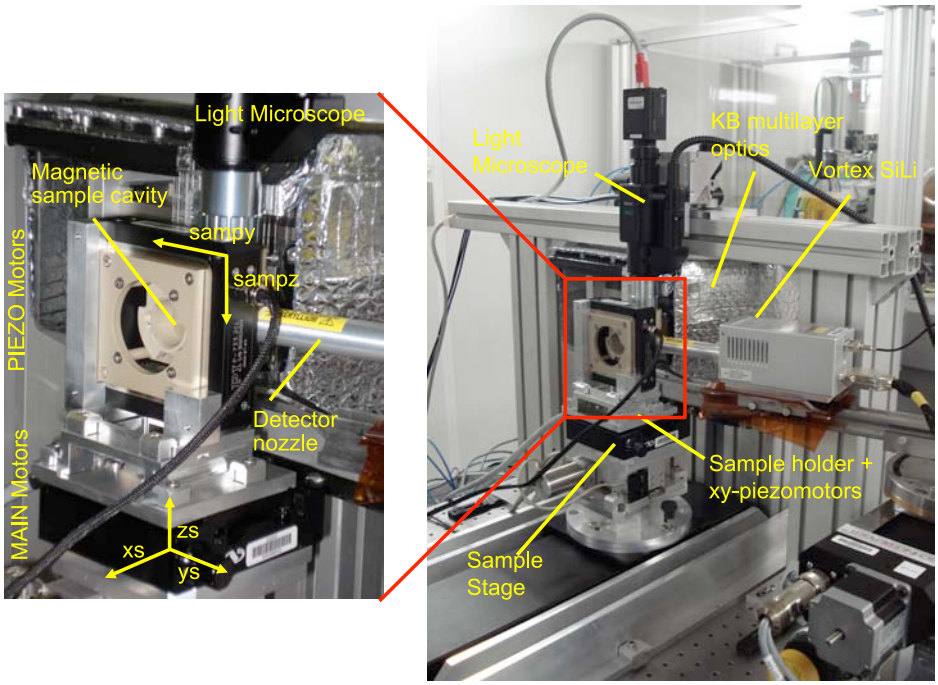

Figure 8.4: Detail of the scanning set-up at ID22NI.

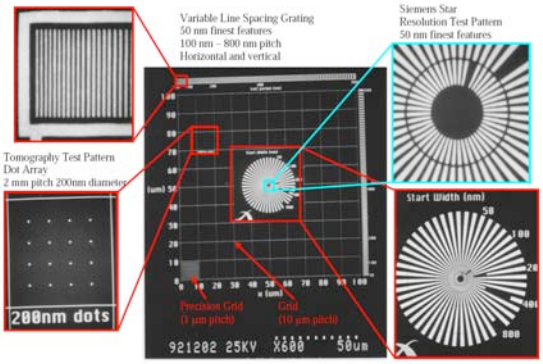

Figure 8.5: Xradia test pattern for beam characterisation (XRadia, 2009c).

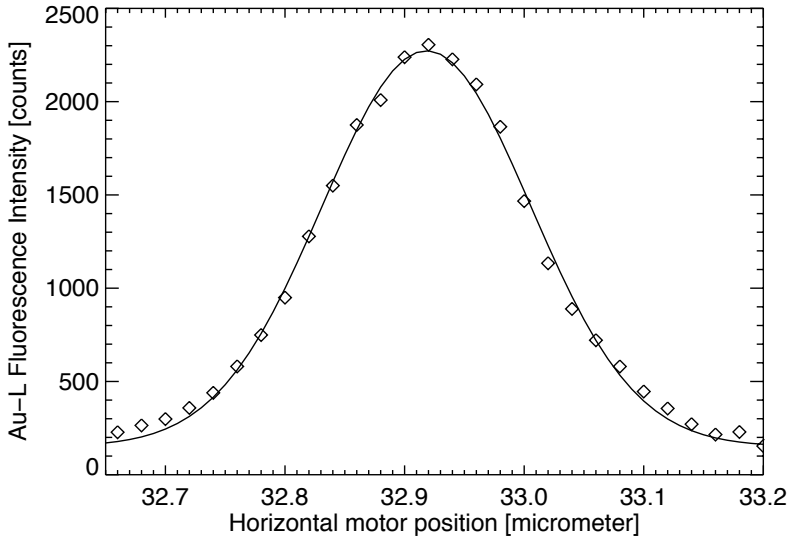

Figure 8.6: Horizontal scan across a 100 nm thick Au line on the Xradia test profile. The deconvoluted horizontal beamsize beamsize is 180 nm.

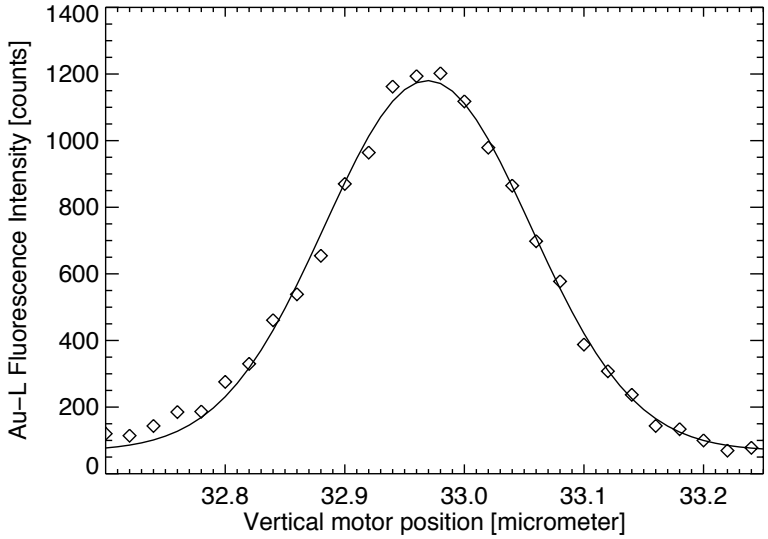

Figure 8.7: Vertical scan across a 100 nm thick Au line on the Xradia test profile. The deconvoluted vertical beamsize beamsize is 177 nm.

8.3.2 Operational elemental yields and detection limits

Next, an estimation of the analytical capabilities of the ID22NI nanoprobe on biological samples was made using SRM 1577C test sample by NIST (Zeisler *et al.*, 2009). A total amount of 17.4 mg of this material was pressed in a self supporting pellet with 13 mm diameter, resulting in an areal mass of 13.1 mg/cm^2. An area of 10 μm by 10 μm was scanned with 200 nm stepsize and a live time of 500 ms/point to investigate the homogeneity of the reference material. A 1500 μm Al absorber was used since the high flux upon the sample caused a too high dead time of the detector. The individual point spectra normalised to 200 mA ring current and corrected for dead time and the presence of the Al absorber. Fig. 8.8 shows an individual point spectrum of 300 ms and a sum spectrum of 300 s. For a scanning time of 300 ms, fluorescence peaks of Ar, K, Mn, Fe, Cu , Zn, Se, Br and Rb can be observed. In the fluorescence spectrum of 300 s the additonal presence of P, S, Cl, As, Kr, and Sr in NIST SRM 1577C can be observed.

In Fig. 8.9 an estimation of the relative and absolute detection limits is given with the corresponding elemental yield. For sub-second scanning times, e.g. 300 ms, 0.7 ppm level relative detection limits for Zn are already obtained corresponding to areal detection limits of 10 ng/cm^2 or, given the beamsize, absolute detection limits of 3 ag. Due to the Poisson counting statistics, the relative detection limits for 300 s reach values down to 20 ppb corresponding to areal detection limits of 0.3 ng/cm^2 or absolute detection limits of 100 zg. An absolute detection limit of 100 zg for Zn corresponds to an absolute detection limit of a few hundred Zn atoms, thus almost reaching the localisation of individual atoms. These absolute detection limits are made possible by the high spatial resolution and X-ray beam flux, allowing the cellular mapping of trace elements.

8.3.3 Submicrometer homogeneity of reference materials

As a result of the lack of suitable reference materials, characterisation of X-ray nanoprobes is being performed by means of bulk reference materials that were never intended for this purpose. In these bulk standards, usually the abundance of one or more trace consituents is certified, however, these certified values can only be relied upon when a suffienctly large quantity of the reference matrial in question is employed. E.g. NIST SRM 1577B Bovine Liver is certified for the elements Cd, Cu, Fe Hg, Mn, Pb, Rb, Se and Zn of which, according to the certificate, a minimum amount of 250 mg must be used. Originally, the minimum mass of a specific standard has been rather arbitrarily determined or has been estimated very conservatively so that the recommended values are higher compared to the estimated minimal mass when the micro-heterogeneity of the material is properly investigated. Certifying the (sub)micron-homogeneity of reference materials is a complex task since only a number of techniques are sensitive enough, making it difficult to assess and affectively remove instrumental

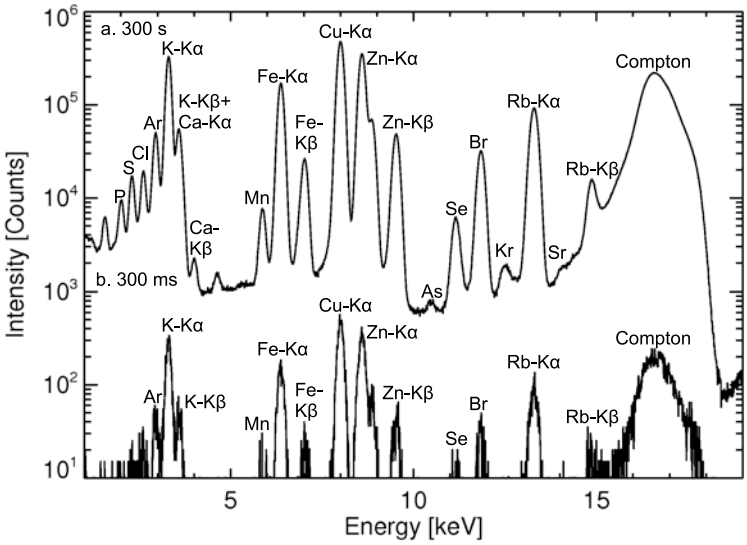

Figure 8.8: Individual point spectrum (LT=300 ms) and sum spectrum (LT=300 s) of NIST SRM 1577C Bovine liver.

or method bias during certification. An evaluation of synchrotron micro-XRF as a method for characterisation of the micro-heterogeneity of reference materials consisting of a low-Z material doped with certain trace elements was made by Kempenaers *et al.* (1999, 2000b).

In Fig. 8.10, the normalized element maps revealing the submicrometer element distributions within the NIST SRM 1577C pressed pellet are given. The sample was moved through the nanobeam in a continuous mode using a step size of 200 nm with a measuring (real) time of 500 ms per point. Since the sample is being analyzed at different locations, the measured total variance $s^2_{measured}$ is composed of the following contributions:

$$s^2_{measured} = s^2_{method} + s^2_{heterog.} \tag{8.1}$$

$$= (s^2_{instr.} + s^2_{stat.}) + s^2_{heterog.} \tag{8.2}$$

It can be stated that $s^2_{instr.}$ is much lower than $s^2_{stat.}$ and $s^2_{heterog.}$ and can therefore be neglected. Moreover, from Poisson statistics it follows that $s^2_{stat.} = I_{peak}$. Therefore, $s_{heterog.}$ can be determined according to the following equation:

$$s_{heterog.} = \sqrt{s^2_{measured} - I_{peak}} \tag{8.3}$$

As a first approximation, the heterogeneity of the SRM was estimated by calculating the relative standard deviation of the entire element map and dividing it by the mean intensity of

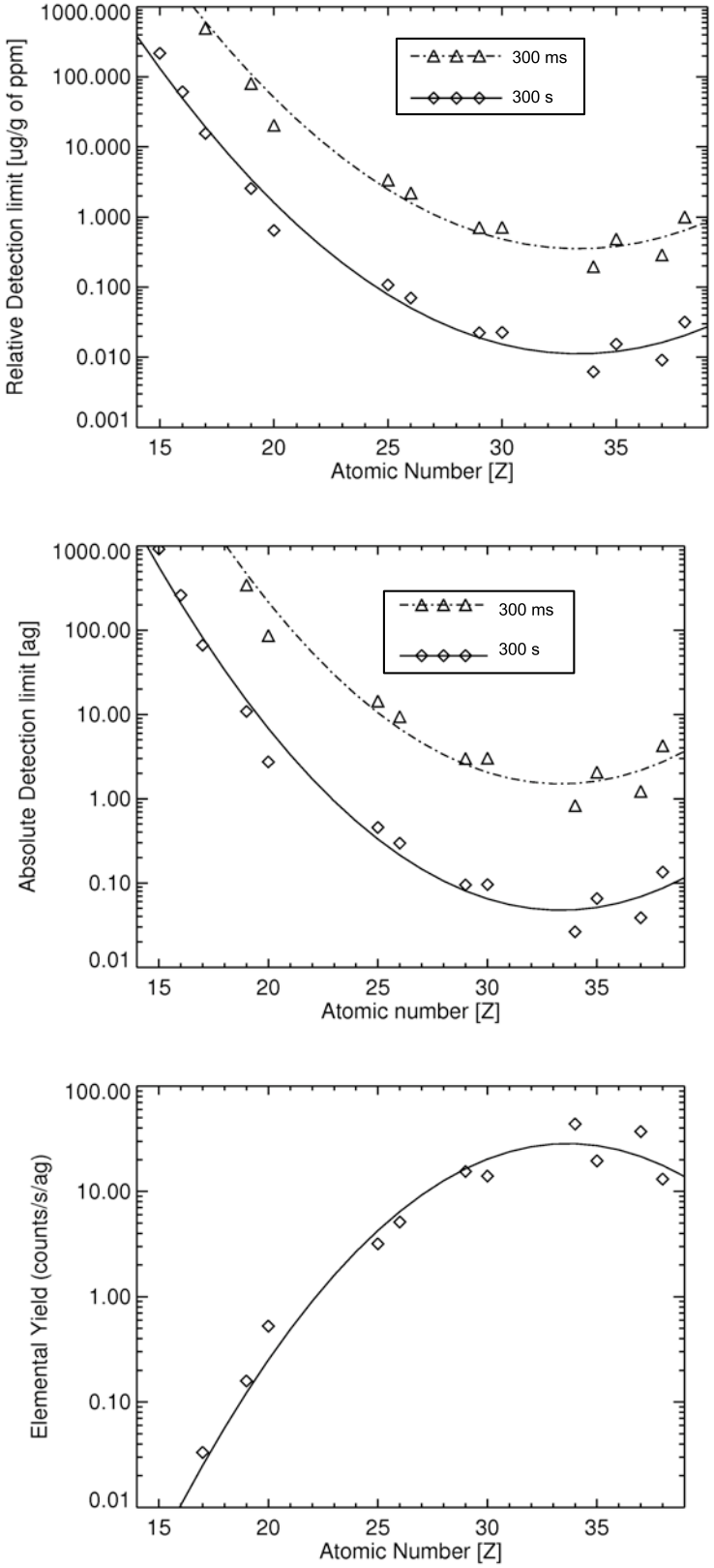

Figure 8.9: Relative and absolute detection limits for LT=300 ms and LT=300 s with corresponding absolute elemental yield curve obtained from a thin NIST SRM 1577C pressed pellet sample.

the entire element map. These corresponding values are given in the lower right corners (in percentages) of Fig. 8.10. However, since $s^2_{stat.}$ is not taken into account in this calculation, these values will be systematically higher than the true $s_{heterog.}$ values. Also, in case that the metals are not normally distributed throughout the material and that hot-spots (featuring a much higher Zn concentration compared to the surrounding material) can be detected (as appears to be the case for certain elements, e.g. Cu), a histogram is better suited for determining I_{peak} and $s_{measured}$. Therefore, the corresponding histograms of the normalised Zn and Cu element distributions (shown in Fig. 8.10) were calculated and are shown in Fig. 8.11 and Fig. 8.12. A total amount of 50 bins was requested and the histogram was fitted by a Gauss function from which I_{mean} and $s_{measured}$ can be found. Interestingly, the histogram of the Zn element distribution agrees very well with respect to the Gaussion shape, whereas the histogram of the Cu element distribution shows a distorted distribution with respect to the fitted Gaussian. This difference can also be confirmed by the difference in χ^2 value of Zn and Cu. In Table 8.1, the heterogeneity results for a few other trace elements in SRM NIST 1577C are listed. From these results, it can be concluded that Zn and Rb show a very good $s_{heterog}$ value of ≈ 4.5 %, followed by Fe with a slightly higher value of 5.8 %. The element Cu reveals a higher $s_{heterog.}$ value of ≈ 10 % and a higher χ^2 value compared with Fe, Zn and Rb due to the presence of nuggets.

Element	$s_{measured}$ (%)	s_{method} (%)	$s_{heterog.}$ (%)	χ^2
Fe	7.0	3.9	5.8	74.2
Cu	11.4	2.6	11.1	287.8
Zn	5.3	2.8	4.5	77.5
Rb	6.5	4.9	4.3	56.7

Table 8.1: Values of $s_{measured}$, s_{method}, $s_{heterog.}$ and χ^2 determined from 250 independant nano-XRF analyses of NIST SRM 1577C (Bovine Liver).

In Kempenaers *et al.* (2000a, 2002), more advanced analyses were made investigating to what extent it is possible to extract the statistical nature and size distribution of the grains of inorganic dopants, also called nuggets. By means of Monte Carlo simulation the effect of nugget enrichment and abundance was estimated in NIST SRM 1577B. From the simulation results, it was concluded that the procedure is able to calculate the magnitude of the minimal sampling mass of a reference material even in the presence of nuggets. The presence of these nuggets can cause serious deviations from the homogeneity of the material. In Molloy & Sieber (2008), an interesting new approach was PCA treatment used to identify which element exhibit nugget effects within the sub-mg mass range. A method of calculating the minimum recommended mass for solid samples is suggested using PCA iteratively on XRF maps from which adjacent data points have been averaged. This is then repeated until the mass sampled

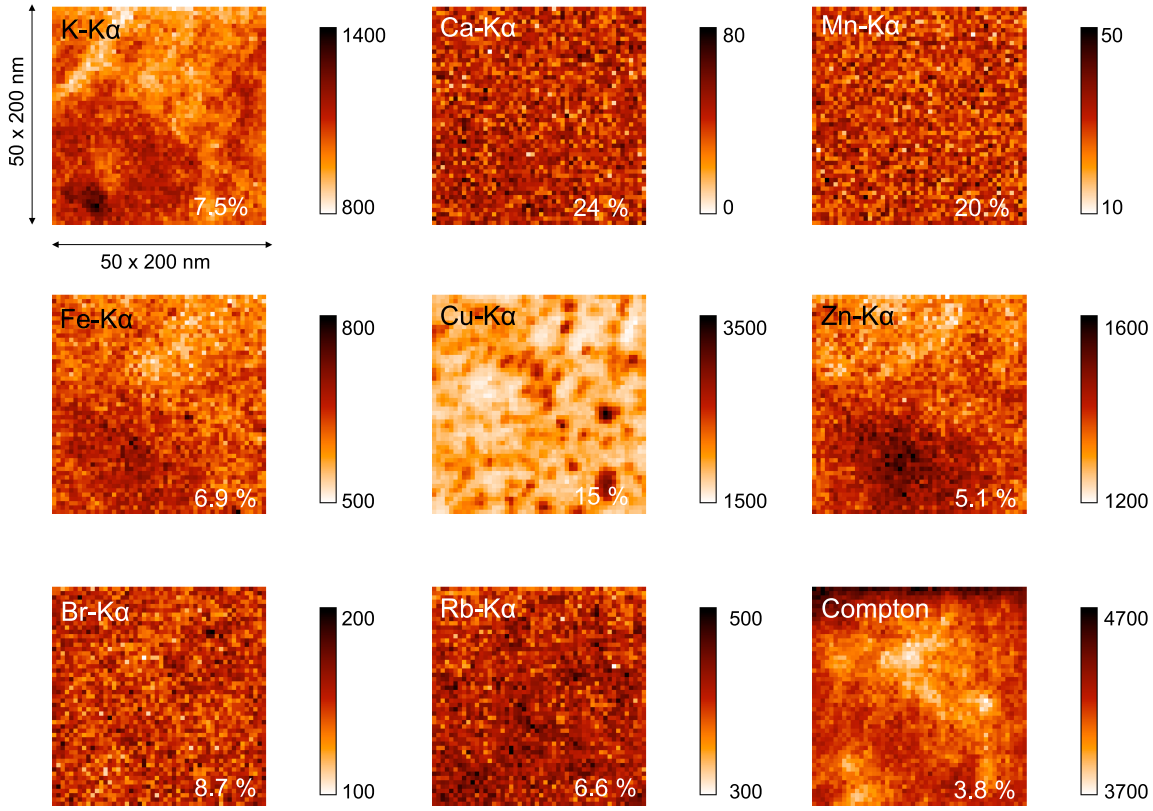

Figure 8.10: Element distributions of K, Ca, Mn, Fe, Cu, Zn, Br, Rb and Compton scattering. An area of 10×10 μm was scanned using a step-size of 200 nm with a measuring (real) time of 500 ms per point.

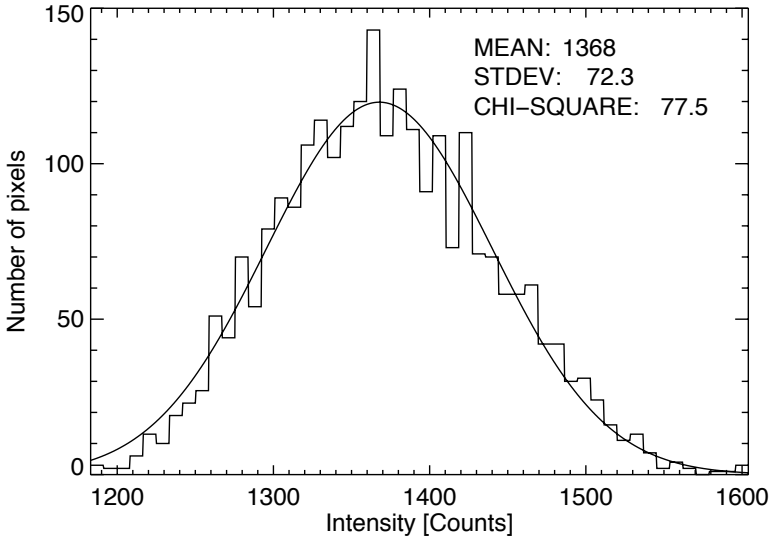

Figure 8.11: Histogram of the detected $Zn - K_\alpha$ line calculated from Fig. 8.10.

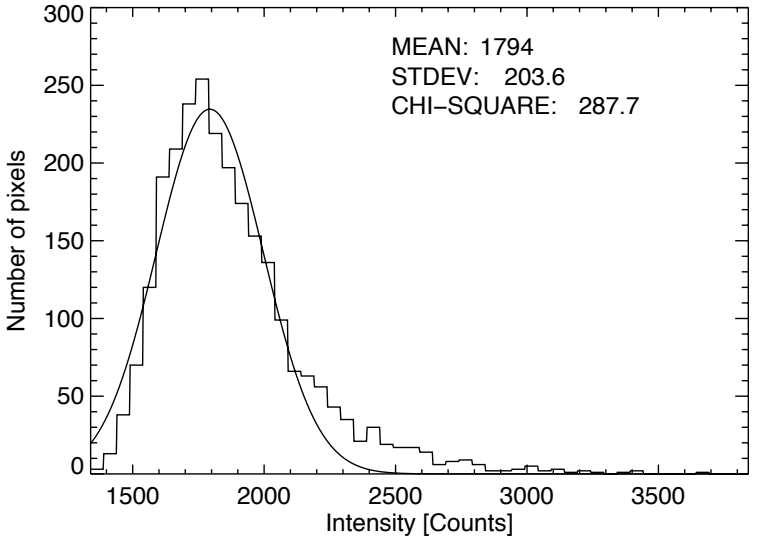

Figure 8.12: Histogram of the detected $Cu - K_\alpha$ line calculated from Fig. 8.10.

in a map is indistinguishable from data taken at a single location, suggesting no nugget effects can be detected. It was concluded that for the NIST SRM 1577C biological material, a mass as low as 370 μg can be used without measurable nugget effects.

8.4 Sample preparation

The laboratory clone juveniles (0-48h) of *Daphnia magna* (clone $K6$), used in all our experiments, were originally collected from a pond in Kiel (Antwerp, Belgium) and have been successfully cultured under controlled laboratory conditions for more than 10 years. The control medium consisted of 0.077 $mmol/L$ $NaHCO_3$, 0.078 $mmol/L$ KCl, 0.5 $mmol/L$ $MgSO_4$. The experiment was designed to investigate the regulation of Zn at a high concentration. The chosen Zn concentration of 1000 mg/L had a 50% LC effect, which means that the chosen Zn concentration was lethal for approximately 50% of the population.

A chemical fixation (Karnovsky, 1965) and alcohol dehydration procedure was used as discussed in Chapter 3. Some of these fixed species were stained with osmiumtetroxide prior to alcohol dehydration with the aim of also having specimens suitable for transmission electron microscopy (TEM) in order to study the morphology of the sample at high resolution. It should be noted that, with respect to spatially resolved investigation of the chemical composition, the drawback of these methods is the risk of altering the chemical composition due to dislocation and/or contamination. After dehydration, embedding in Spurr resin (Spurr, 1969) and subsequent cutting in thin sections was performed and finally deposition upon an adequate sample support. For TEM investigations, 70 nm thin sections were deposited on a carbon coated grid, whereas for nano-XRF a silicon nitride window was preferred.

8.5 Experimental results

8.5.1 Conventional nanochemical imaging

Daphnia posesses highly specialized thoracic appendages for the collection of food particles, probably the most developed filtering apparatus within the Branchiopoda. The number of the trunk limbs or exopodites is reduced to five, which, together with the carapace, form a suction-and-pressure pump. Only the third and fourth pair of appendages carry large filter-like screens, which are supposed to retain the particles from the water passed through the filter apparatus. Fig. 8.13a shows a schematic drawing of this system, indicating that exopodites are attached to the abdomen by means of a filter plate (Seidl *et al.*, 2002). These exopodites consist of many different setae and setules as shown in Fig. 8.13b. In Fig. 8.13c, a microscope image of a 2 μm thin section of *Daphnia magna* (3 $mmol/L$ $CaCl_2$, 0 $\mu g/L$ Zn, OsO_4) brought into the focus of the nanobeam can be observed. The carapace structure surrounds the internal tissues. Within the carapace, the filter plates are attached to the exopodites,

since the thin sections were cut at the height of the thoracic appendages. Unfortunately, no epipodite or gill was present within this dorsoventral section. Epipodites are brachial sacs present upon the exopodites and are the osmoregulatory regions of *Daphnia magna* where exchange of cations and anions occurs. Therefore, two different exopodites ($z1$ and $z2$) were analyzed with the nanobeam. Fig. 8.13d shows a detailed microscope image of one of the exopodites (z1), indicating the scanned area by nano-XRF, as well as the scanned area of a subsequent thin section of the exopodite by TEM. In Fig. 8.13e, the $Os-L$ element distribution within the exopodite is provided by nano-XRF and in Fig. 8.13f a TEM image is given. Although the TEM image was made on a 70 nm thin section, good correlation was obtained with the $Os-L$ XRF element map. If difficulties are encountered to determine which histological region to scan due to too low contrast in the microscopy image, recognising the $Os-L$ XRF map in the TEM image can be useful to track the region of interest for XRF analysis. Unfortunately, since this is one of the first nanochemical analyses of exopodites within *Daphnia magna*, the internal structures of the exopodite sections are hard to define. In Fig. 8.13g and Fig. 8.13h, an RGB representation of both analyzed exopodites ($z1$ and $z2$ in Fig. 8.13c) is shown, delivering information on the conjoint presence of Os (red), Ca (green) and Ca (blue). When comparing Fig. 8.13g and Fig. 8.13h, it can be confirmed that both thoracic appendages differ significantly from each other (Watts & Petri, 1981). As previously described, the exopodites are composed of different setae, which can be observed in Fig. 8.13g as Fe containing structures surrounding the exopodite. Although Os staining of the sample allowed a useful identification of the target structures of interest, information concerning other metal distributions is lost due to peak overlap and/or the high $Os-L$ fluorescent count rate.

Fig. 8.14a shows a microscope image of a 2 μm thin section of *Daphnia magna* (3 $mmol/L$ $CaCl_2$, 1000 $\mu g/L$ Zn, unstained) brought into the focus of the nanobeam. As in Fig. 8.13a, a filter plate ($z1$) and an exopodite ($z2$) can be recognised. Fig. 8.14b shows an RGB representation of the conjoint presence of Ca (red), Zn (green) and Fe (blue) within the exopodite, which is again notably different from both exopodites analysed in Fig. 8.13g and Fig. 8.13h. Fig. 8.14c shows an RGB representation of the filter plate of the conjoint presence of Ca (red), Zn (green) and Cl (blue). Interestingly, a cross-section of an epipodite was present within this dorsoventral section, allowing the investigation of cations and anions within this osmoregulatory gill tissue. The marked presence of Fe confirms the haemolymph flowing through the tissue. Subsequently, this iron vesicle is enclosed by respectively a Ca containing exoskeleton and a nanometer thin Zn layer. These observations agree very well with previous ecotoxicological research (Muyssen & Janssen, 2002) in which the accumulation of Zn within the exoskeleton was suggested. Previous studies show that *Daphnia* then resorts to excretion of metals by renewing the carapax every 2 days by molting (Biesinger *et al.*, 1982; Hall, 1982; Carney & Shore, 1986). Elemental yields were used to estimate the areal concentrations of

Ca, Fe, Cu and Zn of the epipodite in Fig. 8.14c in closer detail. Elemental yields of Ca, Fe, Cu and Zn were extracted from the elemental yield curve in Fig. 8.9, providing yields of 0.170259, 1.66077, 5.01575, 4.53722 $counts/(s \times (ng/cm^2))$ for the elements Ca, Fe, Cu and Zn respectively. The areal concentrations of Ca, Fe, Cu and Zn of the epipodite are given in Fig. 8.14e-h.

8.5.2 Confocal nanochemical imaging

The feasibility of a confocal detection arrangement was also explored. In this case, instead of scanning a thin-section of *Daphnia magna*, the entire sample can be mounted in the sample stage and a thin slice (defined by the polycapillary attached to the detector) within this sample can be scanned with high lateral resolution. In Fig. 8.15 and Fig. 8.16 respectively, the horizontal and vertical acceptance of the setup was measured using a gold test structure, resulting in an acceptance of approximately 10 μm for the $Au - L$ lines. It should be noted when considering different elements, the thickness of the thin virtual section will vary. In Fig. 8.17, the principle of the confocal optic detecting fluorescent signals from a virtual thin section is illustrated in (a), whereas in (b) an overview of a thin virtual section within a HMDS dried *Daphnia magna* control organism is given. It is also likely that this confocal detection alignment will allow the realization of a new variant of X-ray fluorescence CT, called local fluorescence tomography. A confocal line scan of 10 μm length through the sample with 100 nm step size has a high lateral resolution, but each measuring point remains a line integral determined by the acceptance of the detection polycapillary. Changing the rotation angle of the sample gives a projection over a different line integral within the sample. When the center of the line scan remains in the center of rotation of the sample, the different line integrals can be reconstructed, providing the element distributions within a 10 μm diameter circle. Instead of a line scan, a 2D map (e.g. 10×10 μm) can be performed under different rotation angles given the center of the map stays within the center of rotation. The element distributions within a cilinder of 10 μm diameter and 10 μm height can subsequently be reconstructed. The advantage of tomography being the increased resolution as determined only by the impinging nanobeam and that of confocal detection involving a rejection of scatter from noninteresting region of the sample and the ability to restrict measurements to an area of interest can thus be handily combined (Vincze *et al.*, 2004).

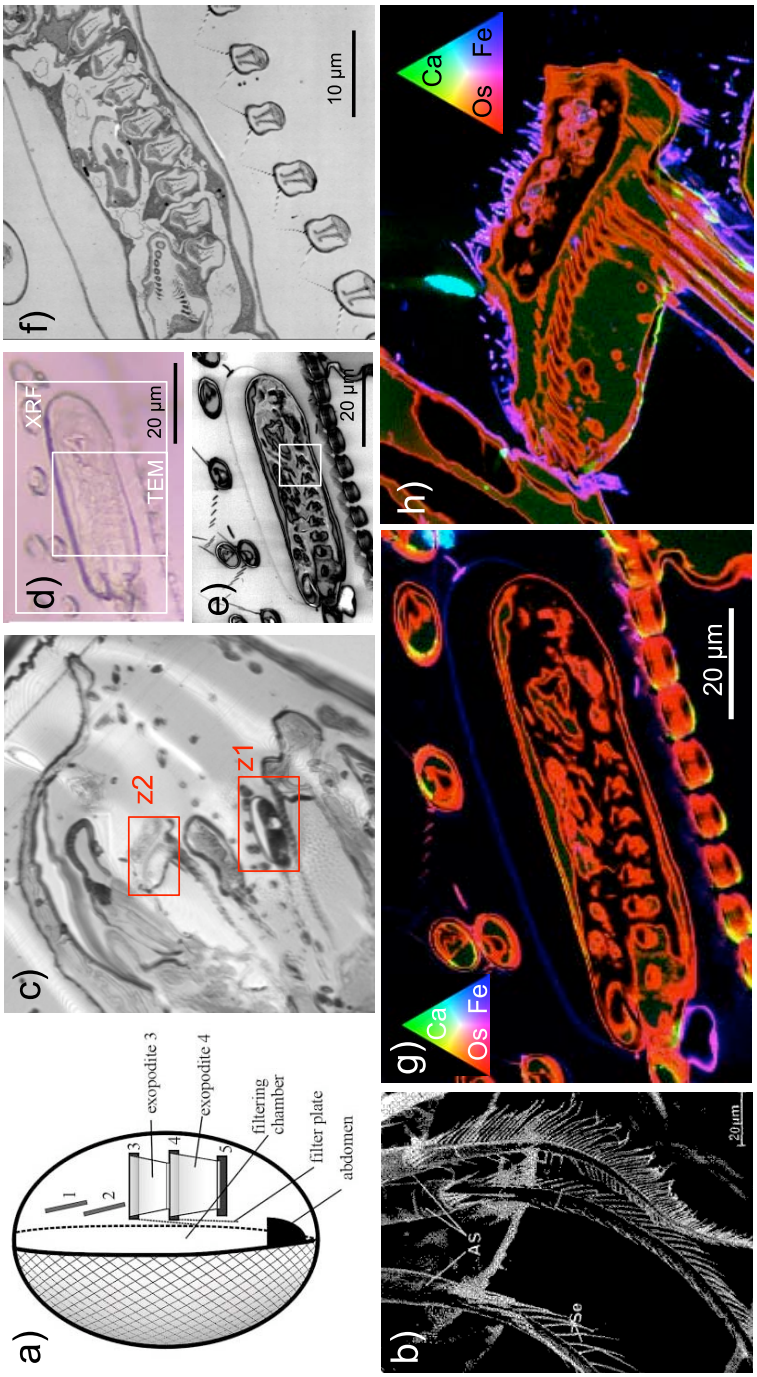

Figure 8.13: a) schematic representation exopodites b) TEM: setae and setules of exopodites of *Daphnia magna* c) microscope image of OsO_4 stained thin section d) detail of exopodite with indication of regions analysed by TEM/XRF e) nano-XRF $Os - L$ (width: 60 × 200 nm, height: 40 × 200 nm, RT=200 ms) f) TEM image of exopodite g) nano-XRF exopodite $z1$ (width: 60 × 200 nm, height: 40 × 200 nm, RT=200 ms, RGB: Os, Ca and Fe) h) nano-XRF exopodite $z2$ (width: 350 × 200 nm, height: 250 × 200 nm, RT= 300 ms, RGB: Os, Ca and Fe).

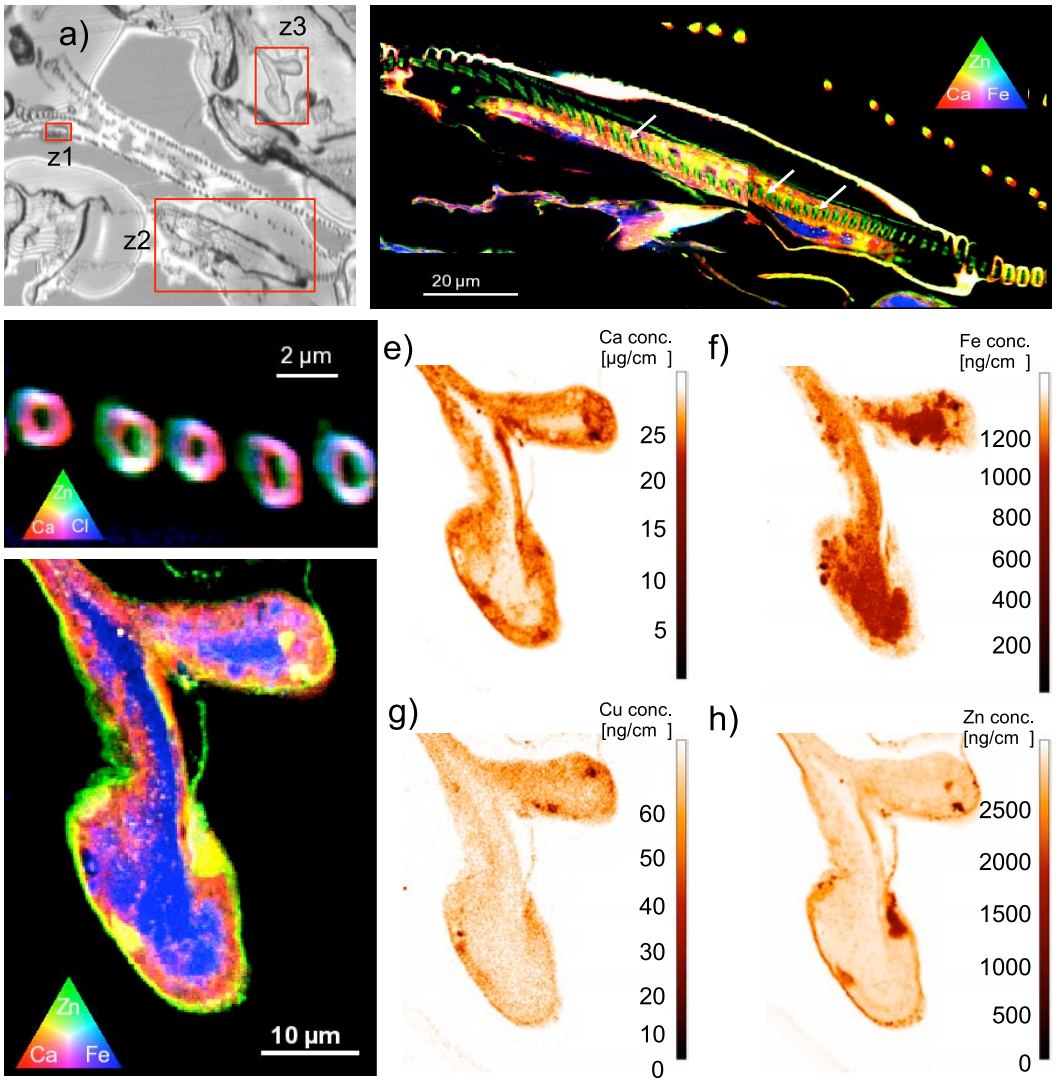

Figure 8.14: a) microscope image of unstained thin section of *Daphnia magna* b) nano-XRF exopodite $z2$ (width 622 $\times$ 200 nm, height: 335 $\times$ 200 nm, RT= 200 ms, RGB: Ca, Zn and Fe) c) filter plate $z1$ (width: 120 $\times$ 100 nm, height: 80 $\times$ 100 nm, RT= 200 ms, RGB: Ca, Zn and Cl) d) epipodite $z3$ (width: 190 $\times$ 200 nm, height: 265 $\times$ 200 nm, RT=200 ms, RGB: Ca, Zn and Fe).

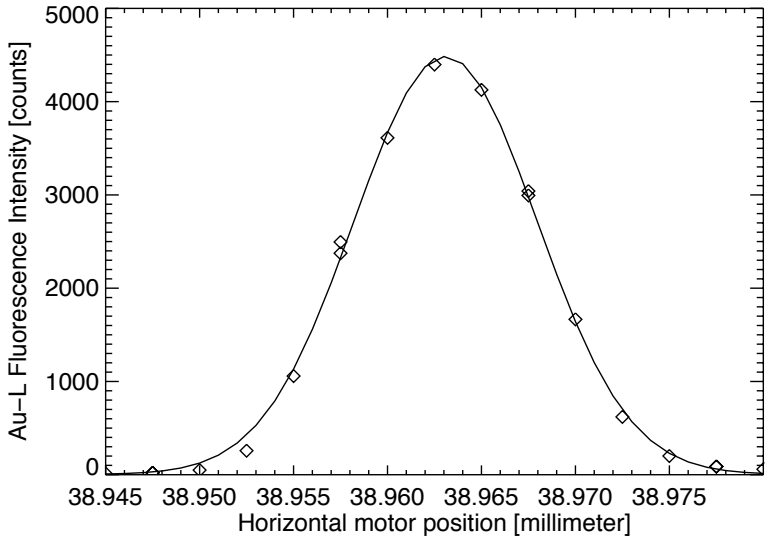

Figure 8.15: Acceptance determination of the confocal detection setup. The horizontal acceptance is 11.47 μm FWHM.

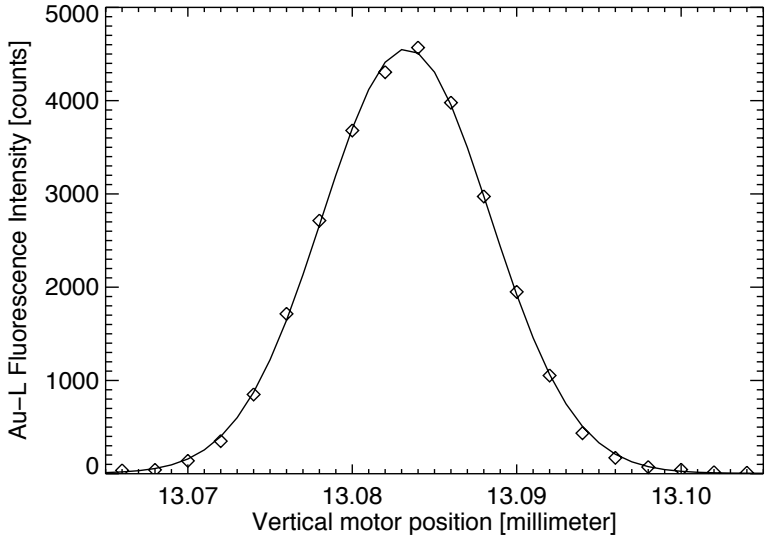

Figure 8.16: Acceptance determination of the confocal detection setup. The vertical acceptance is 12.02 μm FWHM.

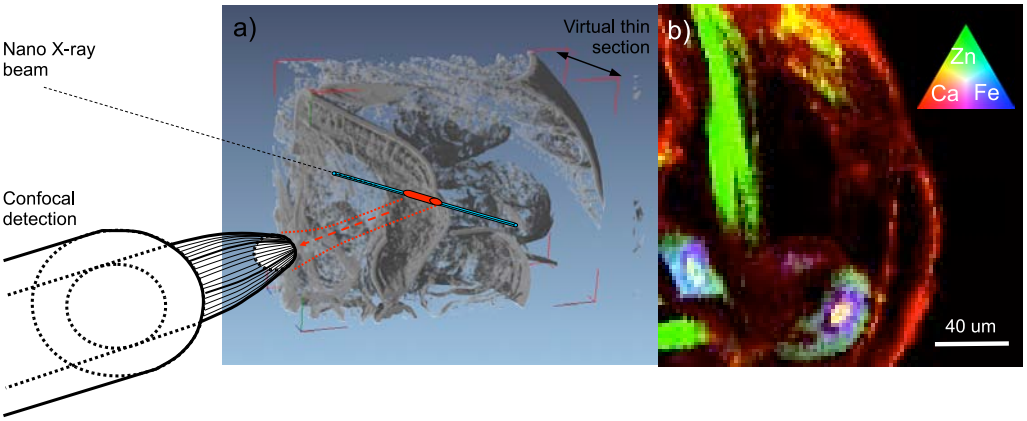

Figure 8.17: HMDS dried *Daphnia magna* analysed using a confocal setup at ID22NI.

Chapter 9

Summary and conclusions

The unique properties of synchrotron radiation offer tremendous potential and new opportunities for scientific exploration in a variety of disciplines. The exponential increase in brilliance obtained at third generation synchrotron sources has initiated the development of new, or significantly enhanced, non-destructive experimental techniques with analytical characteristics previously unthinkable.
Coupled with the development of X-ray optics and detectors, X-ray microanalysis has progressed at an unprecedented pace during the last two decades, and has entered a highly visual phase via the development of various types of X-ray imaging techniques. These developments are expected to result in new insights in understanding complex processes taking place in nature on the micro- and nanoscopic scales, for example in life sciences.
In order to demonstrate and further develop this potential, in this thesis the unique capabilities of X-ray micro-spectroscopic and imaging techniques (discussed in Chapter 2) were explored to detect, visualise and quantitatively characterise metal enriched (sub)microscopic regions within a biological model organism, *Daphnia magna*. This organism is frequently used as a model system for studying the effects of controlled exposure to metals in environmental toxicology.

Chapter 3 provides an introduction to the ecotoxicological aspects of this model organism and which sample preparation techniques can be used for X-ray analysis. Although X-ray micro-spectroscopy and -imaging have the advantage to investigate a sample in an essentially non-destructive manner, biological specimens pose considerable challenges in this context due to their high sensitivity to radiation damage. Since X-ray fluorescence (XRF) imaging methods are mainly based on scanning techniques which require the sample to remain unchanged while being scanned by an intense X-ray micro/nanobeam, an adequate sample preparation procedure for *Daphnia magna* was required. In the work presented in this thesis, we explored the applicability of both cryogenic and chemical fixation based sample preparation methods. Since the best measuring conditions for such samples can be achieved by keeping them clos-

est to their natural state, the straightforward solution is based on rapid cryogenic cooling, preserving the micro-structure of the sample. Plunge freezing in a liquid cryogen or high pressure freezing has been shown to result in high quality freezing of a sample to a depth of approximately 200 μm. Larger samples are therefore typically dissected towards smaller structures, which is difficult to apply for delicate aquatic organisms such as *Daphnia magna*, and can cause changes in the sample micro-structure. When X-ray fluorescence analysis on the microscopic scale is envisaged, the sample can be simply cooled by a cryostream set-up, since the resulting ice microcrystal formation and induced sample vibration do not influence significantly the element distributions measured at this resolution. On the other hand, when performing nanoscopic X-ray fluorescence analysis, after plunge-freezing the sample, a quick transfer towards the cryogenic sample-stage is required in order to avoid recrystallization of the sample. An integrated approach, in which the sample water content is frozen to vitreous ice at the cryogenic sample-stage and is immediately analysed on a (vibration free) cryostage would be ideal, but is still far from available.

The laboratory micro-XRF experiments on *Daphnia magna* presented in Chapter 4 were performed under non-cryogenic conditions since the design of the small spectrometer vacuum chamber does not allow cooling. Moreover, due to the fixed design of the instrument, only conventional 2D micro-XRF experiments can be performed and no local (i.e. depth selective) 2D X-ray analysis within the sample is possible. Therefore, scanning XRF analyses were performed on thin-sections (10-20 μm) of *Daphnia magna*, which were prepared by a dehydration procedure in water/aceton series, followed by substitution with paraffin.
For the SR micro-XRF/XAS analyses on *Daphnia magna* discussed in Chapters 5-7, local (depth selective) 2D/3D analyses were possible within *Daphnia magna*. In this case, we opted the use of chemical dehydration followed by fixation using hexamethyldisilazane (HMDS) on *Daphnia magna*, preserving the 3D microstructure of the sample as compared to critical point drying/freeze drying. During the second phase of this work a cryostream set-up was tested at the used SR microprobe (beamline L), and detailed comparisons were made of element imaging results obtained using HMDS based sample preparation methods with those obtained by using cryogenic freezing. Although changes in element distributions in certain cases (e.g. Cu) could be observed, no substantial differences for the target metal Zn were detected.
The SR nano-XRF experiments on *Daphnia magna* presented in Chapter 8, were performed under ambient temperature. Cryostream based analysis was hampered due to known associated problems at SR-XRF nanoprobes, e.g., sample vibrations and misalignment of the optics due to temperature drift. For these experiments, the sample preparation procedures had to be adapted. Cryosectioning followed by dehydration did not preserve the micro-structure within *Daphnia magna* and logically also not the metal distributions. Chemical dehydration in water/alcohol series followed by substitution with paraffin ensured morphological preservation on the microscale, although polymer fixation was required to obtain morphological cellular

preservation of the sample. Therefore, chemical fixation followed by substitution with an LR white resin was the method of choice which inferred the necessary rigidity to the sample for thin-sectioning. Thin-sections of *Daphnia magna* were prepared ($\approx 2\ \mu m$) to investigate specific areas of interest. However, potential element redistribution in this case should be further studied in future projects.

In Chapter 4, laboratory based scanning micro-XRF analysis was used as a complementary element analysis technique for the detection of elements with atomic numbers below 19 and for sample pre-characterisation before performing high-sensitivity SR-XRF measurements on *Daphnia magna*. The employed commercial microbeam XRF spectrometer (EDAX Eagle-III) is composed of a Rh microfocus X-ray tube, a polycapillary full-lens and a $Si(Li)$ detector. Due to the polychromatic nature of the excitation source, coupled with the energy dependent focusing properties of polycapillary optics, the effective micro beam size variation was determined to be 50 - 15 μm (FWHM) within an energy range of 1-20 keV. Larger beamsizes of up-to 300 μm can be obtained by changing the distance of the employed polycapillary optics with respect to the sample surface. Measured relative detection limits determined by using the biological reference material NIST SRM 1577B are in the 10-100 ppm range for higher Z elements (e.g. Mn, Fe, Cu and Zn), corresponding to absolute detection limits in the 1-10 pg range for a live time of 300 s. Detection limits for the lower Z elements (e.g. P, S, Cl, K and Ca) present in biological materials, were also in this range when a vacuum sample environment was used. The laboratory microprobe is therefore a valuable complementary tool for low-Z element analysis, compared with synchrotron radiation XRF microprobes operating in air.
Using this instrument, analysis of an entire HMDS fixed *Daphnia magna* was possible when scanning for several days, revealing depth integrated element distributions for P, S, Ca and Fe. Next to the analysis of the entire organisms, the analysis of thin (10-20 μm) paraffin embedded sections of *Daphnia magna* provided insight in the local distributions of these elements. While Ca is mainly present in the carapax and the presence of Fe could be detected in the digestive gland, P and S are distributed in the internal tissues such as gut, gills and embryos. Unfortunately, the instrument was not able to determine the element distribution of Zn due to insufficient trace level sensitivity.
Additionally, the detection limits and spatial resolution of laboratory micro-XRF was compared with laser ablation inductively coupled plasma mass spectrometry (LA-ICPMS) for microchemical imaging on *Daphnia magna*. Based on the detection limits of both techniques obtained on NIST SRM 1577B, and the fact that for element imaging on *Daphnia magna* laboratory micro-XRF was operated under vacuum conditions (LT= 5 s) and LA-ICPMS with 15 μm beam diameter was used, the relative detection limits obtained under these conditions were compared. In the case of P, the relative detection limit was better using micro-XRF (230 ppm) compared to 600 ppm obtained by LA-ICPMS. The determination of S by ICPMS

is hampered by spectral overlap, which causes its detection limit to be a factor 100 higher than the 160 *ppm* obtained with micro-XRF. Also Ca determination by ICPMS is hampered by spectral overlap, therefore its detection limit was comparable to micro-XRF (100 vs 120 *ppm*). Zn remained undetected within the reference material by micro-XRF, whereas its relative detection limit using LA-ICPMS was 30 *ppm*.
After analytical characterisation of both techniques, the laboratory micro-XRF based element imaging results on *Daphnia magna* were compared with those obtained from LA-ICPMS. After non-destructive analysis with the laboratory XRF microprobe, the tissue thin-sections (10-20 μm) were subjected to LA-ICPMS, providing a minimal ablation diameter of 15 μm. Given the comparable detection limits of micro-XRF and LA-ICPMS for P and Ca, the obtained element distributions could be cross-validated between both techniques by appropriate scaling of the element maps using histogram analysis. Micro-XRF provided better quality S distribution within *Daphnia magna* due to its better sensitivity as compared to LA-ICPMS, which suffers heavily from spectral interferences for this element. Since a higher sensitivity for the target element Zn was obtained by LA-ICPMS, a Zn distribution map of *Daphnia magna* could be provided by this technique. Both techniques are thus complementary in providing an exhaustive chemical profiling on *Daphnia magna*. In terms of spatial resolution an distortions, it can be concluded that the image quality obtained by LA-ICPMS suffers from wash-out effects in the ablation chamber and the presence of spikes when compared to micro-XRF results. However, due to the chromatic nature of the X-ray beam in laboratory micro-XRF, the actual resolution is heavily dependent on the element studied and therefore often lower as compared to LA-ICPMS.

In contrast to laboratory micro-XRF experiments on *Daphnia magna*, the use of a synchrotron XRF microprobe (discussed in Chapter 5 and 6) allowed the study of trace level metal distributions (including Zn) in this organism in a non-destructive and distortion-free manner due to the high element sensitivities provided by the use of linearly polarized, monochromatic X-ray microbeams. The increased element sensitivities of the Beamline L microprobe, installed at the second generation synchrotron source HASYLAB, Hamburg, Germany, were ideally suited and necessary to investigate the 2D/3D microscopic distribution of Zn within *Daphnia magna*.

The essential components of the employed experimental set-up for our initial micro-SRXRF experiments discussed in Chapter 5 were a multilayer monochromator for high flux applications, coupled with a single bounce monocapillary providing a low divergence beam size of 15 μm (FWHM). Due to the monochromatic excitation and high degree of linear polarisation, relative detection limits were situated in the 10-100 *ppb* range, corresponding to absolute detection limits in the 1-10 fg range for transition metals for a live time of 300 s. These detection limits are approximately three orders of magnitude lower compared to a laboratory XRF microprobe. Two dimensional (2D) and computed tomography (CT) micro-XRF experiments

were performed by means of a dynamic scanning approach. A high resolution CCD-based X-ray camera was used to select the regions of interest for the scanning micro-XRF measurements. In a pilot experiment, a cryogenic gas (N_2) stream was used in combination with two silicon drift detectors (SDD) allowing dual detector cryomapping and cryotomography, analysing the sample close to its native state. The dual detector set-up under the cryogenic conditions proved to be vital to correct for self-absorption effects influencing the detection of lower Z elements due to the presence of the absorbing water matrix as compared to chemically fixed and dried samples. In order to quantify the 2D micro-XRF measurements, an adequate normalisation procedure was established using the ionisation chamber signal, taking into account the ionisation chamber offset and SDD detector dead time.
K-means clustering was applied to isolate sub-regions of interest for the comparison of the multi-element content of 1) different tissues within a *Daphnia magna* and 2) similar tissues between differently exposed *Daphnia magna*. Principal component analysis (PCA) was used to highlight the variance-covariance of the element concentrations of the different clusters. When analysing a control specimen and a Zn exposed *Daphnia magna* sample, accumulation of Zn was observed in the gill-like osmoregulatory tissue, the gut and the digestive gland. When analysing control (unexposed) and Zn exposed *Daphnia magna* samples with a different genetic background (showing low and high metal tolerance) under cryogenic conditions, a lower Zn content could be observed in the Zn exposed high metal tolerant samples as compared to the Zn exposed low metal tolerant samples, suggesting a lower Zn uptake or a higher elimination of this metal.
Finally, by applying a Fourier filtering based noise reduction algorithm on the sinograms obtained from the micro-XRF CT measurements, improved reconstructed element distributions could be obtained for P, Cl, K, Mn and Br. The obtained 2D/CT micro-XRF measurements on *Daphnia magna* were coupled with laboratory absorption micro-CT experiments with a resolution of $\approx 1\ \mu m$ providing accurate element-to-tissue correlation information.

When the element distributions in virtual thin-sections for a variety of samples need to be investigated and compared, e.g. in case of several *Daphnia magna* samples from an elaborate ecotoxicological study, micro-XRF CT is cumbersome due to (1) long scanning times, (2) challenging alignment of the sample and (3) difficult quantification. Recently, a new variant of micro-XRF has been developed which overcomes these issues: polycapillary based confocal micro-XRF. In Chapter 6, this technique was thoroughly characterised and applied for *Daphnia magna* element imaging studies. At beamline L, a so-called free standing thin film (FSTF) standard was used to determine the energy dependent acceptance of the detection side polycapillary lens, providing geometrical information concerning the sensitive confocal volume. By means of the FSTF standard, it was verified that detection limits were in the same order of magnitude for confocal micro-XRF as for 2D/CT micro-XRF. Unfortunately, confocal micro-XRF measurements could not be performed under cryogenic conditions. The

low working distance of the detection side polycapillary optic would bring it close to the cryostream initiating misalignment and/or damage of the optical system.
Daphnia magna originating from an ecotoxicological experiment investigating the uptake of Zn via different routes (water and/or food) were subjected to confocal micro-XRF analysis. By means of K-means clustering and region of interest (ROI) growing analysis, the relative increase of Zn in the different organs was calculated for both water/food exposed series. The relatively high increase of Zn accumulation in the gills, in comparison to other tissues, is likely due to its function as primary site for ion uptake and as the main site for active ion transport involved in osmoregulation of the body fluids. The increased accumulation in the carapace is probably the result of the employment of this tissue as a metal sink in the detoxification process of this element. The similar concentration of Zn in the gut/ovarium and eggs, as well as their similar proportional increase after Zn exposure, are supporting the assumption that the main part of Zn accumulation into the eggs is not due to ventilation of the broodpouch with culture water after disposal of the eggs, but most probably mainly to a transfer of Zn from the ovaries via the haemolymph to the developing embryos.
Besides providing the element distributions within several *Daphnia magna* from an elaborate ecotoxicological study, confocal micro-XRF allowed also to 1) scan regions of interest in greater detail after a general overview scan by means of smaller step sizes and longer measuring times 2) scan a different plane of interest without repositioning of the sample and 3) measure the full three-dimensional element distributions within a sub-volume of interest. By means of the different absorption of K_α and K_β lines of Ca, an estimation of the self-absorption effects within these samples was obtained. As a proof of principle, a laboratory micro-CT dataset obtained from the same sample was also coupled with dorsoventral and sagittal element distributions within a *Daphnia magna* specimen.

Although X-ray fluorescence micro-analysis provides information on the location and concentration of metals, it does not provide information on the chemical state/local environment of these metals. Recently, X-ray Absorption Fine Structure (XAFS) spectroscopy techniques, able to obtain this extra information, have been shown to be compatible with microfocus and confocal modes of analysis. Therefore, Chapter 7 highlights the potential of XAFS at the Dutch-Belgian Beamline (DUBBLE) at the ESRF, Grenoble, France, to provide additional information concerning the speciation of the target metal Zn. In a pilot experiment, 2D micro-XRF analysis was first applied to obtain an overview of the element distributions within the tissues of interest before performing XAFS analysis. Although micro Extended X-ray Absorption Fine Structure (micro-EXAFS) gave too low count rates for the trace metal Zn, micro X-ray Absorption Near Edge Structure (micro-XANES) spectroscopy revealed a different coordination environment for this metal in the full depth of gut, embryos and digestive channel. The local Zn environment in two eggs appeared to be identical and similar to that obtained from the NIST SRM 1577B Bovine Liver, while the spectrum taken on

the digestive channel has significant changes compared to the eggs, indicating that Zn has a tissue-specific local environment. In order to completely identify the spectra, more reference materials are required, which was not within the scope of this explorative study. Since detoxified Zn is often chelated with metallotheonin or condensed in granules, compounds such as Zn-cysteine, Zn-oxalate, $ZnPO_4$, ZnS and $ZnCl_2$ could include important reference materials.
Conventional micro-XANES spectra represent the full line integral along the beam penetrating the sample and could therefore also include information regarding the local environment before or behind the target tissue. Therefore, the possibility of confocal micro-XANES was explored on a single egg, which allowed the determination of the local environment of Zn within a specific subvolume within a target tissue. Interestingly, the confocal micro-XANES spectrum shows good agreement with the conventional micro-XANES spectrum of a single egg, showing that the confocal detection does not introduce significant artefacts in the XANES spectrum.

The combination of the previously discussed 2D micro-XRF, XRF micro-CT, confocal micro-XRF, micro-XANES and absorption microtomography under conventional and cryogenic sample environments provided valuable information regarding the tissue-specific metal accumulation and speciation within *Daphnia magna*. With the aim of shifting from the microscopic towards a subcellular field of view, Chapter 8 discusses the analysis of tissue thin-sections ($2\ \mu m$) of *Daphnia magna* at the ID22NI XRF-nanoprobe at the ESRF, Grenoble, France. At this instrument, a crossed elliptical Rh coated graded multilayer-mirror pair in the Kirkpatrick-Baez (KB) geometry is available, which allows monochromatisation and focusing of a pink (wide-bandwidth) X-ray beam to a spot smaller than 90 nm in both directions, which is a major breakthrough in X-ray optics. Since the achievable relative detection limits are also in the 10-100 *ppb* range (similarly to that of beamline L, HASYLAB), the absolute detection limits fall in the range of 10-100 zg. The high flux (i.e. $> 10^{11}\ ph/s$) and sensitivity is critical to provide the trace level metal distributions within *Daphnia magna* thin-section samples at the inter- and intra-cellular level. A drawback of the extreme flux-density is that during analysis clearly visible sample damage is occurring, therefore the scanning time should be as short as possible. The unprecedented resolution ($\approx 100\ nm$) revealed that NIST SRM 1577C is heterogeneous for specific elements (e.g. Cu), which demonstrates the need for the development of new standard/certified reference materials adapted for these resolution levels. Analysis of thin-sections of *Daphnia magna* allowed a correlation between high resolution TEM images and nano-XRF element maps, enabling the identification of the thoracic appendages, filter plates and gill-like structures. Interestingly, an element map of an epipodite could be obtained, allowing the investigation of cations and anions within this osmoregulatory gill tissue. The marked presence of Fe within the gill tissue confirms the haemolymph flowing through the tissue, while the enclosure of the haemolymph by respectively a Ca supporting structure and a nanometer thin Zn layer agree very well with previous ecotoxicological re-

search, in which the accumulation of Zn within the exoskeleton was suggested, followed by excretion of metals by renewing the carapax. The installation of a detection side polycapillary allowed the coupling of a nanometer sized beam with a confocal detection scheme. In combination with a tomography set-up, this should allow local confocal tomography, allowing the determination of local three-dimensional metal distribution within a virtual cylinder in the sample with nanoscopic resolution.

Chapter 10

Samenvatting en besluit

De unieke eigenschappen van synchrotronstraling (SR) bieden een enorm potentieel en nieuwe mogelijkheden voor wetenschappelijke exploratie in verscheidene disciplines. De exponentiële toename in *brilliance* verkregen aan derde generatie synchrotronfaciliteiten heeft een ongeziene ontwikkeling van nieuwe of sterk verbeterde, niet-destructieve analytische technieken mogelijk gemaakt.
Mede dankzij de ontwikkeling van X-straal optica en detectoren, heeft X-straal microanalyse sterke vooruitgang geboekt en is deze discipline bovendien een sterk visueel gerichte periode binnengetreden door de ontwikkeling van verschillende X-straal beeldvormingstechnieken. Verwacht wordt dat deze ontwikkelingen zullen resulteren in nieuwe inzichten in complexe processen die in de natuur plaatsvinden op de micro- en nanoscopische schaal, bijvoorbeeld in de biowetenschappen.
Om dit potentieel te demonstreren en verder te ontwikkelen, werden in dit werk de unieke eigenschappen van X-straal microspectroscopie en beeldvorming (besproken in Hoofdstuk 2) verkend om metaaldistributies op (sub)microscopisch niveau te detecteren, visualiseren en kwantificeren in het biologische modelorganisme *Daphnia magna*. Dit organisme wordt frequent gebruikt als modelorganisme in de milieutoxicologie om de effecten van gecontroleerde metaalblootstellingen te onderzoeken.

Hoofdstuk 3 geeft een introductie omtrent de ecotoxicologische aspecten van dit modelorganisme en de monstervoorbereidingstechnieken die aangewend kunnen worden voor X-stralen analyse. Hoewel X-straalspectroscopie en -beeldvorming het potentieel hebben om een monster te analyseren op een niet-destructieve manier, vormen biologische monsters een uitdaging in deze context omwille van hun grote gevoeligheid voor stralingschade. Aangezien X-straalfluorescentie (XRF) beeldvormingsmethodes vooral gebaseerd zijn op scanning technieken waarbij het te onderzoeken staal ongewijzigd moet blijven terwijl het gescand wordt door een intense X-straal micro/nanobundel, was een adequate monstervoorbereidingsprocedure voor *Daphnia magna* noodzakelijk. In dit werk werden zowel cryogene als chemische

fixatie gebaseerde monstervoorbereidingsmethodes aangewend.
De beste meetcondities kunnen voor dergelijke stalen bereikt worden door ze zo dicht mogelijk bij hun natuurlijke staat te analyseren. Daarom is cryogene koeling een logische stap om de microstructuur van het staal te bewaren. *Plunge freezing* of *High pressure freezing* hebben immers aangetoond de (sub)micron morfologie van het staal intact te houden door de vorming van vitreus ijs, echter maar tot op een diepte van 200 μm. Stalen die groter zijn, moeten noodgedwongen gedissecteerd worden, wat praktisch niet altijd haalbaar is en bovendien ook veranderingen kan induceren in de microstructuur. Wanneer een micro-XRF analyse wordt uitgevoerd, kan het staal gekoeld worden met een *cryostream*, aangezien de resulterende microscopische ijskristallen de elementverdelingen niet significant wijzigen op dit resolutieniveau. Nanoscopische X-straalfluorescentie analyse op biologische monsters daarentegen, vereist na de *plunge freezing* van het staal een snelle transferstap naar een experimentele setup met cryogene koeling om herkristallisatie te vermijden. Een geïntegreerde aanpak, waarbij de vloeibare fase van het staal wordt omgezet tot vitreus ijs aan een vibratievrije cryo-setup is een ideale oplossing, maar is op dit moment nog niet beschikbaar.

De laboratorium micro-XRF experimenten op *Daphnia magna* beschreven in Hoofstuk 4 werden uitgevoerd onder niet-cryogene condities aangezien het ontwerp van de spectrometer vacuümkamer geen cryogene koeling toelaat. Tengevolge van de vaste opbouw van het instrument zijn enkel conventionele 2D micro-XRF experimenten mogelijk en is geen lokale (dieptegevoelige) X-straal analyse van het staal mogelijk. Daarom werden er raster XRF analyses uitgevoerd op dunne weefselcoupes van *Daphnia magna*, die gemaakt werden door middel van een dehydratatie in water/aceton series, gevolgd door een substitutie met paraffine.
Voor de SR micro-XRF/XAS analyses op *Daphnia magna* beschreven in de Hoofdstukken 5, 6 en 7, waren lokale (dieptegevoelige) X-straal analyses in *Daphnia magna* mogelijk. In dit geval werd voor een dehydratatie in water/aceton reeksen geopteerd, gevolgd door fixatie met hexamethyldisilazane (HMDS) op *Daphnia magna*, wat de 3D microstructuur van het staal bewaarde in tegenstelling tot methodes zoals kritisch punt drogen/vriesdrogen. Tijdens de tweede fase van dit werk werd een *cryostream* getest aan een SR microprobe bundellijn en werden gedetailleerde vergelijkingen gemaakt van de elementdistributies verkregen op *Daphnia magna*, chemisch gefixeerd met HMDS enerzijds en cryogene fixatie anderzijds. Hoewel veranderingen in elementdistributies voor sommige elementen vastgesteld werden (bvb. Cu), werden geen substantiële verschillen waargenomen voor het targetmetaal Zn.
De SR nano-XRF analyses beschreven in Hoofdstuk 8 werden uitgevoerd onder omgevingstemperatuur. Analyse onder cryogene omstandigheden werd in dit geval niet uitgevoerd wegens gekende problemen aan SR-XRF nanoprobes, zoals bijvoorbeeld vibratie van het staal en foute uitlijning van de optica ten gevolge van temperatuurdrift. Voor deze experimenten moest de monstervoorbereiding aangepast worden. Cryosectie gevolgd door dehydratatie bewaarde de

structurele integriteit van *Daphnia* niet en bijgevolg ook niet de metaaldistributies. Chemische fixatie gevolgd door substitutie met een paraffine verzekerde de morfologische structuur op de microschaal, terwijl inbedding in een polymeer (LR white) noodzakelijk was om voldoende stevigheid te verschaffen en zodoende dunne weefselcoupes te verkrijgen. Daarom werd chemische fixatie aangewend gevolgd door substitutie met LR white om de cellullaire morfologie van het staal te vrijwaren. Dunne coupes van *Daphnia magna* werden gemaakt (2 μm dikte) om specifieke gebieden van interesse te onderzoeken. Echter, de mogelijke herdistributie van metalen op nanoscopische schaal tijdens verschillende monstervoorbereidingsmethodes moet verder onderzocht worden.

In Hoofdstuk 4 werd laboratorium gebaseerde scanning micro-XRF analyse gebruikt als een complementaire analysetechniek voor de detectie van elementen met atoomnummers onder 19 en voor monster prekarakterisatie vooraleer een hoge gevoeligheid SR-XRF analyse uit te voeren op *Daphnia magna*. De gebruikte commerciële microbundel XRF spectrometer (EDAX Eagle-III) is opgebouwd uit een Rh microfocus X-straalbuis, een polycapillaire lens en een $Si(Li)$ detector. Ten gevolge van de polychromatische aard van de excitatiebron, gekoppeld met de energieafhankelijke focuseigenschappen van de capillaire optica, lag de effectieve bundelvariatie in een bereik van 50-15 μm in het energiegebied van 1-20 keV respectievelijk. Bovendien kan door defocussering van de polycapillaire optica ten opzichte van het monsteroppervlak een bundelgrootte tot 300 μm bekomen worden. Gemeten relatieve detectielimieten bepaald met behulp van het biologisch referentiemateriaal NIST SRM 1577B bevonden zich in het 10-100 ppm gebied voor de hogere Z elementen (bijvoorbeeld voor Mn, Fe, Cu en Zn), wat overeenkomt met een absolute detectielimiet in het 1-10 pg gebied voor een meettijd van 300 s. Detectielimieten voor lage Z elementen (bijvoorbeeld P, S, Cl, K en Ca) aanwezig in biologische stalen bevonden zich ook in dit gebied wanneer de vacuüm mogelijkheid van het toestel gebruikt werd. Daarom is een laboratorium microprobe een waardevol complementair instrument voor lage Z elementanalyse, vergeleken met SR XRF microprobes die zelden over een vacuüm monsterkamer beschikken.
Met behulp van dit instrument werd een HMDS gefixeerde *Daphnia magna* geanalyseerd en werden de geïntegreerde elementdistributies voor P, S, Ca en Fe na een analysetijd van enkele dagen bekomen. Naast de analyse van een volledig organisme, leverde de analyse van dunne, in paraffine ingebedde weefselcoupes (10-20 μm) van *Daphnia magna* verder inzicht in de lokale distributie van deze elementen. Terwijl Ca vooral aanwezig was in de carapax en Fe gedetecteerd werd in de verteringsklier, werden P en S voornamelijk gedetecteerd in de inwendige weefsels zoals darm, kieuw en embryo's. Elementdistributies van het targetelement Zn konden niet verkregen worden door onvoldoende gevoeligheid voor dit spoorelement.
Vervolgens werden de detectielimieten en de ruimtelijke resolutie van de laboratorium micro-XRF analyse op *Daphnia magna* (uitgevoerd onder vacuümcondities, LT=5 s/punt) vergeleken met een laser ablatie inductief gekoppeld plasma massaspectrometrie (LA-ICPMS) opstelling

(15 μm laserbundel) met behulp van het biologisch referentiemateriaal NIST SRM 1577B. In het geval van P was de relatieve detectielimiet verkregen met micro-XRF (230 ppm) beter dan met LA-ICPMS (600 ppm). De bepaling van S met LA-ICPMS wordt gehinderd door spectrale overlap, waardoor de detectielimiet een factor 100 hoger is dan de relatieve detectielimiet van 160 ppm verkregen met micro-XRF. Ook de bepaling van Ca met ICPMS wordt verstoord door spectrale overlap, waardoor de verkregen relatieve detectielimiet vergelijkbaar is met micro-XRF (100 vs 120 ppm). De detectie van Zn in het referentiemateriaal was niet mogelijk met micro-XRF onder deze condities, terwijl de relatieve detectielimiet verkregen met LA-ICPMS 30 ppm was.
Na de analytische vergelijking van beide technieken met NIST SRM 1577B, werden de elementdistributies verkregen op *Daphnia magna* vergeleken met die bekomen met LA-ICPMS. Na een niet-destructieve analyse met de laboratorium XRF microprobe, werden de dunne weefselcoupes (10-20 μm) onderworpen aan LA-ICPMS, met een minimale ablatie diameter van 15 μm. Gezien de vergelijkbare detectielimieten van micro-XRF en LA-ICPMS voor P en Ca, konden deze elementverdelingen vergeleken worden door een geschikte schaling met behulp van histogram analyses. Micro-XRF leverde een meer kwaliteitsvolle distributie van S in *Daphnia magna* als gevolg van zijn hogere gevoeligheid vergeleken met LA-ICPMS, dat sterk onderhevig is aan spectrale interferenties voor dit element. Door de hogere gevoeligheid die LA-ICPMS voor het target element Zn bezit, kon met deze techniek een Zn elementdistributie van *Daphnia magna* verkregen worden. Beide technieken zijn dus complementair om een uitgebreide chemische profilering te verkrijgen op *Daphnia magna*. Betreffende de ruimtelijke resolutie en verstoringen kan geconcludeerd worden dat de kwaliteit van de elementdistributies verkregen met LA-ICPMS verstoord wordt door *wash-out* effecten in de ablatiekamer en de aanwezigheid van spikes vergeleken met de micro-XRF resultaten. Echter, door de chromatische aard van de X-straalbundel in laboratorium micro-XRF is de eigenlijke resolutie sterk afhankelijk van het bestudeerde element en daarom vaak lager vergeleken met LA-ICPMS.

In tegenstelling tot de laboratorium micro-XRF experimenten op *Daphnia magna*, liet het gebruik van een synchrotron XRF microprobe (beschreven in de Hoofdstukken 5 en 6) de studie van spoorelementdistributies in dit organisme op een niet-destructieve manier toe wegens de hoge elementgevoeligheden verkregen door het gebruik van lineair gepolariseerde, monochromatische X-straal microbundels. De verhoogde elementgevoeligheden van de bundellijn L microprobe, aanwezig aan de tweede generatie synchrotronfaciliteit HASYLAB, Hamburg, Duitsland, waren ideaal geschikt en noodzakelijk om de microscopische spoorelementdistributie van Zn in *Daphnia magna* te visualiseren.

De essentiële opbouw van de initiële experimentele set-up in Hoofdstuk 5 bestaat uit een multilaag monochromator voor hoge flux applicaties gekoppeld met een *single bounce* monocapillair met een lage divergentie bundelgrootte van 15 μm (FWHM). Ten gevolge van de monochromatische excitatie en hoge graad van polarisatie, werden relatieve detectielimieten bekomen

in het 10-100 *ppb* gebied voor transitiemetalen, wat overeenkomt met detectielimieten in het 1-10 fg gebied. Deze detectielimieten zijn ongeveer drie grootte-ordes lager vergeleken met een laboratorium XRF microprobe. Twee dimensionele (2D) and computertomografie (CT) micro-XRF experimenten werden uitgevoerd met behulp van een dynamische scanning routine. Een hoge resolutie CCD camera werd gebruikt om de targetregio's te bepalen voor de scanning micro-XRF experimenten. In een pilootexperiment werd tevens een cryogene gasstroom (N_2) gebruikt in combinatie met twee silicium driftdetectoren (SDD), wat een duale detector cryomapping en -tomografie toeliet van het organisme dicht bij zijn natuurlijke staat. De duale detector set-up onder cryogene omstandigheden was van vitaal belang om zelfabsorptie effecten te corrigeren van lage Z elementen ten gevolge van de hogere absorptie in de waterige matrix van het organisme, vergeleken met gedroogde stalen. Om de 2D micro-XRF elementdistributies te kwantificeren werd een adequate normalisatieprocedure opgesteld gebruik makende van de ionisatiekamer offset en de SDD detector dode tijd.
K-means clustering werd gebruikt om weefsels van interesse te selecteren en de multi-element samenstelling te vergelijken van 1) verschillende weefsels binnen *Daphnia magna* 2) gelijkaardige weefsels tussen verschillend blootgestelde *Daphnia magna*. Principale component-analyse werd aangewend om de (co)variantie van de elementconcentratie tussen verschillende clusters te analyseren. Wanneer niet blootgestelde *Daphnia magna* vergeleken werden met Zn blootgestelde *Daphnia magna* werd een aanrijking van Zn vastgesteld in het kieuwweefsel, de darm en de verteringsklier. Wanneer genetisch verschillende organismen met hoge en lage metaaltolerantie blootgesteld werden aan Zn en geanalyseerd onder cryogene omstandigheden, werd een lagere Zn accumulatie vastgesteld bij de Zn blootgestelde metaaltolerante organismen vergeleken met de Zn blootgestelde niet-metaaltolerante organismen, wat aantoont dat Zn minder snel opgenomen wordt en/of sneller geëlimineerd wordt bij metaaltolerante organismen.
Door gebruik te maken van een fouriertransformatie op de elementsinogrammen van de micro-XRF CT experimenten, konden verbeterde elementdistributies bekomen worden voor P, Cl, K, Mn en Br. Tenslotte werd laboratorium micro-CT op *Daphnia magna* met een minimale resolutie van 1 μm gekoppeld met verkregen 2D/CT micro-XRF om accurate correlaties te verkrijgen tussen de weefselstructuur en elementdistributie.

Wanneer de elementdistributies van virtuele dunne doorsnedes onderzocht moeten worden op een groot aantal stalen, bijvoorbeeld in het geval van verschillende *Daphnia magna* van een uitgebreide ecotoxicologische studie is micro-XRF CT niet de methode bij uitstek wegens: 1) lange scanning tijden 2) complexe uitlijning van het staal 3) moeilijke kwantificatie. Recent werd echter een nieuwe variant van micro-XRF ontwikkeld die tegemoet komt aan deze gebreken: polycapillair gebaseerde confocale micro-XRF. In Hoofdstuk 6 werd deze techniek grondig gekarakteriseerd en toegepast voor elementbeeldvorming op *Daphnia magna*. Aan bundellijn L werd een *free standing thin film* (FSTF) aangewend om de energie afhankelijk

acceptantie van het detectiezijde polycapillair te bepalen wat geometrische informatie verschafte over het confocaal volume. Met behulp van deze FSTF standaard, werd geverifieerd dat confocale micro-XRF beschikt over gelijkaardige detectielimieten als 2D/CT micro-XRF. Aangezien het detectiezijde polycapillair heel dicht bij het staal komt door zijn lage werkafstand, is de meting van een staal onder cryogene condities moeilijk. De lage werkafstand van het detectiezijde polycapillair zou het te dicht bij de *cryostream* brengen en verkeerde alignering en/of beschadiging van het optisch systeem veroorzaken. *Daphnia* afkomstig van een ecotoxicologisch experiment dat de opname van Zn via verschillende routes onderzoekt (water en/of voedsel) werden onderworpen aan confocale micro-XRF analyse. Met behulp van *K-means clustering* en *region growing*, werd de relatieve toename van Zn in de verschillende organen berekend voor beide blootstellingreeksen (water/voedsel). De relatief hoge toename van Zn in de kieuwen is waarschijnlijk te wijten aan de primaire functie van dit weefsel, nl. actief iontransport om de osmoregulatie van de weefselvloeistoffen te handhaven. De toename van Zn in de carapax is waarschijnlijk het resultaat van het gebruik van dit weefsel als een opslagplaats voor metalen voor detoxificatie. De gelijkaardige concentratie van Zn in de darm en embryo's, alsook hun gelijkaardige proportionele toename na Zn blootstelling, bevestigen dat de Zn accumulatie in de embryo's niet te wijten is aan de ventilatie van de broedzak met omgevingswater tijdens het vrijlaten, maar waarschijnlijk aan een Zn transfer van de ovaria via de hemolymfe naar de ontwikkelende embryo's. Naast het analyseren van de elementdistributies in *Daphnia magna* uit een uitgebreide ecotoxicologische studie, liet confocale micro-XRF ook toe om: 1) bepaalde *regions of interest* (ROIs) met betere resolutie en/of betere telstatistiek te analyseren 2) een andere virtuele elementdistributie doorheen het staal te analyseren zonder herpositionering van het staal 3) een volledig 3D elementdistributie te verkrijgen binnen een volume van interesse. Aan de hand van de verschillen in absorptie van de K_α en K_β lijnen van Ca, werd een schatting van de zelfabsorptie binnen deze stalen uitgevoerd. Tenslotte werden dorsoventrale en sagittale elementdistributies van *Daphnia magna* verkregen met confocale micro-XRF gecombineerd met laboratorium absorptie micro-CT.

Hoewel X-straal fluorescentie microanalyse informatie kan leveren over de metaaldistributie en -concentratie binnenin stalen, kan er met deze techniek geen vorm van speciatie uitgevoerd worden. X-straal absorptie fijnstructuur (XAFS), een techniek die wel over deze mogelijkheid beschikt, toonde recentelijk zijn compatibiliteit met een microfocus en confocale geometrie. Daarom werd in Hoofdstuk 7 XAFS aan de *Dutch Belgian Beamline* (DUBBLE) aan de Europese Synchrotronstralingfaciliteit (ESRF), Grenoble, Frankrijk besproken om additionele informatie te verkrijgen betreffende de speciatie van het targetmetaal Zn. In een pilootexperiment werd initieel een 2D micro-XRF analyse uitgevoerd om een overzicht te krijgen van de elementdistributies in de targetweefsels voorafgaand aan XAFS analyse. Hoewel de micro-Extended X-ray Absorption Fine Structure (micro-EXAFS) analyse te lage telstatistiek voorzag voor het spoorelement Zn, reveleerde micro X-ray Absorption Near Edge

Structure (micro-XANES) spectroscopie een verschillende coördinatieomgeving voor Zn over de volledige diepte van verschillende weefsels, zoals darm, embryo's en darmkanaal. De Zn coördinatie in twee eitjes was identiek en gelijkaardig als in NIST SRM 1577B, terwijl het XANES spectrum van de darm significant verschillend was, wat aantoont dat Zn een weefselspecifieke coördinatie bezit. Voor een volledige identificatie van de spectra, zijn meer spectra van referentiematerialen nodig, wat verder onderzoek vereist. Aangezien gedetoxificeerd Zn vaak gechelateerd is aan metallothionines of gecondenseerd in granules, zijn verbindingen zoals Zn-cysteine, Zn-oxalaat, $ZnPO_4$, ZnS en $ZnCl_2$ mogelijke referentiematerialen. Conventionele micro-XANES spectra zijn representatief voor de hoeveelheid materiaal geëxciteerd langs het volledig bundelpad doorheen het staal en kunnen daardoor ook informatie bevatten betreffende de coördinatie van Zn voor of na het targetweefsel. Daarom werd confocale micro-XANES geïllustreerd op een individueel ei, wat de bepaling van de coördinatie van Zn in een specifiek subvolume in een targetweefsel toeliet. Het confocale micro-XANES spectrum toonde grote overeenkomst met het conventioneel micro-XANES spectrum, wat aantoont dat het confocaal detectievolume geen significante artefacten in het XANES spectrum induceert.

De combinatie van de besproken 2D micro-XRF, XRF micro-CT, confocale micro-XRF, absorptie micro-CT, micro-XANES onder conventionele en cryogene omstandigheden voorzagen belangrijke informatie betreffende de weefselspecifieke metaalaccumulatie en -speciatie in *Daphnia magna*. Echter, om het effect van Zn verder te onderzoeken op het (sub)cellullaire niveau, werd in Hoofdstuk 8 de analyse van dunne weefselcoupes van *Daphnia magna* aan de ID22NI XRF nanoprobe aan de Europese Synchrotronstraling Faciliteit (ESRF) besproken. Aan dit instrument is een gekruist elliptisch Rh gecoat spiegelpaar in de *Kirkpatrick-Baez* geometrie aanwezig dat tegelijkertijd monochromatisatie en focussering toelaat van de polychromatische X-straalbundel tot een nanobundel van 90 nm in beide richtingen, wat een uitzonderlijke doorbraak is in X-straal optica. Aangezien relatieve detectielimieten zich ook in de 10-100 *ppb* range bevinden voor 300 s meettijd, kunnen absolute detectielimieten bereikt worden in het 10-100 zg gebied. De hoge flux ($> 10^{11}$ $fotonen/s$) en gevoeligheid is essentieel om de inter- en intracellulaire spoorelementdistributie te visualiseren in dunne (2 μm) weefselcoupes van *Daphnia magna*. Een nadeel van de hoge flux-densiteit is dat tijdens de analyse duidelijk zichtbare schade van het staal optreedt waardoor de analysetijd zo kort mogelijk moet gehouden worden. De ongeziene resolutie ($\approx$ 100 nm) reveleerde dat NIST SRM 1577C heterogeen is voor bepaalde spoorelementen (Cu bijvoorbeeld), wat de noodzaak aanduid voor nieuwe standaarden binnen deze wetenschappelijk discipline. Analyse van dunne weefselcoupes van *Daphnia magna* liet een correlatie toe tussen hoge resolute TEM beelden en nano-XRF elementdistributies, wat de identificatie toeliet van kieuwpoten (exopodieten), filterplaten en kieuwblaasjes (epipodieten). De elementdistributies in een epipodiet konden gevisualiseerd worden, wat een nauwer onderzoek van de ionen in dit osmoregulatorisch kieuwweefsel toeliet. De duidelijke aanwezigheid van Fe bevestigt de aan-

wezigheid van hemolymfe, terwijl een Ca-houdende draagstructuur omgeven werd door een Zn laag van enkele nanometer. De accumulatie van Zn in het exoskelet, gevolgd door excretie van metalen door vervelling werd reeds vroeger gesuggereerd en bevestigt deze elementdistributies. Installatie van een detectiezijde polycapillair liet de koppeling van een nanobundel met een confocaal detectieschema toe. In combinatie met een tomografie set-up, wordt lokale confocale tomografie mogelijk, wat de 3D metaaldistributie kan visualiseren binnenin een virtuele cilinder in het biologisch staal met nanoscopische resolutie.

Appendix A

Publications and activities

A.1 List of (contributions to) Publications

A.1.1 Articles

A1 (ISI Web of Science)

1. TRPC6 channels from iron-conducting channels in cortical neurons, S. Bohic, P. Tu, B. De Samber, A. Bouron, Journal of Cellullar Biology (submitted)

2. Hard X-ray Nanoprobe Investigations of the Sub-tissue Metal Distributions within Daphnia magna, B. De Samber, S. Vanblaere, K. De Schamphelaere, C.R. Janssen, T. Schoonjans, G. Silversmit, B. Vekemans, S. Bohic, G. Martinez-Criado, R. Tucoulou, P. Cloetens, J. Susini, F. Vanhaecke, G. Falkenberg, L. Vincze, Analytical Chemistry (submitted)

3. Comparison of Laser Ablation-Inductively Coupled Plasma-Mass Spectrometry and Micro X-ray Fluorescence Techniques for Elemental Imaging in Daphnia magna, D. S. Gholap, A. Izmer, B. De Samber, J. T. van Elteren, V.S. Selih, R. Evens, C. Janssen, L. Balcaen, L. Vincze, F. Vanhaecke, Analytica Chimica Acta (submitted)

4. Element-to-tissue Correlation in Biological Samples Determined by Three-dimensional X-ray Imaging Methods, B. De Samber, K. De Schamphelaere, R. Evens, G. Silversmit, T. Schoonjans, B. Vekemans, C.R. Janssen, B. Masschaele, L. Van Hoorebeke, I. Szaloki, F. Vanhaecke, K. Rickers, G. Falkenberg, L. Vincze, Journal of Analytical Atomic Spectrometry (accepted)

5. Multi-disciplinary characterisation of a sandstone surface crust, V. Cnudde, G. Silversmit, M. Boone, J. Dewanckele, B. De Samber, T. Schoonjans, D. Van Loo, Y. De Witte, M. Elburg, L. Vincze, L. Van Hoorebeke, P. Jacobs, Science of the Total Environment, 407: 5417-5427 (2009)

6. Fate and effects of CeO_2 nanoparticles in Aquatic Ecotoxicity Tests, K. Van Hoecke, J.T.K. Quik, J. Mankiewicz-Boczek, K.A.C. De Schamphelaere, A. Elsaesser, P. Van der Meeren, C. Barnes, G. McKerr, C.V. Howard, D. Van De Meent, K. Rydzynski, K.A. Dawson, A. Salvati, A. Lesniak, I. Lynch, G. Silvermit, B. De Samber, L. Vincze, C.R. Janssen, Environmental Science & Technology, 43: 4537-4546 (2009)

7. A combination of Synchrotron and Laboratory X-ray Techniques for Studying Tissue Specific Trace Level Metal Distributions in Daphnia magna, B. De Samber, R. Evens, K. De Schamphelaere, G. Silversmit, B. Masschaele, T. Schoonjans, B. Vekemans, C. Janssen, L. Van Hoorebeke, I. Szaloki, F. Vanhaecke, G. Falkenberg, L. Vincze, Journal of Analytical Atomic Spectrometry, 23:829-839 (2008)

8. Three-dimensional elemental imaging by means of synchrotron radiation micro-XRF: developments and applications in environmental chemistry, B. De Samber, G. Silversmit, R. Evens, K. De Schamphelaere, C. Janssen, B. Masschaele, L. Van Hoorebeke, L. Balcaen, F. Vanhaecke, G. Falkenberg, L. Vincze, Analytical and Bioanalytical Chemistry, 390:267-271 (2008)

9. Use of bromine isotope ratio in HPLC-ICP-MS and HPLC-ESI-MS analysis of a new drug in development, F. Cuyckens, L. Balcaen, K. De Wolf, B. De Samber, C. Van Looveren, R. Hurkmans, F. Vanhaecke, Analytical and Bioanalytical Chemistry, 390:1717-1729 (2008)

10. Hyphenation of reverse-phase HPLC and ICP-MS for metabolite profiling: application to a novel antituberculosis compound as a case study, L. Balcaen, B. De Samber, K. De Wolf, F. Cuyckens, F. Vanhaecke, Analytical and Bionanalytical Chemistry, 389:777-786 (2007)

A2 (Reviewed International Journals)

1. Dual detection X-ray Fluorescence Cryotomography and -mapping on the model organism Daphnia magna, B. De Samber, S. Vanblaere, R. Evens, K. De Schamphelaere, G. Wellenreuther, F. Ridouitt, G. Silversmit, T. Schoonjans, B. Vekemans, B. Masschaele, L. Van Hoorebeke, K. Rickers, G. Falkenberg, I. Szaloki, C. Janssen, L. Vincze, Advances in X-ray Analysis, (submitted) 2009

A3 (Reviewed National Journals)

1. Binnengluren binnenin objecten, EOS magazine 2007

A4 (Others)

1. Metal Contaminations in small waterfleas: a combination of X-ray imaging experiments, Photon Science 2008: Research Highlights HASYLAB, 38-39 (2009)

2. Chemische beeldvorming met synchrotronstraling, Micro Macro Mega in de Microscopie, Museum voor de geschiedenis van de Wetenschappen, 100-103 (2009)

3. Focused ion beam etching, Micro Macro Mega in de Microscopie, Museum voor de Geschiedenis van de Wetenschappen, 103-106 (2009)

4. Investigation of *Daphnia magna* genotypes with different Zn tolerance using micro-XRF under cryogenic conditions, B. De Samber, K. De Schamphelaere, G. Falkenberg, K. Appel, L. Vincze, HASYLAB Annual Report 2009 (in press)

5. Dual Detector micro-XRF Cryotomography and Mapping on the Model Organism *Daphnia magna*, B. De Samber, G. Wellenreuther, R. Evens, K. De Schamphelaere, C. Janssen, I. Lindemann, G. Silversmit, T. Schoonjans, B. Vekemans, I. Szaloki, G. Falkenberg, K. Appel and L. Vincze, HASYLAB Annual Report 2009 (in press)

6. 3D element-to-tissue correlation determined by continuous confocal micro-XRF scanning at Beamline L, B. De Samber, R. Evens, K. De Schamphelaere, C. Janssen, B. Masschaele, L. Van Hoorebeke, B. Vekemans, G. Falkenberg, K. Rickers, I. Szaloki, L. Vincze, HASYLAB Annual Report 2008

7. Cryomapping on Daphnia magna at Beamline L using a cryostream: experimental setup and comparison, B. De Samber, R. Evens, K. De Schamphelaere, C. Janssen, F. Ridoutt, K. Rickers, G. Falkenberg, I. Szaloki, L. Vincze, G. Wellenreuther, HASYLAB Annual Report 2008

8. A weathered Belgian sandstone surface crust studied with laboratory micro-XRF and synchrotron micro-XANES, G. Silversmit, V. Cnudde, B. De Samber, L. Van Hoorebeke, L. Vincze, HASYLAB Annual Report 2008

9. Trace element distribution in Hungarian and Chinese rice by confocal micro-XRF, G. Silversmit, B. De Samber, T. Schoonjans, L. Vincze, V. Mihucz, G. Zaray, I. Szaloki, HASYLAB Annual Report 2007, 1283-1284

10. $Eu-L2$ XANES on $CsBr:Eu$ needle image plates for X-ray radiography, G. Silversmit, J. Lenaerts, B. De Samber, J.-P. Tahon, P. Leblans, L. Vincze, HASYLAB Annual Report 2007, 967-968

11. Evaluation of the capabilities of ICP-MS and confocal micro-XRF for studying the pharmacodynamical properties of intraperitoneal chemohyperthermia with oxaliplatin

in rats, B. De Samber, V. Van Lierde, W. Bouquet, W. Ceelen, A. Heyse, L.Vincze, G. Falkenberg, F. Vanhaecke, HASYLAB Annual Report 2007, 1477-1478

12. Combining laboratory X-ray absorption tomography and SR confocal micro-XRF for studying a full factorial Zn exposure experiment on Daphnia magna, B. De Samber, G. Silversmit, R. Evens, K. De Schamphelaere, C. Janssen, M. Dierick, L. Van Hoorebeke, L. Balcaen, F. Vanhaecke, I. Szaloki, K. Rickers, G. Falkenberg, L. Vincze, HASYLAB Annual Report 2007, 1281-1282

13. Synchrotron radiation based X-ray Fluorescence reveals tissue-specific distribution of metals in Daphnia magna, B. De Samber, G. Silversmit, R. Evens, K. De Schamphelaere, C. Janssen, B. Masschaele, L. Van Hoorebeke, L. Balcaen, F. Vanhaecke, I. Szaloki, G. Falkenberg, L. Vincze, HASYLAB Annual Report 2007, 1291-1292

14. Implementation of a High Resolution CCD camera at Beamline L, B. De Samber, G. Falkenberg, L. Vincze, HASYLAB Annual Report 2006, 1389-1390

15. Micro-X-ray Fluorescence Computed Tomography and Radiography on Daphnia magna, B. De Samber, G. Silversmit, T. Schoonjans, R. Evens, K. De Schamphelaere, C. Janssen, L. Balcaen, F. Vanhaecke, I. Szaloki, G. Falkenberg, L. Vincze, HASYLAB Annual Report 2006, 1087-1088

A.1.2 Books

B2 (Chapter in books)

1. Microscopic X-Ray Fluorescence Analysis with Synchrotron Radiation Sources, F. Adams, B. Vekemans, G. Silversmit, B. De Samber and L. Vincze, Handbook of Nuclear Chemistry, 2nd Edition, A. Vertes, S. Nagy, Z. Klencsar (Eds.), Kluwer Academic Publishers, The Netherlands, 2009 (in press).

A.1.3 Other publications

C1 (Articles in Proceedings)

1. Laboratory and synchrotron radiation micro- and nano X-ray fluorescence: instrumental developments and applications in life science, JST Symposium on Micro and Trace X-ray analysis, B. De Samber, G. Silversmit, R. Evens, K. De Schamphelaere, C. Janssen, B. Masschaele, L. Van Hoorebeke, L. Balcaen, F. Vanhaecke, I. Szaloki, G. Falkenberg, L. Vincze, Osaka City University Media Center (invited lecture, 12-14/02/2009)

C2 (Conference Abstracts)

1. Hard X-ray Nanoprobe Investigations of the Metal Distribution within the Biological Model Organism *Daphnia magna*, B. De Samber, S. Vanblaere, K. De Schamphelaere, C. Janssen, I. Lindemann, T. Schoonjans, G. Silversmit, B. Vekemans, S. Bohic, G. Martinez-Criado, R. Tucoulou, P. Cloetens, J. Susini, L.Vincze, Synchrotron Radiation for Bio-Imaging at PETRAIII, Hamburg, Germany (poster+talk, 29-30/03/2010)

2. Dual Detector X-ray Fluorescence Cryotomography and -Mapping on the Model Organism Daphnia magna, B. De Samber, I. Lindemann, T. Schoonjans, G. Silversmit, B. Vekemans, R. Evens, S. Vanblaere, K. De Schamphelaere, C. Janssen, G. Wellenreuther, K. Rickers, G. Falkenberg, L.Vincze, Flemish Youth Conference of Chemistry (VJC-10), Blankenberge, Belgium (poster, 01-02/03/2010)

3. Comparison of Laser Ablation-Inductively Coupled Plasma-Mass Spectrometry and Micro X-ray Fluorescence Techniques for Elemental Imaging in Daphnia magna, D. S. Gholap, A. Izmer, B. De Samber, J. T. van Elteren, V.S. Selih, R. Evens, C. Janssen, L. Balcaen, L. Vincze, F. Vanhaecke, 2010 Winter conference on Plasma Spectrochemistry, Fort Myers, Florida (presentation, 04-09/01/2010)

4. Non-Negative Matrix Approximation (NNMA) on Daphnia magna : an alternative to principal component analysis, G. Wellenreuther, B. De Samber, L. Vincze, IXCOM 2009, Karlsruhe, Germany (presentation, 14-18/09/2009)

5. X-ray Imaging on Biological Model Organisms using Micro- and Nano X-ray Fluorescence, 2009 Denver X-ray conference, B. De Samber, G. Silversmit, R. Evens, K. De Schamphelaere, C. Janssen, B. Masschaele, L. Van Hoorebeke, L. Balcaen, F. Vanhaecke, I. Szaloki, G. Falkenberg, L. Vincze, Colorado Springs, USA (presentation, 27-31/07/2009)

6. Hard X-ray nanoprobe investigations of the metal influx through transient receptor potential canocical ion channels of individual cortical neurons, B. De Samber, P. Tu, A. Bouron, J. Susini, P. Cloetens, J. Susini, L. Vincze, 2009 Doctoral Symposium Faculty of Sciences, ICC Gent, Belgium (poster, 28/04/2009)

7. X-ray Fluorescence and Absorption Microtomography reveal Tissue Specific Distribution of Metals in Daphnia magna, B. De Samber, G. Silversmit, R. Evens, K. De Schamphelaere, C. Janssen, B. Masschaele, L. Van Hoorebeke, L. Balcaen, F. Vanhaecke, I. Szaloki, G. Falkenberg, L. Vincze, 2009 Synchrotron and Neutron Workshop, Brussels, Belgium (Best poster award, 23/04/2009)

8. X-ray Fluorescence and Absorption Microtomography reveal Tissue Specific Distribution of Metals in Daphnia magna, B. De Samber, G. Silversmit, R. Evens, K. De Scham-

phelaere, C. Janssen, B. Masschaele, L. Van Hoorebeke, L. Balcaen, F. Vanhaecke, I. Szaloki, G. Falkenberg, L. Vincze, JST Symposium on Micro and Trace Analysis, Osaka City University Media Center (poster, 12-14/02/2009)

9. Non-Negative Matrix Approximation on Daphnia magna: an alternative to principal component analysis?, G. Wellenreuther, B. De Samber, L. Vincze, G. Falkenberg, 2009 HASYLAB Users meeting, Hamburg, Germany (poster, 30/01/2009)

10. Laboratory and synchrotron radiation micro and nano X-ray fluorescence: methodological developments and applications in life science, Meeting of the contact group for synchrotron radiation, B. De Samber, G. Silversmit, R. Evens, K. De Schamphelaere, C. Janssen, B. Masschaele, L. Van Hoorebeke, L. Balcaen, F. Vanhaecke, I. Szaloki, G. Falkenberg, L. Vincze, Brussels, Belgium (presentation, 12/12/2008)

11. First experiences with a cryostream setup for X-ray fluorescence applications at Beamline L, G. Wellenreuther, B. De Samber, L. Vincze, G. Falkenberg, HASYLAB User Meeting 2009, Hamburg, Germany (presentation, 03/11/2008)

12. Studying Tissue-Specific Distributions of metals in Daphnia magna using scanning X-ray Fluorescence and Absorption Tomography, HyCT Meeting Days: Tomographic Imaging and Image Processing at the Ghent University, B. De Samber, G. Silversmit, R. Evens, K. De Schamphelaere, C. Janssen, B. Masschaele, L. Van Hoorebeke, L. Balcaen, F. Vanhaecke, I. Szaloki, G. Falkenberg, L. Vincze, Ghent, Belgium (presentation, 4-5/09/2008)

13. A Top-Down Approach Using X-ray Imaging Techniques: Instrumental Developments and Applications in Life Science, B. De Samber, G. Silversmit, R. Evens, K. De Schamphelaere, C. Janssen, B. Masschaele, L. Van Hoorebeke, L. Balcaen, F. Vanhaecke, I. Szaloki, G. Falkenberg, L. Vincze, 2008 Denver X-ray conference, Denver, USA (presentation, 4-8/08/2008)

14. Three dimensional SR-confocal micro-XRF combined with absorption microtomography on Daphnia magna, B. De Samber, G. Silversmit, R. Evens, K. De Schamphelaere, C. Janssen, B. Masschaele, L. Van Hoorebeke, L. Balcaen, F. Vanhaecke, I. Szaloki, G. Falkenberg, L. Vincze, 2008 European Conference on X-ray Spectrometry, Cavtat, Croatia (presentation, 16-20/06/2008)

15. Synchrotron Radiation based X-ray Fluorescence (SR-XRF) reveals Tissue-specific Distributions of Metals in Daphnia magna, B. De Samber, G. Silversmit, R. Evens, K. De Schamphelaere, C. Janssen, B. Masschaele, L. Van Hoorebeke, L. Balcaen, F. Vanhaecke, I. Szaloki, G. Falkenberg, L. Vincze, 2008 Koninklijke Vlaamse Chemische Vereniging, Antwerp, Belgium (presentation, 04/04/2008)

16. Synchrotron Radiation based X-ray Fluorescence (SR-XRF) reveals Tissue-specific distribution of metals in Daphnia magna, B. De Samber, G. Silversmit, R. Evens, K. De Schamphelaere, C. Janssen, B. Masschaele, L. Van Hoorebeke, L. Balcaen, F. Vanhaecke, I. Szaloki, G. Falkenberg, L. Vincze, 2008 HASYLAB Users meeting, Hamburg, Germany (poster, 01/2008)

17. Studying tissue-specific distributions of metals in Daphnia magna using scanning X-ray Fluorescence and Absorption Tomography, B. De Samber, G. Silversmit, R. Evens, K. De Schamphelaere, C. Janssen, B. Masschaele, L. Van Hoorebeke, L. Balcaen, F. Vanhaecke, I. Szaloki, G. Falkenberg, L. Vincze, EUROANALYSIS XIV, Antwerp, Belgium (presentation, 09-14/09/2007)

18. Synchrotron radiation based X-ray-fluorescence (SR-XRF) reveals tissue-specific element distributions in Daphnia magna, K. De Schamphelaere, B. De Samber, R. Evens, G. Silversmit, T. Schoonjans, F. Vanhaecke, I. Szaloki, G. Falkenberg, D. Adriaens, L. Vincze, C. Janssen, Proceedings of the 9th international conference on the biogeochemistry of trace elements (ICOBTE), Beijing, China (presentation, 15-19/07/2007)

19. Synchrotron Radiation Based X-ray-Fluorescence (SR-XRF) Reveals Tissue-Specific Distribution of Metals in Daphnia magna, B. De Samber, G. Silversmit, R. Evens, K. De Schamphelaere, C. Janssen, B. Masschaele, L. Van Hoorebeke, L. Balcaen, F. Vanhaecke, I. Szaloki, G. Falkenberg, L. Vincze, 2007 Doctoral symposium Faculty of Sciences, Gent, Belgium (24/04/2007, nominated poster)

20. A combination of ICP-mass spectrometry and synchrotron X-ray techniques for studying Zn uptake by Daphnia magna, F. Vanhaecke, L. Balcaen, B. De Samber, L. Vincze, K. De Schamphelaere, C. Janssen, 2007 European Winter Conference on Plasma Spectrochemistry, Taormina, Italy (presentation + nominated poster, 18-23/02/2007)

21. The use of HPLC-ICP-MS and HPLC-ESI-MS for the metabolite profiling and identification of a bromine-containing new anti-TB compound, F. Cuyckens, L. Balcaen, C. van Looveren, B. De Samber, K. De Wolf, R. Hurkmans, F. Vanhaecke, Belgian Society for Mass Spectrometry (BSMS) Annual Meeting, Leuven, Belgium (presentation, 16/02/2007)

22. Micro X-ray Fluorescence and Absorption Tomography on Daphnia magna: an ecotoxicological case study, B. De Samber, G. Silversmit, R. Evens, K. De Schamphelaere, C. Janssen, B. Masschaele, L. Van Hoorebeke, L. Balcaen, F. Vanhaecke, I. Szaloki, G. Falkenberg, L. Vincze, 2007 Satellite Meeting X-ray Fluorescence and Applications at Beamline L (invited lecture, 01/2007)

23. The use of HPLC-ICPMS and HPLC-ESI-MS for the metabolite profiling and identification of a bromine-containing new anti-TB compound, F. Cuyckens, L. Balcaen, B. De

Samber, F. Vanhaecke, 2007 Annual Meeting Belgian Society for Mass Spectrometry, Belgium (2007, poster)

24. The use of HPLC-ICPMS and HPLC-ESI-MS for the metabolite profiling and identification of a bromine-containing new anti-TB compound, F. Cuyckens, L. Balcaen, B. De Samber, F. Vanhaecke, 2006 International Mass Spectrometry Conference, Praag, Tsjechië (2006, poster)

A.2 List of Attended Beamtimes

1. Cr XANES and TiO_2 EXAFS study, Hasylab Summer Student programme, Hasylab Beamline E4, (06/09/2006 until 07/09/2006)
2. Daphnia magna experiments, Hasylab Summer Student programme, Hasylab Beamline L (08/2006 until 09/2006)
3. Three-dimensional micro-XRF/XANES I, Hasylab Beamline L (01/10/2006 until 08/10/2006)
4. Three-dimensional micro-XRF/XANES II, Hasylab Beamline L (22/03/2007 until 27/03/2007)
5. XANES and EXAFS studies on Computer screens, Hasylab Beamline L (04/05/2007 until 07/05/2007)
6. Three-dimensional micro-XRF/XANES III, Hasylab Beamline L (24/11/2007 until 31/11/2007)
7. Cellular imaging on neuron cell lines, ESRF Beamline ID22NI (16/02/2008 until 21/02/2008)
8. Cryogenic micro-XRF, Hasylab Beamline L (13/10/2008 until 15/10/2008)
9. Three-dimensional micro-XRF/XANES IV, Hasylab Beamline L (16/10/2008 until 20/10/2008)
10. Cellular imaging on *Daphnia magna*, ESRF Beamline ID22NI (25/02/2009 until 02/03/2009)
11. Cryogenic micro-XRF, Hasylab Beamline L (29/05/2009 until 01/06/2009)
12. Nano XRF/XRD on Instellar grains, ESRF Beamline ID13 (11/11/2008 until 16/11/2008)
13. Confocal XANES on diamond inclusions, Hasylab Beamline L (19/11/2008 until 24/11/2008)
14. Three-dimensional micro-XRF/XANES V, Hasylab Beamline L (02/06/2009 until 08/06/2009)
15. Three-dimensional micro-XRF/XANES VI, Hasylab Beamline L (01/11/2009 until 07/11/2009)
16. Conventional/Confocal XANES, ESRF Beamline BM26 (DUBBLE) (12/02/2010 until 19/02/2010)
17. Three-dimensional micro-XRF/XANES VII, Hasylab Beamline L (21/05/2010 until 27/05/2010)

Bibliography

F. Adams (2008). Analytical atomic spectrometry and imaging: Looking backward from 2020 to 1975. *Spectrochimica Acta Part B*, 63:738–745.

J. Als-Nielsen & D. McMorrow (2001). *Elements of modern X-ray physics*. John Wiley & Sons, Ltd.

N. Alstad, L. Skardal & D. Hessen (1999). The effect of calcium concentration on the calcification of daphnia magna. *Limnol. Oceanogr.*, 44:2011–2017.

S. Barkan (2003). A new high performance silicon drift detector for XRD and XRF applications. *Advances in X-Ray Analysis*, 46:332–337.

M. Barron & S. Albeke (2000). Calcium control of zinc uptake in rainbow trout. *Aquatic Toxicology*, 50:257–264.

B. Beckhoff, B. Kanngiesser, N. Langhof & H. Wolff (2005). *Handbook of Practical X-ray Fluorescence Analysis*. Springer.

K. Biesinger, L. Anderson & J. Eaton (1982). Chronic effects of inorganic and organic mercury on Daphnia magna: toxicity, accumulation, and los. *Arch. Environ. Contam. Toxicol.*, 11:769–774.

T. Bouvet, C. Detlefs, E. Mitchell & J. revol (2007). ESRF Science and Technology Programme 2008-2018. Technical report, European Synchrotron Radiation Facility.

Bruker AXS (2009). Bruker Handheld. URL `www.bruker-axs.com`.

A. Brunetti, M. Sanchez del Rio, G. B., A. Simionovice & A. Somogyi (2004). A library for X-ray-matter interaction cross sections for X-ray fluorescence applications. *Spectrochimica Acta Part B*, 59:1725–1731.

P. Campbell, A. Lewis, P. Chapman, A. Crowder, W. Fletcher, B. Imber, P. Luoma, S.N. an Stokes & M. Winfrey (1988). Biologically available metals in sediments. *National Research Council Canada, Ottawa*.

G. Carney & H. Shore, P. an Chandra (1986). The uptake of cadmium from a dietary and soluble source by the crustacean Daphnia magna. *Environ. Res.*, 39:290–298.

Z. Chen, L. Mayer, D. Weston, M. Bock & P. Jumars (2002). Inhibition of digestive enzyme activities by copper in the guts of various marine benthic invertebrates. *Environ. Toxicol. Chem.*, 21:1243–1248.

P. Cloetens (2009). Energy dispersive detector requirements for nanoimaging and nanoanalysis. Energy Resolving X-ray Array Detectors for Synchrotron Science Brainstorming.

V. Cnudde (2005). *Exploring the potential of X-ray tomography as a new non-destructive research tool in conservation studies of natural building stones*. Ph.D. thesis, University of Ghent.

Coolview (2005). Coolview EM 1000/TV, Electron Multiplication Low Light Level CCD Camera with Digital Gain Management System. Technical report, Photonic Science.

B. De Samber, G. Falkenberg & L. Vincze (2006). Implementation of a high resolution CCD camera for microradiography at beamline L. *Hasylab Annual Report*.

K. De Schamphelaere (2002). *Bioavailability models for predicting copper toxicity to freshwater organisms*. Ph.D. thesis, University of Ghent.

E. Di Fabrizio, F. Romanato, M. Gentili, S. Cabrini, B. Kaulich, J. Susini & R. Barret (1999). High-efficiency multilevel zone plates for keV X-rays. *Nature*, 401:895–898.

Edax (2009). Edax Eagle III. URL `www.edax.com`.

W. Elam, S. R.B., B. Scruggs & J. Nicolosi (2004). Accuracy of standardless fp analysis of bulk and thin film samples using a new atomic database. *Advances in X-Ray Analysis*, 47:104–109.

F. Elder, A. Gurewitsch, R. Langmuir & H. Pollock (1947). Radiation from electrons in a synchrotron. *Physical Review*, 71(11):829–830.

R. Erickson (1996). The effects of water chemistry on the toxicity of copper to fathead minnows. *Environ. Toxicol. Chem.*, 15:181–193.

ESRF (2009). The European Synchrotron Radiation Facility. URL `www.esrf.eu`.

European XFEL (2009). Brilliances with time. URL `http://www.xfel.eu/`.

G. Falkenberg (2006). Characterization of a Strongly Focussing Capillary Half-lens. *Hasylab Annual Report*.

G. Falkenberg (2007a). More Polycapillary Half-lenses for the Hard X-ray Microprobe at Beamline L. *Hasylab Annual Report 2007*, pp. 1643–1644.

G. Falkenberg (2007b). Personal communication.

G. Falkenberg, O. Clauss, A. Swiderski & T. Tschentscher (2001). X-ray Optics for the Microfocus Beamline L. *Nucl. Instrum. Methods Phys. Res. A.*, 467-468:737–740.

G. Falkenberg, R. Dietsch, U. Fittschen, R. Simon & D. Weissbach (2007a). A New Approach to Free Standing Thin Film Reference Samples for Micro XRF Analysis. *Hasylab Annual Report 2007*, pp. 1619–1620.

G. Falkenberg, R. Dietsch, T. Holz & D. Weisbach (2007b). Energy Resolution and photon fluxes proveded by multilayer and Silicon monochromators at beamline L. *Hasylab Annual Report 2007*, pp. 1639–1640.

G. Falkenberg, T. Kracht & M. Küchbacher (2005). Fast X-Ray Fluorescence imaging in continuous scanning mode at beamline L. *Hasylab Annual Report*, Part 1:91–95.

G. Falkenberg, K. Rickers, D. H. Bilderback & R. Huang (2003). A Single-bounce Capillary for Focusing of Hard X-rays. *Hasylab Annual Report*.

L. Feng (2004). A New High Performance Silicon Drift Detector for XRF and XRF Applications. In *Hard X-ray and Gamma-ray Detector Physics V, Proceedings of SPIE, International Society of Optical Engineering*, volume 5198, pp. 103–110.

S. Fields & M. Johnston (2005). Whither model organism research. *Science*, 307:1885–1886.

L. Finney & T. O'Halloran (2003). Transition metal speciation in the cell: Insights from the chemistry of metal ion receptors. *Science*, 300:931–936.

N. Gao & K. Janssens (2004). *X-Ray Spectrometry: Recent Technological Advances*, chapter Polycapillary X-ray Optics, pp. 89–110. John Wiley & Sons, Ltd.

W. Gibson & M. Kumakhov (1992). Guiding and focusing neutron beams using capillary optics. *Nature*, 357(6377):391–393.

J. Goldstein, D. Newbury, D. Joy, C. Lyman, P. Echlin, E. Lifshin, L. Sawyer & J. Michael (2004). *Scanning Electron Microscopy and X-ray Microanalysis*, chapter Low temperature specimen preparation. Springer.

J. Goldstein, D. Newbury, D. Joy, C. Lyman, P. Echlin, E. Lifshin, L. Sawyer & J. Michael (2007). *Scanning Electron Microscopy and X-ray Microanalysis*, chapter Ambient-Temperature Specimen Preparation of Biological Material. Springer.

B. Golosio, A. Simionovici, A. Somogyi, L. Lemelle, M. Chukalina & A. Brunetti (2003). Internal elemental microanalysis combining X-ray fluorescence, Compton and transmission tomography. *Journal of Applied Physics*, 94(1):145–156.

R. Guan & W.-X. Wang (2004). Dietary assimilation and elimination of cd, se and zn by daphnia magna at different metal concentrations. *Environmental Toxicology and Chemistry*, 23(11):2689–2698.

T. Hall (1982). Free ionic nickel accumulation and localization in the freshwater zooplankter Daphnia magna. *Limnol. Oceanogr.*, 27:718–727.

H. Haraguchi (2004). Metallomics as integrated biometal science. *J. Anal. At. Spectrom.*, 19:5–14.

Hasylab (2009a). Lectures Students at Teaching. URL `www.hasylab.de`.

Hasylab (2009b). The Hamburg Synchrotronstrahlungslabor. URL `www.hasylab.de`.

Hasylab (2009c). What is SR, how is it generated and what are its properties? URL `www.hasylab.de`.

E. Haug & W. Nakel (2004). *The elementary process of bremsstrahlung*. World Scientific.

G. Heijerick, K. De Schamphelaere, P. Van Sprang & C. Janssen (2005). Development of a chronic zinc biotic ligand model for Daphnia Magna. *Ecotoxicology and Environmental Safety*, 62:1–10.

O. Hignette, P. Cloetens, G. Rostaing, P. Bernard & C. Morabe (2005). Efficient sub 100 nm focussing of hard X rays. *Review of scientific instruments*, 76(6):063709.

C. Hogstrand, S. Reid & C. Wood (1995). Ca versus Zn transport in the gills of freshwater rainbow-trout and the cost of adaptation to waterborne Zn. *Journal of Experimental Biology*, 198:337–348.

C. Hogstrand, P. Verbost, S. Bonga & C. Wood (1996). Mechanisms of zinc uptake in gills of freshwater rainbow trout: interplay with calcium transport. *Am. J. Phys.*, 270(1141-1147).

S. Hopkin (1989). *Ecophysiology of metals in terrestrial invertebrates*. Elsevier Applied Science Publishers, Barking, UK.

Y. Hosokawa, S. Ozawa, H. Nakazawa & Y. Nakayama (1997). An x-ray guide tube and a desk-top scanning x-ray microscope. *X-Ray Spectrometry*, 26(6):380–387.

ICME (1995). Persistence, bioaccumulation and toxicity of metals and metal compounds. *Parametrix*.

A. Ide-Ektessabi (2007). *Applications of Synchrotron Radiation: Micro Beams in Cell Micro Biology and Medicine*. Springer.

Innov-X Systems (2009). Handheld XRF Overview. URL `www.innovx.com`.

S. Iwanczyk (1999). Large Area Silicon Drift Detectors for X-Rays-New Results. *IEEE Trans. Nucl. Sci.*, 46:284–288.

J. Jackson (1975). *Classical Electrodynamics*. New York: Wiley.

C. Jacobsen (2009). Compound refractive lenses for X-rays. URL `http://laser.physics.sunysb.edu/~tanya/report1/`.

K. Janssens, K. Proost & G. Falkenberg (2004). Confocal microscopic x-ray fluorescence at the hasylab microfocus beamline: characteristics and possibilities. *Spectrochimica Acta Part B*, 59:1637–1645.

K. Janssens, B. Vekemans, L. Vincze & A. Rindby (1996). A micro-XRF spectrometer based on a rotating anode generator and capillary optics. *Spectrochimica Acta Part B-Atomic Spectroscopy*, 51:1661–1678.

A. C. Kak & M. Slaney (1988). *Principle of Computerised Tomographic Imaging*. The institute of Electrical and Electronics Engineers.

B. Kanngieser, W. Malzer, M. Pagels, L. Lühl & G. Weseloh (2007). Three-dimensional micro-XRF under cryogenic conditions: a pilot experiment for spatially resolved trace analysis in biological specimens. *Anal Bioanal Chem*, 389(1171-1176).

B. Kanngieser, W. Malzer & I. Reiche (2003). A new 3d micro x-ray fluorescence analysis set-up - first archaemetric applications. *Nucl. Instrum. Methods Phys. Res.*, 211(2):259–264.

Karnovsky (1965). A formaldehyde-glutaraldehyde fixative of high osmolality for use in electron microscopy. *J. Cell. Biol.*, 27:137–138.

M. Kemp (2008). Seeing the smaller picture. *Nature*, 453:596.

L. Kempenaers, C. De Koster, W. Van Borm & K. Janssens (2000a). Micro-heterogeneity study of trace elements in BCR CRM 680 by means of synchrotron micro-XRF. *Fresenius J Anal Chem*, 369:733–737.

L. Kempenaers, K. Janssen, L. Vincze, B. Vekemans, A. Somogyi, M. Drakopoulos, A. Simionovici & F. Adams (2002). A Monte Carlo Model for Studying the Microheterogeneity of Trace Elements in Reference Materials by Means of Synchrotron Microsocpic X-ray Fluorescence. *Anal. Chem*, 74:5017–5026.

L. Kempenaers, L. Vincze & K. Janssens (1999). The use of synchrotron micro-XRF for characterisation of the micro-heterogeneity of low-Z reference materials containing heavy metals. *Hasylab Annual Report*.

L. Kempenaers, L. Vincze & K. Janssens (2000b). The use of synchrotron micro-XRF for characterisation of the micro-heterogeneity of heavy metals in low-Z reference materials. *Spectrochimica Acta Part B*, 55:651–669.

S. Kikuchi & M. Matsumasa (1997). Ultrastructural evidence for osmoregulatory function of the sternal epithelia in some gammaridean amphipods. *Journal of Crustacean Biology*, 17:377–388.

G. Knol (1979). *Radiation Detection and Measurement*. John Wiley and Sons.

Komitee Forshung mit Synchrotronstrahlung (2009). What is synchrotron radiation. URL `http://www.physik.uni-kiel.de/kfs/Infos/Quellen/synchrotronradiation.php?menu=s`.

T. Kracht & T. Núnez (2007). Recent Developments in Computing. *Hasylab Annual Report 2007*, pp. 363–364.

C. Laforsch & R. Tollrian (2000). A new preparation technique of Daphnids for scanning electron microscopy using hexmethyldisilazane. *Archiv fur Hydrobiologie*, pp. 587–596.

Leica microsystems (2009). Electron microscope sample preparation. URL `http://www.leica-microsystems.com/products/electron-microscope-sample-preparation/`.

M. Linder (1991). *Nutritional Biochemistry and Metabolism with Clinical Applications*, chapter Nutrition and metabolism of the trace elements, pp. 215–276. Elsevier, New York, NY.

L. Maltby & C. Naylor (1990). Preliminary observation on the ecological relevance of the gammaus scope for growth assay: effect of zinc on reproduction - functional ecology. *New Horizons in Ecotoxicology*, pp. 393–397.

I. Marigomez, M. Soto, M. Cajaraville, E. Angulo & L. Giamberini (2002). Cellular and subcellular distribution of metals in molluscs. *Micros. Res. Tech.*, 56:358–392.

A. Mason & K. Jenkins (1995). *Metal Speciation and Bioavailability in Aquatic Systems*, chapter Metal Detoxification in Aquatic Organisms, pp. 479–608. John Wiley & Sons, NY, USA.

B. Masschaele, V. Cnudde, M. Dierick, P. Jacobs & J. Vlassenbroeck (2007). Ugct: New x-ray radiography and tomography facility. *Nucl. Instrum. Methods Phys. Res. A.*, 580:266–269.

H. Mimura, S. Matsuyama, H. Yumoto, H. Hara, K. Yamamuro, Y. Sano, K. Endo, Y. Mori, M. Yabashi, Y. Nishino, K. Tamasaku, T. Ishikawa & K. Yamauchi (2007). Efficient focusing of hard x rays to 25 nm by a total reflection mirror. *Applied Physics Letters*, 90:051903.

J. Molloy & R. Sieber (2008). Classification of microheterogeneity in solid sample using micro-XRF. *Anal Bioanal Chem*, 392:995–1001.

B. Muyssen, K. De Schamphelaere & C. Janssen (2006). Mechanisms of chronic waterborne zn toxicity in daphnia magna. *Aquatic Toxicology*, 77:393–401.

B. Muyssen & C. Janssen (2002). Accumulation and regulation of zn in Daphnia magna: links with homeostasis and toxicity. *Archives of Environmental Contamination and Toxicology*, 43:492–496.

M. Newman & C. Jagoe (1994). *Bioavailability: Physical, Chemical and Biological Interactions*, chapter Ligands and the Bioavailability of Metals in Aquatic Environments. Lewis Publishers, Boca Raton, USA.

M. Newville (2009). Fundamentals of X-ray Absorption Spectroscopy. URL `http://cars9.uchicago.edu/xafs/xas_fun/xas_fundamentals.pdf`.

Nobel Prize Website (2009). Nobelprize.org. URL `http://nobelprize.org`.

Oxford Cryosystems (2009a). 700 series nitrogen gas cryostream cooler. Technical report, Oxford Cryosystems.

Oxford Cryosystems (2009b). Desktop cooler simple stress-free cooling. Technical report, Oxford Cryosystems.

Oxford Instruments (2009). X-MET 5000. URL `www.oxford-instruments.com`.

OxfordCryosystems (2009). Cobra non-liquid nitrogen cryostream. Technical report, Oxford Cryosystems.

P. Paquin, J. Gorsuch, S. Apte, G. Batley, K. Bowles, P. Campbell, C. Delos, D. Dit Toro, R. Dwyer, F. Galvez, R. Gensemer, G. Goss, C. Hogstrand, C. Janssen, J. McGeer, R. Naddy, R. Playle, R. Santore, U. Scheider, W. Stubblefield, C. Wood & K. Wu (2002). The biotic ligand model: a historical overview. *Comp. Biochem. Phys. C*, 133:3–35.

R. Peter (1987). *Daphnia*. Istituto Italiano di Idrobiologia.

C. Petitbois & M. Guidi (2008). Bioimaging of cells and tissues using accelerator-based sources. *Anal Bioanal Chem*, 391:1599–1608.

Photon Production Laboratory (2009). Mirrorcle. URL `www.photon-production.co.jp`.

R. Pirow, F. Wollinger & R. Paul (1999a). The importance of the feeding current for oxygen uptake in the water flea Daphnia magna. *The Journal of Experimental Biology*, 202:553–562.

R. Pirow, F. Wollinger & R. Paul (1999b). The sites of respiratory gas exchange in the planktonic crustacean Daphnia magna: an in vivo study employing blood haemoglobin as an internal oxygen probe. *The Journal of Experimental Biology*, 202:553–562.

H. Poynton, J. Varshavsky, B. Chang, G. Cavigiolio, S. Chan, P. Holman, A. Loguinov, D. Bauer, K. Komachi, E. Theil, E. Theil, E. Perkens, O. Hughes & C. Vulpe (2007). Daphnia magna ecotoxicogenomics provides mechanistic insights into metal toxicity. *Environ. Sci. Technol.*, 41:1044–1050.

K. Proost, K. Janssens, L. Vincze, G. Falkenberg, N. Gao & P. Bly (2002). Feasibility and characteristics of Confocal micro-XRF as Hasylab BL L. *Hasylab Annual Report*.

Quorumtech (2009). K750X peltier cooled freeze dryer. URL `www.quorumtech.com`.

C. Raven (1998). *Microimaging and Tomography with High Energy Coherent Synchrotron X-Rays*. Ph.D. thesis, RWTH Aachen.

A. Rindby (1986). Applications of fiber technique in the x-ray region. *Nucl. Instrum. Methods Phys. Res. A.*, 249(2-3):536–540.

A. Rindby, A. Engstrom, S. Larsson & B. Stocklassa (1989). Microbeam technique for energy-despersive x-ray fluorescence. *X-Ray Spectrometry*, 28(109).

R. Rousseau (2006). Corrections for matrix effects in x-ray fluorescence analysis-a tutorial. *Spectrochimica Acta Part B*, 61:759–777.

J. Russ (1995). *The Image Processing Handbook*. CRC Press.

R. Ruth (2009). The compact light source. URL `http://www.lynceantech.com`.

RWTH Aachen (2009). Compound refractive lenses for X-rays. URL `http://www.institut2b.physik.rwth-aachen.de/xray/imaging/crl.html`.

C. Ryan, D. Siddons, G. Moorhead, R. Kirkham, G. De Geronimo, B. Etschmann, A. Dragone, P. Dunn, A. Kuczewski, P. Davey, M. Jensen, J. Ablett, J. Kuczewski, R. Hough & D. Paterson (2009). High-throughput X-ray fluorescence imaging using a massively parallel detector array, integrated scanning and real-time spectral deconvolution. *Journal of Physics: Conference Series*.

K. Ryan (1992). Cryofixation of tissues for electron-microscopy: A review of plunge cooling methods. *Scanning Microscopy*, 6:715–743.

A. Sasov, X. Liu & D. Rushmer (2008). Compact Micro-CT/Micro-XRF system for non-destructive 3D analysis of internal chemical composition. *Developments in X-ray Tomography VI*, 7078:780.

C. Schroer (2001). Reconstructing X-ray fluorescence microtomograms. *Applied Physics Letters*, 79(12):1912–1914.

T. Schultz & J. Kennedy (1976). Fine-structure of digestive system of Daphnia pulex. *Tissue & Cell*, 8:479–490.

M. Seidl, R. Pirow & R. J. Paul (2002). Water fleas provide a separate ventilatory mechanism for their brood. *Zoology*, 105(15-23).

Silson (2009). URL `www.silson.com`.

G. Silversmit, B. Vekemans, S. Nikitenko, W. Bras, V. Czhech, G. Zaray, I. Szaloki & L. Vincze (2009). Polycapillary-optics-based micro-XANES and micro-EXAFS at a third-generation bending-magnet beamline. *Journal of Synchrotron Radiation*, 16:237–246.

Skyray (2009). Pocket-III. URL `www.skyray-instrument.com`.

A. Snigirev (1996). A compound refractive lens for focusing high-energy X-rays. *Nature*, 384:49–51.

V. Solé, E. Papillon, M. Cotte, P. Walter & J. Susini (2007). A multiplatform code for the analysis of energy-dispersive X-ray fluorescence spectra. *Spectrochimica Acta Part B*, 62:63–68.

A. Somogyi, K. Janssen, L. Vincze, B. Vekemans, A. Rindby & F. Adams (2000). Interpretation and use of inter-element correlation graphs obtained by scanning X-ray fluorescence micro-beam spectrometry from individual particles. *Spectrochimica Acta Part B-Atomic Spectroscopy*, 55:75–89.

A. Somogyi, R. Tucoulou, G. Martinez-Criado, A. Homs, J. Cauzid, P. Bleuet, S. Bohic & A. Simionovici (2004). ID22: a multitechnique hard X-ray microprobe beamline at the European Synchrotron Radiation Facility. *J. Synchr. Rad.*, 12:208–212.

M. Soto, I. Marigomez & I. Cancio (2009). Biological aspects of metal accumulation and storage. URL `http://www.ehu.es/europeanclass2003/biological_aspects_of_metal_accu.htm`.

Spectro (2009). Spectro xSORT. URL `www.spectro.com`.

D. Spry & C. Wood (1985). Ion flux rates, acid-base status, and blood-gases in rainbow-trout, salmo-gairdneri, exposed to toxic zinc in natural soft-water. *Can. J. Fish Aquat. Sci.*, 42:1332–1341.

A. Spurr (1969). A low viscosity resin embeddding medium for electron microscopy. *J Ultrastruct Res*, 1:31–43.

F. Stanley (2003). *Studies on the metal-containing granules in the mussels*. Ph.D. thesis, Murdoch University.

D. Studer, W. Graber, A. Al-Amoudi & P. Eggli (2001). A new approach for cryofixation by high-pressure freezing. *J. Microsc.*, 203(3):285–294.

J. Susini, M. Salome, R. Tucoulou, G. Martinez-Criado, S. Bohic, D. Eichert, P. Bleuet, I. Letard, M. Cotte, J. Cauzid, B. Fayard, R. Baker & S. Laboure (2006). X-ray microanalysis activities at the esrf. *Proc. 8th Conf. X-ray Microscopy*, 7:18–21.

J. Szpunar (2004). Metallomics: a new frontier in analytical chemistry. *Anal Bioanal Chem*, 378:54–56.

Thermo Scientific (2009). NITON XRF Analyzers. URL `www.niton.com`.

T. Trojek, T. Cechak & M. L. (2008). Ratios of fluorescence X-rays as an information source on the depth distribution of iron in a low z matrix. *Analytical Sciences*, 24.

R. Truhaut (1977). Eco-Toxicology - objectives, principles and perspectives. *Ecotoxicology and Environmental Safety*, 1(2):151–173.

B. Vallee (1991). *New Trends in Bioinorganic Chemistry*, chapter Zinc biochemistry and physiology, pp. 11–57. Academic, London, UK.

F. Van Assche (1996). Environmental risk assessment for essential elements. In E. Langley & S. Mangas, editors, *Zinc-Report of an International Meeting*, 2, pp. 33–47. National Environmental Health monographs, Adelaide, Australia.

R. Van Grieken & A. Markowicz (2002). *Handbook of X-Ray Spectrometry: Methods and Techniques*. Marcel Dekker, Inc.

B. Vekemans (2000). *Microscopische X-stralen fluorescentie analyse: instrument-bouw en methode-ontwikkeling*. Ph.D. thesis, Universiteit Antwerpen.

B. Vekemans, K. Janssen, L. Vincze, F. Adams & P. Van Espen (1995). Comparison of several background compensation methods useful for evaluation of energy-dispersive X-ray fluorescence spectra. *Spectrochimica Acta*, 50:149–169.

B. Vekemans, K. Janssens, L. Vincze, F. Adams & P. Vanespen (1994). Analysis of X-Ray Spectra by Iterative Least-Squares (AXIL)-New Developments. *X-Ray Spectrometry*, 23(6):278–285.

L. Vincze (1995). *Monto Carlo Simulation of Conventional and Synchrotron X-ray Fluorescence Spectrometers*. Ph.D. thesis, Universiteit Antwerpen.

L. Vincze (2004). *X-Ray Spectrometry: Recent Technological Advances*, chapter 6. New Computerisaton Methods, pp. 435–461. John Wiley & Sons, Ltd.

L. Vincze, K. Janssens, B. Vekemans & F. Adams (1999). Monte Carlo simulation of X-ray fluorescence spectra: Part 4. Photon scattering at high X-ray energies. *Spectrochimica Acta*, 54:1711–1722.

L. Vincze, A. Somogyi, J. Osán, B. Vekemans, S. Török, K. Janssens & F. Adams (2002). Quantitative Trace Element Analysis of Individual Fly Ash Particles by Means of X-ray Microfluorescence. *Analytical Chemistry*, (74):1128–1135.

L. Vincze, B. Vekemans, F. Brenker, G. Falkenberg, K. Rickers, A. Somogyi, M. Kersten & F. Adams (2004). Three-Dimensional Trace Element Analysis by Confocal X-ray Microfluorescence Imaging. *Analytical Chemistry*, 76:6786–6791.

A. Von Bohlen & M. Tolan (2008). Editorial for synchrotron radiation. *J. Anal. At. Spectrom.*, 23:790–791.

S. Waervagen, N. Rukke & D. Hessen (2002). calcium content of crustacean zooplankton and its potential role in species distribution. *Freshwater Biol.*, 47(1866-1878).

J. Wagner (1979). *Fundamentals of clinical pharmacokinetics*. Drug intelligence publications, Inc., Hamilton, IL, USA.

W. Wallace, B. Lee & S. Luoma (2003). Subcellular compartmentalization of Cd and Zn in two bivalves. I. Significance of metal-sensitive fractions (MSF) and biologically detoxified metal (BDM). *Marine Ecology-Progress Series*, 249:183–197.

W. Wallace & S. Luoma (2003). Subcellular compartmentalization of Cd and Zn in two bivalves. II. Significance of trophically available metal (TAM). *Marine Ecology-Progress Series*, 183:125–137.

E. Watts & M. Petri (1981). A scanning electron microscope study of the thoracic appendages of Daphnia magna Strauss. *Journal of Natural history*, 15:463–473.

E. Weckert (2004). *PETRA III: A Low Emittance Synchrotron Radiation Source*. DESY.

Wikipedia (2009a). K-means clustering. URL `http://en.wikipedia.org/wiki/K-means_clustering`.

Wikipedia (2009b). Synchrotron Radiation. URL `http://en.wikipedia.org/`.

Wikipedia (2009c). X-ray tube. URL `http://en.wikipedia.og/`.

XRadia (2009a). Fresnel zone plate lenses. URL `http://www.xraymicroscopy.com/Products/zoneplates.html`.

XRadia (2009b). Nano XFI imager. URL `www.xradia.com`.

XRadia (2009c). Resolution and calibration targets. URL `www.xradia.com`.

R. Zeisler, S. Christopher, S. Long, E. Macky, K. Murphy & R. Spatz (2009). NIST renews benchmark SRMs for accurate determinations of trace elements in serum and liver. Technical report, NIST.